Novel Saturable Absorber Materials and Devices for Laser Modelocking

by

Igor P. Bilinsky

B.S., Moscow Institute of Physics and Technology (1992)

Submitted to the Department of Physics
in Partial Fulfillment of the Requirements for the
Degree of
Doctor of Philosophy in Physics
at the
Massachusetts Institute of Technology
February 1999

© 1998 Massachusetts Institute of Technology
All Rights Reserved

Signature of Author ______________________
Department of Physics
November 30, 1998

Certified by ______________________
James G. Fujimoto
Professor of Electrical Engineering
Thesis Supervisor

Certified by ______________________
Daniel Kleppner
Lester Wolfe Professor of Physics
Thesis Co-Supervisor

Accepted by ______________________
Thomas J. Greytak
Professor of Physics, Associate Department Head for Education

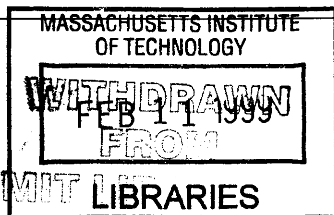
MASSACHUSETTS INSTITUTE OF TECHNOLOGY
FEB 11 1999
LIBRARIES
Science

Novel Saturable Absorber Materials and Devices for Laser Modelocking

by

Igor P. Bilinsky

Submitted to the Department of Physics on November 30, 1998 in partial fulfillment of the requirements for the degree of Doctor of Philosophy in Physics

Abstract

The recently developed semiconductor saturable absorbers have made a major impact on the field of ultrashort pulse generation. Most of the previously demonstrated saturable absorber structures require epitaxial fabrication techniques which impose severe design constraints leading to performance limitations. In addition, the complexity and cost of epitaxial fabrication limit the widespread application of such devices. The goal of this thesis was to develop simpler and more versatile saturable absorber materials and devices, investigate their properties, and apply them to ultrashort pulse generation from solid-state lasers. Three types of saturable absorbers were studied, namely semiconductor saturable Bragg reflectors, semiconductor-doped glasses, and thin silica films doped with semiconductor quantum dots.

Modeling of optical properties of epitaxially grown saturable Bragg reflectors was performed. Reflectivity, dispersion, and electric field distribution were calculated for various saturable Bragg reflector designs. The demonstrated techniques can be applied to analysis of arbitrary multilayer dielectric structures incorporating saturable absorbers.

Using several different semiconductor-doped glasses, self-starting fast saturable absorber passive modelocking and saturable-absorber-assisted Kerr Lens Modelocking of a Ti:sapphire laser were demonstrated. Nonlinear absorption dynamics of the semiconductor-doped glasses were investigated using a pump-probe technique. Photodarkening effects in the glasses were observed and characterized on a femtosecond time scale.

A new saturable-absorber materials system for solid-state laser modelocking was developed, based on thin, nonepitaxially grown, semiconductor-doped films. Films of InAs and GaSb semiconductor quantum dots in silica were fabricated using rf sputtering. The properties of InAs-doped silica films were characterized by means of linear and nonlinear absorption spectroscopy, femtosecond pump-probe technique, x-ray photoemission spectroscopy, transmission electron microscopy, energy dispersive x-ray spectroscopy, and electron diffraction. The absorption saturation cross-section and recovery time could be adjusted by use of rapid thermal annealing.

For the first time, an application of semiconductor-doped dielectric films to laser modelocking was demonstrated. Self-starting saturable-absorber-assisted Kerr Lens Modelocking operation of a Ti:sapphire laser was achieved using InAs-doped silica films fabricated by rf sputtering. The concept of semiconductor-doped dielectric films can be extended to a number of dopants and host materials to obtain simple and versatile saturable absorbers for ultrashort pulse generation from various solid-state lasers.

Thesis Supervisor: James G. Fujimoto
Title: Professor of Electrical Engineering

Thesis Co-Supervisor: Daniel Kleppner
Title: Lester Wolfe Professor of Physics

Acknowledgments

The moment has come. The moment to which I have been looking forward for a long time. The moment to write the most frequently read part of this thesis.

The work I have done over the past six years would not have been possible without the contributions, direct and indirect, of a large number of individuals. I would like to thank all of you.

I would like to thank Professor James Fujimoto for giving me the opportunity to work in one of the world's leading femtosecond optics laboratories, for his ideas and support. My thanks go to Professors Erich Ippen and Hermann Haus for their help over the years. In addition, I would like to thank Professor Ippen for serving on my thesis committee. I am grateful to Professor Daniel Kleppner for helping me come to MIT, for being my academic advisor during these years, and for serving on my thesis committee. It was a pleasure meeting Professor June Matthews and I would like to thank her for being a member of my thesis committee.

I was fortunate to work closely with a number of extraordinary individuals who not only helped me in my work and professional development, but also were great people to discuss life, Universe, and everything, to share long junky lunches, to go on ski and long CLEO trips, etc. Dr. Brett Bouma taught me a lot about modelocking and about the ways to make things work in the lab. We spent a lot of time working together, both at MIT and in such an unlikely place as Nashville, TN and I always enjoyed his advice and his company. I shared a lot of late nights and late mornings in the lab with Boris Golubovic, Costas Pitris, Gary Tearney, and Stephen Boppart, and I learned a lot from each of them. My thanks go to Rohit Prasankumar who helped me with the later stages of this research and I wish him success in the further development of saturable absorber films. I would like to thank Nick Ulman and Chi-Kuang Sun who taught me the basics of the 'femtosecond art'. I would like to thank Dave "Hey Guy" Jones, Nanda Ramanujam, Ravi Ghanta, Erik Thoen, Mike Hee, Lynn Nelson, Malini Paye, Siegfried Fleischer, Dave Dougherty, and Charlie Hultgren for their camaraderie. My special thanks go to Cindy Kopf for making the paperwork move, for resolving all those numerous administrative details, and for adding a touch of humor to the daily routine.

I am thankful to my collaborators at the MIT Lincoln Laboratory, Dr. Jim Walpole, Leo Missaggia, Bob Bailey, Paul Nitishin, and the other members of group 83. Without their help and support this work would not have been possible. The advice and insights of Dr. Walpole were critical for the success of this research and I greatly enjoyed our numerous conversations. Leo Missaggia taught me a lot about the clean room techniques and was always a fun person to talk to.

I am thankful to Elizabeth Koontz for fabricating the SBRs and for sharing her film deposition knowledge with me. I would like to thank Dr. Anthony Garratt-Reed for helping me with the TEM measurements and Libby Shaw for her assistance with the XPS characterization of my samples.

I would like to thank Dr. Eric McFarland and all the folks at Symyx Technologies for the opportunity to see and appreciate the small company world during the summer I spent there, and for being able to contribute to the company growth.

I would like to thank all my friends for making graduate school so much fun for me.

I would like to thank all my teachers, past and present, for helping me along the way.

I would like to thank my parents and my brother Oleg for their faith in me, for their love and support. You are far away but I always feel your presence.

Finally, in addition to doing all this physics in graduate school, I met my wife Elena. Or should I say that in addition to meeting Elena, I studied physics? The second sentence seems to more precisely reflect the significance of these events to my life as a whole. Jokes aside, I would like to thank Elena for her love, patience, and support over the years of my Ph.D. work.

I acknowledge all those who helped me, for making my life easier, and all those who did not help, for not letting me relax too much. Thank you all.

Contents

Chapter 1 **17**

Introduction

Chapter 2 **23**

Laser modelocking

2.1 Introduction 23

2.2 Passive modelocking 24

2.3 Self-starting modelocking operation 33

2.4 Kerr lens modelocking 36

2.5 Saturable absorbers for laser modelocking 40

2.5.1 Linear absorption....41

2.5.2 Nonsaturable losses 42

2.5.3 Absorption saturation intensity and fluence....42

2.5.4 Absorption recovery time....46

2.5.5 Bandwidth of operation and other characteristics 49

2.6 Epitaxially-grown semiconductor saturable absorbers 51

2.6.1 Semiconductor saturable absorber mirrors and saturable Bragg reflectors....51

2.6.2 General principles of A-FPSA operation 52

2.6.3 High-finesse A-FPSA....54

2.6.4 AR-coated SESAM 55

2.6.5 Low-finesse A-FPSA (SBR) 56

2.6.6 Broadband SESAM with a silver mirror 56

2.6.7 Control of the carrier recombination dynamics....57

2.6.8 Modelocking of various laser systems using semiconductor saturable absorbers ...58

Chapter 3 63

Design of saturable Bragg reflectors

3.1 Introduction 63

3.2 SBR structure 64

3.3 Reflectivity and bandwidth 65

3.4 Dispersion...68

3.5 Field distribution inside an SBR 72

3.6 Two-photon absorption effects...76

3.7 Conclusions 81

Chapter 4 83

Semiconductor-doped glasses for laser modelocking

4.1 Introduction 83

4.2 Review of optical properties of semiconductor quantum dots 85

4.2.1 Quantum confinement effects 85

4.2.2 Optical properties of composite materials..91

4.3 Linear optical properties...93

4.4 Saturable absorber devices incorporating semiconductor-doped glass............95

4.5 Absorption saturation dynamics and photodarkening effects 96

4.6 Application of semiconductor doped glasses to laser modelocking 105

4.6.1 Saturable absorber modelocking 105

4.6.2 Saturable absorber assisted Kerr lens modelocking.....................................107

4.6.3 Modelocking self-starting dynamics 109

4.7 Conclusions 111

Chapter 5 114

Semiconductor-nanocrystallite-doped silica films

5.1 Introduction 114

5.2 Film fabrication 116
5.2.1 RF sputtering technique 116
5.2.2 Post-annealing 118
5.2.3 Selection of semiconductor dopants 120
5.2.4 Fabrication of RG-850 films 121
5.2.5 Fabrication of GaSb-doped silica films 123
5.2.6 Fabrication of InAs-doped silica films 126
5.3 Chemical composition of InAs-doped films (XPS) 129
5.4 Film morphology (TEM) 137
5.5 Element distribution within the film (STEM + EDX) 139
5.6 Nanoparticle crystalline structure (electron diffraction) 142
5.7 Linear optical properties 148
5.8 Nonlinear optical properties 152
5.8.1 Pump-probe measurements 152
5.8.2 Single-beam absorption saturation measurements 155
5.9 Conclusions 160

Chapter 6 **162**

Application of InAs-doped films to modelocking initiation in a Ti:Al2O3 laser

6.1 Introduction 162
6.2 Transmissive saturable absorber devices 163
6.3 Laser cavity design 163
6.4 Self-starting modelocking operation using InAs-doped films for KLM initiation 165
6.5 Wavelength tuning 168
6.6 Self-starting operation for various intracavity dispersions 169
6.7 Pulse instabilities for high pump powers 170
6.8 Saturable absorber operation without KLM 174
6.9 Design of reflective saturable absorber devices 177
6.10 Conclusions 182

Chapter 7 184

Summary and future work

Appendix A 190

Design of multilayer dielectric stacks

Appendix B 204

Sputtering deposition procedure

Appendix C 207

Photolithography procedure

References 209

List of figures

Figure 2-1 25
Passive saturable absorber modelocking (a) with a fast saturable absorber and (b) with a slow saturable absorber and dynamic gain saturation.([24])

Figure 2-2 29
Predictions of the master equation for fast saturable absorber modelocking. Normalized pulse parameters are plotted as a function of normalized dispersion for constant saturable absorber action and varying self-phase modulation. a) Chirp parameter. b) Pulse duration. c) Stability parameter. d) Bandwidth. [33]

Figure 2-3 33
Pulse shortening rates for the various modelocking mechanisms.

Figure 2-4 37
Schematic of KLM operation.

Figure 2-5 38
Schematic of a typical KLM laser cavity. HR, high reflector; P, Brewster-cut prism; CM, curved mirror; OC, output coupler.

Figure 2-6 43
Nonlinear absorption change of a saturable absorber due to absorption bleaching with cw intensity. |dA/dI| is an important parameter for modelocking initiation.

Figure 2-7 44
Nonlinear absorption change of a saturable absorber due to absorption bleaching with short pulses.

Figure 2-8 52
Semiconductor saturable absorber mirror devices in historical order. a) High-finesse A-FPSA. b) Thin AR-coated device. c) SBR (low-finesse A-FPSA). ([22])

Figure 3-1 65
a) Schematic of the saturable Bragg reflector (Sub |(AlAs GaAs)22 Cap| Air). b) Cap layer design for a high saturation intensity device. c) Cap layer design for a low saturation intensity device.

Figure 3-2 66
Calculated GaAs/AlAs DBR (Sub |(AlAs GaAs)N| Air) reflectivity as a function of number of quarter-wave pairs N.

Figure 3-3 67
Comparison of measured and calculated transmission through a GaAs/AlAs DBR (Sub |(AlAs GaAs)22| Air). The calculated data accounts for the 30% Fresnel reflection from the back side of an SBR substrate.

Figure 3-4 68

Measured transmission of a GaAs/AlAs DBR (Sub |(AlAs GaAs)22| Air). The transmission is a strong function of the position on the 2-inch wafer. The four traces correspond to the locations shown on the wafer schematic.

Figure 3-5 69
Calculated reflectivity of a GaAs/AlAs DBR (Sub |(AlAs GaAs)22 InP| Air) with a quarter-wave InP cap layer. The peak reflectivity is decreased significantly compared to an uncapped DBR. For a half-wave cap layer (not shown) the high DBR reflectivity was not affected.

Figure 3-6 70
Calculated reflectivity and phase acquired on reflection for a GaAs/AlAs DBR capped with a half-wave layer of InP (Sub |(AlAs GaAs)22InP InP| Air).

Figure 3-7 71
Calculated group delay dispersion and reflectivity of a GaAs/AlAs DBR capped with a half-wave layer of InP (Sub |(AlAs GaAs)22InP InP| Air).

Figure 3-8 71
Calculated third order dispersion and reflectivity of a GaAs/AlAs DBR capped with a half-wave layer of InP (Sub |(AlAs GaAs)22InP InP| Air).

Figure 3-9 73
Calculated field distribution at the center wavelength (1.55 μm) inside a GaAs/AlAs DBR capped with a half-wave layer of InP (Sub |(AlAs GaAs)22InP InP| Air).

Figure 3-10 74
Calculated field distribution at the center wavelength (1.55 μm) inside a GaAs/AlAs DBR capped with a quarter-wave layer of InP (Sub |(AlAs GaAs)22InP| Air).

Figure 3-11 75
PL (solid line) and transmission data (dotted line) for a high-saturation intensity SBR (Sub |(AlAs GaAs)22InP InP| Air). PL output is depressed in the SBR stop-band due to the quantum wells' location at the node of a standing wave (see Figure 2-1).

Figure 3-12 76
Calculated field distribution inside the top layers of a GaAs/AlAs SBR capped with a half-wave InP layer (Sub |(AlAs GaAs)22InP InP| Air) for three different wavelengths.

Figure 3-13 77
Proposed structure for an epitaxially-grown semiconductor saturable absorber mirror without a DBR and with no need for extensive post-processing.

Figure 3-14 80
Energy fluence dependence of reflectivity for an AR-coated SBR. Two-photon absorption effects are observed at high energy densities. Data courtesy of E. Thoen.

Figure 4-1 93
Measured transmission of the three investigated Schott semiconductor doped glasses. Glass thickness 200 μm.

Figure 4-2 94

Measured absorption coefficients of three investigated Schott semiconductor doped glasses.

Figure 4-3 ... 96
Saturable absorber structure using Schott semiconductor doped glass. CG, colored glass; G, glue; S, substrate.

Figure 4-4 ... 97
Schematic of the pump-probe setup.

Figure 4-5 ... 98
Spot size measurement using a knife-edge scan. The beam waist diameter was measured to be 40 μm.

Figure 4-6 ... 99
Absorption saturation dynamics of 'fresh' RG-830 glass. The pump average power was 6 mW at 820 nm.

Figure 4-7 ... 101
Pump-probe traces of RG-830 glass on sapphire showing faster absorption recovery times due to the photodarkening effect. Exposure average power is 40 mW. Exposure pulse duration is 30 fs at 80 MHz repetition rate. Pump average power is 6 mW. Exposure times, from top to bottom, 0, 1, 2, 4, 8, 16, 32 minutes. The traces are vertically displaced for clarity.

Figure 4-8 ... 102
Pump-probe traces of RG-830 glass on sapphire showing faster absorption recovery times due to the photodarkening effect. Exposure average power is 80 mW. Exposure pulse duration is 30 fs at 80 MHz repetition rate. Pump average power is 6 mW. Exposure times, from top to bottom, 0, 1, 2, 4, 8, 16 minutes. The traces are vertically displaced for clarity.

Figure 4-9 ... 103
Pump-probe traces of RG-830 glass on sapphire showing faster absorption recovery times due to the photodarkening effect. Exposure average power is 230 mW. Exposure pulse duration is 30 fs at 80 MHz repetition rate. Pump average power is 12 mW. Exposure times, from top to bottom, 0, 1, 2, 4, 8, 16 minutes. The traces are vertically displaced for clarity.

Figure 4-10 ... 105
Laser cavity schematic: CM, 10 cm radius of curvature mirror; SA, saturable absorber; P, fused silica prism; OC, output coupler.

Figure 4-11 ... 108
Typical autocorrelation and spectrum of self-starting saturable-absorber-assisted KLM pulses. The spectrum is limited by the gradual increase of the colored glass absorption on the short wavelength side and by the mirror set reflectivity on the long wavelength side.

Figure 4-12 ... 110
Self-starting dynamics of saturable-absorber-assisted KLM using RG-850 glass structure. The modelocking build-up time is determined from the delay in the second harmonic generation (SHG) signal onset.

Figure 5-1 ... 117
Schematic of a sputtering system layout.

Figure 5-2 119
A typical rapid thermal annealing temperature trace.

Figure 5-3 122
Transmission of sputtered RG-850 films.

Figure 5-4 125
Transmission of sputtered GaSb-doped silica films and of a 500-μm-thick bulk GaSb. The two traces for the GaSb-doped films are from the same sputtering run and demonstrate the typical variation in the film absorption depending on the substrate position.

Figure 5-5 127
A typical profilometer trace of an etched InAs-doped silica film. The film thickness is 2750Å.

Figure 5-6 128
Optical absorption spectra of InAs-doped silica films on fused silica and BK-7 glass substrates. Film thickness 1200 Å. The observed oscillations in the absorption spectra are the result of interference.

Figure 5-7 130
XPS spectrum of a bulk InAs reference sample.

Figure 5-8 130
XPS spectrum of an InAs-doped silica film.

Figure 5-9 132
XPS spectrum of a bulk InAs reference sample after sputter etching. The O and C peaks produced by the contaminants have diminished significantly compared to the unsputtered InAs reference (Figure 5-7).

Figure 5-10 132
XPS spectrum of the indium 3d lines acquired from the bulk InAs reference.

Figure 5-11 133
XPS spectrum of the indium 3d lines acquired from the sputtered InAs-doped film.

Figure 5-12 133
XPS spectrum of the indium MNN Auger lines acquired from the bulk InAs reference.

Figure 5-13 134
XPS spectrum of the indium MNN Auger lines acquired from the sputtered InAs-doped film.

Figure 5-14 136
3d5/2 binding energies, M4N45N45 Auger electron energies and Auger parameters for Mg Kα excitation for various indium compounds. From reference [167].

Figure 5-15 138
Bright-field TEM image of a 150-Å-thick InAs-doped silica film. The substrate is a 100-Å-thick carbon film on a 200-μm-mesh copper grid.

Figure 5-16 138

Dark-field TEM image of a 150-Å-thick InAs-doped silica film. The substrate is a 100-Å-thick carbon film on a 200-μm-mesh copper grid.

Figure 5-17 140
EDX spectrum of a 150-Å-thick InAs-doped silica film on a 100-Å-thick carbon film on a copper grid.

Figure 5-18 141
Compositional maps of an InAs-doped silica film. The image size is 80 by 80 nm. BF, bright field image; As, arsenic; O, oxygen; In, indium.

Figure 5-19 143
Electron diffraction from a crystalline specimen. *dhkl* is the interplane separation, *q* is the diffraction angle, *L* is the camera length, and *R* is the radius of the diffraction ring.

Figure 5-20 144
Electron diffraction pattern observed for InAs-doped silica films. The concentric rings indicate a polycrystalline nature of the specimen, while the ratio of the ring radii corresponds to diamond cubic and zinc blende lattice types.

Figure 5-21 146
Selected angle dark-field image. InAs nanocrystallites oriented to match the selected diffraction angles show up as bright spots, significantly brighter then the misoriented crystallites.

Figure 5-22 147
Bright field TEM image corresponding to the selected angle dark-field image in Figure 5-21.

Figure 5-23 148
Optical absorption spectrum of an InAs-doped silica film on sapphire. Film thickness 2500 Å.

Figure 5-24 149
Absorption coefficient of an InAs-doped silica film on sapphire.

Figure 5-25 150
Tauc plot for the absorption coefficient of an InAs-doped silica film. At higher energies, linearly depends on photon energy. The intercept of the extrapolated linear part of the curve with the energy axis is the Tauc optical gap.

Figure 5-26 151
Optical absorption spectrum of InAs-doped silica films before and after RTA treatment. Film thickness ~ 2500 Å on a sapphire substrate.

Figure 5-27 153
Absorption saturation dynamics of InAs-doped silica films before and after RTA treatment at different temperatures. Absorption recovery time becomes faster for films annealed at higher temperatures. The top two traces have been vertically displaced for clarity by 4·10-3 and 8·10-3.

Figure 5-28 155
Absorption saturation dynamics of an InAs-doped silica film annealed in N2 at 750 °C for 60

s for 3 different pump energy fluences. The absorption bleaching scales with pump fluence. The pump average power corresponding to the highest energy fluence was 140 mW at an 80 MHz repetition rate, the pump spot size was 40 μm.

Figure 5-29 156
Schematic of the single-beam absorption saturation measurement setup.

Figure 5-30 157
Single-beam absorption saturation measurement of InAs-doped silica film. The solid lines represent the theoretical fits for the absorption saturation fluences of 20 and 30 mJ/cm2. The dashed lines show the sequence in which the experimental data points were acquired. The dashed lines do not return all the way to 1 due to the optical damage which occurs beyond ~ 3 mJ/cm2.

Figure 5-31 159
A schematic example of two inhomogeneously broadened spectra with homogeneous line-widths different by a factor of 2. The total absorption is approximately the same, but the non-linearity is a factor of 2 higher for the spectrum with a narrower homogeneous linewidth.

Figure 6-1 164
Schematic diagram of the Ti:Al2O3 laser cavity. OC, output coupler; SA, saturable absorber; CM1, 10-cm ROC mirrors; CM2, 7.5-cm ROC mirror; CM3, 5-cm ROC mirror; P, fused silica prisms.

Figure 6-2 166
Ti:Al2O3 laser output power as a function of the incident pump power. Modelocking threshold was 4.0 W and self-starting modelocking threshold was 5.0 W.

Figure 6-3 167
Interferometric autocorrelation of self-starting saturable-absorber-assisted KLM pulses. The pulse duration is 25 fs assuming a sech2 pulse shape.

Figure 6-4 167
Spectrum of self-starting 25 fs pulses corresponding to the autocorrelation in Figure 6-3.

Figure 6-5 168
Normalized pulse spectra of modelocked pulses. The center wavelength could be tuned over 80 nm while sustaining self-starting modelocking operation.

Figure 6-6 169
Non-collinear autocorrelation of self-starting saturable-absorber-assisted KLM Ti:Al2O3 laser output with positive intracavity GDD.

Figure 6-7 170
Spectrum of self-starting saturable-absorber-assisted KLM Ti:Al2O3 laser output with positive intracavity GDD.

Figure 6-8 171
Normalized pulse spectra of self-starting modelocked pulses for various intracavity dispersions. Modelocking could not be obtained around zero-dispersion point. The relative change in the net intracavity GDD between the adjacent spectra is on the order of 50 fs2.

Figure 6-9 172
Collinear interferometric autocorrelation of a laser output in a double-pulse operation mode.

Figure 6-10 172
Spectrum of a laser output in a double-pulse operation mode corresponding to autocorrelation in Figure 6-9.

Figure 6-11 175
Non-collinear autocorrelation traces of a Ti:Al2O3 laser output using only an InAs-doped film for modelocking, without KLM, for three intracavity group delay dispersions. The laser output consisted of a short pulse and a longer background pulse.

Figure 6-12 176
Spectrum of a Ti:Al2O3 laser output using only an InAs-doped film for modelocking, without KLM.

Figure 6-13 178
Schematic diagram of the Ti:Al2O3 laser cavity with a saturable absorber mirror. OC, output coupler; SAM, saturable absorber mirror; CM1, 10-cm ROC mirrors; CM2, 5-cm ROC mirror; P, fused silica prisms.

Figure 6-14 179
Saturable absorber mirror with a gold high reflector, InAs-doped silica saturable absorber, and silica spacers.

Figure 6-15 181
Surface of a saturable absorber mirror structure with a gold reflector and silica spacer layers following rapid thermal annealing at 500 °C for 60 seconds. The image size is 640 by 480 μm.

Figure A-1 191
Multilayer notation.

List of Acronyms

A-FPSA	Antiresonant Fabry-Perot saturable absorber
DBR	Distributed Bragg reflector
EDX	Energy dispersive x-ray spectroscopy
FWHM	Full width at half maximum
GDD	Group delay dispersion
GVD	Group velocity dispersion
KLM	Kerr lens modelocking
LT	Low temperature grown
MQW	Multiple quantum well
QW	Quantum well
SBR	Saturable Bragg reflector
SESAM	Semiconductor saturable absorber mirror
SPM	Self-phase modulation
TEM	Transmission electron microscopy
XPS	X-ray photoemission spectroscopy

Chapter 1

Introduction

Ultrashort pulse laser physics is a rapidly evolving area of science which brings together optical, atomic, and solid state physics as well as materials science. Ultrashort pulse lasers are now used to generate pulses of sub-10-femtosecond duration enabling researchers to study processes on a femtosecond time scale. The time scales involved here are fascinating; 1 femtosecond compares to one second as 5 minutes compare to the age of our Universe.

Since the development of the ruby laser in 1960 [1], lasers have become an indispensable tool for researchers in many realms of science and enabled a number of practical applications in communications, medicine, and industrial manufacturing. Further applications have been stimulated by the ability to produce laser pulses of short durations. The first demonstration of laser modelocking was performed in 1964 [2] and utilized an acousto-optic modulator to actively modelock a Helium-Neon laser. It was soon followed by the demonstration of passive modelocking in 1965 [3]. Since that time, ultrashort pulse laser technology has progressed tremendously.

The rapid progress in the field of ultrashort pulse lasers has been stimulated by the numerous potential applications in physics, chemistry, biology, medicine, communications, and engineering. The applications benefit from one or several of the properties unique for ultrashort laser pulses, namely short temporal duration, high brightness and peak power, and broad coherent spectrum. The list of the applications is long and includes time-resolved spectroscopy [4], high-harmonic generation [5], laser-driven particle accelerators [6], x-ray lasers [7], coherent control of chemical dynamics [8], high-density wavelength-division multiplexing [9], optical data storage [10], THz generation and imaging [11], and optical coherence tomography [12].

Over the past 10 years, the field of ultrashort pulse generation has advanced significantly. The invention of a Ti:sapphire (Ti:Al_2O_3) laser medium [13], Kerr lens modelocking (KLM) technique [14], and double-chirped mirrors for precise dispersion control [15] enabled generation of sub-10 fs laser pulses, as short as 5.5 fs directly out of the laser oscillator [179]. Self-phase modulation in gas-filled capillaries [17] and optical fibers was used to broaden the spectrum of femtosecond pulses and allowed to compress pulses to durations as short as 5 fs [18] [19]. A number of solid-state laser materials has been developed and demonstrated for ultrashort pulse generation in various wavelength regions of the near infrared.

In recent years, significant advances in the field of ultrashort pulse generation have been associated with the development of saturable absorber devices for laser modelocking [20] [21]. Semiconductor saturable absorber mirrors (SESAM) and saturable Bragg reflectors (SBR) are based on semiconductor quantum wells grown by molecular or chemical beam epitaxy to form multilayer semiconductor dielectric structures. While KLM remains the dominant technique for ultrashort pulse generation in solid-state lasers, SESAMs and SBRs offer a number of advantages compared to KLM alone. They provide self-starting modelocking operation, make modelocking more stable and insensitive to external perturbation, simplify the laser design and alignment, and allow design of more compact laser resonators. In the past several years, SESAMs and SBRs have become widely used for short pulse generation and have been applied to a wide range of solid-state lasers both for saturable absorber modelocking and for initiating KLM to obtain femtosecond pulse durations in the 800 nm, 1.0, 1.3, and 1.5 μm wavelength ranges [22] [23]. Since their development several years ago, semiconductor saturable absorber devices have had a major impact on the field of short pulse generation.

Although semiconductor saturable absorbers have many positive features, all of the previously demonstrated devices have the disadvantage of requiring epitaxial fabrication techniques. Epitaxial growth requires lattice matching of the film and the substrate; this limits the materials that can be used as substrates as well as the composition of the epitaxial layers, imposing severe constraints on device design. Moreover, epitaxial fabrication techniques are generally complex

and costly, which limits the widespread availability of saturable absorber devices. It appears that a radically different approach to saturable absorbers for laser modelocking is required to allow further progress in this area.

This thesis describes the development of novel saturable absorbers that do not require epitaxial fabrication techniques. Both the materials properties of saturable absorbers and their practical applications to ultrashort pulse generation from solid-state lasers were investigated. The research utilized the methods of nonlinear optics, laser physics, solid state physics, and materials science. The presented work can be divided into three logical parts.

The first part focuses on gaining better understanding of the design issues, properties and limitations of the previously proposed saturable Bragg reflector devices. It attempts to advance the saturable absorber technology further using the existing approaches and at the same time build a foundation of techniques that can be used to design novel saturable absorber devices.

The second part of the presented research investigates the applications of semiconductor doped glasses to laser modelocking. Such glasses possess properties which make them a very attractive saturable absorber materials system. In addition, they are much less complex and less expensive than the epitaxially grown semiconductors.

An entirely new, and probably the most promising, approach to the choice of the saturable absorber materials is demonstrated in the third part of the presented work. Semiconductor-doped dielectric thin films fabricated by rf sputtering are proposed as a saturable absorber materials system for laser modelocking applications. Such films are significantly simpler and less expensive to fabricate and could potentially offer superior performance compared to the epitaxially grown semiconductors. The presented research encompasses all the development stages of this novel saturable absorber materials system, from a rough idea, to the fabrication of novel semiconductor doped films, to characterization of their optical, compositional and structural properties, to saturable absorber device design, to laser modelocking experiments. It has been a very rewarding experience to see a loosely defined idea grow into a new type of saturable absorber capable of initiating KLM in a laser.

Three dominant and somewhat independent trends in the field of ultrashort pulse laser development can be identified in the recent years. The first trend is toward generation of laser pulses of even shorter durations. The second trend is in the direction of development of high power laser systems with multi-TW peak powers. The third trend is aimed at development of small, compact, and efficient ultrashort pulse lasers pumped by semiconductor laser diodes.

All of the above research directions could benefit from simple and versatile saturable absorber materials, such as semiconductor doped films. The broad bandwidth of operation and the ability to incorporate such absorbers into broadband dielectric mirrors should allow researchers to develop self-starting ultrashort pulse laser systems with record pulse durations. Similarly, the high power laser systems would greatly benefit from simpler saturable absorbers in laser oscillators which serve as a foundation of such systems. The currently existing femtosecond laser systems are generally large and complex and frequently require a highly skilled laser physicist to operate them. The development of simpler, more robust and less expensive femtosecond pulse sources would greatly benefit many scientific applications and would allow numerous new applications outside a laboratory environment.

The organization of this thesis is as follows:

Chapter 2 begins with an overview of the physical principles behind the laser modelocking and the laser modelocking techniques. It then discusses the key characteristics of the saturable absorbers for laser modelocking. The Chapter concludes with a literature review of the solid-state laser modelocking results obtained using epitaxially grown semiconductor saturable absorbers.

Chapter 3 describes the design of distributed Bragg reflector mirrors and saturable Bragg reflectors. The Chapter presents the calculations of SBR parameters such as reflectivity, dispersion, and electric field distribution for various structures. The calculations demonstrate how SBRs can be modeled and designed and in addition builds a foundation of modeling techniques which can be used to design novel saturable absorber devices. The limitations of SBRs, including two-photon absorption effects, are also discussed.

Chapter 4 begins with a brief overview of the optical properties of semiconductor quantum dots and composite optical materials. The fabrication of novel saturable absorber devices incorporating commercial semiconductor doped glasses (also referred to as colored glasses) is then described. The results of femtosecond pump-probe experiments, that were performed in order to characterize the saturable absorber properties of the semiconductor doped glasses, are presented. Photodarkening effects in the colored glasses were observed and investigated. The semiconductor doped glasses were applied to modelocking and KLM initiation in a Ti:Al_2O_3 laser. The Chapter concludes with the description of the modelocking results including the modelocking self-starting dynamics.

Chapter 5 describes fabrication of novel semiconductor-doped silica films and characterization of their properties. The Chapter demonstrates the fabrication of films of RG-850 colored glass, GaSb-nanocrystallite-doped silica, and InAs-nanocrystallite-doped silica by rf sputtering. The description of the film fabrication is followed by the results of the film characterization measurements. The properties of InAs-doped silica films are characterized using linear absorption spectroscopy, x-ray photoemission spectroscopy, transmission electron microscopy, energy dispersive x-ray spectroscopy, electron diffraction, femtosecond pump-probe experiments, and absorption saturation measurements.

Chapter 6 presents the first application of semiconductor-doped films to laser modelocking. The Chapter demonstrates stable saturable-absorber-assisted KLM operation of a Ti:Al_2O_3 laser with a broad wavelength tuning range using InAs-doped films for KLM initiation. Various possible modelocking instabilities are also discussed. The Chapter concludes with the description of saturable absorber mirror design which incorporates InAs-doped silica films.

Chapter 7 summarizes the results and suggests directions for future research efforts.

Appendix A describes modeling of optical properties of multilayer dielectric stacks. The theoretical background and MATLAB codes for calculating the reflectivity, dispersion, and field distribution of an arbitrary multilayer non-absorbing dielectric stack are presented.

Appendix B describes the rf sputtering fabrication procedure.

Appendix C describes the procedure for performing photolithography to determine the thickness of sputtered dielectric films.

Chapter 2

Laser modelocking

2.1 Introduction

This chapter will summarize the most important physical principles and the key results relevant to modelocking of solid-state lasers. The principle of laser modelocking is based upon synchronizing the phases of a number of longitudinal laser modes. A laser output consists of a superposition of discrete transverse and longitudinal modes. The longitudinal modes of a laser are separated in frequency by $c/2L$ where L is the optical length of the laser resonator and c is the speed of light. If the relative phases of the modes are not fixed, the laser output power is approximately constant in time. On the other hand, if the relative phases of the modes are fixed with respect to each other (the modes are 'locked') and appropriately adjusted, then the resulting temporal output becomes a periodic train of pulses with a period equal to the cavity round-trip time $T_{rt} = 2L/c$.

The shortest pulse duration is approximately equal to the inverse of the total modelocked bandwidth $\Delta\nu$: $\tau \sim 1/(\Delta\nu)$. The ratio of the period of the pulse train to the pulse width is approximately equal to the number of locked modes. The ultimate limitation on the shortest pulse duration is imposed by the laser bandwidth and the nonuniformity of mode spacing due to variations of the effective index of refraction of the resonator with frequency (frequency chirp).

The topic of modelocking has been extensively studied and a number of reviews exists on the subject [24], [25], [26], [27]. A number of techniques has been proposed for laser modelocking, falling into one of the two broad categories, active or passive modelocking. Modelocking techniques generally rely on a periodic modulation of intracavity gain (or loss) to provide condi-

tions for pulse formation. Active modelocking is based on using an amplitude modulator (active device) to provide a temporal transmission gate at the cavity round trip time. The first modelocking results were obtained in 1964 using active modelocking [2]. In case of passive modelocking, first demonstrated in 1966 [28], the periodic modulation of gain (loss) is provided by the laser itself. Passive modelocking was used to generate subpicosecond pulses for the first time [29] and has become the most widely used technique for solid-state laser modelocking.

The organization of this chapter is as follows. The introduction discusses the basic principles of modelocking. Section 2.2 reviews the principles of passive modelocking and the pulse shaping mechanisms. Section 2.3 discusses the conditions for self-starting modelocking operation. The concept of Kerr lens modelocking (KLM) and the modelocking results achieved using KLM are reviewed in chapter 2.4. The key properties and design criteria for saturable absorbers are discussed in section 2.5. The concepts and design techniques of epitaxially-grown semiconductor saturable absorbers are discussed in section 2.6. The section also describes the recent results in laser modelocking using epitaxially-grown saturable absorber devices and justifies the need for new, non-epitaxial, saturable absorber materials.

2.2 Passive modelocking

Passive modelocking is based on the pulse inside the laser modulating itself, faster than it would be possible with any kind of active modulation. Generally, passive modelocking techniques utilize an intracavity saturable absorber which is a lossy element that has lower loss for higher optical intensities. Depending on the saturable absorber recovery time compared to the pulse duration, passive modelocking techniques can be separated into the categories of slow saturable absorber modelocking and fast saturable absorber modelocking. A slow saturable absorber cannot recover its absorption on a time scale of a pulse duration itself. The transmission of a slow saturable absorber is a function of the total pulse energy (energy fluence). In contrast, a fast saturable absorber responds almost instantaneously to the changing intensity and can recover its absorption on a time scale short compared to the pulse duration. Therefore, the fast saturable absorber loss follows the temporal intensity profile of the pulse.

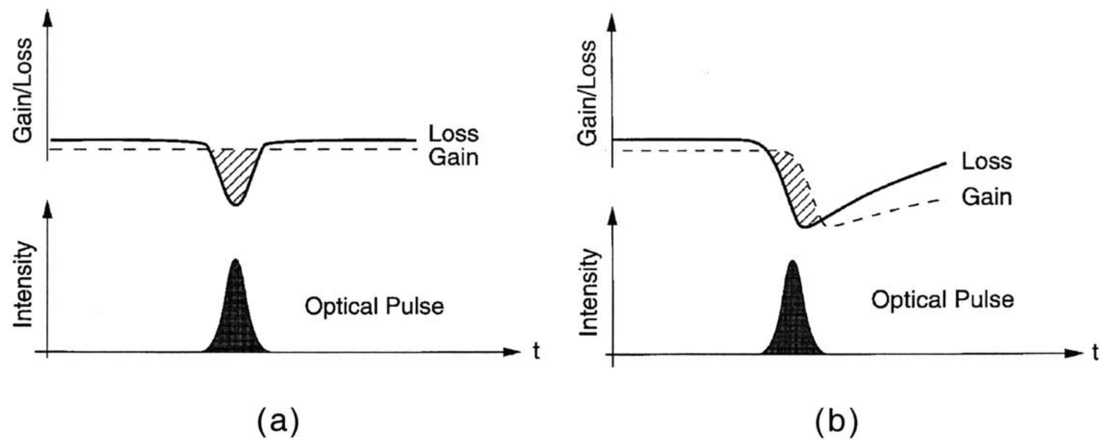

FIGURE 2-1: Passive saturable absorber modelocking (a) with a fast saturable absorber and (b) with a slow saturable absorber and dynamic gain saturation.([24])

A slow saturable absorber requires dynamic gain saturation to provide a pulse formation mechanism (Figure 2-1 (b)) [30], [24]. A combination of dynamic gain saturation with a slow absorber can be used to produce a narrow temporal window having net intracavity gain. Absorbers with nanosecond recovery times in conjunction with dynamic gain saturation can be used to generate subpicosecond pulses, e.g. as short as 27 fs directly out of a colliding pulse modelocked dye laser [31]. Because of the required dynamic gain saturation, this technique can only be applied to laser systems with short upper state lifetimes (in the nanosecond range) of the lasing medium, such as dyes or semiconductors.

The conditions for slow saturable absorber modelocking are not satisfied however for most solid-state lasers with an upper state lifetimes in the microsecond to millisecond range and small gain cross-sections (see Table 2-1 on page 48). Dynamic gain saturation, required for pulse formation in the slow saturable absorber regime, does not occur in solid-state lasers on nanosecond scale corresponding to the cavity round trip time. Therefore, fast saturable absorber techniques are essential for short pulse generation from solid-state laser materials. Fast saturable absorber modelocking (Figure 2-1 (a)) relies solely on the absorber to provide saturable loss and does not require dynamic gain saturation. In this case, the problem is to find absorbers that relax on a femtosecond time scale.

The theory of fast saturable absorber modelocking is well established [32], [33]. In addition to fast saturable absorber action, the technique relies on a number of additional pulse shaping mechanisms. They include gain dispersion, self-phase modulation (SPM), and group velocity dispersion (GVD).

Self-phase modulation is due to the optical Kerr effect which arises from the nonlinear polarization induced in the optical media by a strong electric field. The third order nonlinear susceptibilty is responsible for the intensity-dependent index of refraction

$$n = n_0 + n_2 I \tag{2-1}$$

Optical crystals typically have a nonlinear index n_2 positive and on the order of 10^{-16} cm^2/W [34]. The Kerr effect becomes significant when the Kerr-induced phase $\frac{2\pi}{\lambda} n_2 I L$, where L is the length of Kerr medium, approaches π. For a laser wavelength in the near-IR and a typical 1-cm-long solid-state material, this condition requires intensities on the order of 100 GW/cm^2. Peak intensities in modelocked lasers can easily reach several GW/cm^2, therefore Kerr nonlinearities are important.

When a laser pulse propagates through a Kerr medium, it acquires a time-dependent phase:

$$\varphi(t) = -\frac{2\pi}{\lambda} n(t) L = -\frac{2\pi}{\lambda} L(n_0 + n_2 I(t)) \tag{2-2}$$

Thus the pulse is modulating its own phase, or in other words, self-phase modulation occurs. An instantaneous frequency is equal to the time rate of phase change and becomes a function of time:

$$\frac{d}{dt}\varphi(t) = -\frac{2\pi}{\lambda} L n_2 \frac{d}{dt} I(t) \tag{2-3}$$

As a result, the leading edge of the pulse will experience a down-shift in frequency (red shift) and the trailing edge, a blue shift. New frequency components are generated and the pulse spectrum is broadened. If the medium has positive dispersion (longer wavelengths travel faster) than the trailing edge of the pulse will fall further and further behind with respect to the leading edge and the pulse will be broadened in time. On the other hand, negative dispersion of the medium (blue travels faster than red) could be used to compress the pulse by making the blue tail catch up with the

red front. This is an effect that serves as a basis for soliton generation [35]. For a small Kerr-induced phase, the effect of the self-phase modulation on the electric field *E(t)* can be represented as:

$$\Delta E(t) = -i\delta|E(t)|^2 E(t) \qquad (2\text{-}4)$$

$$\delta = \frac{\omega_0}{c}\frac{n_2 L}{A_{eff}} \qquad (2\text{-}5)$$

where A_{eff} is the mode area.

The above argument stresses the importance of group velocity dispersion for pulse shaping in a fast-saturable-absorber-modelocked laser. Dispersion accounts for the fact that light propagating in a material has a phase which is nonlinearly dependent on the frequency.

$$\phi(\omega) = \phi(\omega_0) + \phi'(\omega_0)(\omega - \omega_0) + \frac{1}{2}\phi''(\omega_0)(\omega - \omega_0)^2 + \ldots \qquad (2\text{-}6)$$

By going from frequency to time domain, the effect of group velocity dispersion could be represented by a dispersion operator:

$$\Delta E(t) = iD\frac{d^2}{dt^2}E(t) \qquad (2\text{-}7)$$

Limited gain bandwidth (gain dispersion) can often be approximated by a parabolic profile:

$$\Delta E(\omega) = g\left(1 - \frac{(\omega - \omega_0)^2}{\omega_g^2}\right)E(\omega) \qquad (2\text{-}8)$$

or in time domain:

$$\Delta E(t) = g\left(1 + \frac{1}{\omega_g^2}\frac{d^2}{dt^2}\right)E(t) \qquad (2\text{-}9)$$

A fast saturable absorber produces self-amplitude modulation, the effect of which can be represented as

$$\Delta E(t) = \gamma |E(t)|^2 E(t) \tag{2-10}$$

where γ is inversely proportional to the saturation fluence.

Taking into account the pulse-shaping mechanisms discussed above, considering their effects per round-trip, and looking for a steady-state solution, the master equation for fast saturable absorber modelocking can be derived [33] (also known as a steady-state Ginzburg-Landau equation):

$$\left[g\left(1+\frac{1}{\omega_g^2}\frac{d^2}{dt^2}\right) - l + i\psi + iD\frac{d^2}{dt^2} + (\gamma - i\delta)|E(t)|^2\right]E(t) = 0 \tag{2-11}$$

where g is linear gain, l is linear loss, ψ is linear accumulated phase shift, ω_g is gain bandwidth, D is group velocity dispersion, γ is the self-amplitude modulation constant, and δ accounts for self-phase modulation. The solution to the master equation is

$$E(t) = E_0 \operatorname{sech}\left(\frac{t}{\tau}\right) \exp[i\beta \ln \operatorname{sech}(t/\tau)] \tag{2-12}$$

where τ is the pulse duration and β is a chirp parameter. By substituting the solution (2-12) back into the master equation (2-11), the pulse duration τ and chirp β, as well as the gain g can be found. The key features of the solution are summarized in Figure 2-2 ([33]) where the normalized parameters are used for pulse duration

$$\tau_n = \frac{W\omega_g^2}{2g}\tau \tag{2-13}$$

dispersion

$$D_n = \frac{\omega_g^2}{g}D \tag{2-14}$$

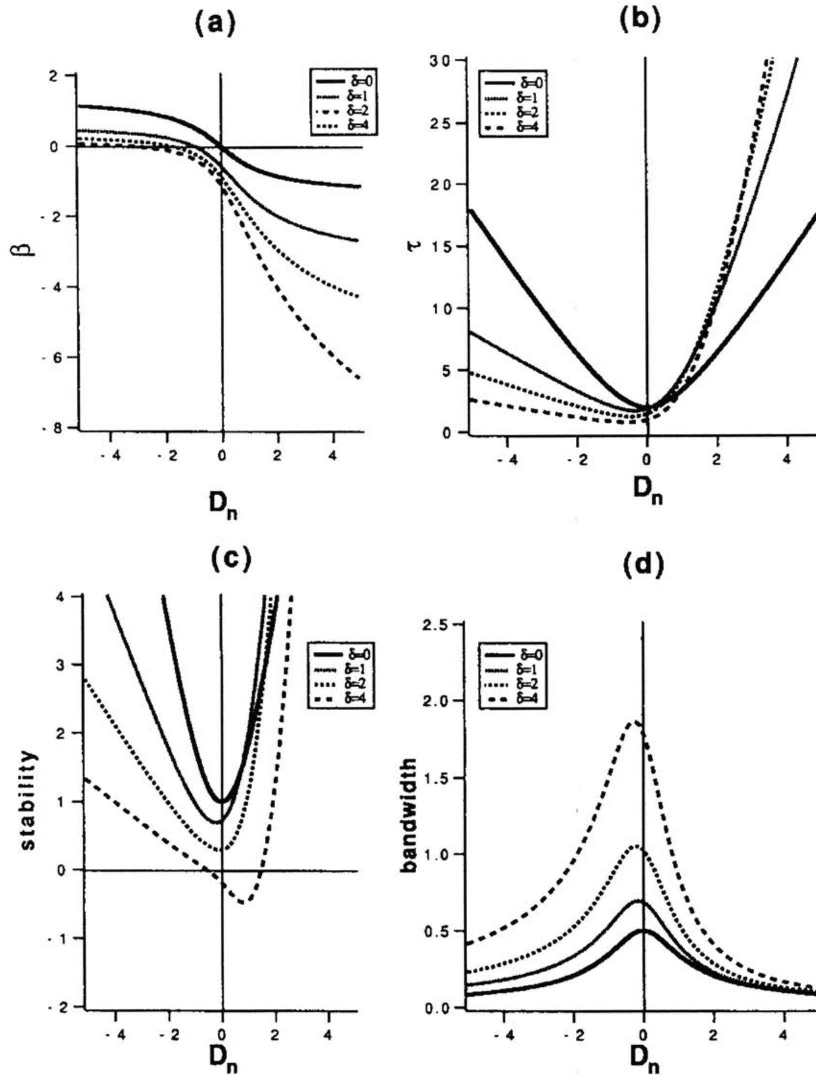

FIGURE 2-2: Predictions of the master equation for fast saturable absorber mode-locking. Normalized pulse parameters are plotted as a function of normalized dispersion for constant saturable absorber action and varying self-phase modulation. a) Chirp parameter. b) Pulse duration. c) Stability parameter. d) Bandwidth. [33]

and bandwidth

$$\Omega = (1 + \beta)^2 (1/\tau_n) \tag{2-15}$$

where W is the pulse energy.

From the solution of the master equation, two distinct regimes of modelocking operation can be identified. In the positive dispersion regime, the chirp β is large and the pulse durations are long. Because the pulses are strongly chirped, increasing bandwidth actually leads to longer pulses, therefore, limited gain bandwidth acts as a pulse shortening mechanism. It balances the pulse broadening caused by positive GVD and SPM. The saturable absorber modulation depth strongly affects the pulse width.

In order to obtain short pulses with a small amount of chirp, negative GVD is required. The physical reason is related to soliton formation and was explained above in the description of SPM. In the case of negative GVD (soliton pulse shaping), saturable absorber action is required to stabilize the soliton and discriminate against coupling to cw radiation. The modelocking is stable if the gain before and after the pulse is less than loss and therefore cw radiation sees loss while the pulse is amplified. It should be noted that even in the presence of a saturable absorber, excessive SPM can lead to instabilities. The spectrum spreading caused by SPM combined with a limited gain bandwidth can make the losses at the wings of the spectrum higher than the gains brought by a saturable absorber.

To compete the discussion of passive modelocking, dispersion in optical systems and techniques for dispersion compensation should be described in greater detail. As it was shown above, the fast saturable absorber passive modelocking mechanism requires a net negative (anomalous) intracavity group delay dispersion for generation of ultrashort pulses. Solid-state gain media and other intracavity materials typically introduce positive (normal) dispersion into the cavity which has to be balanced. The material dispersion arises from the wavelength dependence of the index of refraction which for solid-state optical materials is typically caused by a resonance in the UV.

For a material with an index of refraction $n=n(\lambda)$, the second order dispersion (group velocity dispersion) can be obtained by differentiating the phase with respect to frequency and expressing the result in terms of $n(\lambda)$ [36]

$$\varphi(\omega) = n(\omega)\frac{\omega}{c} \tag{2-16}$$

$$\frac{d^2\varphi}{d\omega^2} = \frac{1}{c}\left(2\frac{d}{d\omega}n(\omega) + \omega\frac{d^2}{d\omega^2}n(\omega)\right)L = \frac{\lambda^3}{2\pi c^2}\frac{d^2 n}{d\lambda^2}L = L\frac{d}{d\omega}\frac{1}{v_g(\omega)} \tag{2-17}$$

where L is the length of the dispersive medium and v_g is the group velocity.

Several methods for the generation of negative group velocity dispersion have been proposed. Diffraction grating pairs can provide large amounts of negative dispersion [37] but are not suitable for intracavity use due to high losses. Pairs of Brewster-cut prisms can provide negative group velocity dispersion [38] and now constitute the most common dispersion-compensating mechanism is femtosecond lasers. The dispersion of a prism pair can be easily derived by considering beam propagation between the two prisms and using the Fermat principle. According to reference [39], the second and third order dispersions of a prism pair made of material with refractive index $n(\lambda)$ are given by

$$\frac{d^2\varphi_p}{d\omega^2} = \frac{\lambda^3}{2\pi c^2}\frac{d^2 P}{d\lambda^2} \tag{2-18}$$

$$\frac{d^3\varphi_p}{d\omega^3} = \frac{-\lambda^4}{4\pi^2 c^3}\left(3\frac{d^2 P}{d\lambda^2} + \lambda\frac{d^3 P}{d\lambda^3}\right) \tag{2-19}$$

where the derivatives of the optical path length P are given by

$$\frac{d^2 P}{d\lambda^2} = 4\left[\frac{d^2 n}{d\lambda^2} + (2n - n^{-3})\left(\frac{dn}{d\lambda}\right)^2\right]l_p\sin\beta - 8\left(\frac{dn}{d\lambda}\right)^2 l_p\cos\beta \tag{2-20}$$

$$\frac{d^3 P}{d\lambda^3} = 4\frac{d^3 n}{d\lambda^3}l_p\sin\beta - 24\frac{dn}{d\lambda}\frac{d^2 n}{d\lambda^2}l_p\cos\beta \tag{2-21}$$

where l_p is the tip-to-tip separation between the prisms and β is the angle between the direction of beam propagation between the prisms and the line connecting the prism tips.

For ultrashort pulse generation, precise control of higher order dispersion (third- and forth-order) is required, which cannot always be provided by the prism pair because of an insufficient number of adjustable parameters. Ultrashort pulse generation also requires resonator mirrors with a high reflectivity over a broad wavelength range necessary to support the broad spectrum of the pulse. Conventional quarter-wave dielectric mirror stacks do not have a sufficient bandwidth and limit the duration of ultrashort pulses. The recently developed chirped and double chirped mirrors [15], [40], [41] provide a high reflectivity over a broad wavelength range and allow to tailor dispersion for a specific laser system. The most recent advances in ultrashort pulse generation [16] are directly related to the development of such chirped mirrors.

For applications of femtosecond pulses, extracavity dispersion compensation is required to preserve the short pulse duration. For an unchirped Gaussian pulse of duration T, the pulse duration after propagating through a dispersive medium with a second order dispersion $(\partial^2\varphi)/(\partial\omega^2)$ and third order dispersion $(\partial^3\varphi)/(\partial\omega^3)$ becomes T_1 [36]:

$$T_1 = T\sqrt{1 + \frac{\left(4\ln 2\frac{\partial^2\varphi}{\partial\omega^2}\right)^2}{T^4} + \frac{\left(4(\ln 2)^{3/2}\frac{\partial^3\varphi}{\partial\omega^3}\right)^2}{T^6} + \dots} \tag{2-22}$$

For example, an unchirped 10 fs pulse with a center wavelength of 800 nm would be broadened to 14 fs after propagating through 1 mm of fused silica or to 19 fs after 1 mm of sapphire. In comparison, the dispersion compensation constraints are not as critical for pulses in the 100-fs range. It would take 100 mm of fused silica to broaden a 100 fs pulse to 140 fs. This demonstrates the importance of dispersion compensation for ultrashort pulse laser applications.

2.3 Self-starting modelocking operation

The pulse shortening rate (PSR), defined as the fractional change in the pulse width per round trip pass $(\Delta\tau)/\tau$, is an important parameter that determines the pulse evolution inside the resonator. For active modelocking, the PSR is proportional to the pulse duration squared [42], [35]. For slow saturable absorber modelocking, the absorber saturation behavior only depends on the pulse energy and is independent of the pulse duration. Therefore, the PSR remains constant as the pulse gets shorter [30]. For fast saturable absorber modelocking, the pulse shortening rate is proportional to the peak intensity which is inversely proportional to the pulse duration for a given pulse energy. Hence, for fast saturable absorber modelocking, the PSR is inversely proportional to the pulse duration and the modelocking mechanism becomes more effective as the pulse gets shorter. The limit is reached when the absorber is completely saturated or when the pulse duration reaches the absorber response time. The pulse shortening rates for various modelocking mechanisms are shown in Figure 2-3.

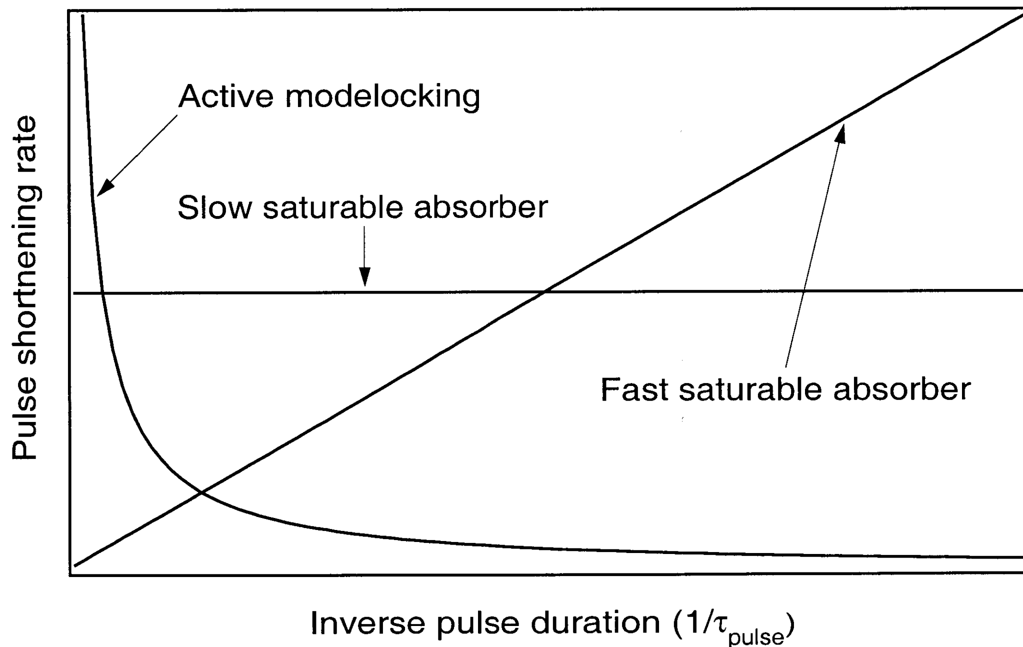

FIGURE 2-3: Pulse shortening rates for the various modelocking mechanisms.

In case of a laser passively modelocked with a fast saturable absorber, a laser pulse gradually builds up from noise fluctuations present in the multimode free-running laser. The presented analysis follows that of references [43] and [25]. For a photon flux perturbation *s(t)* on top of the steady-state flux S_0, the effect of a fast saturable absorber on the round-trip gain is

$$\Delta g_a = ks(t) \tag{2-23}$$

where k is a proportionality constant that depends on the strength of the saturable absorber nonlinearity (proportional to *dA/dI* in Figure 2-6). Shorter pulses experience increased net gain in the laser and the peak of the pulse experiences higher gain than the wings. The increased gain of the short pulse provides the amplitude modulation necessary for modelocking build up towards the steady state. If the gain of the laser medium has a long response time (longer than the cavity round-trip time) such that it saturates only with the average power (typically true for solid-state lasers), modelocking should always self-start from the fluctuations even though the PSR depends on the duration of fluctuation and can initially be very slow.

On the other hand, if dynamic gain saturation is taken into account, another condition for self-starting has to be satisfied. Assuming that the gain recovery time is long compared to the duration of fluctuation, for a small fractional gain change, the change in the laser medium gain is

$$\Delta g_g = -\sigma g \int_{-\infty}^{t} s(t) dt \tag{2-24}$$

where g is the saturated gain prior to the fluctuation and σ is the gain emission cross-section.

The perturbation *s(t)* will grow if the overlap of the change in gain with the perturbation is positive:

$$\int_{-\infty}^{+\infty} (\Delta g_a(t) + \Delta g_g(t)) s(t) dt > 0 \tag{2-25}$$

$$k\int_{-\infty}^{+\infty} s^2(t) dt - \sigma g \int_{-\infty}^{+\infty} s(t) dt \int_{-\infty}^{t} s(t') dt' > 0 \tag{2-26}$$

or

$$\frac{k}{g} > \sigma \frac{\left[\int_{-\infty}^{+\infty} s(t)dt\right]^2}{\int_{-\infty}^{+\infty} s^2(t)dt} \tag{2-27}$$

If the perturbation is square with duration τ_{pert}, then the ratio (2-27) is just τ_{pert}. In a general case, the ratio is a function of the shape and duration of the perturbation:

$$\frac{\left[\int_{-\infty}^{+\infty} s(t)dt\right]^2}{\int_{-\infty}^{+\infty} s^2(t)dt} = \beta\tau_{pert} \tag{2-28}$$

where β equals to 0.85 for a sech^2 pulse and 0.75 for a Gaussian pulse shape. Finally, the necessary condition for start-up of fast saturable absorber modelocking is obtained:

$$\frac{k}{g} > \beta\sigma\tau_{pert} \tag{2-29}$$

Start-up is easier for gain media with lower gain cross-sections, for stronger saturable absorber action in the cw regime (lower saturation intensity), and for a shorter perturbation width (larger number of competing modes). Modelocking in KLM lasers (see below) is frequently initiated by shaking a resonator mirror or prisms, or simply banging on the optical table to provide a strong perturbation to cw regime.

If a saturable absorber is slow rather than fast, then the change in gain due to saturable absorber action follows an integral of the intensity rather than the intensity itself. The start-up condition is then independent of the perturbation width and is similar to the condition for slow saturable absorber modelocking [30]: the effective cross-section of the saturable absorber should be greater than the that of the gain (absorber saturates faster than the gain).

The self-starting condition (2-29) suggests that modelocking should self-start immediately at lasing threshold. Experimentally however, a laser typically has two thresholds, one threshold for cw operation and a higher one for modelocked operation. The existence of the threshold

power for modelocking can be explained if the perturbation decay time due to mode dephasing is introduced [44], [45]. Significant pulse shortening of the perturbation should occur on a time scale short compared to the perturbation decay time. Neglecting the dynamic gain saturation effects, the change in the photon flux $S = S_0 + s(t)$ per round trip induced by the perturbation and the saturable absorber action is

$$\frac{d}{dt}\Delta S \propto \frac{1}{T_{rt}} g S \qquad (2\text{-}30)$$

where $\Delta g = ks(t)$. Therefore,

$$\frac{d}{dt}s(t) \propto \frac{1}{T_{rt}} S_0 s(t) \qquad (2\text{-}31)$$

and the perturbation grows faster for higher initial photon flux S_0. In order for the perturbation growth rate to be faster than the decay time, a threshold value of the intracavity power may be required.

To summarize the self-starting conditions for a fast saturable absorber modelocking, self-starting is easier for stronger saturable-absorber-induced modulation in the cw regime, for gain media with smaller cross-sections, for shorter width of the perturbation and may require a threshold intracavity power.

2.4 Kerr lens modelocking

Solid state laser materials typically have an upper-state lifetime on a scale of a few microseconds to a few milliseconds, which is significantly longer than that for dyes, ~10 ns, and semiconductors, ~1ns. The gain cross section is also relatively small, typically a few times 10^{-19} cm^2, compared to ~10^{-16} cm^2 for dyes and ~10^{-14} cm^2 for semiconductors. A summary of gain cross-sections and upper state lifetimes for several solid-state laser materials is presented in Table 2-1 on page 48. As a result, dynamic gain saturation is negligible on a time scale of a femto- or pico-

second laser pulse. Therefore, slow saturable absorber modelocking, that utilizes gain saturation, cannot be used for solid-state laser modelocking and a fast saturable absorber is required to generate ultrashort pulses.

Such a fast saturable absorber mechanism, Kerr lens modelocking (KLM), based on a dynamic self-focusing effect, was discovered in 1991 [14]. The technique utilizes self-focusing in one of the cavity elements to obtain intensity-dependent mode size in a laser resonator. An intracavity hard aperture or a 'soft' gain aperture is used to translate the intensity-dependent beam size into intensity-dependent loss, in case of a hard aperture, or gain, in case of a soft aperture. If the resonator is optimized such that the mode at the aperture becomes smaller for a higher intracavity intensity, a laser pulse experiences lower loss (or higher gain) than cw radiation, creating an artificial fast saturable absorber. The KLM temporal response is determined by the index of refraction nonlinearity in glass $n(t) = n_0 + n_2 I(t)$, that has a response time of a few femtoseconds [46].

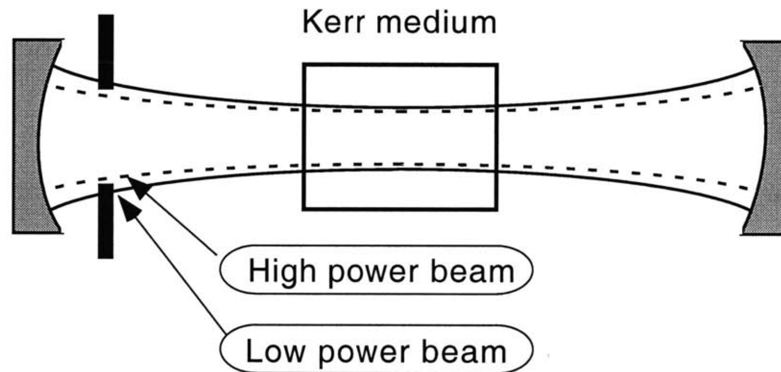

FIGURE 2-4: Schematic of KLM operation.

A realistic KLM resonator, however, is significantly more complex than the schematic shown in Figure 2-4. A z-cavity typically used in KLM lasers is shown in Figure 2-5. The cavity consists of two curved mirrors around the laser crystal, a pair of Brewster-cut prisms for dispersion compensation, with a high reflector mirror and an output coupler terminating the two arms of the cavity. The Brewster-cut laser crystal introduces astigmatism into the cavity which should be compensated by choosing the correct incident angles on the curved mirrors CM1 and CM2 [47].

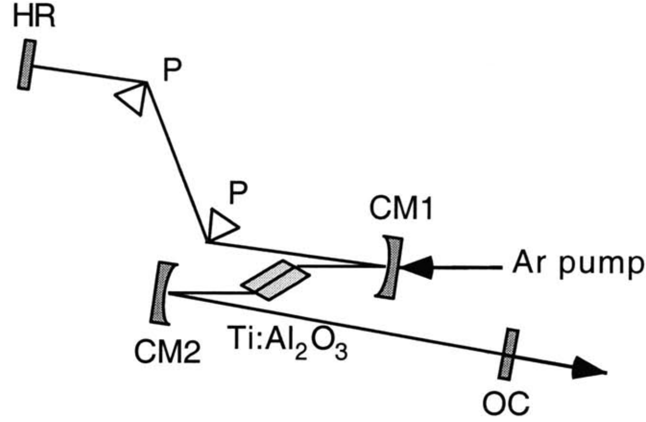

FIGURE 2-5: Schematic of a typical KLM laser cavity. HR, high reflector; P, Brewster-cut prism; CM, curved mirror; OC, output coupler.

Laser resonator analysis for KLM can be performed using a standard ABCD matrix formalism [26] [35] combined with a nonlinear scaling of the q-parameter [48], [49]. It can be shown that in order to account for self-focusing effects in a nonlinear medium, the q-parameter of a Gaussian beam should be scaled at the boundary of the medium according to the relation:

$$Im\left(\frac{1}{q}\right) \rightarrow Im\left(\frac{1}{q}\right)\xi \tag{2-32}$$

where the scaling factor ξ is defined as

$$\xi = \sqrt{1 - \frac{P}{P_{crit}}} \tag{2-33}$$

where P is the instantaneous power and P_{crit} is the critical power for self-focusing

$$P_{crit} = \frac{a\lambda^2}{8\pi n_0 n_2} \tag{2-34}$$

where λ is the wavelength in vacuum, n_0 is the linear refractive index, n_2 is the nonlinear index, and a is a correction factor predicted to be in the range from 3.7 to 6.4 [50]. Intuitively, the transformation of the q-parameter is easy to understand: self-focusing reduces the effects of diffraction

in the imaginary part of the q-parameter. Using the above transformation, the beam propagation through a nonlinear medium having a linear ABCD matrix *M*, can be written as

$$q' = N^{-1}MNq \tag{2-35}$$

where q and q' describe the Gaussian beam before and after it passes through a nonlinear medium, and N and N^{-1} are the forward and reverse transformations applied at the entrance

$$Nq \equiv \frac{1}{Re(1/q) + i\xi Im(1/q)} \tag{2-36}$$

and at the exit of the nonlinear medium:

$$N^{-1}q \equiv \frac{1}{Re(1/q) + i\xi^{-1} Im(1/q)} \tag{2-37}$$

Using the above formalism, the laser resonator should be modeled and the saggital and tangential resonator mode sizes in the laser crystal should be calculated for low (cw) power and high (modelocked) power as a function of the curved mirror separation, the incidence angles on the curved mirrors, and the crystal position. If the linear mode size in the crystal is chosen to be smaller than the pump beam size and the operating point within the resonator stability range is chosen such that the mode size decreases for higher intracavity power owing to the self-focusing effects, then the mode with higher power will have a better overlap with the pump and will experience higher gain than the cw beam. As a result, the gain increases for higher instantaneous intracavity intensity and an artificial saturable absorber is created. For a z-shaped resonator with asymmetric arms, the stability range, plotted as a function of the curved mirror separation, is split into two parts. Optimal KLM operation is usually obtained near the inner edge of the outer stability region. The net dispersion of the laser resonator should be calculated and the material of the prism pair should be chosen to minimize net third and higher order dispersion while providing a desired amount of the second order (group delay) dispersion. For a comprehensive review of the techniques for modeling and designing KLM laser resonators reader is referred to references [51] [52] [53] [47] [54].

Soon after its discovery, KLM was applied to obtain record pulse durations from a number of solid-state lasers. Pulses as short as 8 fs were generated from a KLM Ti:sapphire laser [55] [56], which was the shortest pulse duration from a laser oscillator at that time. The current shortest pulse duration of 5.5 fs directly from of a laser oscillator [179] was obtained using KLM in conjunction with a semiconductor saturable absorber mirror. Today, KLM remains the most widely used technique for generation of ultrashort pulses from solid-state lasers.

Despite the great modelocking results achieved using KLM, the technique has several significant drawbacks. First, although self-starting KLM pulses have been demonstrated [57], pure KLM lasers are generally not self-starting and no sub-50-fs self-starting results have been obtained. The reason is that in a typical 10-fs-pulse-duration laser with a 100 MHz repetition rate, the peak power changes by 6 orders of magnitude when the laser switches from cw to modelocked operation. Therefore, self-focusing effects, proportional to the peak power, which are strong in the short pulse regime, are typically too weak in the cw regime and are not sufficient to initiate modelocking. On the other hand, if self-starting is optimized, KLM saturates in the short pulse regime and modelocking becomes unstable. The second drawback of KLM is that it requires the laser to operate near the edge of the resonator stability range in order to obtain a sufficiently large self-focusing-induced change of beam diameter. This results in very strict requirements on the positioning of the resonator mirrors and the laser crystal, to a precision of a few hundred microns. Therefore, KLM resonators are typically rather complex to align and are sensitive to external perturbations. Third, in soft-aperture KLM lasers, both the gain and the KLM mechanisms rely on the overlap between the pump beam and the resonator mode within a laser gain medium. As a result, for the resonator alignment dictated by efficient KLM conditions, the cavity gain is often not optimized and the laser is not efficient.

2.5 Saturable absorbers for laser modelocking

A saturable absorber for laser modelocking applications should provide saturable optical losses in the laser resonator in a chosen wavelength region, with desired recovery times and saturation intensity. Generally, a saturable absorber can operate in one of three ways: 1) provide a

starting mechanism for modelocking; 2) provide a pulse shortening mechanism once the modelocking has been initiated; 3) provide both a strong starting and an effective pulse shortening mechanisms. In the first case, a saturable absorber provides only a small modulation of an intracavity loss which, while insufficient to modelock the laser all by itself, introduces a perturbation into the cw lasing regime. At this point, another modelocking mechanism, which requires a higher intracavity intensity, becomes efficient, shortens the laser pulse and sustains modelocking. In the second case, the saturable absorber is only weakly saturated by the cw intracavity intensity and cannot provide an efficient starting mechanism. Such an absorber is effective only for relatively high intracavity intensities and requires another mechanism to initiate modelocking. In the third case, the saturable absorber is effective for both low and high intracavity intensities.

The key characteristics of saturable absorbers for laser modelocking include linear absorption, ratio of saturable and nonsaturable losses, absorption saturation intensity and fluence, absorption saturation recovery dynamics, bandwidth of operation, damage threshold, ease of fabrication and constraints on laser cavity design.

2.5.1 Linear absorption

A saturable absorber for modelocking should have optical absorption at the lasing wavelength. The magnitude of linear absorption should be sufficient to provide a modulation of intracavity loss required to sustain modelocking and lead to short pulse formation. Generally, shorter pulse durations require deeper modulation depth of saturable absorption ΔA [32] [33] [58]:

$$\tau_p \propto \frac{1}{\Delta A^{|\alpha|}} \tag{2-38}$$

where ΔA is the absorption modulation depth and the parameter α depends on the modelocking theory. On the other hand, absorption should not be excessively high, so that when a saturable absorber is introduced into a laser cavity, both the lasing and modelocking thresholds can be obtained.

2.5.2 Nonsaturable losses

A nonsaturable loss of a saturable absorber should be small compared to a saturable loss and to laser output coupling, which is typically on the order of a few percent. The nonsaturable loss component makes the laser less efficient, requires higher pumping power, and in some cases decreases the damage threshold. It also makes the laser operate fewer times above threshold which increases the tendency for instabilities such as Q-switched modelocked behavior (see equation (2-53) below). Nonsaturable losses can be caused by free carrier absorption and by imperfections and scattering defects in the material. Several techniques such as low-temperature epitaxial growth, ion implantation, and proton bombardment are frequently used to create materials with a high density of carrier traps and recombination centers in order to shorten the carrier lifetime. For such materials, the nonsaturable losses are generally increased. Various other phenomena competing with saturable absorption such as excited state absorption and thermal effects should also be minimized.

2.5.3 Absorption saturation intensity and fluence

Absorption saturation in semiconductor saturable absorbers is caused by band filling due to the Pauli exclusion principle. Near the bandedge, several additional effects should also be taken into account including AC Stark shift, bandgap renormalization, and excitonic effects [59]. The electron and hole populations excited by the laser radiation typically have a bitemporal relaxation behavior. The fast component (typically ~ 10 fs to 1 ps) results from intraband relaxation dynamics due to carrier-carrier and carrier-phonon scattering and the slow component (~1 ps to 10 ns depending on the material system) is caused by interband carrier recombination and carrier trapping.

It can be shown that for a two-level system with an upper state lifetime τ, the absorption coefficient α saturates with the incident intensity of cw radiation I as

$$\alpha = \frac{\alpha_0}{1 + I/I_{sat}} \qquad (2\text{-}39)$$

where α_0 is the small signal absorption coefficient and where I_{sat} is the saturation intensity given by:

$$I_{sat} = \frac{h\nu}{2\sigma\tau} \tag{2-40}$$

where σ is the absorption cross-section:

$$\sigma = \frac{\text{absorption rate}}{\text{incident photon flux}} = \frac{\text{absorption coefficient}}{\text{density of absorbing centers}} \tag{2-41}$$

With increasing intensity, the absorption coefficient decreases to the limit $\alpha(I) \to 0$ as $I \to \infty$. The product $\alpha(I)I \to \alpha_0 I_{sat}$, i.e. the absorbed intensity saturates (neglecting power broadening effects).

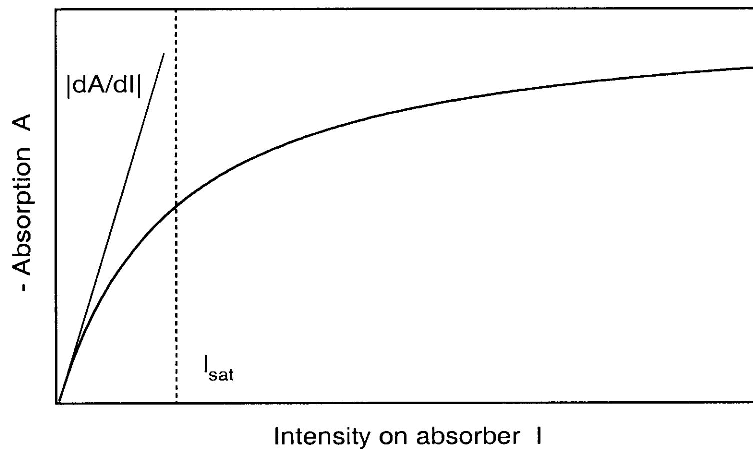

FIGURE 2-6: Nonlinear absorption change of a saturable absorber due to absorption bleaching with cw intensity. |dA/dI| is an important parameter for modelocking initiation.

In a case of a pulsed rather than cw radiation, the incident light intensity is a function of time $I = I(t)$. If the pulse duration is long compared to the lifetime τ (a fast saturable absorber), the saturation behavior is similar to the cw regime and equation (2-39) still holds where intensity I is now $I(t)$. If the pulse duration is significantly shorter than the lifetime τ (a slow saturable absorber) then, after introducing the energy fluence Γ

$$\Gamma(t) = \int_{-\infty}^{t} I(t)dt \tag{2-42}$$

and the saturation fluence Γ_{sat}

$$\Gamma_{sat} = \frac{h\nu}{2\sigma} \tag{2-43}$$

the absorption coefficient for a slow saturable absorber is then given by (Figure 2-7):

$$\alpha(t) = \alpha_0 \exp[-\Gamma(t)/\Gamma_{sat}] \tag{2-44}$$

$$\alpha = \alpha_0 \exp(-\Gamma/\Gamma_s) \tag{2-45}$$

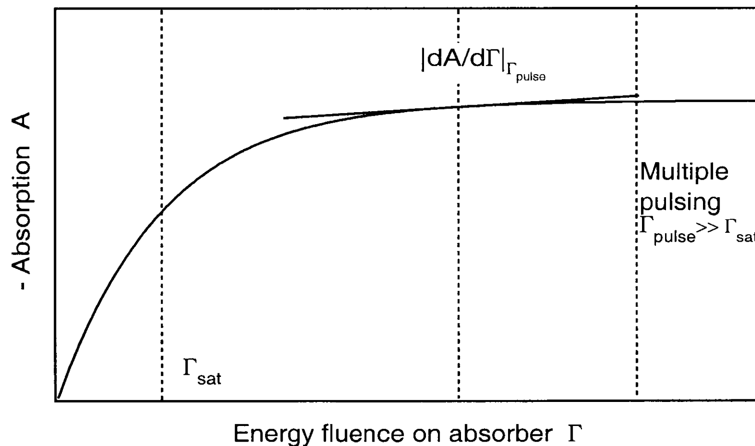

FIGURE 2-7: Nonlinear absorption change of a saturable absorber due to absorption bleaching with short pulses.

Generally, a nonsaturable component of the absorption coefficient α_{ns} should be accounted for:

$$\alpha = \frac{\alpha_0}{1 + I/I_{sat}} + \alpha_{ns} \tag{2-46}$$

$$\alpha = \alpha_0 \exp(-\Gamma/\Gamma_s) + \alpha_{ns} \tag{2-47}$$

The saturation intensity of a saturable absorber for laser modelocking needs to be sufficiently high so that the absorption is not bleached at the cw intracavity intensity I:

$$I \ll I_{sat} \tag{2-48}$$

If the absorber were fully bleached by the cw intensity, it would not be able to provide further absorption modulation needed to support short pulse formation.

In order for a saturable absorber to support short pulse formation, the loss should be smaller for pulsed than for cw operation. In case of a cw modelocked laser, the output power does not change significantly between the cw and pulsed modes of operation. Therefore, the energy fluence on the absorber Γ is given by

$$\Gamma = IT_{rt} \tag{2-49}$$

where T_{rt} is the pulse repetition rate equal to the cavity round trip time. A saturable absorber typically has a carrier lifetime τ longer then the laser pulse duration τ_p $(\tau > \tau_p)$ and much shorter than the typical pulse repetition rate $T_{rt} \approx 1$ - 10 ns (the absorption saturation recovers between the consecutive pulses) ($\tau \ll T_{rt}$). Comparing the absorption bleaching factors for cw and pulsed operation, x_{cw} and x_p, we obtain:

$$x_{cw} = \frac{I}{I_{sat}} \qquad x_p = \frac{\Gamma}{\Gamma_{sat}} \tag{2-50}$$

$$x_p = \frac{\Gamma}{\Gamma_{sat}} = \frac{IT_{rt}}{I_{sat}\tau} = x_{cw}\frac{T_{rt}}{\tau} > x_{cw} \tag{2-51}$$

Equation (2-51) demonstrates that the absorption is more strongly bleached for pulsed than for cw operation provided that the bleaching is negligible for cw intensities ($x_{cw} \ll 1$). The difference between the cw and modelocked losses increases with shorter carrier lifetime and lower pulse repetition rate. For a pulse repetition rate T_{rt} of 10 ns and carrier lifetime τ of 1 ns, $x_p = 10x_{cw}$. For the same pulse repetition rate and the carrier lifetime of 10 ps, $x_p = 1000x_{cw}$.

2.5.4 Absorption recovery time

The above argument already demonstrates the importance of short carrier lifetime for saturable absorber operation. For an efficient operation of a saturable absorber, the absorption recovery time should be shorter than the pulse repetition rate (see equation (2-51)). In addition, the absorption recovery time is an important parameter that determines modelocking build-up time, self-starting performance, pulse duration, and modelocking stability.

For fast saturable absorber modelocking and for soliton modelocking, the saturable absorber recovery time determines the shortest achievable pulse duration. In the absence of other limiting factors, the shortest possible pulse duration is on the order of the fast saturable absorber recovery time [32] [60].

Under certain approximations (neglecting the gain saturation effects), the modelocking build-up time T_{mlb} is determined by the intracavity absorption A dependence on intensity at low (cw) intensity as follows (see section 2.3 and [61] [58]):

$$T_{mlb} \approx \frac{T_{rt}}{\left.\frac{dA}{dI}\right|_{I=0} I} \tag{2-52}$$

Shorter modelocking build-up time and better self-starting performance are obtained for a larger slope dA/dI (lower saturation intensity I_{sat}) (see Figure 2-6) which can result from a longer carrier lifetime or a lower saturation fluence Γ_{sat} (equations (2-40) and (2-43)).

Along with the constraints on the absorption recovery time and saturation fluence required for efficient modelocking operation, another set of conditions has to be satisfied to guarantee stable cw modelocking and avoid instabilities. The upper limit on the carrier lifetime is determined by the onset of Q-switching. The condition for no Q-switching is given by [61], [22]:

$$\left|\frac{dA}{dI}\right| I < r\frac{T_{rt}}{\tau_{laser}} \tag{2-53}$$

where r determines how many times the laser is pumped above threshold and τ_{laser} is the upper state lifetime of the laser medium. Equation (2-53) suggests that Q-switching can be more easily suppressed for a small slope *dA/dI* (large saturation intensity), a large r (a laser is pumped far above threshold, small signal gain is high and losses are low), and a long cavity round trip time. The physical interpretation of the non-Q-switching condition (2-53) is as follows. The left-hand-side determines how fast the intracavity loss saturates due to bleaching of the saturable absorber, which in turn increases the intracavity intensity. The right-hand-side determines how fast the gain can respond to compensate for the reduced losses and maintain the intracavity intensity constant. If the gain response time is too slow, the average intensity increases until the absorber is completely bleached and Q-switching takes place.

If the absorber recovery time is much shorter than the cavity round-trip time ($\tau \ll T_{rt}$), the condition (2-53) is usually fulfilled. In this case, another condition has to be satisfied in order to avoid Q-switched modelocking. The reduction in the absorber loss in now caused by the bleaching by short pulses, not the cw intensity. For $\tau \ll T_{rt}$, this is a much larger effect. Similar to (2-53), it can be shown that the no Q-switched modelocking condition is:

$$\left|\frac{dA}{d\Gamma}\right| \Gamma < r\frac{T_{rt}}{\tau_{laser}} \tag{2-54}$$

This condition can be fulfilled if the pulse energy fluence is greater than the absorber saturation fluence $\Gamma \gg \Gamma_{sat}$ (Figure 2-7). Energy fluence much higher than the saturation fluence also results in a high absorption modulation depth which leads to generation of shorter pulses.

The upper limit on the pulse energy and the fluence incident on the saturable absorber is given by the onset of multiple pulsing instabilities (Figure 2-7) [62] [63]. For a fluence much higher than the absorber saturation fluence, the absorption is saturated and is no longer a strong function of pulse energy. In addition, shorter pulses have broader bandwidth and experience lower gain due to the limited gain bandwidth of the laser medium. Beyond a certain pulse energy, two pulses of lower energy, longer duration and narrower spectrum would see a higher gain than a single pulse. As a result, a pulse breaks up into two or several separate pulses.

Equations (2-48), (2-52), (2-53), (2-54) give the criteria for the saturation intensity and fluence of the saturable absorber. Generally, the saturation fluence is a fixed material parameter depending on the absorption cross-section (2-43). The saturation intensity can be adjusted independently from the saturation fluence by controlling the recovery time.

To summarize, here are the key requirements on the absorption saturation and absorption recovery properties of saturable absorbers. The saturation intensity should be higher than the cw intracavity intensity. The absorption recovery time should be faster than the pulse repetition rate. Longer absorption recovery time leads to better self-starting performance and faster modelocking build-up time. Faster absorption recovery time supports shorter pulse durations. The saturation fluence should be low enough to provide significant absorption saturation by the laser pulse as well as to avoid Q-switching instabilities. The saturation fluence should not be excessively small in order to avoid multiple pulsing instabilities.

Table 2-1 presents a summary of the cross-sections and upper-state lifetimes for typical quantum-well-based saturable absorbers and most relevant solid-state laser materials.

Material	Cross-section [cm^2]	Upper-state lifetime
Dyes	$\sim 10^{-16}$	~ 10 ns
Semiconductors	$\sim 10^{-14}$	~ 1 ns
LT-grown semiconductors	$\sim 10^{-14}$	100 fs - 1 ns
High-finesse A-FPSA	$\sim 10^{-16}$	~ 100 fs & ~ 10 ps

TABLE 2-1: Gain cross-sections for laser materials, absorption cross-sections for saturable absorbers, and upper state lifetimes for various materials and devices.

Low-finesse A-FPSA	~ 10^{-14} - 10^{-16}	~ 100 fs & ~ 10 ps
Semiconductor doped glasses	~ 10^{-15} - 10^{-16}	~ 100 fs & ~ 100 ps
$Ti:Al_2O_3$ (Ti:sapphire)	$30 \cdot 10^{-20}$	3.3 μs
Nd:YAG	$65 \cdot 10^{-20}$	230 μs
Nd:YLF	$18 \cdot 10^{-20}$	450 μs
Nd:glass	$4 \cdot 10^{-20}$	350 μs
$Cr^{3+}:LiSrAlF_6$ (Cr:LiSAF)	$4.8 \cdot 10^{-20}$	67 μs
$Cr^{4+}:Mg_2O_3$ (Cr:forsterite)	$20 \cdot 10^{-20}$	2.7 μs
Cr^{4+}:YAG	$30 \cdot 10^{-20}$	3.6 μs

TABLE 2-1: Gain cross-sections for laser materials, absorption cross-sections for saturable absorbers, and upper state lifetimes for various materials and devices.

2.5.5 Bandwidth of operation and other characteristics

Ideally, the key parameters of a saturable absorber should be independent of wavelength. This would be optimal for a broad wavelength tunability as well as for generation of short pulses with a broad bandwidth of operation. For semiconductors, the absorption coefficient, saturation fluence, and carrier dynamics are typically strong functions of photon energy compared to the bandgap. Away from the optimal wavelength of operation, the absorption of a saturable absorber device, based on semiconductor quantum wells or a bulk semiconductor, rapidly becomes too small toward longer wavelengths and too high toward shorter wavelength. This wavelength dependence limits the spectral operation range of a saturable absorber. A solution may be to use several quantum well with different energy gaps and to place them in the appropriate spots relatively to the standing wave inside the device, according to the principles described in Section 2.6.5 and in Chapter 3. A wavelength-dependent laser mode size in case of KLM can also act as a bandwidth limiting factor [64].

In addition, a saturable absorber should have a high enough damage threshold to withstand the high intracavity laser intensity needed to bleach the absorption. An ideal saturable absorber should not impose any significant constraints on the laser resonator design and not require a critical alignment of the laser cavity. Simple absorber fabrication methods and low cost are also desirable.

The summary of the most important requirements on the saturable absorber characteristics is given in Table 2-2.

Characteristic	**Ideal saturable absorber**
modulation depth	high
nonsaturable loss	none
saturation intensity	• higher than cw intracavity intensity • low enough to facilitate self-starting
saturation fluence	• low enough to provide high modulation depth and avoid Q-switching • high enough to avoid multiple pulsing
absorption recovery time	• faster than the cavity round trip time • slow enough to facilitate self-starting • fast enough for pulse-shortening
wavelength dependence	none
damage threshold	high
laser resonator alignment	not critical
constraints on device design (e.g. lattice matching)	none
fabrication technology	simple
cost	low

TABLE 2-2: Summary of the key characteristics of an ideal saturable absorber.

2.6 Epitaxially-grown semiconductor saturable absorbers

Semiconductor saturable absorbers can provide a compact optical nonlinearity without need for critical alignment with adjustable bandgap wavelength and nonlinearity. In the past, semiconductor saturable absorbers have been used to modelock color-center [65] and diode lasers [66]. However, bulk semiconductors are not well suited for modelocking most solid-state lasers, because semiconductors tend to have too high loss, low saturation intensity, low damage threshold, and long upper-state lifetime.

2.6.1 Semiconductor saturable absorber mirrors and saturable Bragg reflectors

A solution to the low saturation intensity and high insertion loss problems was found with the invention of the semiconductor saturable absorber mirrors (SESAMs) [67] [68] [22] and saturable Bragg reflectors (SBRs) [23] that incorporate epitaxially-grown semiconductor absorbers into multilayer reflective structures. The techniques that are used to overcome the problem of the long carrier lifetimes are discussed in section 2.6.7 below. By adjusting the device parameters, SESAMs and SBRs allow linear and nonlinear absorption characteristics of a semiconductor to be engineered in order to design efficient saturable absorbers. In practical terms, a device like this is a nonlinear mirror that replaces one of the laser cavity mirrors to passively modelock a laser. SESAMs and SBRs modify the effective optical properties of the semiconductor absorber by adjusting the optical intensity on the absorber compared to the intensity incident on the device. A SESAM is typically comprised of two reflectors forming a Fabry-Perot resonator with a saturable absorber layer in between. Several designs have been proposed which can be classified according to the top surface reflectivity as a high-finesse antiresonant Fabry-Perot saturable absorber (A-FPSA), low-finesse A-FPSA also called a saturable Bragg reflector (SBR), and AR-coated SESAM (see Figure 2-8). High-finesse A-FPSAs have a dielectric high reflector (~ 95%) on top of the device, SBRs have a top surface reflectivity of ~30% due to the Fresnel reflection from the air-semiconductor interface, and AR-coated SESAMs have an antireflection coating on top. The choice of the top coating determines the optical intensity inside the device and changes a contribution of the bottom mirror to an overall device reflectivity and dispersion.

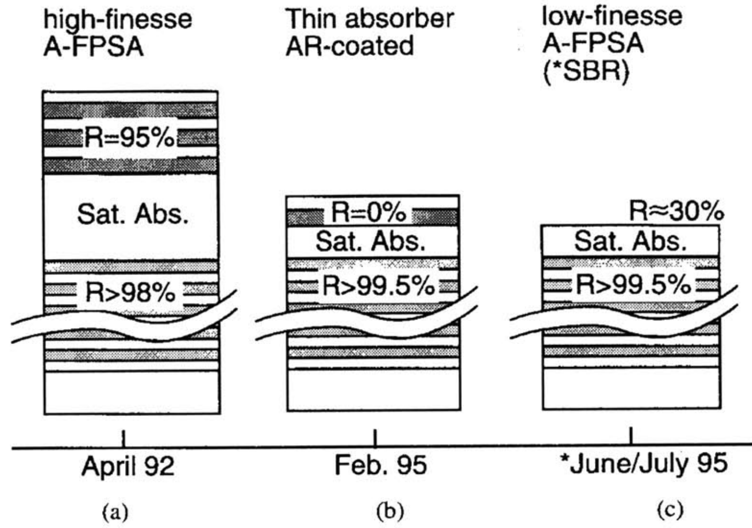

FIGURE 2-8: Semiconductor saturable absorber mirror devices in historical order. a) High-finesse A-FPSA. b) Thin AR-coated device. c) SBR (low-finesse A-FPSA). ([22])

2.6.2 General principles of A-FPSA operation

In an A-FPSA [20], a semiconductor absorber is integrated inside a Fabry-Perot resonator which is operated at antiresonance. At antiresonance, the intensity inside the Fabry-Perot is lower than the incident intensity. As a result, for a given intracavity intensity, the intensity on the saturable absorber is reduced, leading to an increased effective saturation intensity and fluence, as well as higher damage threshold. It can also be shown that operation at antiresonance reduces the dispersion that is introduced into the laser resonator [67] [68]. A typical A-FPSA is composed of two mirrors with a saturable absorber layer and possibly a non-absorbing spacer layer in between. The semiconductor absorber layer is grown on top of the bottom mirror using molecular beam epitaxy and therefore requires a reflective substrate that is lattice-matched to the absorber material.

The bottom mirror is typically a semiconductor distributed Bragg reflector (DBR) fabricated by MBE or MOCVD. A DBR is formed by ~ 20 pairs of alternating high-low index semiconductor layers (e.g. GaAs and AlAs), each layer having a quarter-wave optical thickness at the design wavelength. Epitaxial fabrication techniques require that the semiconductor layers be lattice-matched to each other and only a small lattice mismatch is allowed relative to the absorber layer.

Due a small refractive index difference between the semiconductors layers, a large number of quarter-wave layers is necessary to provide a high DBR reflectivity. Compared to standard dielectric mirrors that use TiO_2 and SiO_2 quarter-wave layers with the refractive indices of respectively 2.4 and 1.45, epitaxially-grown DBRs require the use of lattice-matched semiconductors such as for GaAs and AlAs with the refractive indices of 3.37 and 2.91. The small difference in the refractive indices of the semiconductor layers imposes a fundamental limitation on the DBR bandwidth (less than 100 nm in the near IR) and also leads to poorly controlled dispersion. The implications of the effect of the DBR on the overall device performance will be discussed below.

A saturable absorber layer, which is epitaxially grown on top of the DBR, can be a multiple quantum well or single semiconductor layer. The top mirror consists of three or four pairs of SiO_2 and TiO_2 quarter-wave layers that are evaporated on top of the device. The material thickness between the two mirrors d is chosen to satisfy the antiresonance condition

$$\varphi_{rt} = \varphi_t + \varphi_b + 2k\bar{n}d = (2m+1)\pi \tag{2-55}$$

where φ_t and φ_b are the phase shifts acquired from the top and bottom mirror reflections, and $\bar{n}$ is the average refractive index of the medium between the mirrors.

At antiresonance, the intensity inside a Fabry-Perot is decreased by a factor of ζ compared to the incident intensity:

$$\zeta = \frac{1-R_t}{(1+\sqrt{R_t R_b}e^{-2\alpha_A d})^2} \tag{2-56}$$

where R_t and R_b are the top and bottom mirror reflectivities, d and α_A are the thickness and the amplitude absorption coefficient of the absorber. Therefore, the effective saturation fluence of an absorber inside an antiresonant Fabry-Perot is increased by a factor of $1/\zeta$ compared to a free-standing absorber:

$$\Gamma_{sat,\,eff} = \frac{1}{\zeta}\Gamma_{sat} \tag{2-57}$$

The saturation intensity in also increased by the same factor. The damage threshold of a high-finesse A-FPSA is high and is determined by the top dielectric high reflector mirror, which is similar to the other dielectric mirrors that constitute a laser resonator. By adjusting the Fabry-Perot parameters such as the top mirror reflectivity, it is possible to choose the desired effective saturation fluence of the absorber. Using the incident laser mode size as an adjustable parameter, the incident energy density can be adapted to the effective saturation fluence of the device.

2.6.3 High-finesse A-FPSA

A high-finesse A-FPSA [20] [68] was the first SESAM device to be used for laser modelocking. The top reflector in this case is a broadband highly reflective SiO_2/TiO_2 mirror. The high reflectivity of the top mirror deemphasizes the effects of the narrow bandwidth and poor dispersion properties of the bottom DBR mirror leading to good overall reflective properties of the device. Reducing the top mirror reflectivity increases the bandwidth-limiting effects of the bottom mirror.

Because of the high reflectivity of the top mirror, the intensity inside the Fabry-Perot is much lower than the incident intensity and the saturation fluence and intensity are significantly increased. For example, for a top and bottom mirror reflectivities of respectively 95% and 98%, the ζ factor is equal to 0.018 and the effective saturation fluence is increased by a factor of ~ 56. However, the same effect also causes the absorption modulation depth to be significantly reduced. Using a high-finesse A-FPSA, 19 fs KLM-assisted pulses were generated from a Ti:Sapphire laser, and 40 fs pulses were generated in the soliton modelocking regime [69]. The pulse duration was limited by the low modulation depth of the absorber of only ~1% which could not support shorter pulses.

2.6.4 AR-coated SESAM

A higher modulation depth can be obtained using an AR-coated SESAM design where a high reflector on top is replaced by an antireflection coating [70] [69] [68]. The AR coating increases the field penetration inside the device, reduces the saturation intensity, and increases the modulation depth. In this case, the saturable absorber thickness is reduced to minimize the insertion losses and a single quantum well is typically used to provide absorption.

AR-coated SESAMs have lower saturation intensity than the high-finesse A-FPSAs, and as a result, have better self-starting performance (see section 2.3). Using such devices, self-starting pulses of 34 fs duration were generated from a Ti:Sapphire laser with a modelocking build up time of only 3 μs [69]. Using saturable-absorber-assisted soliton modelocking, modelocking could be obtained throughout the whole resonator stability region. The significant drawback of an AR-coated A-FPSA is that its reflectivity relies entirely on the bottom DBR mirror and although the device has an absorption modulation depth sufficient to support shorter pulses, the pulse duration is limited by the narrow bandwidth of the DBR.

The small saturable absorber thickness on a scale of several nanometers opens new possibilities for controlling the saturation behavior and wavelength dependence of optical properties. For a EM wave reflected from a mirror, a standing wave pattern is formed by the incident and reflected light. With the quantum well thickness much smaller than the wavelength, it is possible to position the absorber at a specific point in the standing wave and in this way control the electric field intensity on the absorber and the effective absorption saturation parameters. The wavelength dependence of the standing wave peak positions allows to adjust the device absorption independently for different wavelengths and partially compensate for the bandgap-induced wavelength dependence of absorption in a semiconductor.

2.6.5 Low-finesse A-FPSA (SBR)

The low-finesse A-FPSA, also referred to as a saturable Bragg reflector [71] [23], is an intermediate design scenario between a high-finesse A-FPSA and an AR-coated SESAM. The ~30% reflection from the top surface is due to the Fresnel reflection from the air/semiconductor interface. Similarly to the AR-coated SESAM, the bottom mirror is formed by up to 30 high-low index pairs of semiconductor layers resulting in reflectivity above 99.5%. The bandwidth of the DBR however is still relatively narrow (less than 100 nm in the near IR) and cannot support ultrashort pulses. A saturable absorption is provided by a single or multiple quantum well buried in one of the top DBR layers. By adjusting the saturable absorber position relative to the peaks of the standing wave pattern, the saturation intensity is controlled. A standing wave intensity decreases rapidly going deeper into the device. If the absorber is located in the top layer, the saturation intensity can be made low, while a high saturation intensity can be obtained by putting the absorber deep inside the structure. An advantage of the SBR over the other SESAM designs is that the whole device can be fabricated in a single MBE run and does require any post-processing such the AR or HR coatings.

2.6.6 Broadband SESAM with a silver mirror

A modification of a low-finesse A-FPSA design that solves the bandwidth limitation due to a DBR mirror was recently proposed [72]. The solution was to replace the Bragg mirror by a broadband metal silver mirror having a reflectivity greater than 97% from ~500 nm to the mid-IR. However, because the saturable absorber layer is fabricated using epitaxial techniques which require a lattice-matched substrate, the semiconductor cannot be grown directly on a silver mirror. Instead, the absorber is grown on a semiconductor substrate which is subsequently etched off, the back surface is metallized and bonded to a heat sinking substrate. Overall, the fabrication requires extensive post-processing and precise etching techniques.

Using a broadband SESAM with a silver mirror, self-starting KLM-assisted 10-fs pulses were generated from a Ti:sapphire laser [72]. In conjunction with the recently developed double-chirped mirrors that provide a broad reflectivity bandwidth together with a precise control of dis-

persion [41] [40], a broadband silver mirror SESAM was used to obtain self-starting KLM-assisted 6.5 fs pulses from a Ti:sapphire laser which is currently the record pulse duration directly out of a laser oscillator [16]. A similar device with a higher modulation depth was used to generate soliton-modelocked 13 fs pulses over the whole cavity stability range without KLM assistance [60].

2.6.7 Control of the carrier recombination dynamics

Carrier lifetimes in bulk semiconductor materials due to interband recombination are typically on the order of several nanoseconds. In order for semiconductor materials to be used as saturable absorbers for modelocking, significantly faster carrier recombination times are desired.

The research motivated by a number of high-speed optoelectronic applications has led to the development of several techniques that reduce semiconductor carrier lifetimes by introducing various imperfections into the semiconductor structure. The techniques use various methods to create traps and recombination centers in a semiconductor material to facilitate faster carrier recombination times. The techniques include proton bombardment [73] [74], ion implantation [75], low-temperature growth [76] [77] [78], and He-plasma-assisted growth [79].

The first two techniques require extensive post-processing, do not allow separate treatment of different parts of a device, and produce a significant amount of optical damage. Low-temperature growth became a widely used technique for tailoring carrier dynamics for saturable absorber applications [67] because it can be combined with standard epitaxial fabrication techniques, allows precise control of carrier recombination rates and does not introduce an excessive amount of damage and scattering defects into the material. It should be noted however that the amount of nonsaturable loss typically does increase for low-temperature-grown semiconductors.

III-IV semiconductors, grown by MBE at low temperature (as low as 200°C) and subsequently annealed, exhibit significantly reduced carrier lifetimes compared to semiconductors grown at standard temperatures (~ 600°C). The effect is attributed to the excessive concentration of group-V elements which form point defects [80] acting as carrier trap sites [81]. The photoge-

nerated carriers in a semiconductor are rapidly trapped into the mid-gap defect states and then recombine [82] [83]. Carrier lifetimes in GaAs and other III-V materials can be reduced drastically, from tens of nanoseconds to picoseconds and even subpicoseconds in annealed low-temperature-grown material. By adjusting the growth temperature, the carrier recombination dynamics can be tailored for specific applications [67] [84].

2.6.8 Modelocking of various laser systems using semiconductor saturable absorbers

In recent years, semiconductor saturable absorber mirrors have become a widely used technology for short pulse generation. A number of modelocking applications of SESAMs and SBRs has been demonstrated, both for saturable-absorber-assisted KLM, and for pure saturable absorber modelocking.

High-finesse A-FPSA was the first semiconductor saturable absorber mirror device applied intracavity for solid-state laser modelocking. Cw passive modelocking of a Nd:YLF laser was obtained in 1992 using an A-FPSA based on low-temperature-grown InGaAs/GaAs multiple quantum wells (MQW) [20]. Pulses of 3.3 ps duration were generated with a center wavelength of 1.047 μm. In 1996, 5.7 ps pulses were obtained from a diode-pumped passively modelocked Nd:YLF laser. Since then, high-finesse A-FPSA devices were applied to modelocking of a number of solid-state laser materials. In 1993, a Nd:glass laser was modelocked using a similar LT-InGaAs-based A-FPSA and produced pulses as short as 130 fs at 1.063 μm [85]. Modelocking was also obtained in a diode-pumped Nd:glass laser to produce pulses of 130 fs duration [86]. Cr:LiSAF, which is a very promising laser material for diode pumping, was modelocked using high-finesse A-FPSAs based on LT-GaAs/AlGaAs MQWs to produce pulses in the 45-100 fs range around 850 nm [87]. Yb:YAG, which is interesting as a very efficient high-power diode-pumped laser material because of its small quantum defect, was modelocked using a high-finesse LT-InGaAs to produce 900-fs pulses around 1.05 μm [88]. Finally, pulses as short as 19 fs were generated from a Ti:Al_2O_3 laser [69]. Overall, the key distinguishing characteristics of high-finesse A-FPSA devices are a relatively high saturation fluence, on the order of 1-10 mJ/cm^2,

small absorption modulation depth, low insertion loss, and broad bandwidth of operation. The major trade-off is between the modulation depth on one side and the operating bandwidth and insertion loss on the other side.

Low-finesse (SBRs) and AR-coated SESAMs typically have a lower saturation fluence, around 0.1-1 mJ/cm^2, higher insertion loss, narrower bandwidth of operation (with the exception of SESAMs with a silver mirror), and can provide a deeper absorption modulation. The first such device was demonstrated in 1995 to modelock a Ti:Al_2O_3 laser [69]. Silver-mirror-based SESAMs with a LT GaAs/AlGaAs QW absorber have been applied in conjunction with KLM to produce 6.5 fs pulses from a Ti:sapphire laser, currently the shortest pulses generated directly out of the laser [16]. They also allowed to produce 13 fs pulses from a Ti:sapphire by saturable-absorber-stabilized soliton modelocking, without KLM [60]. Low-finesse A-FPSAs with InGaAs/InAlAs, InGaAs/InP, and InGaAs/GaAs QWs were used by several research groups to passively modelock Cr:forsterite lasers at 1.3 μm and Cr:YAG lasers at 1.5 μm [89] [90] [91] [92]. Picosecond pulses were generated from Nd:LSB and Nd:YVO_4 lasers around 1.06 and 1.34 μm respectively with similar low-finesse devices [93] [94]. In order to obtain a broader operating range of low-finesse A-FPSAs and compensate for the wavelength-dependent QW absorption, devices were demonstrated with several QWs with different absorption edges that were placed at different positions in the standing wave field pattern. Such broadband design allowed to obtain 50-nm tuning range in Cr:LiSAF laser [95] and a 300-nm tuning range in a Ti:sapphire laser with two separate SESAMs in conjunction with broadband double-chirped mirrors [96] [97].

A summary of the key operating parameters for the most significant solid-state laser modelocking results obtained using epitaxially grown semiconductor saturable absorbers is presented in Table 2-3 and Table 2-4.

In summary, compared to a pure KLM operation, semiconductor saturable absorbers offer a number of advantages. They provide self-starting modelocked operation, decouple the gain and modelocking mechanisms, simplify the laser cavity design, allow more compact laser resonators, and make modelocking more robust and insensitive to external perturbation.

However, SESAMs and SBRs do have an important drawback, namely the necessity of using epitaxial growth techniques such as molecular beam or chemical beam epitaxy for their fabrication. Because quantum wells must be lattice-matched, there exist severe constraints on the choice of absorber materials and substrates as well as on the overall device design. Semiconductor DBRs, that have to be used as substrates for the saturable absorber quantum wells, have narrow bandwidth and limit the pulse durations and wavelength tunability. They also require a long and complex fabrication process. Alternatively, the broadband SESAMs based on the silver mirrors require complex and extensive post-processing. The idea of combining saturable absorbers with the recently developed chirped mirrors is very attractive but is impossible for the epitaxially-grown semiconductors. In addition, epitaxial growth techniques are relatively complex and costly, limiting the widespread availability of saturable absorber devices.

These considerations motivated our search for new saturable absorber materials and devices that would not require epitaxial fabrication, would be versatile and easy to integrate into various dielectric devices, and would be simple and easy to fabricate.

Laser material	SA type	SA materials	Type of mode locking	Pump	Pump power [W]	Output power [mW]	OC [%]	τ [fs]	λ_0 [nm]	Tuning range [nm]	Rep rate [MHz]	Year	Ref
$Ti:Al_2O_3$ 2 mm	high-finesse A-FPSA	LT GaAs	SA+KLM SA	Ar ion	2.3 absorbed	300	3	19 40-90	840	-	97	95	[69]
$Ti:Al_2O_3$ 2 mm	AR A-FPSA	LT GaAs	SA	Ar ion	3.2 absorbed	120	3	34	840	-	97	95	[69]
$Ti:Al_2O_3$ 2.3 mm	Ag - SESAM	LT GaAs	SA+KLM SA	Ar ion	4.0	120	3	10 16	800	-	86	96	[72]
$Ti:Al_2O_3$ 2 mm	Ag - SESAM	LT GaAs	SA	Ar ion			3	13	810			96	[60]
$Ti:Al_2O_3$ 2.3 mm	Ag - SESAM	LT GaAs	SA+KLM	Ar ion	5.0	200	3	6.5	800	-	86	97	[16]
$Ti:Al_2O_3$ 2.3 mm	Ag - SESAM		SA+KLM	Ar ion	7.0	< 330		30	800	700-1000 with 2 SESAMs		98	[97] [96]

TABLE 2-3: Summary of $Ti:Al_2O_3$ laser modelocking results obtained using epitaxially grown saturable absorbers. SA, saturable absorber; LT, low temperature grown; OC, output coupler; τ, pulse width; λ_0, center wavelength.

Laser material	SA type	SA materials	Type of ML	Pump	Pump power [W]	Output power [mW]	OC [%]	τ [fs]	λ_0 [nm]	Tuning range [nm]	Rep rate [MHz]	Year	Ref
Cr:forsterite 7mm	SBR	InGaAs/ InAlAs	SA+KLM SA	$Nd:YVO_4$	5.0 absorbed	60	2	40 15 ps	1295	-		97	[89]
Cr:LiSAF 2.5 mm	SBR	GaAs	SA	diode	0.38	11	1	100	865	-	178	95	[71]
Cr:LiSAF 2.5 mm	SBR	GaAs	SA	MOPA	0.5	100	1	70	866	~ 10	100	96	[98]
Cr:LiSAF 2 mm	low-finesse A-FPSA	LT GaAs	SA	diode	0.7 absorbed	125	0.8	45	850	825-875	176	97	[95]
Cr:YAG 20 mm	SBR	InGaAs/ InP	SA	$Nd:YVO_4$	8.0	70	1.5	110	1541	-		96	[90]
Cr:YAG 20 mm	low-finesse A-FPSA	InGaAs/ GaAs LT	SA	$Nd:YVO_4$	6.0 absorbed	94	1.7	114	1514	-	185	97	[91]
Cr:YAG 20 mm	SBR	InGaAs/ InAlAs	SA	Nd:YAG	3.0 absorbed	80	1	122	1488	1488-1535		97	[92]
Nd:glass 4 mm	high-finesse A-FPSA	LT InGaAs	SA	$Ti:Al_2O_3$	1.0 absorbed	160	1	130	1063	-		93	[85]
Nd:glass 4 mm	low-finesse A-FPSA	LT InGaAs	SA	diode	1.1 absorbed	84	1	60	1064	-	114	97	[63]
Nd:LSB 2.5 mm	low-finesse A-FPSA	InGaAs	SA	diode	1.2	400	2	2.8 ps	1062	-	177	96	[93]
Nd:YLF 5 mm	high-finesse A-FPSA	InGaAs/ GaAs	SA	$Ti:Al_2O_3$	2.0	700	2	3.3 ps	1047	-	220	92	[20]
Nd:YAG Nd:YLF	low-finesse A-FPSA	LT InGaAs	SA	diode	1.0 2.0	100 225	0.8	8.7 5.1	1064 1047	-	100	93	[99]
Yb:YAG 3.5 mm	high-finesse low-finesse	LT InGaAs	SA	$Ti:Al_2O_3$ at 940 nm	1.0 0.9	150 170	2	900 570	1050	-	81 75	95	[88]
Nd:YLF 4 mm	high-finesse A-FPSA	LT InGaAs	SA	diode	1.1 absorbed	130	1	5.7 ps	1314	-	98	96	[100]
$Nd:YVO_4$ 3.5 mm	low-finesse A-FPSA	LT InGaAs	SA	diode	1.2 absorbed	50	1	4.6 ps	1342	-	93	96	[100]

TABLE 2-4: Summary of the key laser modelocking results obtained using epitaxially grown saturable absorbers.

Chapter 3

Design of saturable Bragg reflectors

3.1 Introduction

This Chapter will describe the results of modeling the characteristics of saturable Bragg reflectors. A saturable Bragg reflector (SBR) is a nonlinear mirror device for laser modelocking that provides saturable absorption while maintaining low insertion loss. An SBR is comprised of a high reflector and a saturable absorber grown on top or buried inside the reflector. The high reflectivity is provided by a distributed Bragg reflector (DBR) and the saturable absorption is due to a single or multiple semiconductor quantum well. SBRs have been demonstrated to modelock a number of laser systems in the 0.8, 1.3, and 1.5 μm wavelength ranges [23], [98] [101] [22].

In order to build an SBR capable of modelocking a laser, its properties need to be modeled and their dependence on the device structure known. The key characteristics of an SBR include reflectivity and insertion loss, saturable loss, dispersion, and field distribution inside the device. The main adjustable parameters include the choice of semiconductor materials that form the DBR, the number of semiconductor layers, the choice of the absorber, and the position of the absorber within the device. There are several constraints imposed on the above parameters that are due largely to the epitaxial fabrication techniques, such as molecular beam epitaxy (MBE), that are used to grow SBRs. The constraints include lattice matching of the subsequent semiconductor layers and the limited choice of semiconductor materials that can be used in a given MBE system.

This chapter discusses the theoretical issues involved in the design of saturable Bragg reflectors and presents the results of modeling the SBR parameters. The characteristics of GaAs/AlAs-based SBRs were calculated for different design parameters using both the matrix (layer) and the interface formulations [102] [103]. The details of the calculations as well as the MATLAB code are presented in Appendix while the results are presented in this Chapter.

The Chapter is organized as follows. The introduction gives an overview of the Chapter. Section 3.2 describes the SBR structure. The results of SBR reflectivity calculations for different designs are presented in Section 3.3. The calculation of SBR dispersion is discussed in Section 3.4. Section 3.5 discusses the field distribution inside the device. The two-photon absorption effects and their influence on SBR performance are discussed in Section 3.6. Section 3.7 summarizes the results presented in the Chapter.

3.2 SBR structure

An SBR considered in this chapter is fabricated in the following way. A DBR is grown on top of a semiconductor substrate. On top of a DBR, a saturable absorber region is grown together with an optional transparent spacer layer. The SBR schematic is shown in Figure 3-1. The wafer is then cleaved and the SBR pieces are attached to heat-sinking substrates such as copper. The SBRs described in this chapter were fabricated by E. Marley-Koontz in Professor L. Kolodziejski's laboratory.

The SBR was designed to provide optimal performance in the 1.55 μm wavelength range for applications to Er-doped fiber laser and Cr:YAG laser modelocking. The design is similar to the one demonstrated in reference [90]. A DBR is formed by pairs of alternating layers of GaAs and AlAs grown by molecular beam epitaxy (MBE) on top of a 2-inch-diameter GaAs wafer. Each semiconductor layer has a quarter-wave optical thickness at the design wavelength. The semiconductors were selected based on the choice of materials that could be grown in a given MBE system as well as by lattice-matching requirements. In order to grow an epitaxial structure thicker than a few monolayers, the lattice constants of the materials have to be matched, such as for GaAs a_{GaAs}=5.65 Å and AlAs a_{AlAs}=5.66 Å [104].

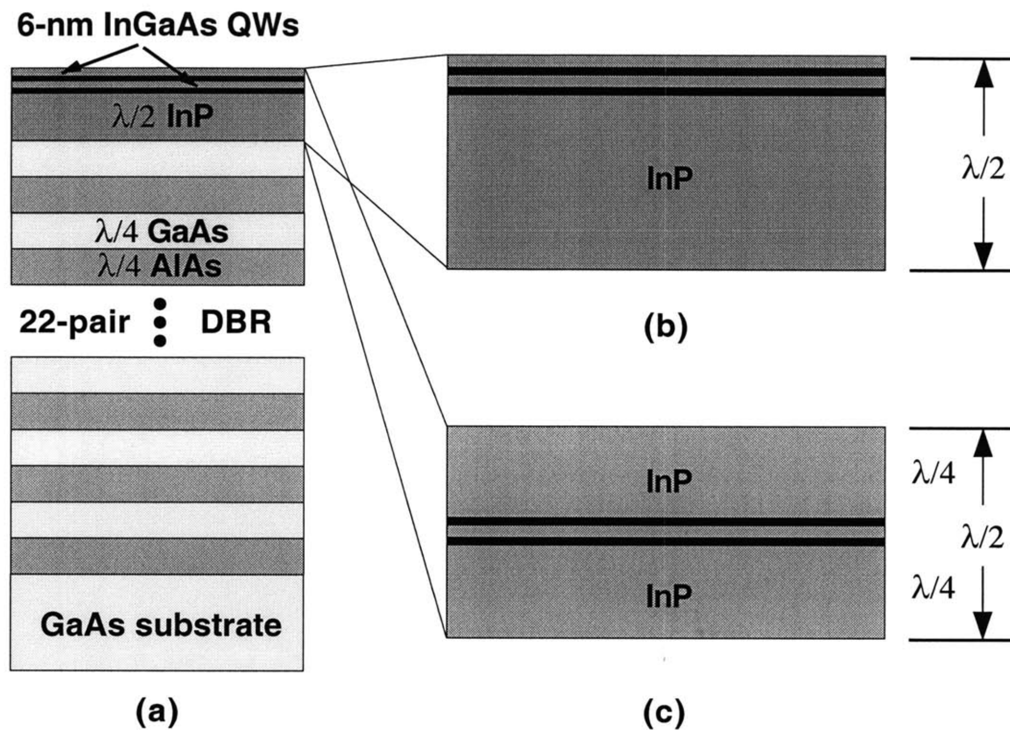

FIGURE 3-1: a) Schematic of the saturable Bragg reflector (Sub |(AlAs GaAs)^{22} Cap| Air). b) Cap layer design for a high saturation intensity device. c) Cap layer design for a low saturation intensity device.

3.3 Reflectivity and bandwidth

In order for a DBR to be used in a laser cavity, its reflectivity should be above ~ 99% throughout the laser bandwidth of operation. The imperfect DBR reflectivity contributes to the nonsaturable loss of the device which should be minimized for optimal performance. Figure 3-2 shows the calculated wavelength dependence of reflectivity for DBRs composed of different numbers of quarter-wave GaAs/AlAs pairs. As the number of pairs is increased, the reflectivity at the design wavelength approaches 100%. To obtain high reflectivity, a large number of pairs is required because of the small index of refraction difference between GaAs and AlAs. For a final DBR design with 22 GaAs/AlAs pairs, the peak reflectivity is over 99.5%.

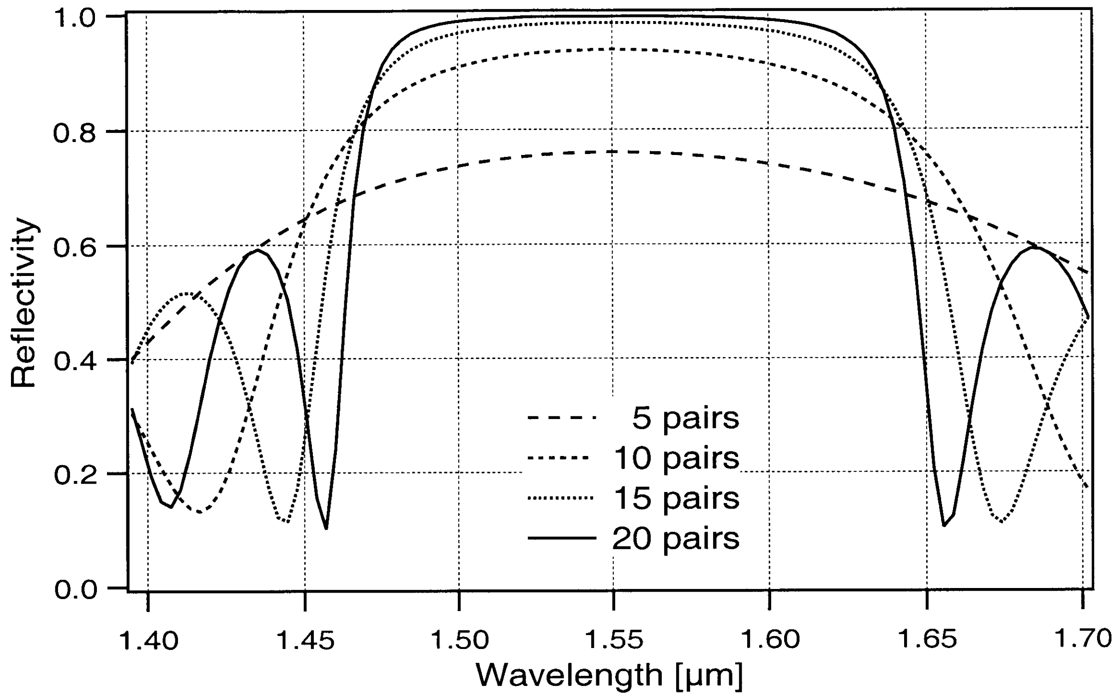

FIGURE 3-2: Calculated GaAs/AlAs DBR (Sub $|(\mathrm{AlAs\ GaAs})^N|$ Air) reflectivity as a function of number of quarter-wave pairs N.

Although the peak reflectivity of the DBR is sufficiently high for application in low-gain solid state lasers, the bandwidth is relatively narrow due to a small difference between the refractive indices of GaAs n_{GaAs} = 3.37 and AlAs n_{AlAs} = 2.91 [104]. As a result, the bandwidth of the semiconductor mirror is considerably smaller than that of conventional dielectric Bragg mirrors composed of quarter-wave layers of SiO_2 and TiO_2 with refractive indices n_{SiO2}= 1.45 and n_{TiO2} = 2.4. When an SBR is used in a modelocked laser resonator, the narrow bandwidth of the DBR acts as a limiting factor on the pulse width as well as on the wavelength tunability of the laser. This fundamental limitation on the bandwidth is a severe drawback of the SBR technology.

The transmission of the fabricated DBR was measured using a CARY 5E spectrophotometer. The measured DBR reflectivity data are in good agreement with the modeling results and are shown in Figure 3-3. Due to the dependence of the semiconductor growth rate on the substrate position inside the MBE chamber, the DBR reflectivity is a function of the position on the wafer.

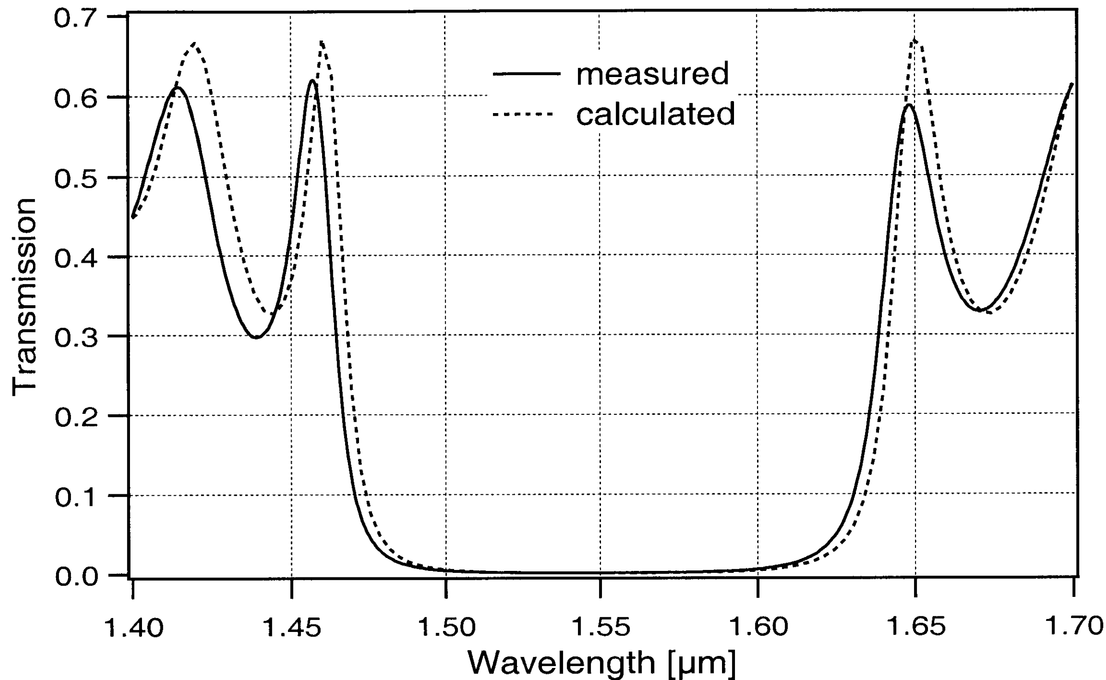

FIGURE 3-3: Comparison of measured and calculated transmission through a GaAs/AlAs DBR (Sub |(AlAs GaAs)^{22}| Air). The calculated data accounts for the 30% Fresnel reflection from the back side of an SBR substrate.

The deposition rate and thickness of the layers decrease toward the edge of the wafer and the reflectivity band shifts to shorter wavelength (Figure 3-4). This limits the usable area of the SBR wafer to regions 1 and 2 on Figure 3-4.

The saturable absorption in the SBR was provided by a single or multiple quantum well, depending on the total desired absorption. The quantum wells were composed of $In_{1-x}Ga_xAs$ with x=0.47, with the bulk bandgap of 0.75 eV (absorption edge at 1.65 μm) buried in InP. The $In_{0.53}Ga_{0.47}As$ lattice constant of 5.87 Å is not matched to those of the DBR materials and is matched to the lattice constant of InP, a_{InP}=5.87 Å [105]. Therefore, in order to relax strain and to be able to grow an InGaAs absorber layer without defects, an InP buffer layer can be used. The thickness of the InP layer sufficient to relax strain and to grow defect-free InGaAs, was experimentally found to be at least 100 nm.

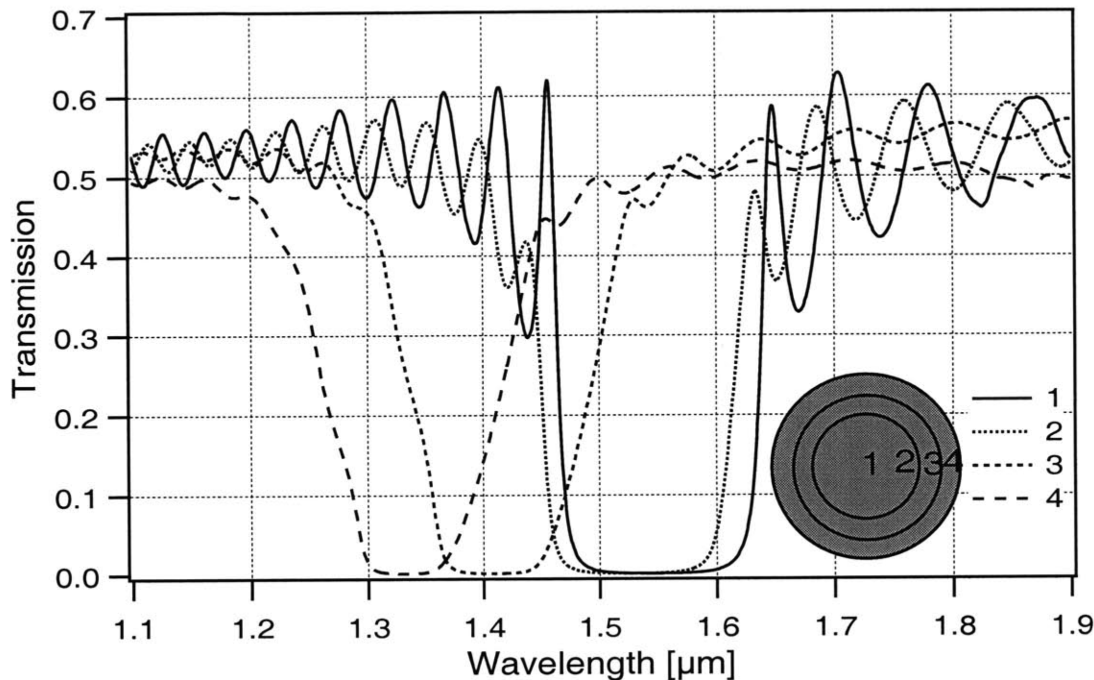

FIGURE 3-4: Measured transmission of a GaAs/AlAs DBR (Sub |(AlAs GaAs)^{22}| Air). The transmission is a strong function of the position on the 2-inch wafer. The four traces correspond to the locations shown on the wafer schematic.

Two designs with different InP capping layer thicknesses, half-wave and quarter-wave, were considered (Figure 3-1). In the first case, with a half-wave InP layer on top of the DBR, the calculated reflective properties of the DBR were not affected and the high reflectivity was preserved. In contrast, if a quarter-wave InP layer was used, the DBR structure was perturbed and the peak reflectivity was decreased to 98%, as can be seen from Figure 3-5. Therefore, a half-wave InP cap design was used throughout the remainder of this work.

3.4 Dispersion

Group velocity dispersion in a laser resonator is a crucial parameter for short pulse generation [33]. Net negative second order dispersion, also referred to as group delay dispersion (GDD), is important for soliton-like pulse formation in a modelocked laser while higher order dispersion is a detrimental factor for short pulse generation and should be minimized. As it was discussed in

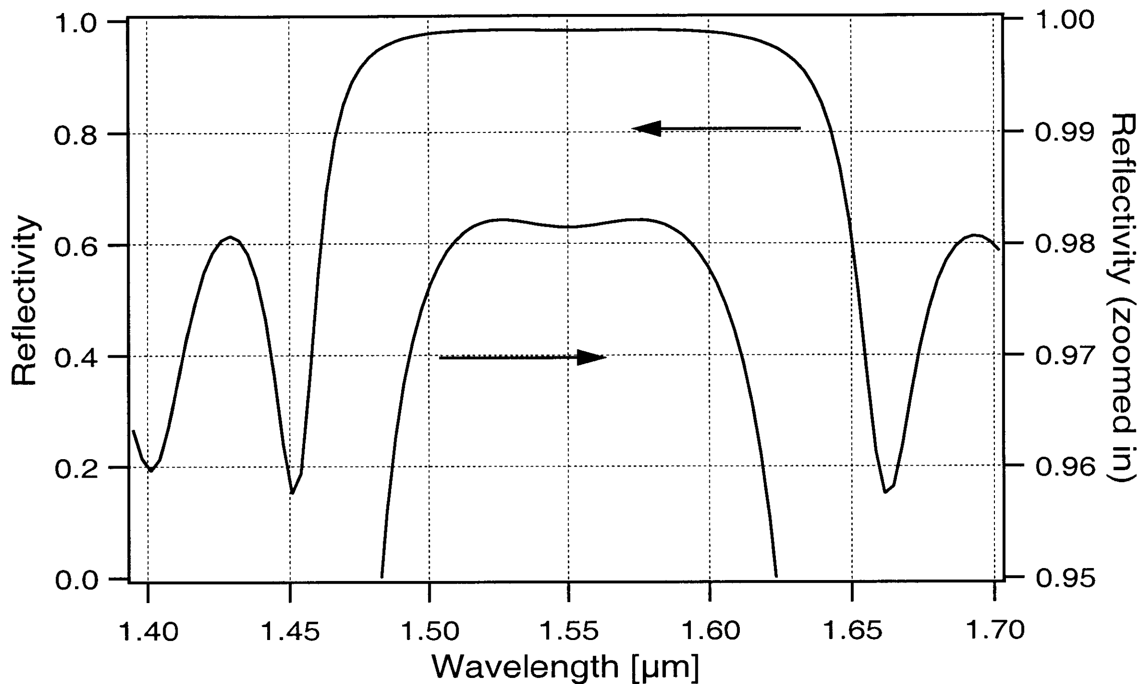

FIGURE 3-5: Calculated reflectivity of a GaAs/AlAs DBR (Sub |(AlAs GaAs)^{22} InP| Air) with a quarter-wave InP cap layer. The peak reflectivity is decreased significantly compared to an uncapped DBR. For a half-wave cap layer (not shown) the high DBR reflectivity was not affected.

Chapter 2, a number of optical elements contribute to the net resonator dispersion, including the resonator mirrors such as a DBR. Ideally, the mirror dispersion should be an adjustable parameter that would provide negative GDD and allow compensation of higher order dispersion due to various other intracavity elements.

The DBR dispersion is caused by a nonlinear wavelength dependence of the phase acquired on reflection. The calculated phase as a function of wavelength for a GaAs/AlAs DBR, together with the reflectivity, is shown in Figure 3-6. The group delay dispersion, shown in Figure 3-7, is obtained by taking a second derivative of the phase with respect to angular frequency. From the figure, it can be seen that the DBR does not introduce any GDD at the center wavelength of 1.55 μm and that, on the other hand, the GDD is a strong function of wavelength. This wavelength dependence of the GDD can be expressed as the third order dispersion (TOD) which is shown in

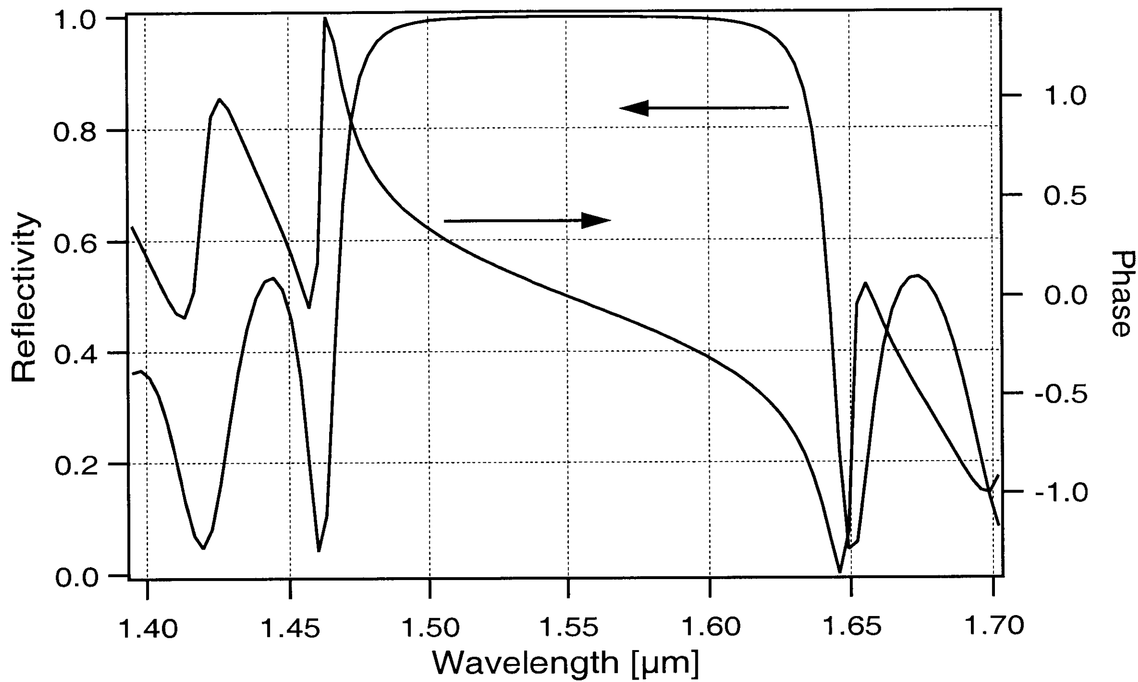

FIGURE 3-6: Calculated reflectivity and phase acquired on reflection for a GaAs/AlAs DBR capped with a half-wave layer of InP (Sub |(AlAs GaAs)^{22}InP InP| Air).

Figure 3-8. In the case of a AlAs/GaAs DBR, the reflector not only provides no negative GDD, but also has high third order dispersion that has to be compensated by some other intracavity dispersive elements, such as a prism pair, complicating the laser design.

Several designs of chirped and double chirped dielectric mirrors have been recently demonstrated in the literature. Such mirrors use a gradual variation of the thicknesses of the dielectric SiO_2/TiO_2 Bragg reflector layers to provide a broader reflectivity bandwidth and tailor the reflection phase to provide desired dispersion [40] [41]. The chirped mirror approach however does not work for semiconductor DBRs because of the small index of refraction differential between the successive layers. The small index differential leads to a low reflection from each layer interface and requires a large number of layers with quarter-wave thickness at a given wavelength to provide appreciable reflection. The Fresnel power reflectivity of a GaAs/AlAs interface is ~0.5% which is an order of magnitude smaller than the ~6% reflectivity for SiO_2/TiO_2.

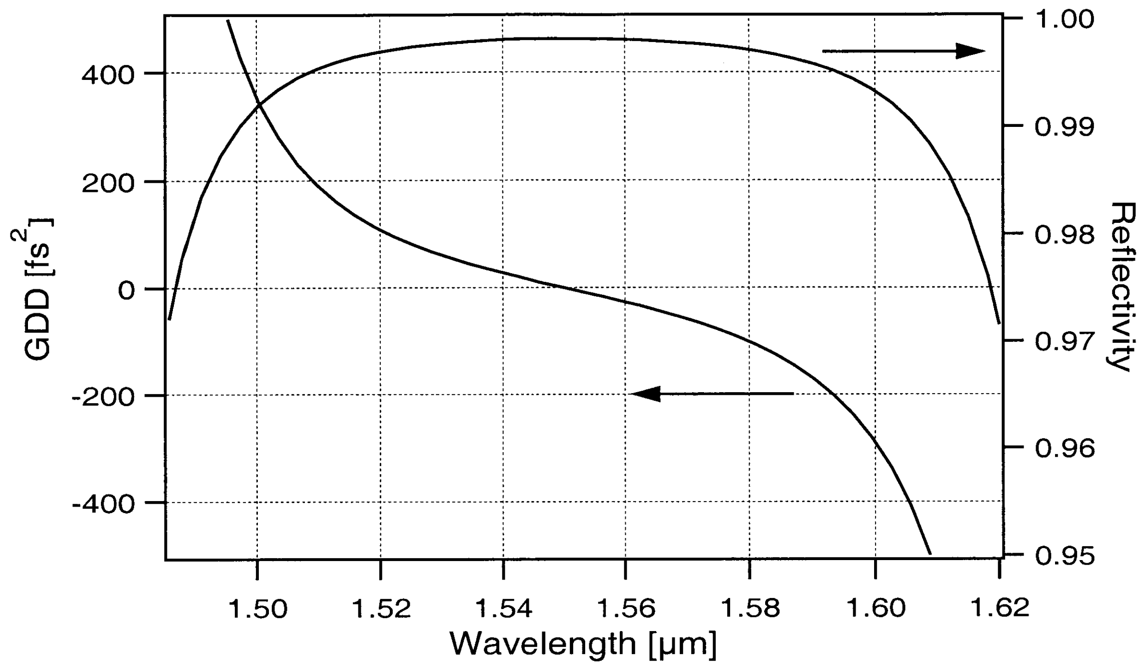

FIGURE 3-7: Calculated group delay dispersion and reflectivity of a GaAs/AlAs DBR capped with a half-wave layer of InP (Sub |(AlAs GaAs)^{22}InP InP| Air).

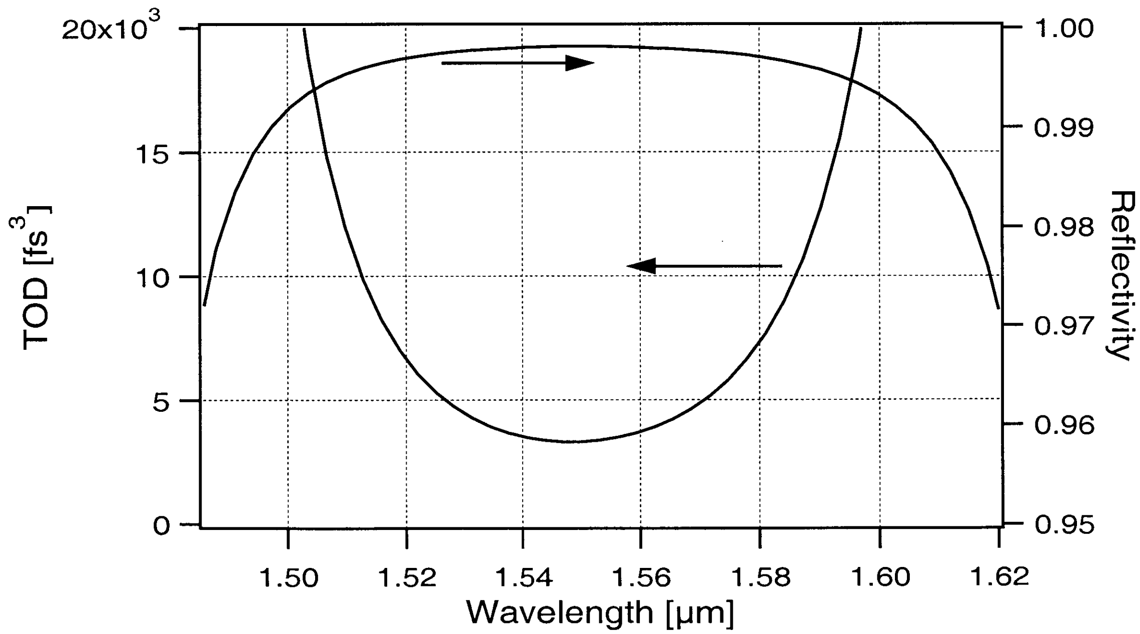

FIGURE 3-8: Calculated third order dispersion and reflectivity of a GaAs/AlAs DBR capped with a half-wave layer of InP (Sub |(AlAs GaAs)^{22}InP InP| Air).

Numerical modeling aimed at design of chirped DBRs was performed, following the method proposed for the dielectric double-chirped mirror design [41], combined with the conjugate gradient [106], and the simulated thermal annealing [106], [107] methods. However, despite tens of hours of computer simulations, the small refractive index difference between GaAs and AlAs did not allow to achieve any appreciable increase in the DBR reflectivity bandwidth, or obtain negative GDD while preserving the bandwidth.

3.5 Field distribution inside an SBR

An SBR allows the saturation intensity of a saturable absorber layer to be adjusted by positioning the absorber at a chosen place in the standing wave pattern, which is formed inside the device by the incident and reflected waves. If the intensity at the absorber is decreased by a factor of ζ relative to the intensity incident on the SBR, the effective saturation intensity is increased by $1/\zeta$. The knowledge of the electric field distribution inside an SBR is required to be able to adjust the effective saturation properties of the absorber. The calculated field intensity at the center wavelength for a GaAs/AlAs DBR with a half-wave InP cap layer is shown in Figure 3-9. The figure suggests that the field is rapidly decreasing as light propagates deeper into the DBR and that even in the top layer, the intensity is already decreased by a factor of ~ 10 compared to the field outside the device. In comparison, for a DBR with a quarter-wave InP cap layer, the field penetration depth is significantly higher (Figure 3-10) which translates into a lower peak reflectivity as shown in Figure 3-5. In addition, the standing wave intensity has a node at the surface of the DBR with a half-wave InP cap, and a maximum for a quarter-wave InP cap. The surface of the semiconductor may oxidize as well as acquire various structural defects and an intensity node at the surface helps reduce the possibility of optical damage caused by absorption in the surface defects.

Using the knowledge of the field distribution, an SBR can be designed to have either a relatively high or low saturation intensity, to match the intracavity intensity for a specific modelocking application. If the absorbing quantum wells are positioned near the top of the half-wave InP cap layer as shown in Figure 3-1 (b), they are located at the node of the standing wave pattern, and

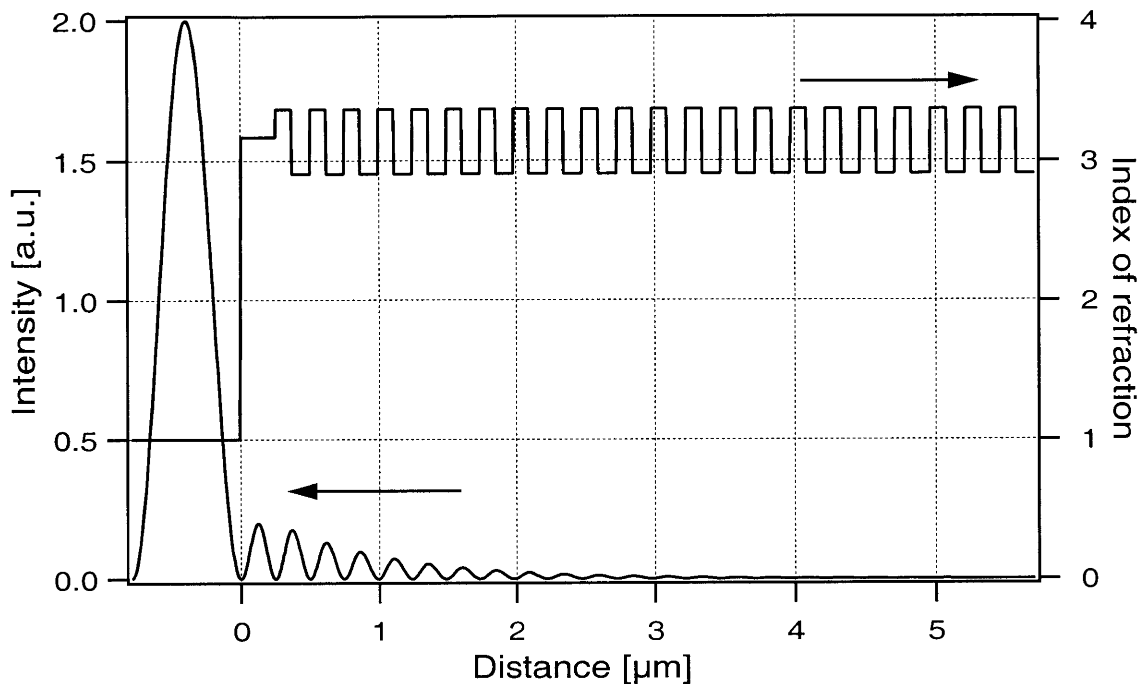

FIGURE 3-9: Calculated field distribution at the center wavelength (1.55 µm) inside a GaAs/AlAs DBR capped with a half-wave layer of InP (Sub |(AlAs GaAs)^{22}InP InP| Air).

the intensity on the absorber is significantly reduced compared to the intensity outside the SBR. Therefore, a high effective saturation intensity is obtained. In contrast, if the absorber is positioned at the center of the half-wave cap layer (Figure 3-1 (c)), it would be at the peak of the standing wave and the effective saturation intensity would be at least an order of magnitude lower than for design (b).

Overall, it can be seen from the standing wave intensity calculations that the intensity at the quantum well in the top layer is in the range of 0.1 to 0.01 of the intensity in the incident wave, depending on the QW position. Therefore, the absorption introduced into the cavity is only 0.1 to 0.01 of the absorption of a free standing QW. The absorption cross-section is scaled by the same factor and is in the 10^{-15}-10^{-16} cm^2 range. The field penetration can be increased if a dielectric antireflection coating is deposited on the surface of the SBR. In this case, the intensity at the QW is only a factor of 1 to 0.1 lower than the intensity in the incident wave, bringing the absorption cross-section into the 10^{-14}-10^{-15} cm^2 range.

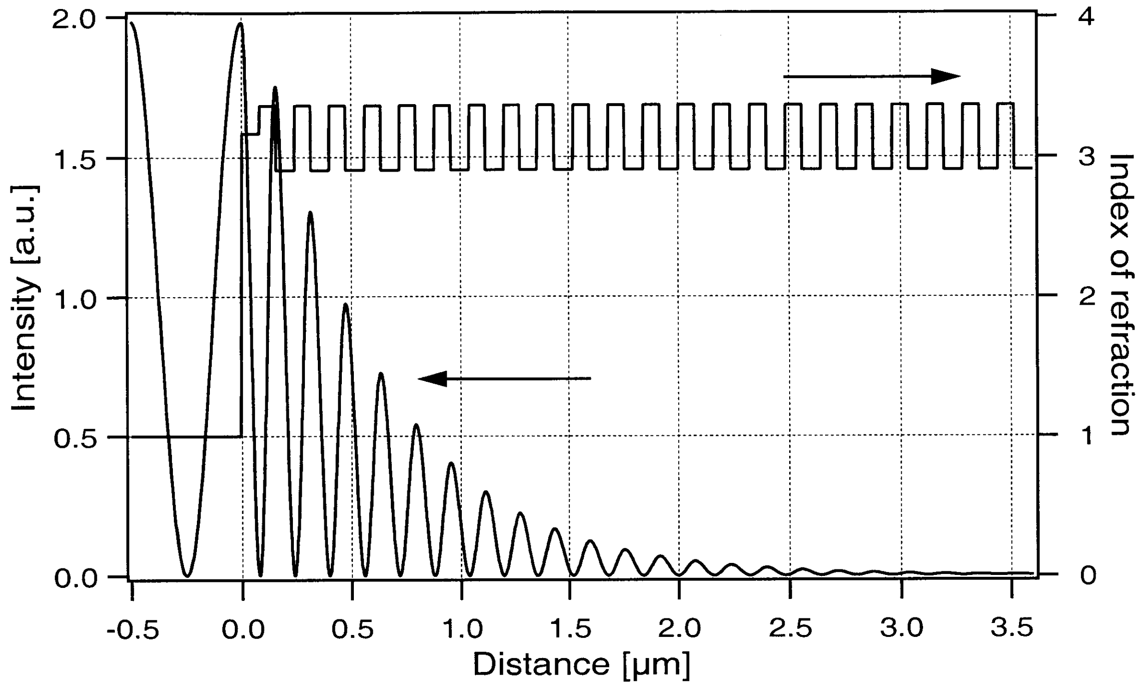

FIGURE 3-10: Calculated field distribution at the center wavelength (1.55 μm) inside a GaAs/AlAs DBR capped with a quarter-wave layer of InP (Sub |(AlAs GaAs)^{22}InP| Air).

Special attention should be paid to the standing wave effects when analyzing photoluminescence (PL) from a saturable absorber layer in an SBR with a high saturation fluence configuration. The measured PL from an InGaAs layer in such an SBR excited by an argon ion laser at 514 nm is shown in Figure 3-11. The PL signal is depressed within the high reflectivity band of the SBR. The effect can be explained as follows. Because the absorber is located at the top of the half-wave InP layer, the PL emitted toward the DBR acquires a 2π phase shift during transit through the InP layer and back, and a π phase shift on reflection from the DBR, adding up to a total of 3π phase shift relative to the PL emitted away from the DBR. As a result, the two waves interfere destructively and the PL signal is suppressed. This effect does not occur for an SBR with the absorber layer placed in the middle of the half-wave cap layer.

Generally, the field distribution inside an SBR is a function of wavelength. The field distribution shown in Figure 3-9 was calculated for the center wavelength of 1.55 μm. In a similar way, the field can be calculated for the other wavelengths of interest within the reflectivity range

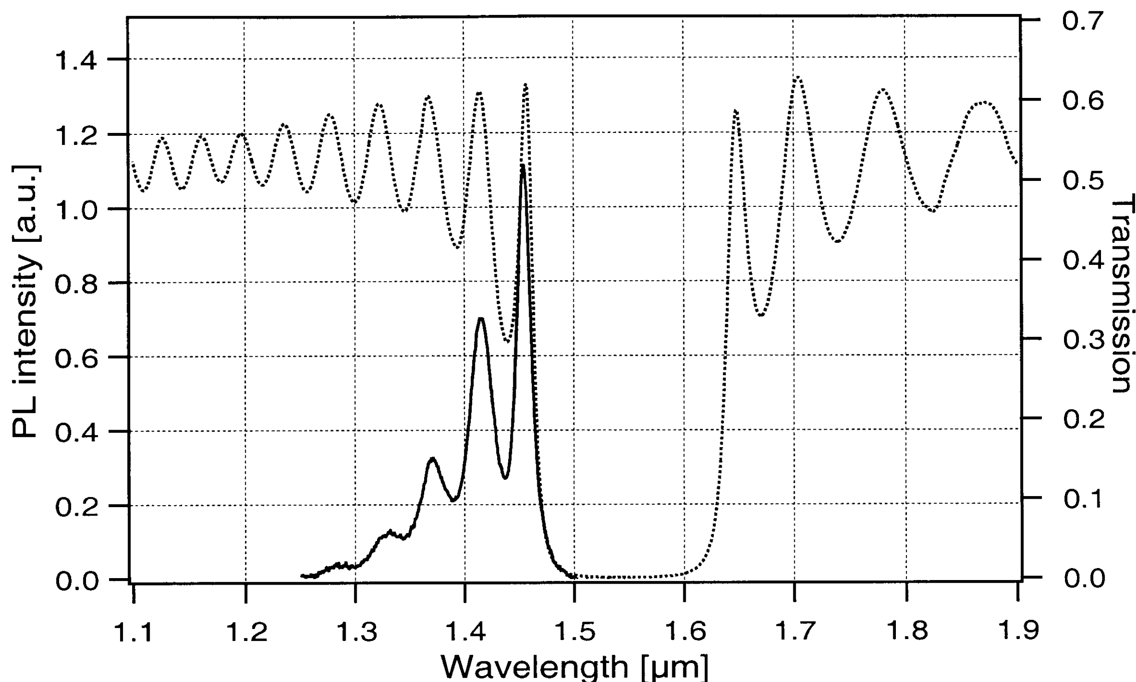

FIGURE 3-11: PL (solid line) and transmission data (dotted line) for a high-saturation intensity SBR (Sub |(AlAs GaAs)^{22}InP InP| Air). PL output is depressed in the SBR stop-band due to the quantum wells' location at the node of a standing wave (see Figure 2-1).

of the device. The results if such calculation for the center wavelength, as well as for the wavelengths corresponding to ~ 99% DBR reflectivity, are presented in Figure 2-1. The figure demonstrates a strong wavelength dependence of the standing wave peak positions which can be exploited to obtain wavelength-dependent small-signal absorption and wavelength-dependent saturation intensity. The absorption of radiation at any point is proportional to the field intensity at the point. For a given wavelength, the absorption can be increased by placing the quantum wells at the peak of the standing wave and by increasing the quantum well thickness or the number of quantum wells. This effect can be used to partly compensate for the wavelength dependence of a quantum well absorption. This idea has since been demonstrated to broaden the SBR wavelength operating range [95]. The saturation intensity can be increased by positioning the absorber at the node of the standing wave for a given wavelength.

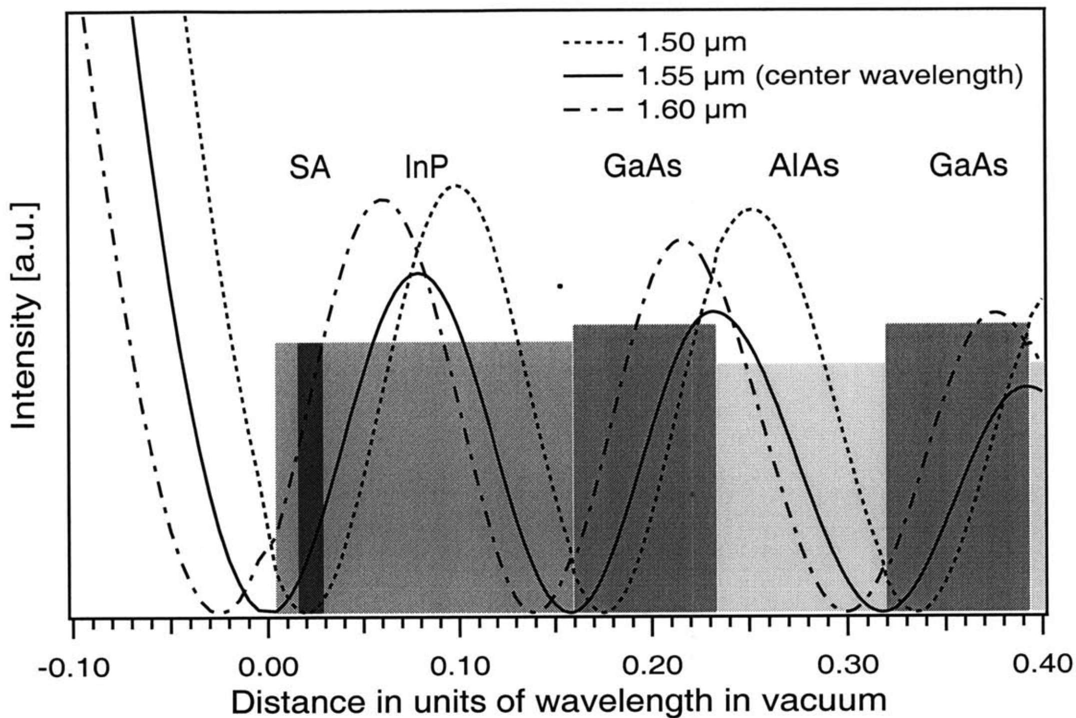

FIGURE 3-12: Calculated field distribution inside the top layers of a GaAs/AlAs SBR capped with a half-wave InP layer (Sub |(AlAs GaAs)^{22}InP InP| Air) for three different wavelengths.

3.6 Two-photon absorption effects

The existing saturable absorber mirror (SAM) designs using a distributed Bragg reflector mirror (DBR) suffer from a complicated and lengthy DBR growth process as well as certain other DBR disadvantages including narrow bandwidth and poor control of dispersion properties. SAM designs without a DBR have been proposed (e.g. a silver-mirror-based SESAM [72]). While eliminating the fabrication and performance problems associated with a DBR, these structures require extensive post-processing during fabrication.

For SAMs designed for modelocking the lasers in the 1.3 and 1.5 μm regions, InP can be used as a substrate. The fact that InP is transparent at these wavelengths may allow a design in which light enters the device through a relatively thick (>200 μm) InP substrate layer.

The fabrication of a proposed "go-through-InP-substrate" device shown in Figure 3-13 would be as follows. On top of an InP substrate, a saturable absorber layer, which may be a single

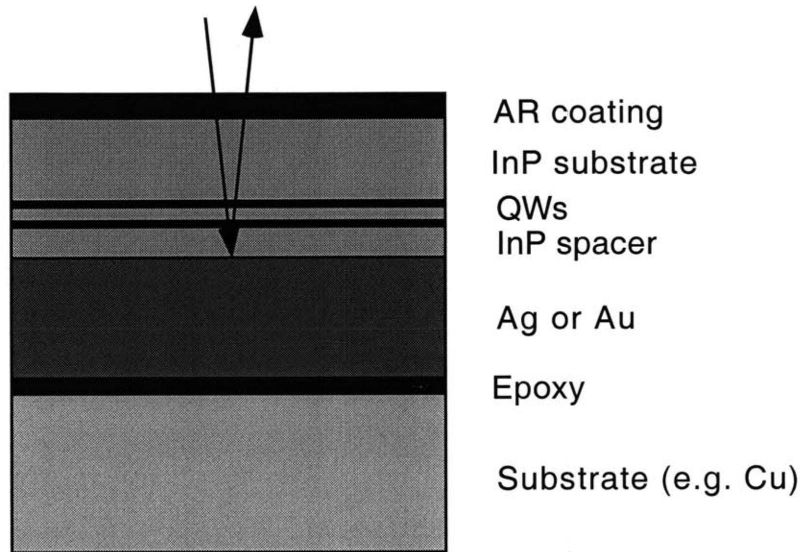

FIGURE 3-13: Proposed structure for an epitaxially-grown semiconductor saturable absorber mirror without a DBR and with no need for extensive post-processing.

or a multiple InGaAs or InGaAsP quantum well, is grown by epitaxy. It is followed by a transparent spacer (InP) layer which places the saturable absorber in a proper location in the standing wave pattern in order to control the effective saturation intensity. The top of the InP substrate is then AR-coated in order to eliminate etalon effects and a metallic (silver or gold) mirror is deposited on the bottom surface of the spaces layer. The whole structure is then bonded to a substrate for structural support and heat sinking.

This method should allow the DBR to be eliminated and thus improve the bandwidth and dispersion properties while still keeping the post-processing relatively straightforward. The problem however turns out to be that, although InP is transparent at 1.3 and 1.55 μm, its bandgap of 1.35 eV (the absorption edge of 0.92 μm) is less than twice the photon energy at these wavelengths and two-photon absorption (2PA) is possible.

The analysis of 2PA effects demonstrates that, for such a device, 2PA becomes a dominant loss mechanism for intensities close to the ones expected in a modelocked laser cavity. In order to account for the 2PA effects, a two-photon absorption coefficient β is introduced, so that the absorption coefficient becomes a function of intensity.

$$\alpha_{NL} = \alpha + \beta I \tag{3-1}$$

To estimate the effects of two-photon absorption, we take a value of the coefficient β for InP at 1.06 μm equal to 90 cm/GW [108], and using the wavelength dependence of the 2PA coefficient for semiconductors [109], the value of β at 1.5 μm can be estimated to be ~ 100 cm/GW. Considering a typical modelocked laser with a 1% output coupler, 100 mW of output power, 10 W of intracavity power, 100 MHz repetition rate, 100 nJ intracavity pulse energy, pulse duration of 100 fs and a 100 μm spot size on the saturable absorber, the peak intensity is ~ 10 GW/cm^2 and the nonlinear absorption βI is ~ 1000 cm^{-1}. A 100 nm of InP would then introduce two-photon absorption of 1%. The conclusion is that for any appreciable InP substrate thickness (typically on the order of a few hundred microns), the 2PA losses would become the dominant effect and would make such a "go-through-InP-substrate" device not usable in the given wavelength range.

Aside from eliminating one of the possible alternative saturable absorber device designs, the two-photon absorption argument brings attention back to the 'standard' SBR. It turns out that for an SBR with a half-wave InP capping layer, two-photon absorption becomes important and may act as a limiting factor for short pulse generation. As the pulse in a laser gets shorter, the absorber-induced self-amplitude modulation increases until the relaxation time of the absorber becomes slow compared to the pulse duration. After that, the absorber modulation depth is only a function of the pulse energy fluence (slow saturable absorber) and does not depend on the pulse duration. On the other hand, the effect of two-photon absorption increases with the decreasing pulse duration. For short enough pulses, the net contribution of the 2PA and absorption saturation leads to higher loss for shorter pulse width, stopping the pulse-shortening process. As an estimate, consider a laser with the parameters described above, so that the two-photon absorption in free-standing InP is ~ 1000 cm^{-1}. However, as it can be se seen from Figure 3-9, the intensity inside the InP cap layer is actually decreased by a factor of ~ 10 compared to the incident intensity. Therefore, the two-photon absorption contribution in InP is reduced to ~ 100 cm^{-1} and for an

InP layer of half-wave optical thickness (~ 250 nm physical thickness), it results in only 0.25% absorption. This value of absorption, although not negligible, can still be small compared to the absorption modulation depth introduced by the saturable absorber. For shorter pulse durations the 2PA effects would become more severe.

If the device design were to be modified such that the InP capping layer be removed, the 2PA effects in the DBR may still be important, especially for short pulses. The bandgaps of the DBR mirror materials, GaAs and AlAs, are respectively 1.42 eV (absorption edge at 0.87 μm) and 2.17 eV (absorption edge at 0.57 μm) such that 2PA in GaAs is possible for a lasing wavelength below 1.74 μm and in AlAs below 1.14 μm. For example, for SBRs designed for 800 nm wavelength range, both GaAs and AlAs have 2PA and the effect becomes important for short pulses or high intensities. The 2PA effect in SBRs have been independently considered in [110] where the authors pointed out that the nonlinear absorption in SBRs is reduced considerably compared to the bulk material of the same thickness due a limited field penetration depth.

The two-photon absorption effects may become especially noticeable if an SBR is used as a starting mechanism for KLM. In order to obtain fast modelocking build-up time

$$T_{mlb} \approx \frac{T_{rt}}{\left.\frac{dR}{dI}\right|_{I=0} I} \tag{3-2}$$

the absorber should be relatively easily saturated by the cw intensity I [61], [58]. For pulsed operation with an incident fluence much higher than the absorber saturation fluence, the linear absorption is completely bleached and does not change with increasing intensity while the two-photon absorption is increasing.

The above estimates of the two-photon absorption effects were confirmed by the measurements of SBR reflectivity as a function of incident intensity performed by E. Thoen (Figure 3-14) [111]. The sample was an AR-coated low-saturation-fluence SBR. An AR coating was used to increase the intensity inside the device, such that the ten-fold decrease in the intensity from free space to InP, typical for 'normal' SBRs (see Figure 3-9) was not present and the field at the satu-

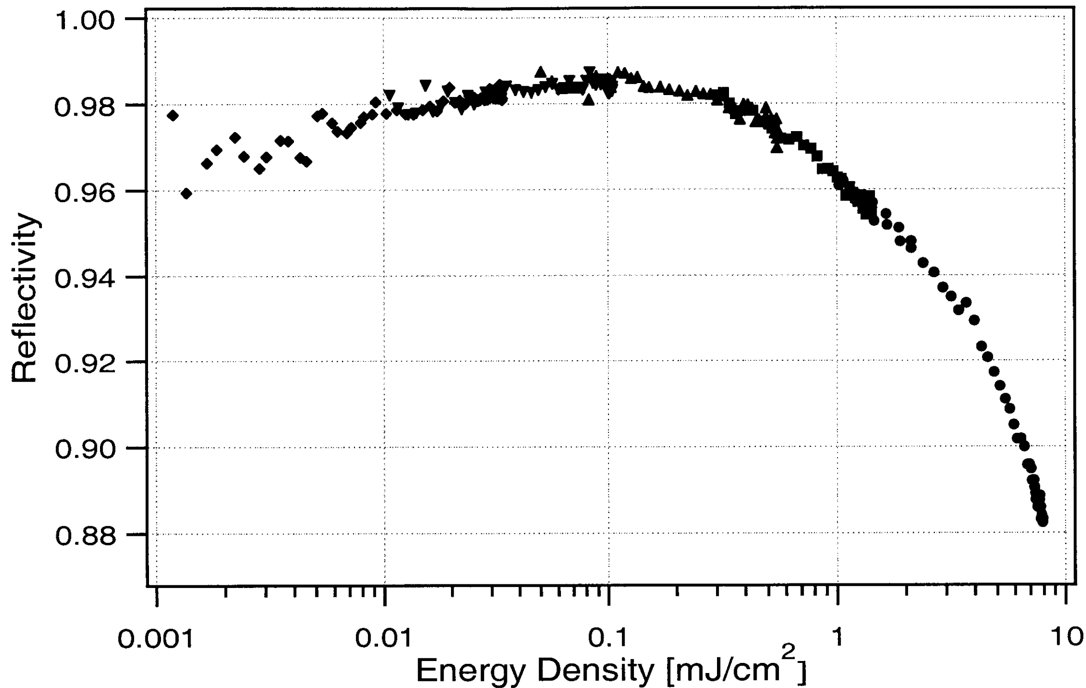

FIGURE 3-14: Energy fluence dependence of reflectivity for an AR-coated SBR. Two-photon absorption effects are observed at high energy densities. Data courtesy of E. Thoen.

rable absorber was approximately equal to the incident field. At lower energy fluences, up to ~ 100 $\mu J/cm^2$, the reflectivity increases with increasing fluence due to the saturation of InGaAs QW absorption. At higher energy fluences, the QW absorption is completely bleached while two-photon absorption in the structure is increasing. The magnitude of the 2PA effect is in a good agreement with the rough estimates presented above. The experimental data was acquired using 100 fs pulses, therefore the energy density of 1000 $\mu J/cm^2$ corresponds to the peak power of 10 GW/ cm^2. According to the estimate, such intensity should result in a 2.5% two-photon absorption in a half-wave layer of InP, which is close to the measured reflectivity decrease of ~ 2%.

3.7 Conclusions

In conclusion, this Chapter numerically analyzed the design properties of saturable Bragg reflectors. SBR parameters including reflectivity, dispersion, and field distribution were calculated for several designs. The modeling results helped design and fabricate actual SBR devices. The demonstrated modeling techniques can be extended to other multilayer films such as structures incorporating semiconductor-doped thin films described in the subsequent sections.

SBRs offer several adjustable parameters. The absorption bandedge can be adjusted by varying the In ratio x in $In_xGa_{1-x}As$ and by varying the QW thickness which changes the bandedge due to confinement effects. The effective absorption saturation intensity can be controlled by adjusting the QW position in the standing wave and the mode spot size on the absorber. The small signal (insertion loss) can be controlled by adjusting the number of quantum wells and their position in the standing wave. The wavelength dependence of the standing wave maxima can be exploited to tailor the wavelength dependence of absorption by placing the QWs in the right positions in the device.

As predicted by the calculations, the fabricated devices had a peak reflectivity over 99.5% and bandwidth of ~ 100 nm, sufficient to support sub-100-fs pulses. Such SBRs provide a small cavity insertion loss and are suitable for modelocking applications in low-gain solid-state laser systems. The analysis of electric field distribution inside the SBRs enabled fabrication of saturable absorber devices with various saturation intensities. The two-photon absorption effects in SBRs were theoretically analyzed and found to have significant impact on sub-100-fs pulse generation.

The drawbacks of the SBRs are largely due to the epitaxial semiconductor growth techniques that are used for their fabrication. Epitaxial fabrication requires lattice-matching of subsequent layers, therefore the choice of materials that can be used is limited. Because the semiconductors that satisfy the lattice-matching condition typically have a small index of refraction differential, a large number of semiconductor layers is required to provide high reflectivity, leading to a long and complicated fabrication process. On the other hand, the small index differential has an effect of reducing the bandwidth of the reflector and makes it not suitable to support

ultrashort pulses. For the same reason, semiconductor Bragg mirrors do not allow control of dispersion and bandwidth in a manner similar to dielectric chirped mirrors. The two-photon absorption effects in the semiconductor mirror material become important for sub-100-fs pulses and high incident intensities and may act as a pulse width limiting mechanism. Overall, the SBRs appear to be best suited for pulse generation in the 100 fs range and longer.

Chapter 4

Semiconductor-doped glasses for laser modelocking

4.1 Introduction

Having established the disadvantages of epitaxial growth techniques for saturable absorbers, we started looking for materials that could be fabricated without epitaxy and have the desired saturable absorption properties. The ultimate goal would be to develop a solid-state materials system that, in addition to having the right saturable absorber properties, would be simple and inexpensive to fabricate, would have a broad bandwidth of operation and could be incorporated into broadband metal or dielectric mirror devices.

The considered problem is rather broad and could possibly allow a large number of approaches. The saturable absorber material could be in a form of a bulk material or a thin film deposited on a substrate. The material itself could be pure or composite.

Thin films are preferable to bulk materials as they can potentially be incorporated into various multilayer devices. Composite materials are preferable to the pure ones because a variable doping density could be used to adjust the absorption coefficients and an additional degree of freedom could be obtained by combining dopants with different properties within the same film (e.g. different semiconductor materials, nanocrystallites with different sizes, etc.). The preliminary selection criteria would include the saturable absorption properties, either expected from general principles or already demonstrated for a similar class of materials, as well as ease and feasibility of fabrication.

The materials classes that were initially considered included semiconductor-doped glasses, semiconductor-doped dielectric films, amorphous and polycrystalline semiconductor films, and optical dyes imbedded in a transparent matrix. Amorphous and polycrystalline semiconductors can be deposited using the relatively simple techniques of RF sputtering [112][113] or flash evaporation [114]. The main disadvantages include the poor film adhesion properties [115] and long carrier lifetimes [116].

The main drawback of the organic dye saturable absorbers is their limited lifetime of operation. Organic dyes, similar to those used in dye lasers can be imbedded in transparent polymers, solgels, and porous glasses [117] [118] [119]. Although the dyes would be expected to possess the desired saturable absorption properties, the dye molecules typically degrade with time. More stable organic dyes have been developed but their limited lifetime remains to be a serious limitation [120].

Realistically, only a couple of approaches could be intensively pursued simultaneously and they were chosen to be semiconductor-doped glasses and semiconductor-doped dielectric films. The former had a smaller potential due the bulk nature of the material and, on the other hand, a higher probability of success as the optical properties of semiconductor-doped glasses have been extensively studied. The latter would potentially be a better saturable absorber materials system because of being a thin film, however although fabrication of semiconductor-doped dielectric films have been demonstrated, no detailed studies of the relevant nonlinear optical properties were previously published.

Semiconductor doped glasses, some of which are routinely used as colored glass filters and are available commercially, present an attractive choice for saturable absorber applications. They have fast carrier relaxation times [121] and appropriate saturation fluences, on the order of 1 mJ/cm^2 [122]. Semiconductor doped glasses are also simple and inexpensive. The first demonstration of semiconductor doped glasses for modelocking was performed by Sarukura, et al. [123]. A 90 μm thick, free standing semiconductor doped glass (Hoya IR76) was used to modelock a Ti:Al_2O_3 laser generating 2.7 ps pulses at 13 mW average power, tunable from 785 to 855 nm. The colored glass was the sole source of the saturable absorber action and no dispersion compensation was used.

The organization of this Chapter is as follows. Section 4.2 briefly reviews the optical properties of semiconductor quantum dot systems including the effects of confinement on the energy spectrum and the general optical properties of composite materials. Section 4.3 discusses the linear optical properties of the Schott colored glasses used in the experiments. The description of saturable absorber devices incorporating the semiconductor doped glasses is presented in Section 4.4. Section 4.5 discusses the measurements of absorption saturation dynamics of the semiconductor doped glasses and the observed photodarkening effects. The application of semiconductor-doped glasses to Ti:Al_2O_3 laser modelocking is described in Section 4.6. The section also discusses modelocking self-starting dynamics. Section 4.7 summarizes the results.

4.2 Review of optical properties of semiconductor quantum dots

This section will introduce a theoretical description basis for understanding the optical properties of semiconductor-doped materials including the properties of semiconductor quantum dots and general optical properties of composite materials. Only the most basic and essential properties of quantum confined semiconductor systems are described here. For a more complete and detailed discussion, the reader is referred to references [124] and [125].

4.2.1 Quantum confinement effects

Some of the first quantum dots were probably made many years ago by people who created colored glass by melting a certain amount of semiconductor, such as CdS or CdSe, together with the usual glass material. The small semiconductor inclusions in red and yellow glasses were first observed by x-ray analysis in the early 1930s [126]. The growth of semiconductor quantum dots in glasses is still one of the most popular techniques along with the synthesis in liquid solvents. Optical properties of semiconductor quantum dots constitute an active research area of solid state physics and a number of reviews exists on the subject [124] [125].

In order to construct a theory of electronic states in quantum dots, one typically assumes that the difference of the band gap of the spatially confined semiconductor from that of the surrounding medium (an insulator or another semiconductor) acts as a potential barrier for the electrons in the conduction band and the holes in the valence band. In many practical systems, the barrier is high and can be approximated by an infinitely deep potential well. If the spatial dimension of the quantum dots is large compared to the lattice constant of the semiconductor, it is reasonable to assume that the band structure is only weakly changed compared to the bulk material. It can be assumed that only the envelope part of the wavefunction is modified while the periodic Bloch component is preserved. This is a so-called envelope function approximation. For the states near the vicinity of the absorption edge, an effective mass approximation can be used.

Laser excitation of quantum dots with photon energy greater than the band gap produces electrons in the conduction band and holes in the valence band. Due to the Coulomb attraction between the electrons and holes, excitons can be formed. The exciton states are characterized by a wavefunction that is a product consisting of center-of-mass motion and electron-hole relative motion contributions. The characteristic length scale of the relative motion is the exciton Bohr radius, which for semiconductors is one the order of 1 to 20 nm. As soon as the quantum dot size becomes comparable to the exciton Bohr radius, quantum confinement effects appear.

In bulk crystalline solids, the electron states are obtained by solving the stationary Schrödinger equation of an electron in a spatially periodic potential

$$\hat{H}\psi(r) = \left[-\frac{\hbar^2}{2m}\nabla^2 + V(r)\right]\psi(r) = E\psi(r) \qquad (4\text{-}1)$$

where V has the periodicity $V(r + R_B) = V(r)$ for all Bravais lattice vectors R_B. According to the Bloch theorem, the eigenstates of (4-1) are composed of an envelope function e^{ikr} which is a plane wave and a function $u_k(r)$ which is periodic with the Bravais lattice vector $u_k(r + R_B) = u_k(r)$.

$$\psi_k(r) = e^{ikr}u_k(r) \qquad (4\text{-}2)$$

The energy eigenvalues in the parabolic band approximation are given by

$$E(k) = \frac{\hbar^2 k^2}{2m_{e,h}} \tag{4-3}$$

where m_e and m_h are the electron and hole effective masses.

In the most simple approach, a quantum dot can be considered as a semiconductor sphere of radius R surrounded by a dielectric matrix represented by an infinitely high potential barrier. Using an envelope function approximation, the wavefunction can be expanded in products of the periodic parts of a bulk Bloch wavefunctions $u(r)$ and a new envelope function $\varphi(r)$ for electrons and holes

$$\psi(r) = \varphi(r)u(r) \tag{4-4}$$

The Hamiltonian in a single parabolic band approximation is given by

$$\hat{H} = -\frac{\hbar^2}{2m_e}\nabla_e^2 - \frac{\hbar^2}{2m_h}\nabla_h^2 + V_e(r) + V_h(r) + \frac{e^2}{\varepsilon|r_e - r_h|} \tag{4-5}$$

where the last term accounts for Coulomb interaction and the confining potential is

$$V_{e,h}(r) = \begin{cases} 0 \text{ for } r < R \\ \infty \text{ for } r > R \end{cases} \tag{4-6}$$

First, consider non-interacting electron-hole pairs and neglect the Coulomb term. Then the wavefunction is a product of the electron and hole wavefunctions $\varphi(r_e, r_h) = \varphi_e(r_e)\varphi_h(r_h)$. The solution of this Schrödinger equation can be found in most quantum mechanics textbooks (see for example [127] or [128]). The electron and hole wavefunctions are given by

$$\varphi_{nlm}^{e,h} = Y_{lm}(\theta, \phi)\sqrt{\frac{2}{R^3}}\frac{J_l\left(k_{nl}\frac{r}{R}\right)}{J_{l+1}(k_{nl})} \tag{4-7}$$

where $n = 1, 2, 3, \ldots$, $l = 0, 1, 2, \ldots$, $-l \leq m \leq l$, $Y_{lm}(\theta,\phi)$ are the spherical harmonics and J_l are the Bessel functions. The energy eigenvalues are given by the requirement that the wavefunction vanish at the well boundary:

$$E_{nl}^{e,h} = \frac{\hbar^2}{2m_{e,h}} \frac{k_{nl}^2}{R^2} \quad (4\text{-}8)$$

$$J_l\left(k_{nl}\frac{r}{R}\right)\Big|_{r=R} = 0 \quad (4\text{-}9)$$

k_{nl} is the n-th zero of the Bessel function of the order l. The $l = 0$ and $l = 1$ Bessel functions are

$$J_0(r) = \frac{\sin(r)}{r} \quad (4\text{-}10)$$

$$J_1(r) = \frac{\sin(r)}{r^2} - \frac{\cos(r)}{r} \quad (4\text{-}11)$$

with the roots given by

$$k_{n0} = n\pi \qquad (n = 1, 2, 3, \ldots) \quad (4\text{-}12)$$

$$\tan(k_{n1}) = k_{n1} \quad (4\text{-}13)$$

Labeling the quantum numbers $l = 0, 1, 2, \ldots$ as $l = s, p, d, \ldots$, the first roots are $k_{1s} = \pi$, $k_{1p} \approx 4.493$, $k_{1d} \approx 5.763$, $k_{2s} = 2\pi$, $k_{2p} \approx 7.725$, etc.

For a spherical dot with an infinitely deep confining potential, the energy of electrons and holes takes discrete values and scales inversely with the dot radius:

$$E^e{}_{nlm} = E_g + \frac{\hbar^2}{2m_e}\left[\frac{k_{nl}}{R}\right]^2 \quad \text{and} \quad E^h{}_{nlm} = \frac{\hbar^2}{2m_h}\left[\frac{k_{nl}}{R}\right]^2 \quad (4\text{-}14)$$

With respect to the bulk semiconductor, the lowest confined state of a single electron-hole pair, which defines the optical absorption edge, has an energy increased by

$$\Delta E = \frac{\hbar^2}{2\mu}\left[\frac{\pi}{R}\right]^2 \tag{4-15}$$

where μ is the reduced electron-hole effective mass.

$$\frac{1}{\mu} = \frac{1}{m_e} + \frac{1}{m_h} \tag{4-16}$$

The energy shift can be expressed in terms of scaled quantities, namely the exciton Bohr radius a_B and exciton Rydberg energy E_R:

$$a_B = \frac{\varepsilon\hbar^2}{\mu e^2} \tag{4-17}$$

$$E_R = \frac{\hbar^2}{2\mu a_B^2} \tag{4-18}$$

$$\Delta E = E_R\left[\frac{\pi a_B}{R}\right]^2 \tag{4-19}$$

The formula for the energy shift ΔE (4-19) relates the two important quantities of the quantum dot, the exciton binding energy and the kinetic energy due to confinement effects. Depending on the ratio of the dot size to the exciton Bohr radius, different confinement regimes can be identified. For small dots, such that $R \ll a_B$ (strong confinement regime), the energy shift is large compared to the exciton binding energy and the individual motions of electrons and holes are quantized. Therefore, in the first approximation, the Coulomb interaction effects may be neglected for small dots. This could also be seen if we notice that for an electron and hole confined in a quantum dot, the Coulomb energy scales as the inverse of the electron-hole separation, while the kinetic energy scales as the square of the inverse dot radius.

In a weak confinement regime ($R \gg a_B$), it can be assumed that the quantum confinement effects do not interfere with the relative motion of the electron-hole pair, i.e. an exciton. If the confinement potential is neglected, the Hamiltonian (4-5) is separable into the relative and center-

of-mass motion the electron-hole pair. The problem can then be solved by considering an exciton as a single particle with a confining potential as a perturbation acting on the center-of-mass motion.

The corrections to the equations for the energy (4-14) and energy shift (4-19) would arise from the Coulomb interaction, valence band mixing, and non-parabolicity of the valence and conduction bands. The two latter corrections become more important for smaller dots because the parabolic band approximation works best for small k-vectors, while the k-vector is always large in small dots due to the uncertainty principle $\Delta x \Delta p \geq h$.

Due to the discrete nature of the electron and hole energy spectrum, the optical absorption spectrum of a quantum dot will consist of a number of discrete lines. The dot susceptibility can be found to be [124]:

$$\chi(\omega) = -\frac{|p_{cv}|^2}{\Omega}\sum_{n,l}\frac{2l+1}{\hbar\omega - E_g + E_R\left(\frac{k_{nl}a_B}{R}\right)^2 + i\gamma} + (\omega \rightarrow -\omega) \qquad (4\text{-}20)$$

where Ω is the dot volume, $|p_{cv}|$ is the momentum matrix element, γ is the phenomenological linewidth (dephasing rate), and the factor $2l+1$ accounts for the degeneracy of the energy levels.

Owing to the discrete energy spectrum of semiconductor quantum dots, the absorption coefficient at one wavelength might be much higher than the in bulk or quantum well materials. The possibility of intense narrow optical transitions in quantum dots due to the resonant nature of the susceptibility has led to predictions of greatly enhanced nonlinearities compared to the bulk semiconductor material [129] [125]. However, the magnitude of the $\chi^{(3)}$ enhancement predicted by theory has not been observed experimentally because of the broad homogeneous transition linewidths.

The homogeneous linewidth, determined by the dephasing time T_2 is an important parameter as it determines the absorption cross-section and in turn the absorption saturation behavior. The main contributions to the dephasing time in quantum dots are exciton-phonon scattering and absorption of optical phonons, which depend on the temperature, as well as scattering on bound-

aries and defects, which depends on the dot size and defect density [130] [131]. The dephasing time becomes faster with decreasing particle size, with increasing defect density, and with higher temperature. It was found that T_2 can be shorter than ~5 fs for dots with strong confinement at room temperature [132] [130] [133]. The values of the homogeneous linewidth γ can vary by orders of magnitude for quantum dots prepared by different methods [129] [131]. In addition, because of the large surface-to-volume ratio for small particles, the environment surrounding the quantum dot also strongly affects the homogeneous linewidth.

Realistic quantum dot systems contain particles of various sizes. Since the energy level structure of quantum dots in a function of dot radius, the size distribution leads to an inhomogeneous broadening in the optical spectra. The average absorption coefficient could be found by averaging over the absorptions of separate dots:

$$\alpha(\omega)|_{ave} = \int_0^{\infty} dRP(R)(R/R_{ave})^3\alpha(\omega)|_R \tag{4-21}$$

where $P(R)$ is the dot size distribution.

4.2.2 Optical properties of composite materials

Semiconductor inclusions in a transparent host material represent an optically inhomogeneous medium. For a composite medium comprised of a transparent host doped with a semiconductor, a 'naive' approach would give an absorption coefficient α_c of

$$\alpha_c = p\alpha_{semicond} \tag{4-22}$$

where p is the volume fraction and $\alpha_{semicond}$ is the absorption coefficient of the semiconductor. To be more precise, the optical properties have to be determined by averaging over the local inhomogeneities and taking into account the local field effects. Maxwell-Garnett theory [134] has been shown to be a good approximation for the optical properties of composites if the inclusion sizes are small compared to the wavelength of light and the volume doping density is small [124] [125]. Both of these conditions hold for the composite materials considered in this and following

Chapters. The crystallite size is typically on the order of a few hundred angstroms while the wavelength of light is on the order of one micron. The volume doping density typically does not exceed 10%.

In Maxwell Garnett theory [134] [124], a composite material is considered as a homogeneous background medium with spherical inclusions of dopant with diameters much less than the wavelength of light. In the analysis, the spheres are replaced with their equivalent electric dipoles and the effective dielectric constant of the composite medium is found:

$$\varepsilon_c = \varepsilon_2 \frac{\varepsilon_1(1+2p)+\varepsilon_2(2-2p)}{\varepsilon_1(1-p)+\varepsilon_2(2+p)} \tag{4-23}$$

where $\varepsilon_1 = \varepsilon_1' + i\varepsilon_1''$ and ε_2 are the dielectric constants of the dopant and of the host medium which is considered non-absorbing. The result can also be expressed as [135]

$$\varepsilon_c = \varepsilon_2 \frac{1+2p}{1-p} - \frac{9p\varepsilon_2^2}{(1-p)^2\left[\varepsilon_1 + \varepsilon_2 \frac{2+p}{1-p}\right]} \tag{4-24}$$

Generally, an absorption coefficient can be found from the dielectric constant by considering a propagating wave $E_0 \exp i((\omega/c)\sqrt{\varepsilon_c}x - \omega t)$ and noting that $\sqrt{\varepsilon_c} = n_c + i\kappa_c$ and $\varepsilon_c = \mathrm{Re}\varepsilon_c + \mathrm{Im}\varepsilon_c = (n_c^2 - \kappa_c^2) + i2n_c\kappa_c$, therefore $\sqrt{\varepsilon_c} = n_c + i\mathrm{Im}\varepsilon/(2n_c)$ and the absorption coefficient is given by:

$$\alpha = \frac{\omega}{c}\frac{\mathrm{Im}\varepsilon_c}{n_c} \tag{4-25}$$

where the extra factor of 2 comes from considering not the field but the intensity of the wave. Therefore, from (4-24) an absorption coefficient for a composite medium is found to be

$$\alpha_c = p\frac{n_1}{n_c}\frac{9\varepsilon_2^2}{(1-p)^2}\frac{1}{\left(\varepsilon_1' + \varepsilon_2\frac{2+p}{1-p}\right)^2 + \varepsilon_1''^2}\alpha_1 \tag{4-26}$$

where n_1 and n_c are the refractive indices of the dopant and the composite, respectively. For a low doping density $p \ll 1$, equation (4-26) reduces to

$$\alpha_c = p\frac{n_1}{n_c}\frac{9\varepsilon_2^2}{(\varepsilon_1' + 2\varepsilon_2)^2 + \varepsilon_1''^2}\alpha_1 \tag{4-27}$$

For a composite material with a dot size distribution, the absorption coefficient should be averaged over the different dot sizes similarly to equation (4-21).

4.3 Linear optical properties

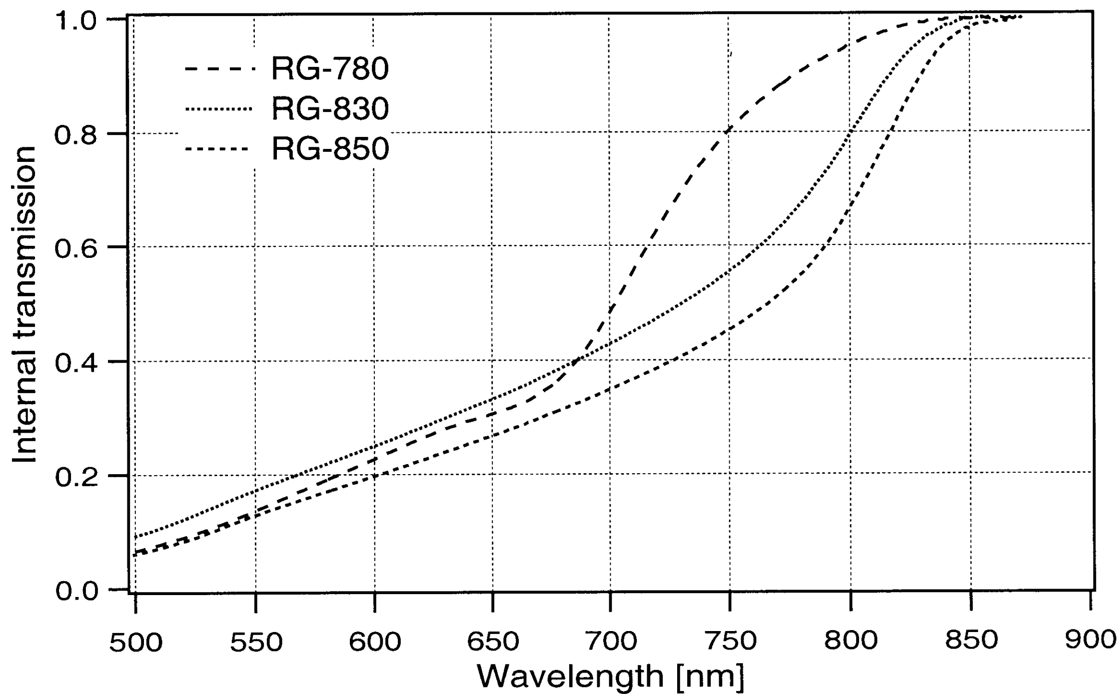

FIGURE 4-1: Measured transmission of the three investigated Schott semiconductor doped glasses. Glass thickness 200 μm.

The semiconductor doped glasses used in the experiments described in this Chapter were commercial colored glass filters from Schott Glass Technologies, RG-780, RG-830, and RG-850. The glasses are zinc-, potassium-, silica-based and are produced by adding a few percent of cad-

mium, selenium, tellurium, and their compounds to the glass melt [136]. After melting, forming, and annealing, the glass is subjected to thermal treatment in the range from 550 to 750°C to form semiconductor microcrystallites. From the previously published studies, the glasses have been demonstrated to be composed of $CdSe_xTe_{1-x}$ microcrystallites in the glass matrix, with the crystallite sizes in the range of one hundred to several hundred angstroms [126] [137]. The absorption edge depends on the chemical composition of the glasses as well as on the crystallite size. The absorption edges of CdSe and CdTe are at 729 nm and 827 nm, respectively, and increasing Te content in $CdSe_xTe_{1-x}$ leads to a longer absorption cut off wavelength. For the considered commercial semiconductor doped glasses, the quantum confinement effects are small due to the large sizes of the crystallites compared to exciton Bohr radius. The exciton Bohr radius of ~ 50 Å [138] is small compared to the crystallite size and the semiconductor particles exhibit the optical properties of the bulk material.

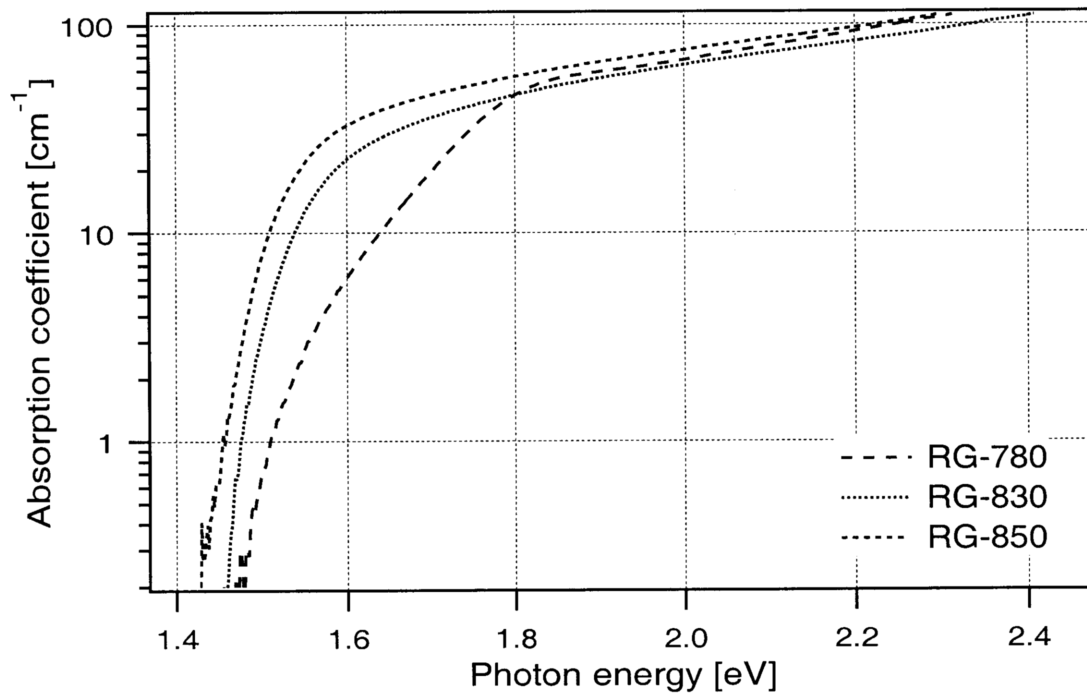

FIGURE 4-2: Measured absorption coefficients of three investigated Schott semiconductor doped glasses.

The absorption spectra of the three glasses were measured with a CARY 5E spectrophotometer and are depicted in Figure 2-1 (internal transmission) and Figure 4-2 (absorption coefficient). The three samples show very similar absorption curves with an absorption edge followed by a plato for photon energies much higher than the bandgap. The volume fraction of the semiconductor dopant in glass can be estimated using Maxwell-Garnett approach and equation (4-27). The absorption plato for the bulk semiconductor of ~$6 \cdot 10^4$ cm^{-1} [121] [139] corresponds to ~100 cm^{-1} for the composite glass. Taking $n_c = 1.5$, $n_1 = 2.5$, $\varepsilon_1' = 6.25$, $\varepsilon_1'' = 1.65$, and $\varepsilon_2 = 2.25$, the filling factor p is estimated to be ~$2.6 \cdot 10^{-3}$. A 'naive' approach using equation (4-22) yields the filling factor of ~$1.7 \cdot 10^{-3}$ which is 1.7 times smaller.

4.4 Saturable absorber devices incorporating semiconductor-doped glass

The considered semiconductor-doped glasses have a relatively high absorption, with a steep absorption edge (Figure 2-1) and thus extremely small glass thickness is necessary in order not to introduce excessive intracavity loss when the glasses are used in a laser resonator. If a thick piece of glass is used, the loss introduced into a laser resonator could be made acceptable by tuning the laser wavelength to the absorption edge of the glass. However, the tuning range of the laser would then be severely limited by the rapidly increasing glass absorption toward shorter wavelengths. To obtain ~2% absorption at 800 nm, which is the center wavelength of our $Ti:Al_2O_3$ laser resonator mirrors, the thickness of RG-830 glass needs to be ~20 μm. It is also desirable to be able to vary the absorption introduced by the glass in a simple fashion.

We have designed and fabricated a wedge-shaped structure which allows a thin, variable glass thickness to be introduced into the laser (Figure 4-3). Pieces of semiconductor-doped

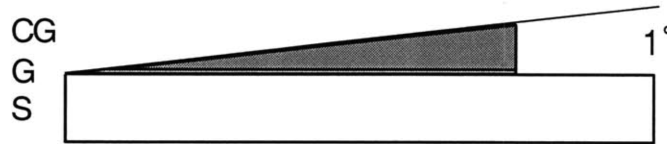

FIGURE 4-3: Saturable absorber structure using Schott semiconductor doped glass. CG, colored glass; G, glue; S, substrate.

glasses were attached to 3-mm-thick fused silica and sapphire substrates using UV-curing optical adhesive and were subsequently ground and polished at an angle of 1 degree.

The proper adhesive should have an index of refraction in between the indices of the glass and the substrate in order to minimize the reflections from the glass-adhesive and the adhesive-substrate interfaces. Several adhesives from Norland Optical and Summers Optical were considered and UV-curing glues NOA-61 and NOA-68 from Norland were found to have the smallest number of cracks and defects after the samples were ground and polished.

The sapphire substrates were single crystal, with the optic axis (sapphire is birefringent) oriented at 0 degrees relative to the surface normal in order to avoid birefringence effects. Sapphire also provided efficient heat sinking to avoid thermal index distortion effects in the glass. Fused silica substrates were easier to machine than sapphire; however, as discussed below, the poor heat transfer properties of amorphous silica caused strong thermal effects when used inside a laser resonator.

Mounting the semiconductor glasses on a substrate enabled the glass to be polished to a thickness which would be too fragile for free standing glass. The wedge design also allowed the thickness of the glass introduced into the laser cavity to be continuously varied (down to a minimum of ~ 20 μm).

4.5 Absorption saturation dynamics and photodarkening

effects

In order to investigate the saturable absorber dynamics of the semiconductor doped glasses, transmission pump-probe experiments were performed on the same saturable absorber structures on sapphire that were intended to be used inside the laser cavity. The pump-probe setup is depicted in Figure 4-4. An ultrashort pulse generated from a Ti:Al_2O_3 laser is separated into two

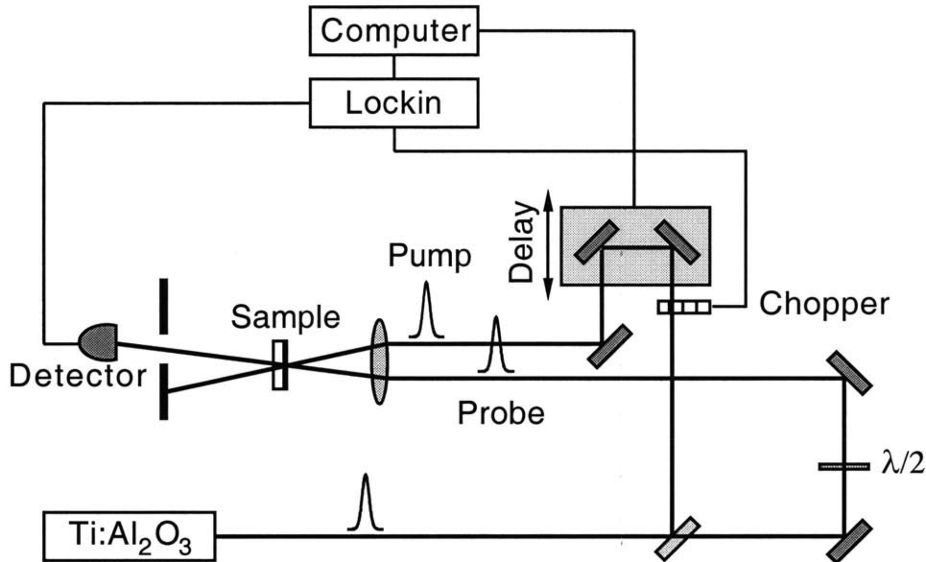

FIGURE 4-4: Schematic of the pump-probe setup.

pulses, the pump and the probe, with a variable time delay between them. The delay is varied by changing the path length of the pump beam with a computer-controlled motorized translation stage having a step size of 0.1 μm (corresponding to ~0.67 fs in a double pass). The pump and the probe beams are then focused onto the same area on the sample. The pump pulse with a photon energy above the semiconductor bandgap excites an electron-hole pair distribution in the semiconductor and changes the sample absorption due to band filling. The change in the sample transmission is detected by the probe pulse. The excited carrier dynamics in the sample are investigated by varying the delay between the pump and the probe. To improve the detection sensitivity, a mechanical chopper, placed in the path of the pump beam, is used to modulate the excitation and the changes in the probe signal are detected with a lockin amplifier. The temporal resolution of the pump-probe measurement is limited by the laser pulse duration at the sample and requires careful dispersion compensation for sub-100-fs resolution.

In the experiment, the pump and probe were cross polarized to avoid interference artifacts at zero time delay. The wavelength was fixed at 820 nm, the laser pulse duration was 30 fs, the pulse repetition rate was 80 MHz. The sample absorption was in the 15 – 20% range. A knife-edge scan was used to measure the pump beam spot size. A sharp razor edge was scanned across the beam

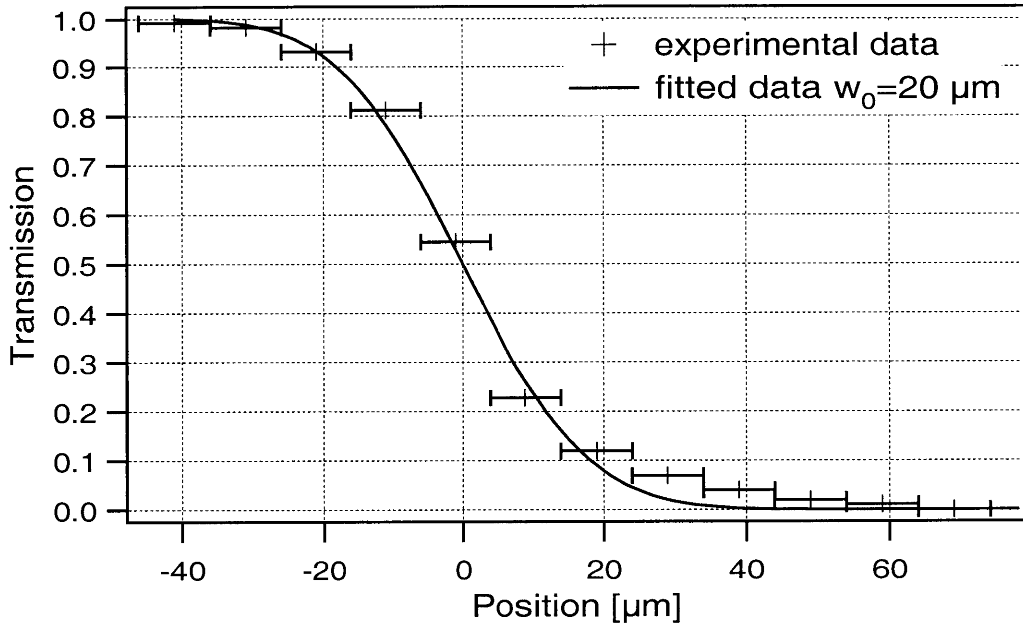

FIGURE 4-5: Spot size measurement using a knife-edge scan. The beam waist diameter was measured to be 40 μm.

at the focus and the transmitted energy was recorded as a function of the razor position. For a Gaussian beam profile with beam waist radius w_0, the transmission as a function of the edge position is

$$T(x) = \frac{\int_{-\infty}^{+\infty} dy \int_{-\infty}^{x} \exp\left(-\frac{x'^2 + y^2}{w_0^2}\right) dx'}{\int_{-\infty}^{+\infty}\int_{-\infty}^{+\infty} \exp\left(-\frac{x^2 + y^2}{w_0^2}\right) dx dy} = \frac{\int_{-\infty}^{x} \exp\left(-\frac{x'^2}{w_0^2}\right) dx'}{\int_{-\infty}^{+\infty} \exp\left(-\frac{x^2}{w_0^2}\right) dx} = \frac{1}{2}(1 + erf(t)) \qquad (4\text{-}28)$$

where $t = \frac{x}{w_0}$ and the error function erf is given by

$$erf(t) = \frac{2}{\sqrt{\pi}}\int_0^t \exp(-x^2) dx \qquad (4\text{-}29)$$

The measured knife-edge scan data and the calculated fit are presented in Figure 4-5. The pump spot size on the sample was measured to be 40 μm.

The absorption saturation dynamics observed in fresh RG-830 and RG-850 colored glasses were consistent with previously reported results [121]. An absorbed photon with an energy above

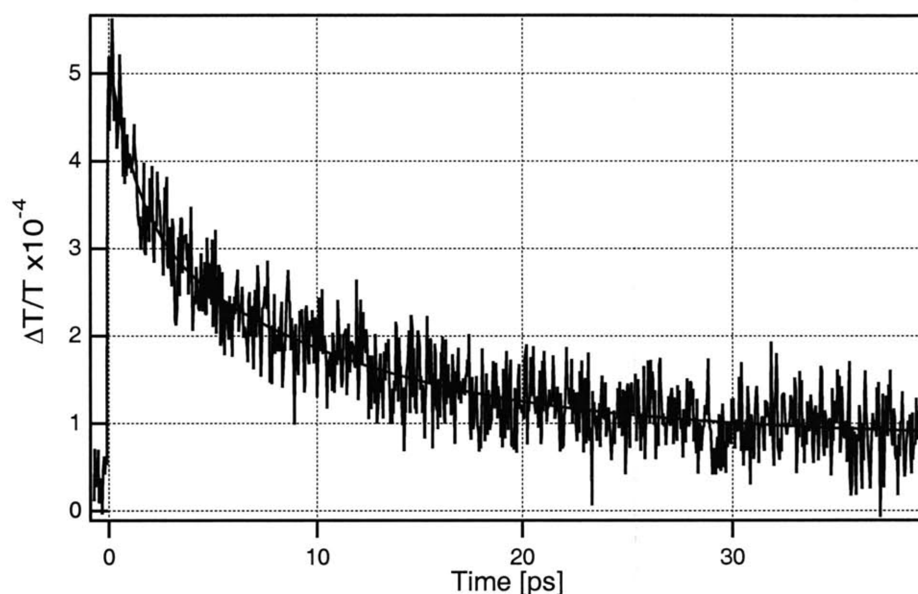

FIGURE 4-6: Absorption saturation dynamics of 'fresh' RG-830 glass. The pump average power was 6 mW at 820 nm.

the bandedge generates an electron in the conduction band and a hole in the valence band leading to a decrease in absorption due to band filling. Following the optical excitation, the excited non-equilibrium carrier population undergoes momentum and energy relaxation. Carrier-carrier scattering, which occurs on a time scale of several femtoseconds, leads to carrier thermalization with a certain temperature. Carrier-phonon scattering with a characteristic time on the order of picoseconds brings phonons and carriers to a thermal equilibrium and relaxes the electron and hole populations to the bottom of the conduction and valence bands, respectively. Radiative recombination typically occurs on the order of nanoseconds. The volume and surface defects present in the semiconductor as well as the interfaces of the crystallites can also act as carrier traps and non-radiative recombination centers, leading to faster absorption recovery dynamics.

In both glasses, we observed that the absorption recovery time became faster with increasing exposure to laser radiation as a result of a photodarkening effect.

The photodarkening effect in semiconductor doped glasses has been previously observed and extensive literature exists on the subject [140] [141] [142] [143]. The effect is characterized by a small (~1%) increase in absorption, shortening of nonlinear-optical response time, and a decrease in luminescence intensity. It has also been shown that a photodarkened glass recovers its initial condition after annealing for several hours at ~400°C. The effect is commonly attributed to a photochemical process which involves the photoexcited electrons trapped in the glass matrix and modification of traps and recombination centers on the surface of semiconductor nanoparticles due to the impurities present in the host glass matrix. An incident photon absorbed in a nanocrystallite creates an electron-hole pair and the photoexcited electron may be trapped in one of the surface states or ejected into the glass matrix and trapped into one of the mid-gap defect states. The trapped electrons create a static electric field which in turn modifies the absorption of the nanoparticle. The number of surface states is also increased leading to a faster nonradiative carrier recombination.

The photodarkening effect is strongly dependent upon the host glass material, and the dopants and impurities that are present. No photodarkening has been observed for sol-gel films doped with semiconductor nanoparticles, and similarly, no photodarkening occurred for the semiconductor-doped silica films that are described in the subsequent Chapters. Numerous time-resolved measurements have been previously performed demonstrating the photodarkening effect [144] [142] [145] [141]; however no femtosecond pump-probe results have been published so far.

In order to investigate the influence of the photodarkening effect on the absorption saturation dynamics, a series of pump-probe measurements was performed (Figure 4-7). After acquiring a pump probe trace, the sample was exposed to a pump beam of higher power than the pump power used during the measurement. The pump power was subsequently reduced and the next pump probe trace was acquired. The exposure process was repeated until the changes in relaxation dynamics became negligible. The exposure times were 1, 2, 4, 8, 16, and in some cases 32 minutes. The exposure powers used were 40, 80, and 230 mW. During data acquisition, the pump

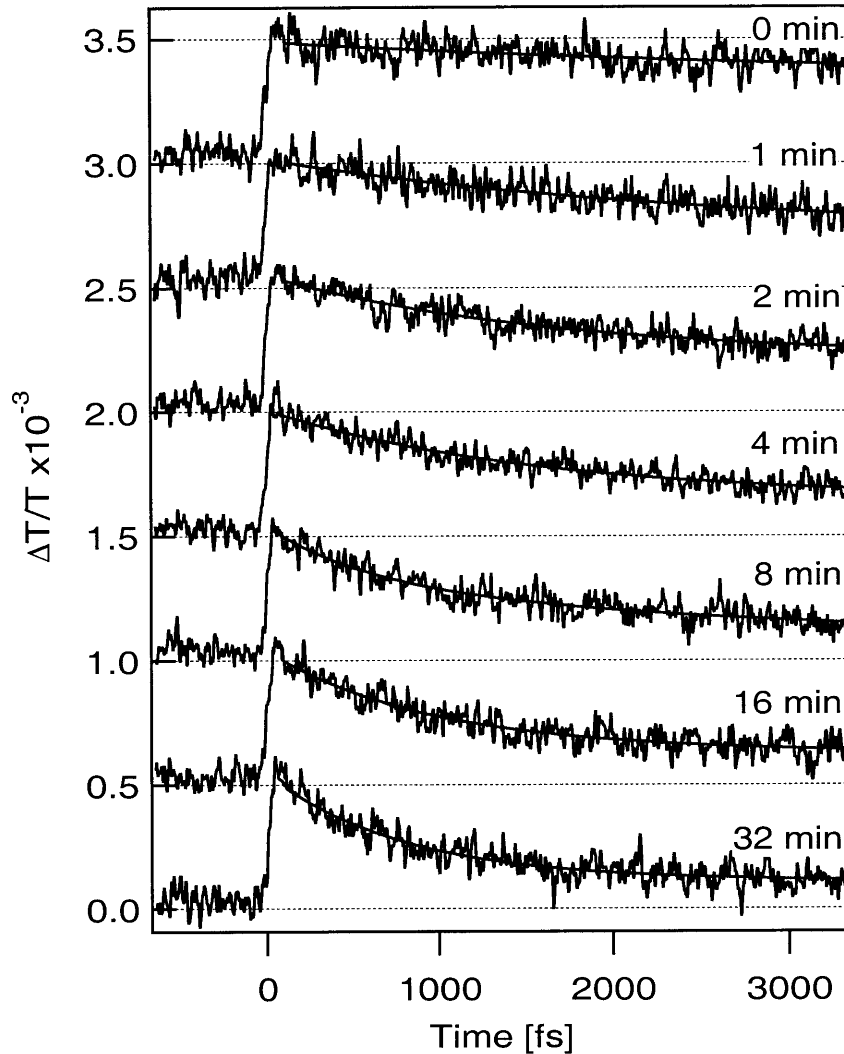

FIGURE 4-7: Pump-probe traces of RG-830 glass on sapphire showing faster absorption recovery times due to the photodarkening effect. Exposure average power is **40** mW. Exposure pulse duration is 30 fs at 80 MHz repetition rate. Pump average power is 6 mW. Exposure times, from top to bottom, 0, 1, 2, 4, 8, 16, 32 minutes. The traces are vertically displaced for clarity.

power was 6 mW for the exposure powers of 40 mW and 80 mW, and 12 mW for the exposure power of 230 mW. The power was kept low in order to avoid photodarkening during the measurement itself.

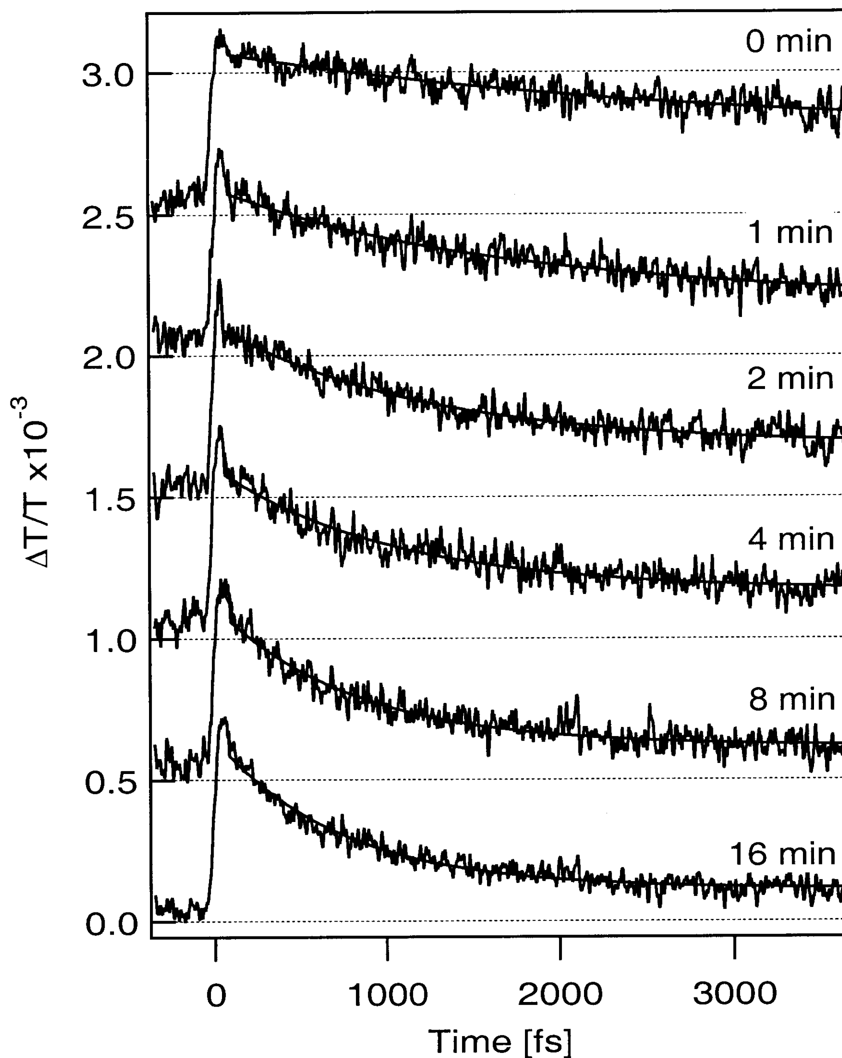

FIGURE 4-8: Pump-probe traces of RG-830 glass on sapphire showing faster absorption recovery times due to the photodarkening effect. Exposure average power is **80** mW. Exposure pulse duration is 30 fs at 80 MHz repetition rate. Pump average power is 6 mW. Exposure times, from top to bottom, 0, 1, 2, 4, 8, 16 minutes. The traces are vertically displaced for clarity.

A significant decrease in the carrier relaxation times for photodarkened samples was observed, from several picoseconds to as short as 400 fs, with relaxation dynamics reaching a certain asymptotic behavior. There were no significant changes in the magnitude of absorption saturation in the photodarkened samples, which indicates that the absorption cross-section is unchanged, while the relaxation times are decreased. The limiting relaxation dynamics depend on

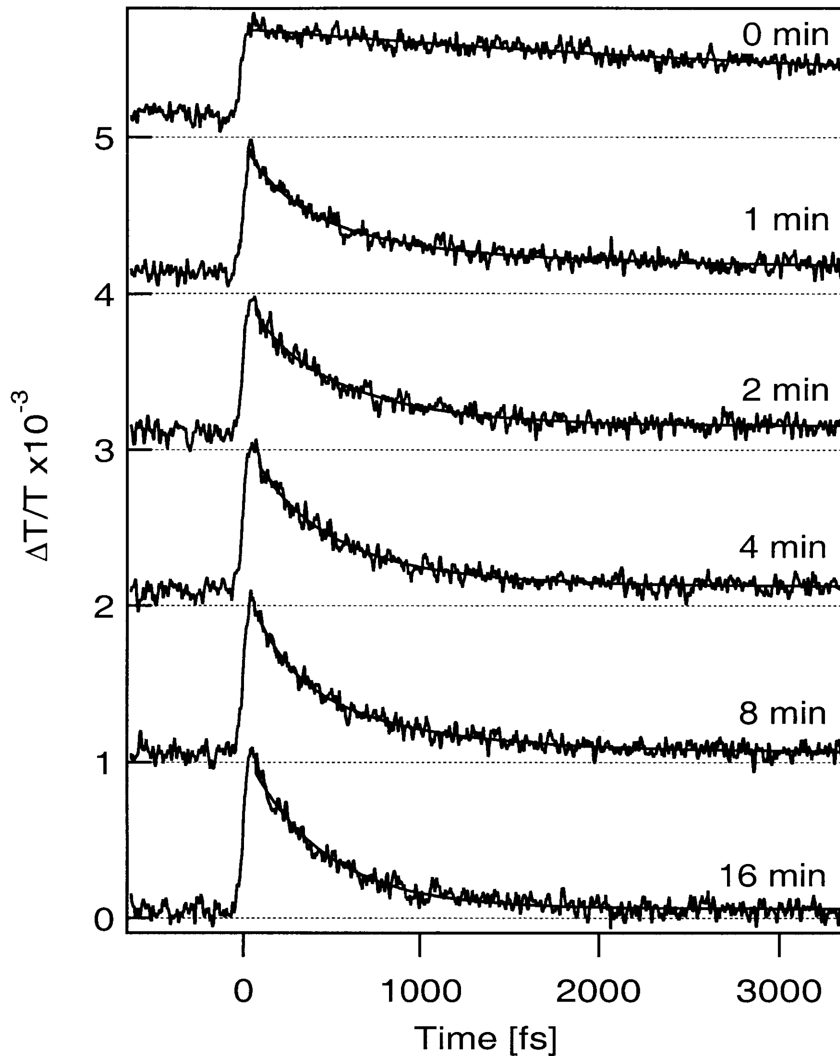

FIGURE 4-9: Pump-probe traces of RG-830 glass on sapphire showing faster absorption recovery times due to the photodarkening effect. Exposure average power is **230** mW. Exposure pulse duration is 30 fs at 80 MHz repetition rate. Pump average power is 12 mW. Exposure times, from top to bottom, 0, 1, 2, 4, 8, 16 minutes. The traces are vertically displaced for clarity.

the intensity incident on the sample and not merely on the integrated incident fluence, with faster asymptotic relaxation times for higher exposure intensities. The saturation of the photodarkening effect may be attributed to filling of all available trap sites.

Photodarkening effects were also investigated in RG-850 glass and the results were very similar to the ones observed in RG-830 glass.

The average intensity absorbed in the saturable absorber used inside a laser resonator is comparable to the average intensity absorbed during the photodarkening exposure time in the pump-probe experiments. This indicates that the photodarkening effect also occurs in the semiconductor-doped glass used inside a laser resonator and may be important for understanding the saturable absorber performance of the semiconductor doped glasses. Faster absorption recovery times due to photodarkening result in a higher saturation intensity and the colored glass becomes less efficient for modelocking initiation. Photodarkening sets the upper limit on the intensity that can be incident on the colored glass saturable absorber. For high incident intensities, the asymptotic absorption recovery time becomes too fast and the colored glass can no longer support modelocking start-up.

From the experimentally measured differential transmission data $\Delta T/T$, a value for the absorption saturation fluence can be deduced. From the measured change in transmission ΔT, a change in the absorption coefficient can be obtained:

$$-\Delta T = \Delta A = \Delta(1-e^{-\alpha d}) = e^{-\alpha_0 d}(1-e^{-\Delta\alpha d}) \approx \Delta\alpha d e^{-\alpha_0 d} = \Delta\alpha d(1-A) \tag{4-30}$$

$$\frac{\Delta\alpha}{\alpha_0} \approx \frac{\Delta A}{A(1-A)} \qquad \text{for} \qquad e^{\alpha_0 d} \approx 1-\alpha_0 d \tag{4-31}$$

From the definition of the saturation fluence,

$$\alpha = \alpha_0 + \Delta\alpha = \alpha_0 e^{-\Gamma/\Gamma_{sat}} \approx \alpha_0(1-\Gamma/\Gamma_{sat}) \tag{4-32}$$

the saturation fluence Γ_{sat} is given by:

$$\frac{\Gamma}{\Gamma_{sat}} \approx -\frac{\Delta\alpha}{\alpha_0} \approx -\frac{\Delta A}{A(1-A)} \tag{4-33}$$

The saturation fluences that were measured from the pump probe experiments were ~ 1 mJ/cm^2 for both RG-830 and RG-850 glasses, similar to the data published for other semiconductor-doped glasses [122]. In comparison, the fluences present in the modelocked laser were typically 0.5 mJ/cm^2.

4.6 Application of semiconductor doped glasses to laser modelocking

4.6.1 Saturable absorber modelocking

The laser used for modelocking experiments utilized a 4.5 mm Ti:Al_2O_3 crystal pumped by an argon ion laser. The pump absorption in the crystal was 80%. The laser cavity was a typical KLM z-cavity with R=10 cm radius of curvature folding mirrors CM1 and CM2 around the laser crystal. In order to incorporate a saturable absorber, the cavity was modified by adding a second fold comprised of two 10 cm radius of curvature mirrors CM3 and CM4 (Figure 4-10). The sepa-

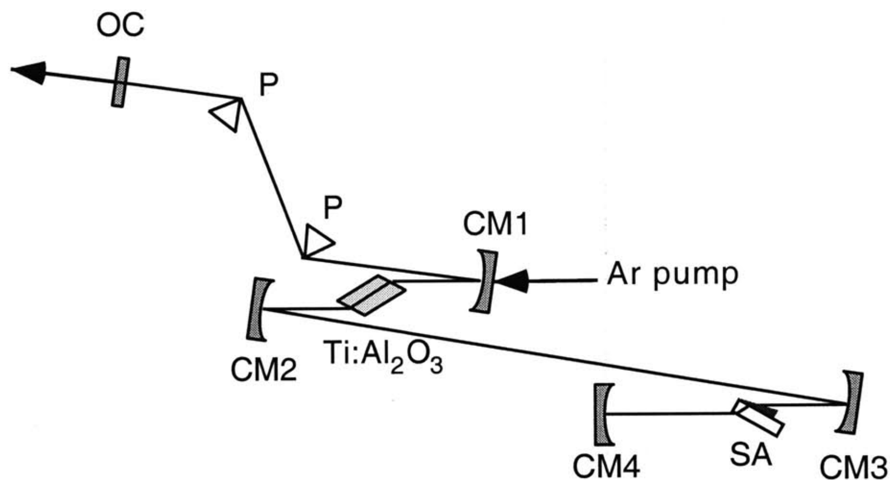

FIGURE 4-10: Laser cavity schematic: CM, 10 cm radius of curvature mirror; SA, saturable absorber; P, fused silica prism; OC, output coupler.

ration between the saturable absorber fold mirrors was chosen to be 15 cm (equal to $3f$ or $1.5R$), to provide a unity ABCD matrix due the second fold and preserve the z-cavity operating region. The saturable absorber structure was positioned at Brewster's angle near the focus of the second cavity fold. The spot size at the focus of the saturable absorber cavity fold was estimated to be 50 μm. The effective nonlinearity of the saturable absorber could be controlled by varying the position of the semiconductor doped glass relative to the focus. The absorption in the semiconductor doped glass saturable absorber depended on the thickness of the glass as well as on the laser wavelength and absorptions in the 1-4% range were typically used for modelocking. Dispersion compensation was provided by a pair of fused silica prisms separated by 76 cm. The prism arm of the cavity

was terminated with a 10% output coupler. An additional extracavity fused silica prism pair was used to eliminate spatial wavelength dispersion in the output beam and to compensate for the group delay dispersion due to the output coupler.

The incidence angle on the curved mirror CM3 was chosen to compensate for the astigmatism introduced by a 3-mm-thick saturable absorber substrate at Brewster's angle. The astigmatism compensation angle θ relative to the surface normal is given by [146]

$$f\left(\frac{1}{\cos\theta} - \cos\theta\right) = d\frac{\sqrt{1+n^2}}{n^2}\left(1 - \frac{1}{n^2}\right) \tag{4-34}$$

where f is the mirror focal length, and d and n are, respectively, the thickness and the refractive index of the Brewster plate. For the considered cavity parameters, f = 5 cm, d = 3 mm, and n = *1.7,* the incidence angle on the mirror CM3 was chosen to be 9.5°.

When the saturable absorber structure on the sapphire substrate was introduced into the cavity, self-starting modelocking operation was obtained resulting in pulses as short as 2 ps. With a pump power of 5.5 W incident on the $Ti{:}Al_2O_3$ crystal, we have obtained modelocked pulse trains of up to 200 mW average output power using RG-780 glass, 90 mW using RG-830 glass, and 70 mW using RG-850 glass. This average output power was a factor of 15 higher than the previously published result [123]. The pulse repetition rate of the laser was 80 MHz.

Using a 200 μm thick quartz birefringent filter in one of the cavity arms, the lasing wavelength was tunable in the ranges of 780 – 850 nm for RG-780 glass and 830 – 860 nm for RG-830 and RG-850 glasses while sustaining modelocking operation. The lower tuning range limit was due to the increasing glass absorption. The upper limit for the RG-830 and RG-850 glasses was due to the cavity mirror reflectivity bandwidth, and for RG-780 due to the insufficient absorption modulation depth introduced by the glass.

4.6.2 Saturable absorber assisted Kerr lens modelocking

The laser resonator was subsequently set for Kerr lens modelocking (KLM) by adjusting the separation of the curved mirrors around the crystal. The modelocking start-up and initial pulse shortening were supported by the colored glass and the final pulse shortening was due to KLM. Using RG-850 glass on sapphire, self-starting saturable-absorber-assisted KLM operation was obtained. The shortest pulse duration, measured by a non-collinear autocorrelation in a 200-μm-thick KTP crystal, was 52 fs. The pulses were transform limited with a spectral bandwidth of 15 nm and a time-bandwidth product of 0.32 compared to 0.315 predicted for a sech^2 pulse. The typical spectrum and autocorrelation of the modelocked pulses are shown in Figure 4-11. Without a saturable absorber structure, KLM was not self-starting. For 5.5 W incident pump power, an average output power of 60 mW was obtained. The laser spectrum and the pulse duration were limited by the mirror set reflectivity on the long wavelength side and by the gradually increasing semiconductor doped glass absorption on the short wavelength side.

Modelocking and KLM initiation were also obtained using semiconductor-doped glass structures with fused silica substrates. However, significant thermal effects were present in this case resulting in a poor laser mode quality. If the laser cavity was blocked for several seconds and then reopened, the spatial mode would deteriorate after about 1 second. While saturable absorber modelocking could still be obtained using colored glass on fused silica substrates, it would in some cases become unstable after several minutes of operation, most likely due to a photodarkening effect. Stable modelocking could be resumed by translating the saturable absorber laterally to a fresh spot. No such problems were observed for the structures on sapphire substrates.

Modelocking could also be obtained with a 3% output coupler instead of a 10% discussed above. With lower output coupling, one would expect to obtain better modelocking performance because of a higher absorption modulation depth due to a higher intracavity power. (Note that for 10% output coupling, the fluence incident on the absorber is only a half of the saturation fluence.) For the same reason, modelocking build-up time (see below) would be expected to be faster. In practice, however, modelocking was not stable with a 3% output coupler and the performance would deteriorate with time, most likely due to the photodarkening effect in the semiconductor doped glass.

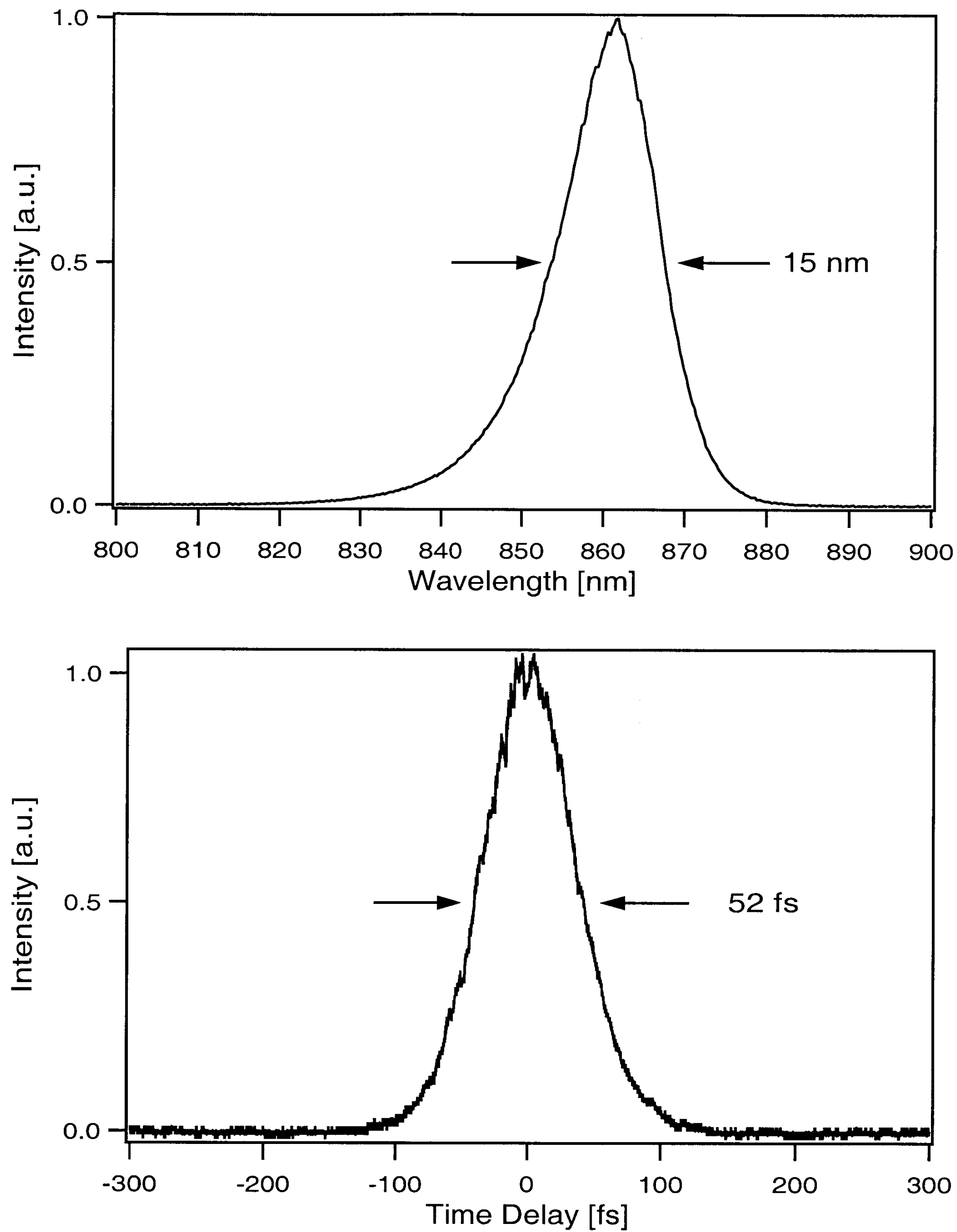

FIGURE 4-11: Typical autocorrelation and spectrum of self-starting saturable-absorber-assisted KLM pulses. The spectrum is limited by the gradual increase of the colored glass absorption on the short wavelength side and by the mirror set reflectivity on the long wavelength side.

The average output powers of 60 mW, obtained during saturable-absorber-assisted KLM operation, and 200 mW, obtained during saturable absorber modelocking, are comparable to the typical output powers for lasers modelocked with SESAMs and KLM. The pulse duration of 2 ps

is typical for modelocking with non-low-temperature-grown SESAMs. The pulse duration of 52 fs, obtained in conjunction with KLM, was limited by the steep optical absorption edge of the colored glass and is longer than the most recent $Ti:Al_2O_3$ modelocking results. This pulse width however is a factor of ~50 shorter than the previously published result by Sarukura et. al. obtained with the semiconductor-doped glass in the laser cavity [123]. The pulse duration could be improved by using colored glasses with a lower doping density. The tuning range of the mode-locked operation from 780 to 860 nm compares very favorably with the best SESAM and KLM results.

4.6.3 Modelocking self-starting dynamics

The modelocking self-starting dynamics of saturable-absorber-assisted KLM operation were investigated by using an intracavity mechanical chopper and measuring the transient behavior of the laser output power and second harmonic (SHG) generated extracavity. The average powers of the SHG and fundamental frequency signals are given by

$$\bar{P}_{SHG} = \frac{E_{SHG}}{T_{rt}} \qquad \text{and} \qquad \bar{P}_{FND} = \frac{E_{FND}}{T_{rt}} \tag{4-35}$$

where $E_{SHG,\ FND}$ are the pulse energies of the fundamental and the second harmonic and T_{rt} is the cavity round trip time. The energy of the second harmonic pulse is given by the SHG instantaneous power integrated over the pulse duration τ_p:

$$E_{SHG} = \int P_{SHG}(t)dt \propto \int P_{FND}^2(t)dt \propto (P_{FND}^{peak})^2\tau_p \propto \left(\frac{E_{FND}}{\tau_p}\right)^2\tau_p \propto \frac{E_{FND}^2}{\tau_p} \tag{4-36}$$

and the ratio of the average fundamental and SHG powers is given by

$$\frac{\bar{P}_{SHG}}{\bar{P}_{FND}} \propto \frac{\bar{P}_{FND}}{\tau_p} \tag{4-37}$$

The ratio of the average SHG and fundamental powers is inversely proportional to the pulse duration and directly proportional to the average power.

In order to measure the starting dynamics, the laser output was split in two beams, one of which was used to generate a second harmonic in a 200-μm-thick KTP crystal. The fundamental wavelength and the SHG signals were detected by a digital oscilloscope. The response times of both the fundamental and the SHG detectors were slower than the pulse separation ($\tau_{det} \gg T_{rt} \approx 10$ ns) in order to respond only to the average power and not to individual pulses and fast compared to the transit time of the chopper wheel's edge across the laser beam ($\tau_{det} \ll T_{chop} \sim 1$ ms). Figure 4-12 shows the self-starting dynamics of the saturable-absorber-assisted KLM pulses. The delay in the second harmonic signal onset relative to the fundamental

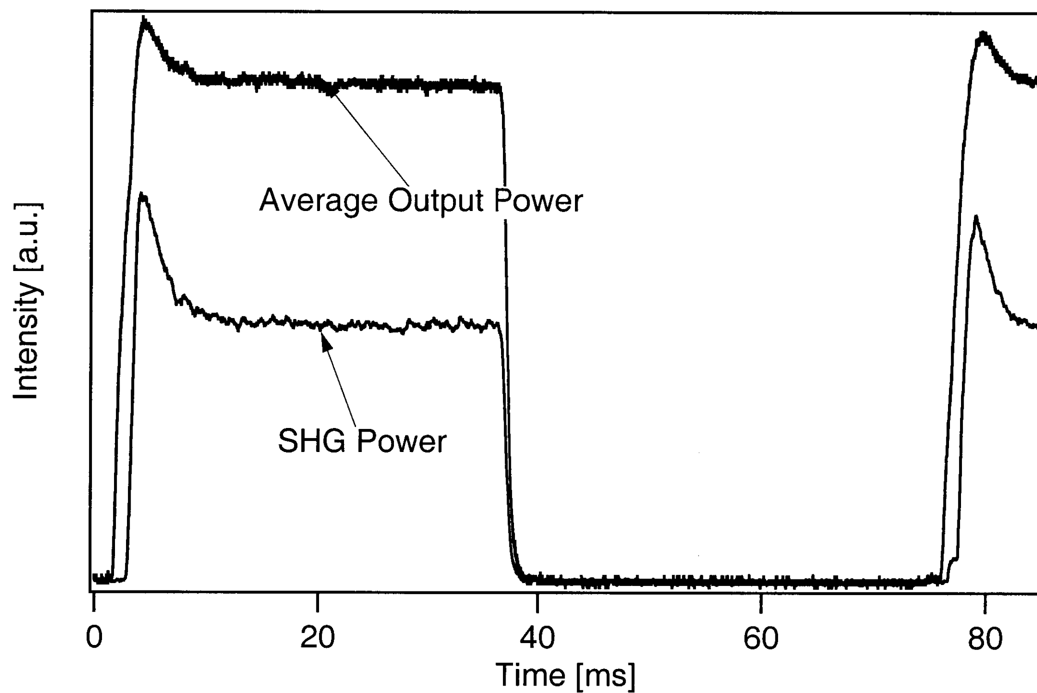

FIGURE 4-12: Self-starting dynamics of saturable-absorber-assisted KLM using RG-850 glass structure. The modelocking build-up time is determined from the delay in the second harmonic generation (SHG) signal onset.

was ~ 1.5 ms and is a measure of the modelocking buildup time.

The measured value for the modelocking build-up time can be compared to an estimate based on the theoretical description of self-starting modelocking in Chapter 2. Neglecting dynamic gain saturation effects, the modelocking build-up time T_{MLB} is given by:

$$T_{MLB} \sim \frac{T_{rt}}{\left|\frac{dA}{dI}\right|\Big|_{I=0} I} \tag{4-38}$$

To find the derivative of the color glass absorption A with respect to the intracavity intensity I, note that for small absorption A, $A = 1 - \exp(-\alpha d) \approx \alpha d$. The absorption saturation is then given by $A \approx A_0/(1 + I/I_{sat}) \approx A_0(1 - I/I_{sat})$ and

$$\frac{dA}{dI} I \approx -A_0 \frac{I}{I_{sat}} \tag{4-39}$$

where A_0 is the small signal absorption. For the output power of 50 mW and the output coupler of 10%, the intracavity power was 500 mW. The laser mode was focused into a spot size of ~50 μm on the absorber, producing average intensity of ~$2.5 \cdot 10^4$ W/cm^2. The saturation intensity can be obtained from the measured saturation fluence of 1 mJ/cm^2 and the absorption saturation recovery time of ~ 5 ps, giving a saturation intensity $I_{sat} = \Gamma_{sat}/\tau$ of ~$2 \cdot 10^8$ W/cm^2. For the colored glass absorption of 4% and the round trip time of 10 ns, the modelocking build up time is then estimated to be ~2 ms which is in good agreement with a measured value of 1.5 ms.

4.7 Conclusions

In conclusion, modelocking and saturable-absorber-assisted KLM in a $Ti:Al_2O_3$ laser were demonstrated using commercial semiconductor-doped glasses RG-780, -830, and -850 from Schott Glass Technologies. A wedge-shaped design of the saturable absorber structure incorporating the semiconductor doped glass was developed, which made it possible to continuously vary the absorption introduced into the cavity and obtain a thin enough layer of glass necessary to provide a broad wavelength tuning range of the laser.

Femtosecond absorption saturation dynamics in semiconductor-doped glasses were investigated using a pump-probe technique. Photodarkening effects were observed and resulted in faster carrier relaxation times with increasing exposure to laser radiation, a decrease from several picoseconds in fresh glasses to as short as 400 fs in photodarkened glasses. The effect is attributed to an increased density of surface traps and recombination centers leading to a faster nonradiative carrier recombination time. The absorption saturation fluence remained constant with exposure to laser radiation and was measured to be 1 mJ/cm^2.

Both modelocking and KLM initiation were demonstrated in a $Ti:Al_2O_3$ laser using commercial semiconductor-doped glasses from Schott. Self-starting 2 ps pulses with a wavelength tunable from 780 to 860 nm were obtained using just the colored glasses as saturable absorbers. The modelocked average power up to 200 mW was obtained, which is a factor of 15 higher than the previously published result [123]. The increase in the output power was made possible by a novel saturable absorber device design with better heat sinking properties. 52 fs transform-limited pulses were obtained when the saturable absorber structure was used in conjunction with KLM. Modelocking self-starting dynamics were investigated and the modelocking build-up time was measured to be 1.5 ms, in agreement with the theoretical predictions.

Overall, semiconductor-doped glasses were demonstrated to have the absorption saturation dynamics and saturation fluence required for solid-state laser modelocking applications. The modelocking results obtained in a $Ti:Al_2O_3$ laser compare well with the SESAM and pure KLM results published in the literature. The modelocked operation was self-starting, which is typical for SESAMs but is not readily obtained with pure KLM. Finally, the saturable absorbers based on semiconductor-doped glasses are much simpler and less expensive to fabricate than SESAMs and make the cavity alignment somewhat simpler compared to pure KLM.

With further development, semiconductor-doped glasses may become an attractive alternative to epitaxially grown semiconductor saturable absorbers. Although photodarkening acts as a limiting factor on the intensity incident on the colored glass absorber, this effect can potentially be made useful. Photodarkening depends on the host glass material. Therefore, new semiconductor-

doped glasses with various host matrices can possibly be developed which would allow control over the photodarkening effect and enable a controlled adjustment of the absorption recovery times.

Chapter 5

Semiconductor-nanocrystallite-doped silica films

5.1 Introduction

This Chapter demonstrates the fabrication and characterization of semiconductor-doped silica thin films for saturable absorber applications. Semiconductor-doped silica films are a logical extension of the bulk semiconductor-doped glasses, from a bulk material to thin layers.

Semiconductor-nanoparticle-doped silica films, deposited by non-epitaxial techniques, have many attractive features as saturable absorbers. They can be deposited using the relatively simple and inexpensive techniques of rf magnetron sputtering with composite [147] [148] or alternating targets [149] [150], or laser ablation [151]. Semiconductor-doped films possess a number of advantages compared to epitaxially grown semiconductors. Doped silica films can be deposited on a variety of substrates without the stringent lattice-matching requirements typical for epitaxial growth. A variety of semiconductors can be incorporated into the films as dopants. The nanoparticle size, together with the choice of the semiconductor dopant can be used to control the optical absorption edge. A broad nanocrystallite particle size distribution can be used to provide a smooth optical absorption edge and a broad optical bandwidth of operation. The doping density can control the linear optical absorption coefficient and the film thickness can be adjusted to obtain the desired total absorption. Compared to bulk semiconductor-doped glasses, semiconductor-doped thin films can be deposited as thin layers and, in addition, allow an order of magnitude higher doping density. Finally, these materials have the potential to be deposited in conjunction with standard dielectric thin films to create nonlinear dielectric mirrors and other structures.

In recent years, semiconductor-doped silica films have been prepared by rf magnetron sputtering and laser ablation using a number of semiconductor dopants including CdS [148], CdTe [149] [147] [152] [151], CdSe [147], GaAs [147] [150], CuCl [153], Ge [154], Si [155], InGaAs [156]. These studies were focused on the effects of quantum confinement on the semiconductor electronic band structure. The compositional, structural, and linear optical absorption properties of the films were characterized by several research groups as a function of deposition conditions and post-annealing. Several possible nonlinear-optical applications of the semiconductor-doped films were considered in the literature, however, no practical applications of such films were demonstrated so far. The proposed optical applications focused primarily on reactive optical nonlinearities.and no detailed studies of absorption saturation properties have been performed except for the pump-probe experiments on CdSe-doped films presented in [152]. No results have been published on the application of semiconductor-doped films as saturable absorbers for laser modelocking, and, to the best of my knowledge, the idea has not been suggested in the literature.

This Chapter focuses on the fabrication and characterization of semiconductor-doped thin films for saturable absorber applications. The research presented here was aimed at developing a saturable absorber material which could be used for saturable absorber modelocking of a Ti:sapphire laser, operating in the wavelength region around 800 nm, or other solid-state near-IR lasers with wavelengths of operation of ~ 1.3 μm (Cr:forsterite) and ~1.5 μm (Cr:YAG).

In order to develop semiconductor-doped saturable absorber thin films suitable for laser modelocking, a series of studies was performed, beginning with film fabrication, and then going to film characterization, to saturable absorber device design, to laser modelocking experiments. The films were deposited by rf sputtering which involved optimizing the deposition conditions as well as the choice of dopants. The film fabrication was performed using facilities at the MIT Lincoln Laboratory and I am most grateful to Dr. J.N. Walpole and L.J. Missaggia for their help and support. The structural, linear and nonlinear optical properties of the fabricated films were then investigated. Based on these studies, saturable absorber devices were designed to be used in a laser resonator. The film fabrication and the film characterization measurements are described in this Chapter. The InAs-doped silica film devices were subsequently applied to Kerr Lens Modelocking initiation in a Ti:Al_2O_3 laser and the results are described in the next Chapter.

This Chapter is organized as follows. Section 5.2 describes the fabrication of semiconductor-doped thin films by rf sputtering. The structural properties of InAs-doped silica films including the results of XPS, TEM, STEM, and EDX measurements are described in Sections 5.4 through 5.6. The linear optical properties InAs-doped films are described in Section 5.7 and nonlinear optical properties in Section 5.8. The results are summarized in Section 5.9.

5.2 Film fabrication

5.2.1 RF sputtering technique

The films used in the experiments were deposited by radio frequency (rf) sputtering. The process of sputtering may be defined as the ejection of particles from a condensed matter target by the impinging energetic particles. The source of the coating material, or the target, is mounted opposite the substrates in a vacuum chamber, evacuated to 10^{-6}-10^{-10} Torr. The chamber is backfilled using a continuous flow of an inert gas, typically argon, to establish a glow discharge. The target is bombarded by the positive ions and the coating material is transferred to a gas phase by a momentum exchange process, rather than a chemical or thermal process. A variety of materials, both conducting and dielectric, can be deposited using this technique. Overall, sputtering, and rf sputtering in particular, is a relatively simple and versatile technique. Composite films can be obtained by alternating several targets made of different materials or using a single composite target.

Many modern sputtering systems use magnetic devices for plasma confinement, called magnetrons. A magnetron confines the discharge plasma to the vicinity of the sputtering target. As a result, the sputtering rate is increased compared to non-magnetron systems, by up to an order of magnitude. In addition, the substrates are not exposed to the plasma discharge. For a review of various sputtering techniques, the reader is referred to reference [157].

The system used for film deposition in the presented experiments was an MRC 8800 rf sputtering system operating at 13.56 MHz. A schematic of the sputtering system is shown in Figure 5-1. The system had 5 sputtering targets, allowing to sequentially deposit several materials onto the

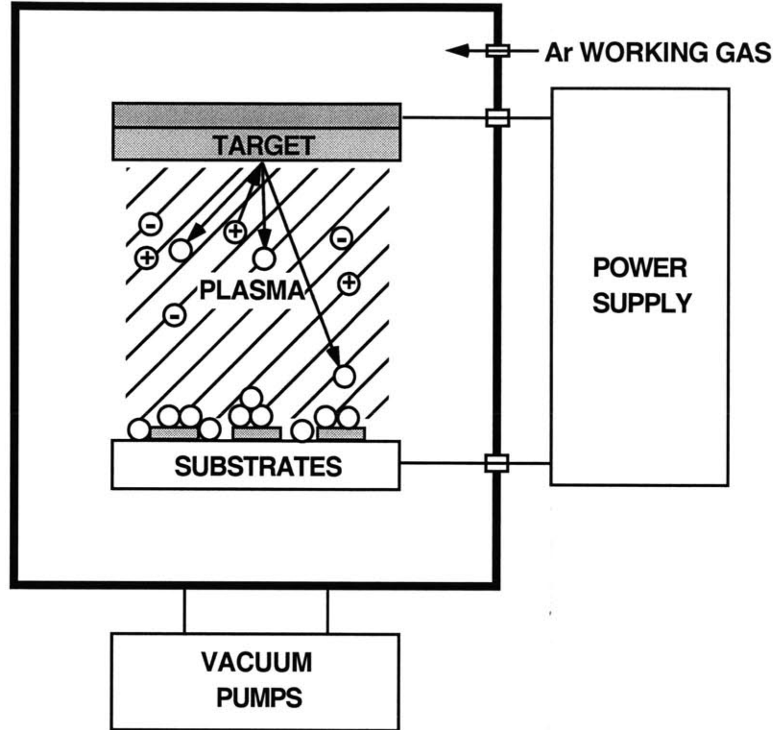

FIGURE 5-1: Schematic of a sputtering system layout.

substrate without breaking vacuum. Argon was used to establish a glow discharge. A small negative potential was maintained at the substrate plate in order to improve the sputtered film quality by performing sputter-etching simultaneously with the deposition. After the substrates were loaded into the sputtering chamber, the whole system was pumped down for about 24 hours, in order to achieve vacuum in the low 10^{-7} Torr range. Because of the pumping down requirements, only one sputtering run per day could be performed. A detailed description of the film deposition procedure is presented in Appendix B.

In contrast to the rf magnetron sputtering systems used for fabrication of semiconductor-doped silica films described in the literature, the sputtering system used for the experiments in this Thesis did not have a magnetron, the reason being that when this research was performed no magnetron rf sputtering systems were available. The absence of a magnetron led to relatively low film deposition rates, a factor of 3 to 10 lower than reported for semiconductor-doped silica films sput-

tered using magnetron systems. It is also believed to be the factor responsible for the inability to control the nanocrystallite size of semiconductor dopants by means of substrate heating (see below).

Once the films were deposited, the film thickness was measured by photolithography in conjunction with profilometry, and the sputtering rate was calibrated. The substrate materials for photolithography were typically GaAs or Si, which are not etched by hydrofluoric acid. To perform photolithography, a thin layer of photoresist was applied on top of the sputtered film under investigation. A mask was then put in contact with the sample using a Zeiss mask aligner and the photoresist was exposed with UV light, generating a pattern of exposed and unexposed areas. A photographic developer was then used and the exposed resist areas were removed. At this point, the sample was covered with a photoresist except for the exposed and then developed areas. The sample was subsequently immersed in buffered HF until the exposed areas of the sputtered film were etched all the way down to the substrate. The photoresist was not etched by HF and the film regions covered by the resist remained intact. After the etching was completed, the photoresist layer was completely removed by applying acetone. As a result, the surface of the sample acquired a number of vertical steps, with the step height equal to the sputtered film thickness. The surface profile was then measured by a profilometer and the film thickness was determined. A typical profilometer trace is depicted in Figure 5-5. The details of the photolithographic procedure are presented in Appendix C.

5.2.2 Post-annealing

Annealing is an integral part of the fabrication process of bulk semiconductor-doped glasses [136]. The semiconductor-doped glasses are colorless after casting. To achieve the final color, the glasses are subjected to an annealing process. During the annealing, semiconductor nanocrystallites grow around nucleation centers in the glass matrix and the final nanocrystallite size is an increasing function of the annealing temperature and duration.

In a similar manner, it has been demonstrated in the literature that the nanocrystallite size in CdSe- and CdTe-doped silica thin films can be increased by post-annealing the films at ~500 - 700 °C for several hours [147][149]. After annealing, the optical absorption edge can be significantly red-shifted.

In attempt to control the semiconductor nanocrystallite size in the sputtered films, some of the fabricated RG-850 and GaSb:SiO_2 films were annealed at a set of temperatures from 200 to 500 °C for several hours.

Rapid thermal annealing (RTA), which is a thermal treatment typically at 500 - 800 °C for ~ 60 seconds, is commonly used to anneal out structural defects in thin films [158] [159]. RTA has been shown to have a significant impact on the chemistry of surface and interface traps in the films [160] [161]. CdTe-doped silica films subjected to RTA showed a slight red shift of the absorption edge for a high doping density [149].

Rapid thermal annealing (RTA) in nitrogen, argon, and forming gas (95% N_2, 5% H_2) at atmospheric pressure at a range of temperatures from 500 to 800 °C was performed on some of the InAs-doped films using an AG Associates Heatpulse 210 RTA system. A typical RTA temperature trace is shown in Figure 5-2. Due to the dopant diffusion out of the film and oxidation, a

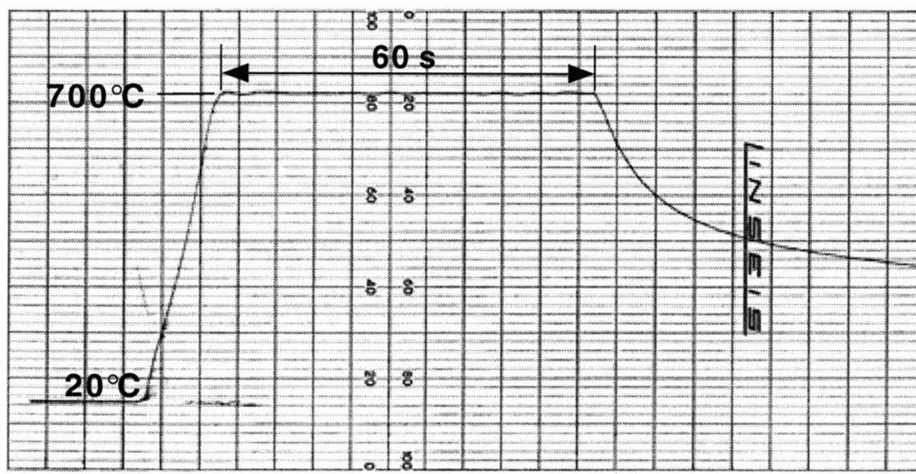

FIGURE 5-2: A typical rapid thermal annealing temperature trace.

reduction in magnitude of the film absorption was observed along with a slight red shift of the

absorption edge due to particle size growth for films annealed at temperatures above 600 °C. More significantly, however, the RTA treatment modified the absorption saturation dynamics of the film which turned out to be crucial for developing efficient saturable absorbers.

5.2.3 Selection of semiconductor dopants

One of the questions that need to be resolved before the films can be fabricated is the choice of a semiconductor dopant. There are two aspects that need to be considered. First, the semiconductor dopant should provide the films with the required saturable absorber properties. Second, the semiconductor dopant should not contaminate the vacuum system in the rf sputtering machine, which was also used for other experiments.

A necessary characteristic of a saturable absorber for modelocking is simply the presence of optical absorption at the laser wavelength. The designed saturable absorbers were intended to be used in the solid state laser systems such as Ti:sapphire, Cr:forsterite, and Cr:YAG, with lasing wavelengths in the near IR. Keeping in mind that the semiconductor bandedge of the nanocrystallites would be blue shifted compared to the bulk material due to the quantum confinement effects, the suitable semiconductor materials should have a bulk bandgap smaller than the laser photon energy. This suggests the use semiconductors with a bandgap in the mid-IR range.

The second consideration, dealing with the vacuum chamber contamination, precluded the use of materials containing lead and sulfur, thus excluding the semiconductors such as PbS, PbSe, and PbTe.

Taking the above considerations into account, three materials were used as targets for rf sputtering, namely RG-850 glass, GaSb+SiO_2, and InAs+SiO_2.

5.2.4 Fabrication of RG-850 films

The first semiconductor-doped film deposited in the system was RG-850 colored filter glass from Schott Glass Technologies, the application of which in a bulk form to $Ti:Al_2O_3$ laser mode-locking was described in the previous Chapter.

There were several reasons to attempt to use the same glass in the thin film form. Bulk glass could only be polished down to approximately 20 μm and the large thickness resulted in a steep absorption edge limiting the laser tunability and the pulse duration out of the laser. Using a thin film should allow to obtain a smaller glass thickness and extend the laser bandwidth of operation. In addition, a thin film can be potentially deposited in conjunction with a standard dielectric thin films and integrated into a nonlinear mirror device. RG-850 glass was already a composite material and made target preparation relatively simple.

The sputtering target was a 1/8-inch-thick 5-inch-diameter disc of RG-850 glass from Schott Glass Technologies mounted on a copper backing plate. In order to attach the RG-850 glass to the backing plate, one surface of the glass disc was metallized by sputtering layers of Ti, Pt, and Au with thicknesses of several hundred angstroms. The metallized surface was subsequently soldered to the backing plate using indium. The same procedure was used for the preparation of the SiO_2+InAs and SiO_2+GaSb targets described in the following Sections. The substrates used for the RG-850 glass deposition were fused silica and BK-7 glass for optical measurements and GaAs for the measurements of film thickness.

The RG-850 film deposition was performed with an rf power of 100 W to the target and 8 W to the substrates, Ar gas pressure of 5 mTorr, and Ar flow of 30 sccm. The separation between the target and the substrates was 3 inches. The deposition rate measured by profilometry was ~9 Å/min.

Most of the deposited films appeared uniform to the eye, while some of the films appeared smoky. Under a microscope, it was observed that the smoky samples had dark defect spots with diameters on a scale of 20 to 50 μm. The films exhibited good initial adhesion properties to the glass substrates, however some of the films peeled off several days after the deposition.

The optical absorption spectrum of the deposited RG-850 films, shown in Figure 5-3, was measured by a CARY 5E spectrophotometer. From the figure, it is seen that the sputtered RG-850

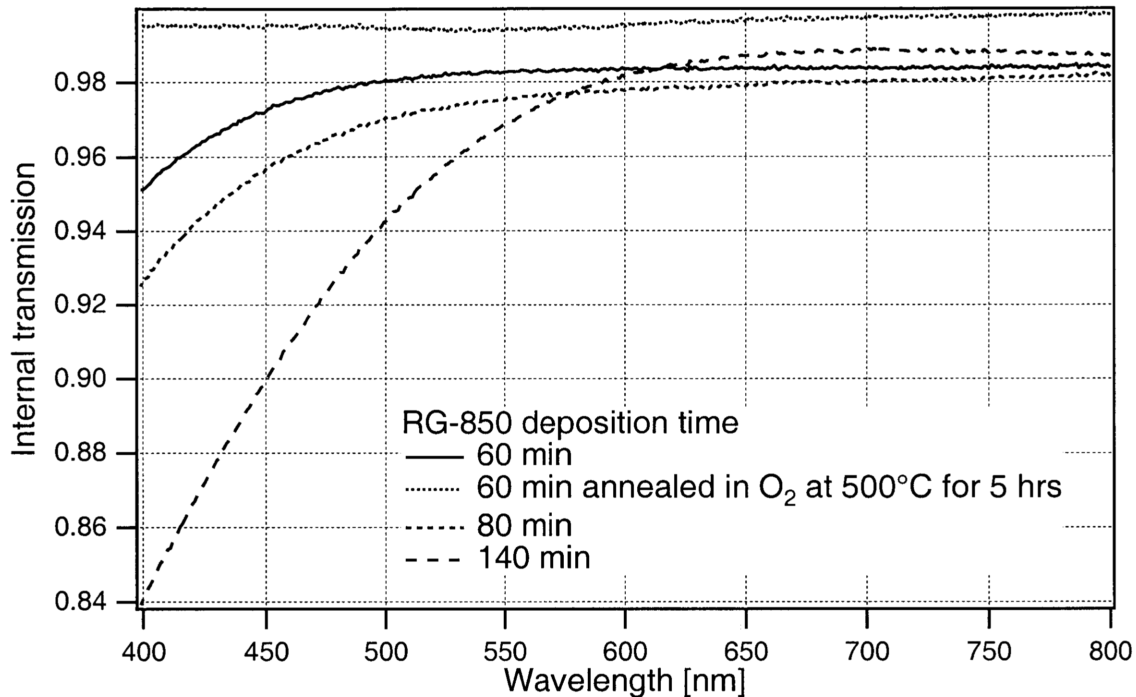

FIGURE 5-3: Transmission of sputtered RG-850 films.

films did not have appreciable absorption around 800 nm, which is the operating wavelength of a Ti:Sapphire laser. The significant blue shift of the absorption edge could be attributed to the quantum confinement effects in the CdTe nanoparticles doped into the glass. It appears that the semiconductor particle size in the film is reduced compared to the target RG-850 glass. In the RG-850 glass, the size of the dopant nanoparticles is in the hundreds of angstroms range [137] and the optical absorption edge is approximately the same as the bulk CdTe absorption edge, ~830 nm. For smaller semiconductor nanoparticles in the sputtered film, the absorption edge is blue-shifted into the visible, making the films not suitable for application to IR solid state laser modelocking.

It has been previously shown that the semiconductor nanoparticle size in the sputtered film can be increased by post-annealing the film at ~500 - 600 °C for several hours [147][149]. In attempt to increase the semiconductor particle size in the sputtered RG-850 films, the samples

were annealed in a furnace in O_2 atmosphere for a set of temperatures from 200 to 500 °C for 5 hours. No significant red shift of the optical absorption edge was observed. The optical density of the films, however, diminished considerably. The reduction in the magnitude of the absorption is believed to be due to loss of the semiconductor from the film due to diffusion and oxidation. A similar effect has been observed for sputtered and annealed CdTe films [149] and for sputtered GaSb-doped silica films described in the following Section. Commercial bulk semiconductor-doped glasses are subjected to a similar heat treatment in the fabrication process. The Auger spectroscopy measurements of the material composition performed on the bulk RG-850 glass revealed a semiconductor depletion layer of ~1 μm thickness near the glass surface [162]. For thicker sputtered RG-850 films, it might be possible to achieve the increase in the semiconductor nanoparticle size by annealing. However, growing significantly thicker films in the same sputtering system was not a realistic task, as the deposition time was already several hours.

In conclusion, semiconductor-doped films were fabricated by rf sputtering using an RG-850 glass target. The films had an optical absorption edge blue-shifted into the visible and were not suitable for application as saturable absorbers for near-IR laser modelocking.

5.2.5 Fabrication of GaSb-doped silica films

Deposition of GaSb-doped silica films was performed by rf sputtering. The sputtering target consisted of a 5-inch-diameter SiO_2 disk with chips of GaSb attached to it using a vacuum compatible epoxy KL-320K from Kurt J. Lesker Co. The epoxy was chosen to be able to withstand fairly high temperatures, up to ~100 °C, resulting from the rf power dissipation in the target (~100 W) and at the same time maintain a high vacuum present in the sputtering system (~10^{-7} Torr). The relative surface area of GaSb on the target was ~8%. The films were deposited on fused silica, BK-7 glass, and GaAs substrates. The deposition was performed with an rf power of 100 W to the target, 7 W to the substrate, an Ar gas pressure of 5 mTorr, and an Ar flow of 20 sccm. The separation between the target and the substrate was 3 inches and the substrates were not heated. Using profilometry, the sputtering rate was measured to be ~20 Å/min.

The deposited films were uniform and no structural defects were observed under a microscope. The films had good adhesion to the substrates, were stable and did not degrade over time. Depending on the substrate position on the 5-inch-diameter substrate holder plate during the deposition process, the film absorption varied significantly. The spatial variation in the film absorption was on a scale of centimeters and was due to the nonuniform distribution of GaSb on the target, with the GaSb chips mounted close to the target center. The sputtered film had the highest optical density directly under the GaSb chips on the target and the lowest density at the edge of the platform. A similar gradual variation of the film absorption as a function of substrate position was also observed for the InAs-doped silica films, with similar semiconductor chips positions on the target. The nonuniform optical density of the films somewhat complicated the analysis of the film properties. On the other hand, it also carried a significant advantage, allowing to deposit films with various values of absorption in one sputtering run, which was an important factor as only one sputtering run could be performed per day.

Figure 5-4 shows a typical absorption spectrum of sputtered GaSb-doped films. The measurements were performed using a CARY 5E spectrophotometer. A significant blue shift of the absorption edge from the bulk GaSb absorption edge of ~1.9 μm resulted from the semiconductor nanoparticle quantum confinement effects. Interference-related oscillation in the absorption spectrum are observed. From the shift of the absorption edge, the size of the GaSb nanoparticles can be estimated using a strong confinement model:

$$\Delta E = \frac{\hbar^2}{2\mu}\left[\frac{\pi}{R}\right]^2 \tag{5-1}$$

For the GaSb effective electron mass $m_e = 0.04m_0$ and heavy hole mass $m_{hh} = 0.28m_0$ [163], the nanocrystallite size is estimated to be in the 70 to 90 Å range, significantly smaller than the exciton Bohr radius,

$$a_B = \frac{\varepsilon\hbar^2}{\mu e^2} \tag{5-2}$$

calculated to be ~ 250 Å.

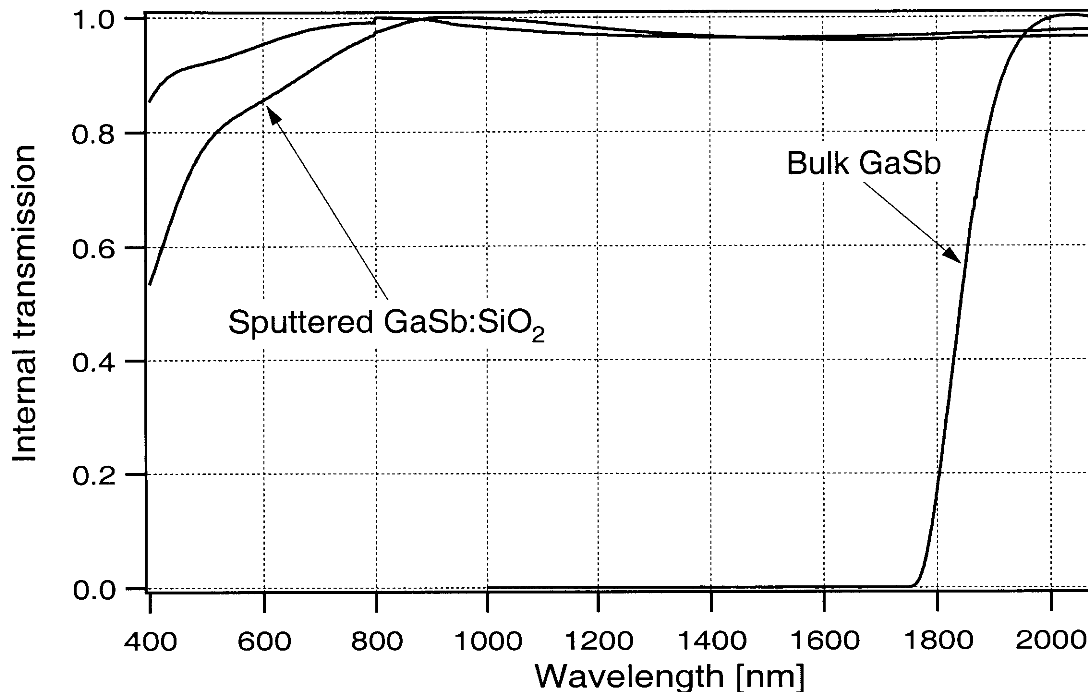

FIGURE 5-4: Transmission of sputtered GaSb-doped silica films and of a 500-μm-thick bulk GaSb. The two traces for the GaSb-doped films are from the same sputtering run and demonstrate the typical variation in the film absorption depending on the substrate position.

The absorption edge of the films was too blue-shifted to use them for IR laser modelocking. Some of the GaSb-doped silica films were annealed at a range of temperatures from 200 to 500 °C in oxygen. As in the case of RG-850 films, the optical absorption decreased after the anneal and no significant shift of the absorption edge was observed.

It was previously shown that for semiconductor-doped films prepared by rf magnetron sputtering, the nanocrystallite size increases with increasing substrate temperature in a range from 100 to 400 °C [147] [156]. In attempt to find a way to increase the size of GaSb crystallites and shift the absorption edge into the IR, a home-built resistive heater was installed into the sputtering system in order to elevate the substrate temperature during deposition. The substrate temperature was monitored with a thermocouple. When the substrate was not heated, the substrate temperature was measured to be ~ 70 °C, elevated from room temperature due to substrate being in contact with the discharge plasma. A series of sputtering runs was performed for substrate

temperatures ranging from 100 to 300 °C, however no significant change in the position of the absorption edge was observed. For higher substrate temperatures, the absorption of the sputtered films diminished considerably. The discrepancy from the results showing the dependence of the nanocrystallite size on the substrate temperature, which are presented in the literature, could be attributed to the absence of magnetron in our sputtering system, leading to a lower deposition rate and a contact of the substrates with the discharge plasma.

Silica films doped with GaSb were fabricated for the first time to my knowledge and presented an interesting materials system for investigation of electronic confinement effects. However, the final goal of the presented research was the development of saturable absorber materials for IR solid-state laser modelocking. GaSb-doped films had an absorption edge in the visible and were not suitable for IR modelocking applications. Therefore no further studies were performed on the GaSb-doped films and instead InAs, having a bulk bandgap farther into the IR, was considered as a dopant.

5.2.6 Fabrication of InAs-doped silica films

InAs-nanocrystallite-doped SiO_2 thin films were prepared by rf sputtering using an MRC 8800 sputtering system. The sputtering target consisted of a 5-inch-diameter SiO_2 disk with chips of undoped InAs attached to it with vacuum epoxy. The relative target surface area of InAs was 10%. The films were deposited on a variety of different substrates, depending upon the measurements that were being performed. Fused silica and sapphire substrates were used to prepare samples for optical transmission measurements, while sapphire substrates were used for pump-probe time-resolved absorption saturation measurements and for laser modelocking experiments. Si and GaAs substrates were used for film thickness measurements which required photolithography and for x-ray photoemission spectroscopy (XPS) measurements. Finally, for performing transmission electron microscopy (TEM) measurements, films were deposited on a 100-Å-thick carbon film on a 200-μm-mesh copper grid. The deposition was typically performed with an rf power of 100 W, an Ar gas pressure of 5 mTorr, and an Ar flow of 20 sccm. The typical separation between the tar-

get and the substrate was 3 inches and the substrates were not heated. For these deposition conditions, the sputtering rate was measured to be ~20 Å/min using photolithography and profilometry. A typical surface profile trace of an etched InAs film is shown in Figure 5-5.

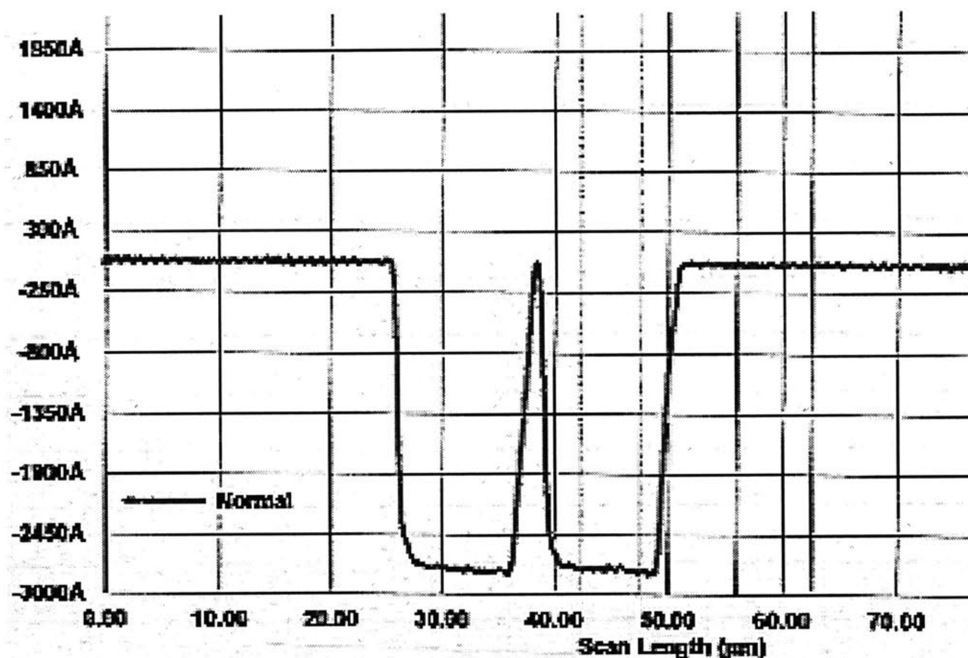

FIGURE 5-5: A typical profilometer trace of an etched InAs-doped silica film. The film thickness is 2750Å.

The deposited films exhibited good adhesion to the substrates and no defects could be observed under a microscope. The films were stable and no changes in film properties occurred over time. Similar to the GaSb-doped films, the film absorption varied depending on the substrate position relative to the center of the substrate platform during deposition. Typical optical absorption spectra of InAs-doped films are shown in Figure 5-6.

In attempt to control the InAs nanoparticle size within the film and the optical absorption edge, several sputtering runs were performed. The rf power was varied in the range from 100 to 150 W, the separation between the target and the substrate was varied between 2 and 3.5 inches. These parameters were found to affect the deposition rate but no significant changes in the position of the absorption edge could be observed. Sputtering runs were also performed with elevated

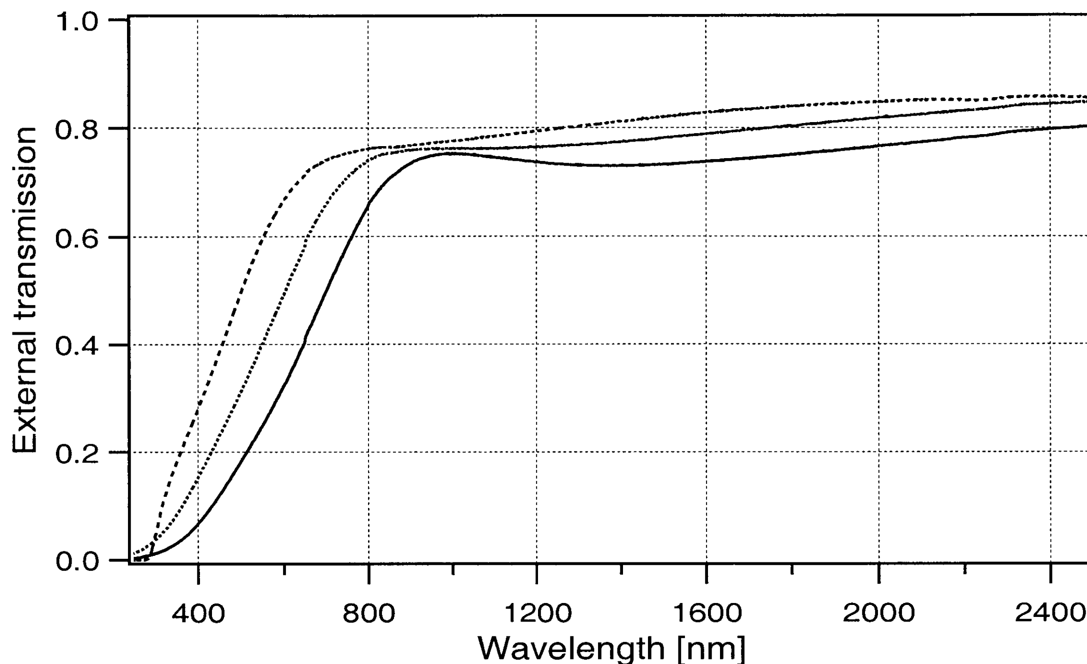

FIGURE 5-6: Optical absorption spectra of InAs-doped silica films on fused silica and BK-7 glass substrates. Film thickness 1200 Å. The observed oscillations in the absorption spectra are the result of interference.

substrates temperatures, in the range from 90 to 250 °C. The thermocouple readings were tested by placing a piece of indium foil on the heated substrate holder and observing whether the foil melted during the deposition. A good thermal contact between the substrates and the heated substrate platform was established by using vacuum-compatible thermal grease and molten indium. Still, these experiments failed to produce a red shift of the absorption edge compared to the unheated substrates.

Rapid thermal annealing (RTA) in nitrogen, argon, and forming gas (95% N_2, 5% H_2) at atmospheric pressure at a range of temperatures from 500 to 800 °C was performed on some of the InAs-doped films. Due to the dopant diffusion out of the film and oxidation, a reduction in magnitude of the absorption was observed along with a slight red shift of the absorption edge due to particle size growth for films annealed at temperatures above 600 °C. More significantly, however, the RTA treatment strongly affected the absorption saturation dynamics, leading to faster absorption recovery times for higher annealing temperatures. The details are presented in Section 5.8.

5.3 Chemical composition of InAs-doped films (XPS)

In order to evaluate the film properties, a comprehensive set of film characterization measurements was performed including measurements of linear optical absorption, femtosecond-time-scale absorption saturation dynamics, film composition, semiconductor nanoparticle size, chemical element distribution within the film, and nanoparticle crystalline structure.

In order to analyze the chemical composition of the InAs-doped films, x-ray photoelectron spectroscopy (XPS) measurements were performed. In x-ray photoemission spectroscopy, x rays striking the sample produce photoelectrons which then go through an energy analyzer and are detected [164] [165]. The electron binding energy is given by

$$E_B = h\nu - E_K - e\varphi_{sp} \tag{5-3}$$

where $h\nu$ is the initial photon energy, E_K is the electron kinetic energy, and $e\phi_{sp}$ is the electron charge times the spectrometer work function. In addition, if the sample is non-conductive, it acquires a positive charge and a positive potential ψ due to loss of photoelectrons. By knowing the energy of the incident radiation and measuring the kinetic energy of the photoelectrons, the ionization energy can be derived, and the elemental composition of the sample can be determined. In addition to the directly photoexcited electrons, Auger electrons can also be detected. When an electron is ejected from an inner shell, the resulting vacancy can be filled with an electron from a higher atomic level. This de-excitation can result in the emission of an x-ray photon or the emission of a secondary electron in a radiationless Auger process.

The measurements were performed using a Perkin Elmer 5200 XPS system with a Mg K_α x-ray source, with an x-ray photon energy of 1253.6 eV. The spectrometer work function was -5.1 V and is accounted for in the displayed spectra. Survey XPS traces were acquired for the reference bulk InAs sample as well as for an InAs-doped silica film on glass. The results are depicted in Figure 5-7 and Figure 5-8. The acquisition time was approximately 2 minutes per trace. The characteristic core electron peaks for the elements contained in the film, including In, As, O, and Si, as well as the MNN Auger In peaks are clearly resolved. The displayed spectra did not

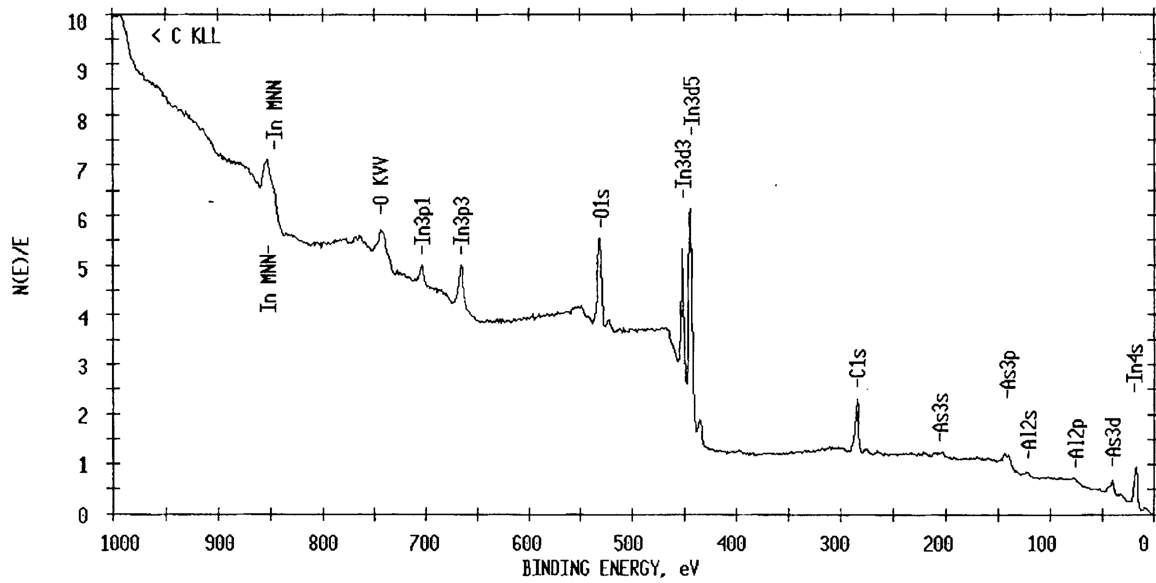

FIGURE 5-7: XPS spectrum of a bulk InAs reference sample.

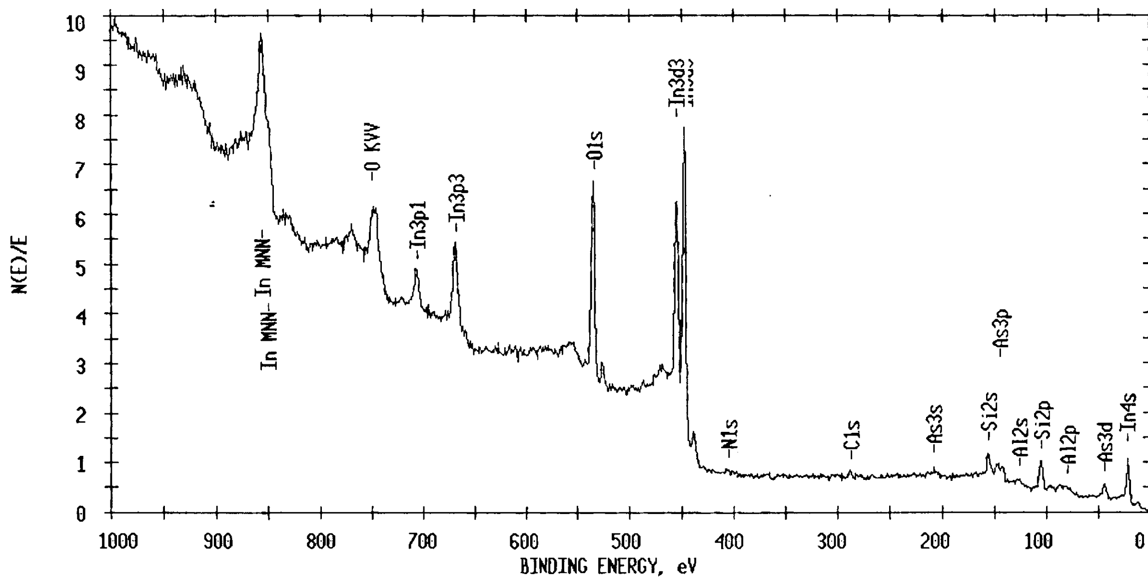

FIGURE 5-8: XPS spectrum of an InAs-doped silica film.

account for the unknown sample charging potential. The quantitative composition of the film was estimated by measuring the total area of the peaks corresponding to the particular elements. InAs was found to be stoichiometric within the measurement error and the InAs doping density was found to be ~ 9 at%.

The next step was to determine the chemical state of In and As within the film and establish whether they form InAs, are oxidized, or are in a pure elemental state. In general, the energy positions of the core XPS lines are not fixed but depend on the surrounding chemical environment [166] [167]. The chemical shifts are indicative of the average atomic potential experienced by the electron as an effect of chemical bonds between the atoms. The chemical shift can be used to identify the chemical state of the element under consideration. The magnitude of the chemical shift is typically less than 10 eV and is frequently of the same order of magnitude as the measurement error. The main source of uncertainty is introduced by the charging of the nonconducting sample during the measurement. However, the difference between the principle core and the secondary (Auger) peaks (also called the Auger parameter) is independent of charging. The changes in Auger parameter from one compound to another are commonly used to determine the chemical state of the element.

To determine the chemical state of indium within the film, higher resolution XPS scans were acquired for the In $3d_{3/2}$ and $3d_{5/2}$ lines as well as for the In $M_5N_{45}N_{45}$ and $M_4N_{45}N_{45}$ Auger lines both for the InAs-doped silica sample and for the reference pure bulk InAs wafer. To ensure that the surface of the reference sample was not contaminated, the InAs reference was cleaned in vacuo by sputter etching with an argon ion gun for 10 minutes. The sputter etch rate was ~ 20 Å/min. The carbon and oxygen lines, representing the contaminants, were monitored during the etching process. After the etching, the oxygen and carbon peaks in the reference InAs spectrum were barely detectable (compare Figure 5-8 and Figure 5-9). The acquisition time for the 3d lines was approximately 4 minutes and for the Auger lines approximately 10 minutes per trace. The spectra of the 3d lines are shown in Figure 5-10 and Figure 5-11 and the spectra of the Auger lines in Figure 5-12 and Figure 5-13. From the line positions, it can be seen that the investigated sample on a glass substrate acquires a larger positive charging potential than the reference InAs wafer, which is manifested in the shift of the spectrum to the higher energies. Taking the In $3d_{5/2}$ line,

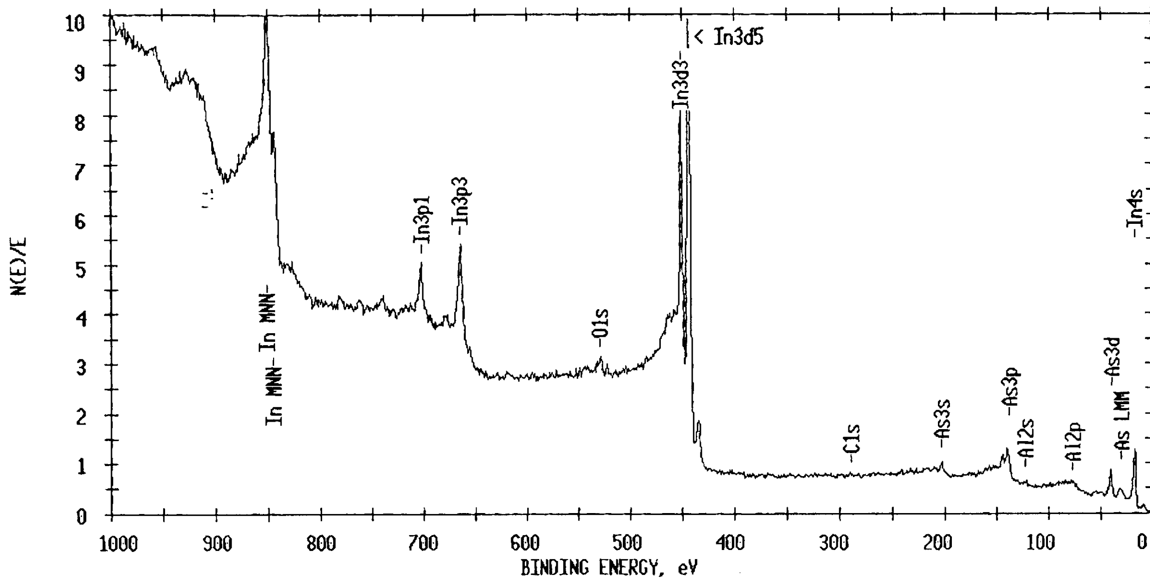

FIGURE 5-9: XPS spectrum of a bulk InAs reference sample after sputter etching. The O and C peaks produced by the contaminants have diminished significantly compared to the unsputtered InAs reference (Figure 5-7).

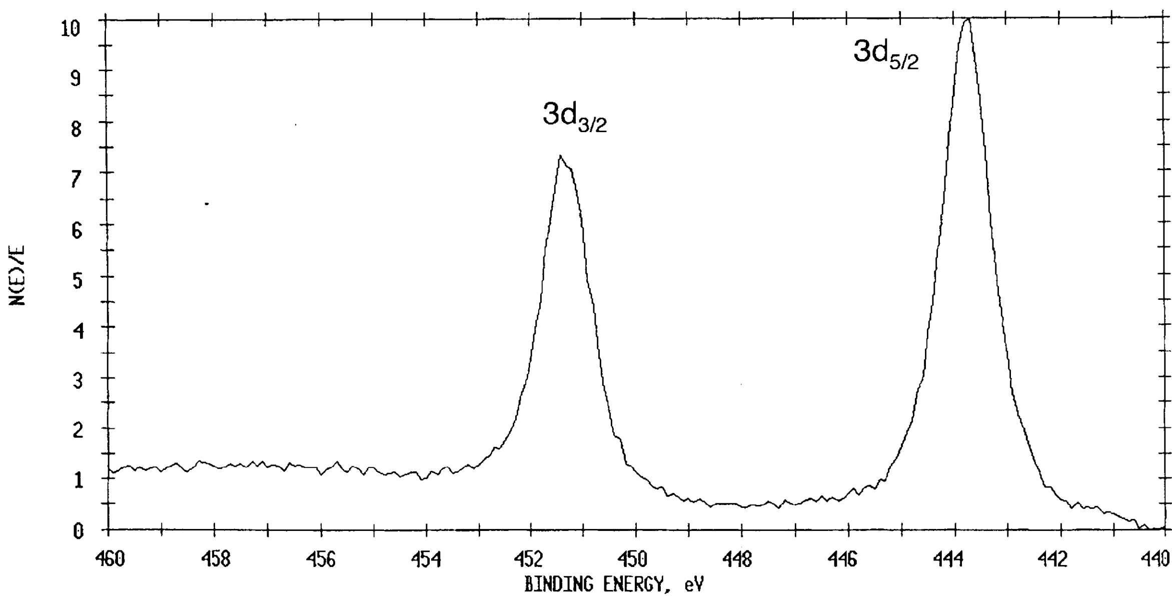

FIGURE 5-10: XPS spectrum of the indium 3d lines acquired from the bulk InAs reference.

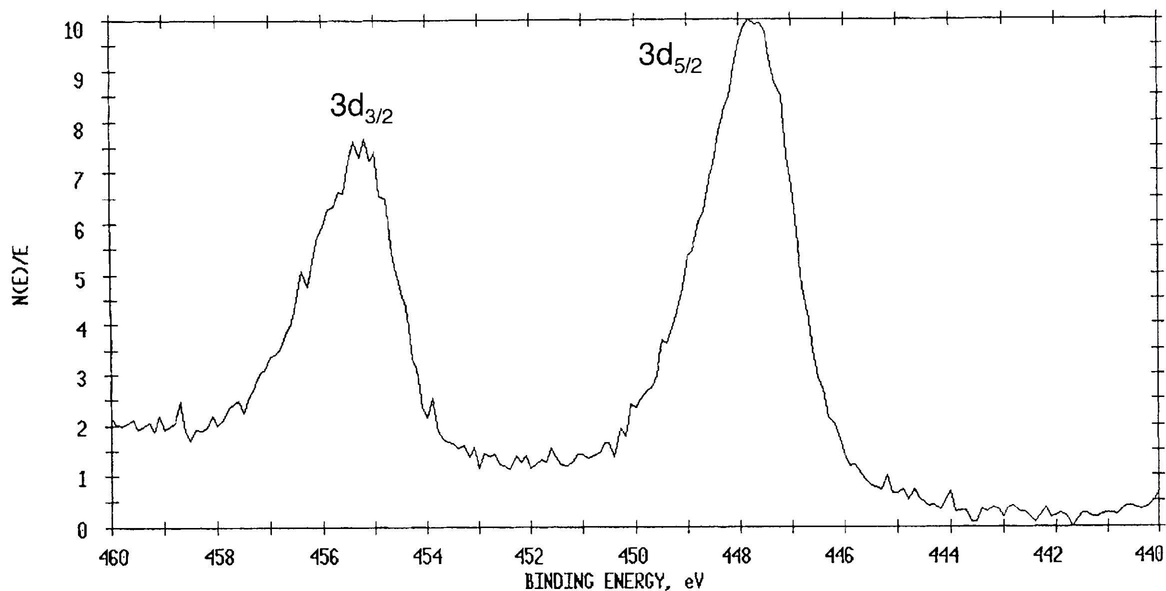

FIGURE 5-11: XPS spectrum of the indium 3d lines acquired from the sputtered InAs-doped film.

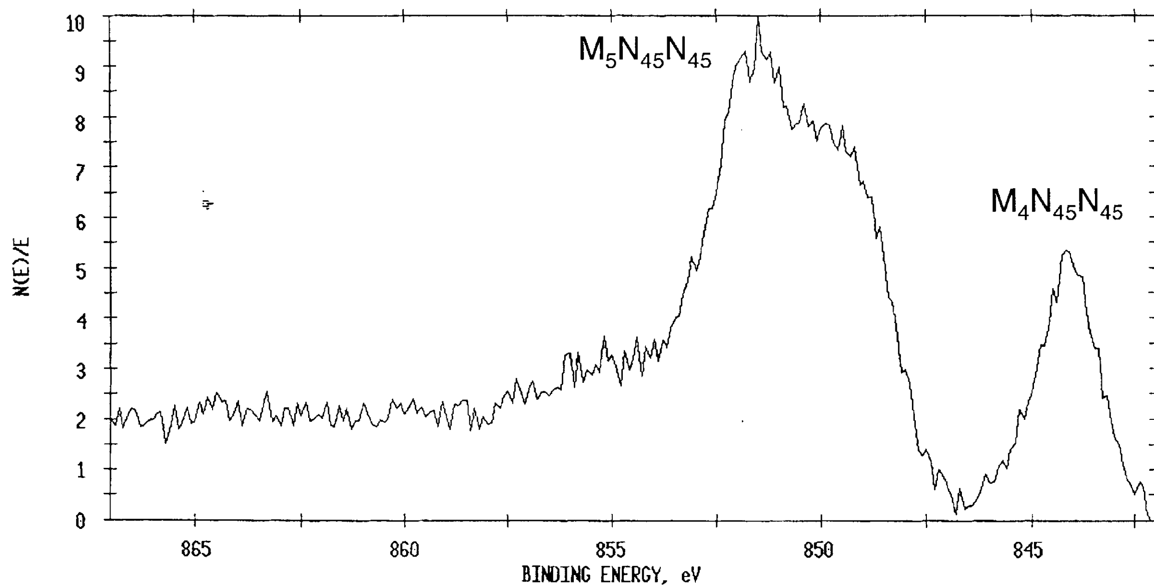

FIGURE 5-12: XPS spectrum of the indium MNN Auger lines acquired from the bulk InAs reference.

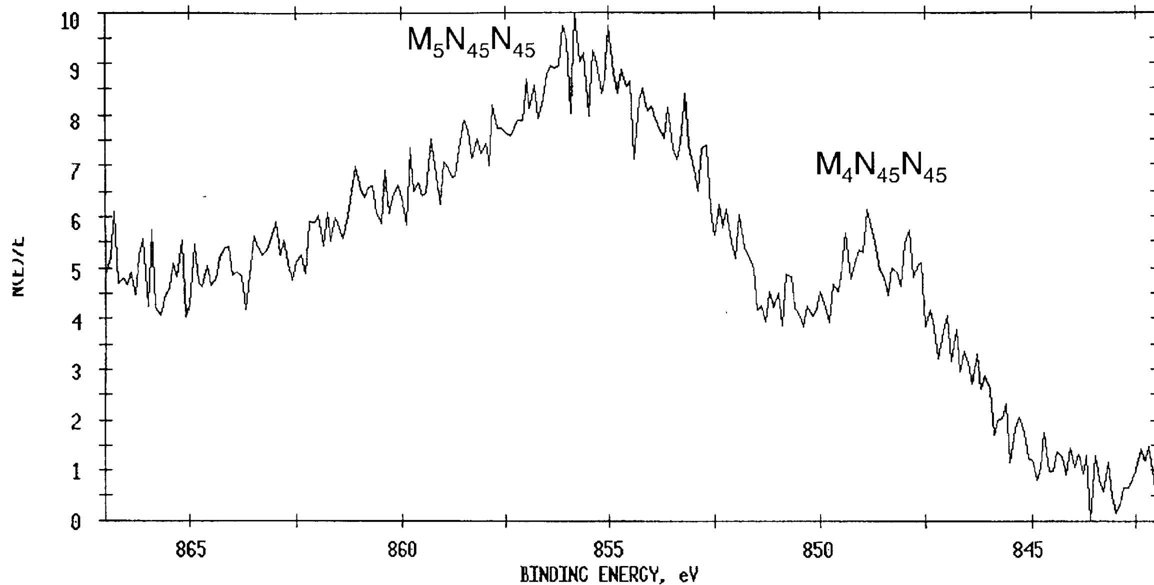

FIGURE 5-13: XPS spectrum of the indium MNN Auger lines acquired from the sputtered InAs-doped film.

which is weakly dependent on the chemical state of In, as a reference (Figure 5-14)[167], the positive potential on the investigated sample can be estimated to be ~ 4V. This charging potential is comparable or greater than the chemical shifts for indium and would lead to significant errors if left unaccounted for.

There exist no published data for the XPS line positions for InAs, however the chemical shifts for a number of other In compounds have been tabulated [167]. The tabulated quantity is the difference between the indium $3d_{5/2}$ and $M_4N_{45}N_{45}$ peaks plus the photon energy for Mg K_α (1253.6 eV). This parameter is independent of the specimen charging and therefore eliminates the uncertainty associated with the unknown positive potential of the sample.

The positions of the $3d_{5/2}$ core and $M_4N_{45}N_{45}$ Auger lines were measured, and the difference was taken to obtain the Auger parameter. The measurement of the $3d_{5/2}$ - $M_4N_{45}N_{45}$ Auger parameter plus the photon energy gave the value of 853.2 eV for the InAs reference and 852.6 eV for the InAs-doped silica film under investigation. The main source of uncertainty, of ~ 1eV, was

the position of the $M_4N_{45}N_{45}$ line for the investigated sample. Therefore, the measured Auger parameter for the investigated film was within the measurement error from the value for measured the reference InAs sample, indicating that indium in the films is likely to be in the form of InAs.

The data was then compared to the tabulated data from the literature (Figure 5-14)[167].

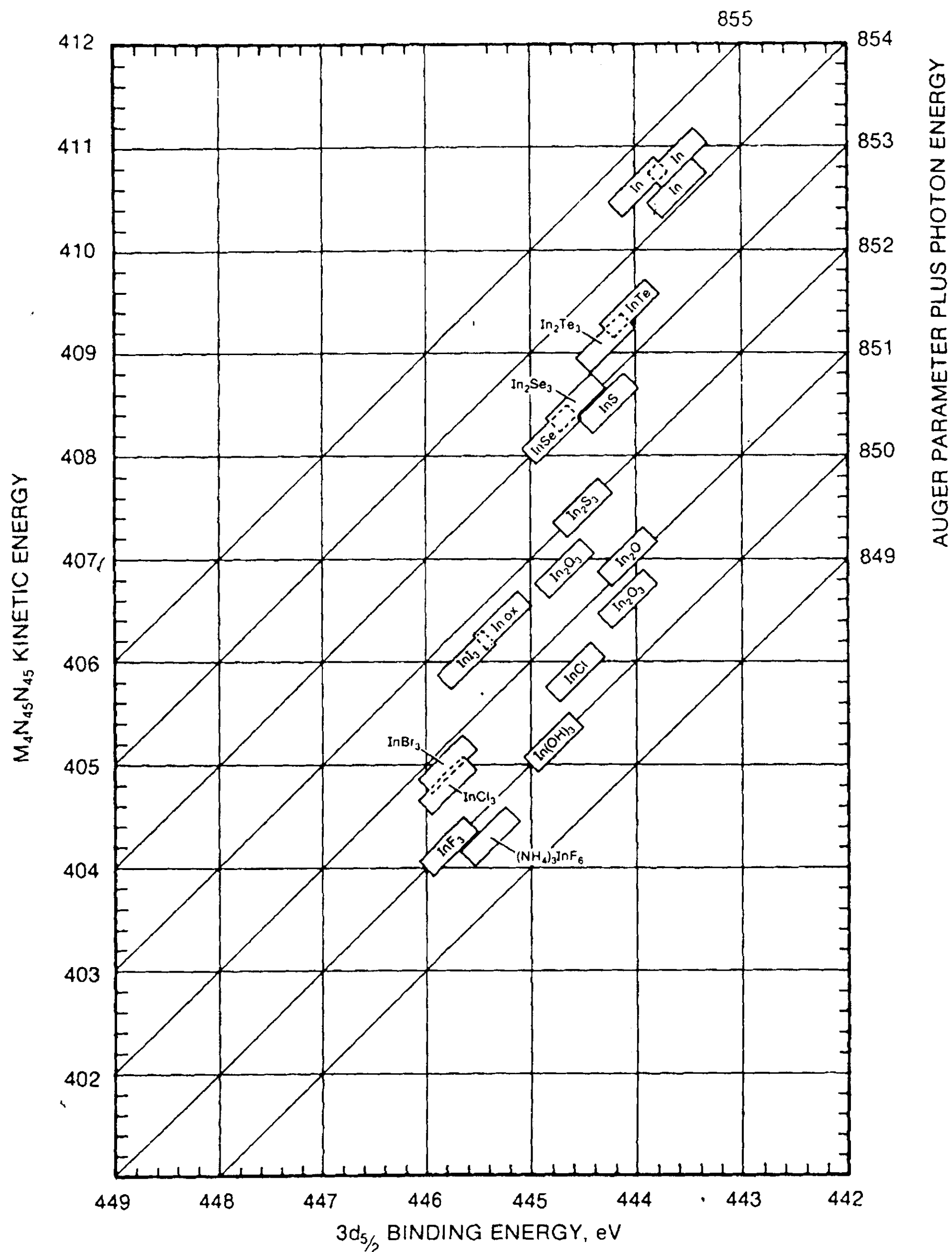

FIGURE 5-14: $3d_{5/2}$ binding energies, $M_4N_{45}N_{45}$ Auger electron energies and Auger parameters for Mg K_α excitation for various indium compounds. From reference [167].

The bottom and the left axes in Figure 5-14 are dependent on the sample charging potential, while the right axis is invariant of charging and is used for comparison. The $3d_{5/2}$ - $M_4N_{45}N_{45}$ Auger

parameter plus the photon energy for pure In is in the 854 - 855 eV range, and for In_2O_3 in the 850.5 - 851.5 eV range. Both are more than 1 eV away from the measured parameter for the investigated InAs-doped silica film.

A more precise comparison between the measured InAs reference and the InAs-doped film can be performed by considering the $M_5N_{45}N_{45}$ Auger line which in more pronounced in the XPS scan. In this case, the difference between the measured sample and reference Auger parameters is only 0.2 eV.

In conclusion, the XPS measurements were performed to determine the chemical composition of the sputtered InAs-doped silica films. The characteristic peaks for In, As, Si, and O were detected and the films were found to contain ~ 9 at% of InAs. The measurements of the chemical shifts and the Auger parameters indicate that the films are likely to contain indium in the form of InAs, not pure In or In_2O_3.

5.4 Film morphology (TEM)

In order to establish the structural composition of the InAs-doped silica films, transmission electron microscopy (TEM) as well as scanning transmission electron microscopy (STEM) measurements were performed.

A major issue in transmission electron microscopy is sample preparation. To obtain TEM images, the TEM electron beam should be able to penetrate the sample, with many electrons transmitted through it. This limits the thickness of the specimen to a few hundred angstroms. TEM sample preparation typically involves various methods of thinning a specimen and subsequently attaching it to a TEM specimen holder. However, in case of the InAs-doped silica, the films could be sputtered directly onto the TEM-compatible substrates. Three kinds of substrates from Ernest F. Fullam, Inc. were used including 100-Å-thick amorphous carbon films on 200-µm-mesh copper grids, formvar films and formvar stabilized with 200-Å-thick silicon monoxide.

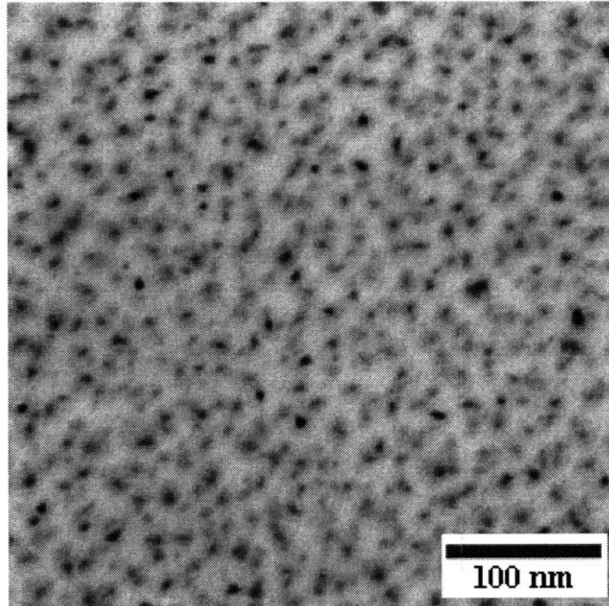

FIGURE 5-15: Bright-field TEM image of a 150-Å-thick InAs-doped silica film. The substrate is a 100-Å-thick carbon film on a 200-μm-mesh copper grid.

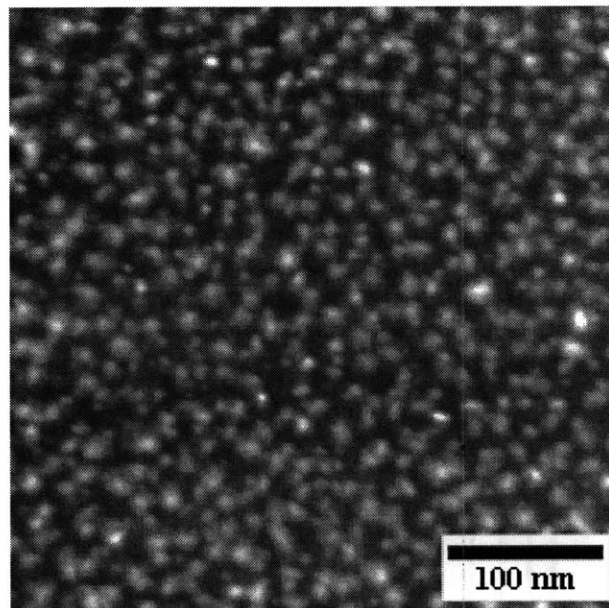

FIGURE 5-16: Dark-field TEM image of a 150-Å-thick InAs-doped silica film. The substrate is a 100-Å-thick carbon film on a 200-μm-mesh copper grid.

Although these substrates attenuate the TEM signal, they do not introduce any features into the TEM image. The InAs-doped silica films sputtered on top of the TEM substrates had the thickness of 150 Å.

During the TEM image acquisition, the substrates and the film experience damage due to bombardment by the electron beam. The damage is manifested as the motion of the sample during the STEM scan creating images elongated in one direction, or as a catastrophic rapture of the substrate. The best results were obtained using the carbon film substrates which experienced the smallest amount of damage.

A bright-field TEM image of an InAs-doped silica film on a carbon film substrate is depicted in Figure 5-15 and the dark-field image in Figure 5-16. Both images were acquired using a VG-STEM model HB 603 scanning TEM. The images show a broad nanoparticle size distribution with particle sizes up to ~ 80 Å.

The broad particle size distribution is a drawback for studies of confinement effects in semiconductors causing inhomogeneous broadening of optical spectra. For saturable absorber applications, however, the broad variation of the nanocrystallite sizes is a useful effect, leading to a variation of the semiconductor band gaps, a smooth optical absorption edge, and, as a result, a broad bandwidth of operation of the saturable absorber.

5.5 Element distribution within the film (STEM + EDX)

The TEM measurements described in the previous section have demonstrated that the films contain nanoparticles embedded in a host matrix. The XPS measurements, discussed in Section 5.3, have shown that the films contain In and As, along with Si and O. Indium was found to be present mostly likely in the form of InAs and not pure In or In_2O_3. Yet another test that would help determine the chemical state of the elements contained within the film would be to measure the spatial correlation between the positions of the nanoparticles and the indium and arsenic concentrations. In order to establish the spatial distribution of elements within the film, energy dispersive x-ray (EDX) measurements were performed in conjunction with STEM measurements.

Energy dispersive x-ray spectroscopy is a useful tool for analyzing the chemical composition of complex samples [168]. It is frequently used in conjunction with electron microscopes where the x-rays are produced as a result of excitation by a electron beam. The electrons incident on the sample, with the energy typically in a few hundred keV range, collide with the electrons in the sample atoms and ionize them. Characteristic x-rays are emitted when electrons from the higher energy states fill the inner shell vacancies. The emitted x-rays are detected and their spectrum is analyzed by an energy dispersive x-ray detector.

The measurements were performed using an Oxford Instruments Pentafet windowless EDX detector in conjunction with a VG-STEM model HB 603 scanning TEM. The sample was a 150-Å-thick InAs-doped silica film deposited on a 100-Å-thick carbon film on a 200-μm-mesh copper grid. The EDX spectrum of an InAs-doped silica film is depicted in Figure 5-17. The figure

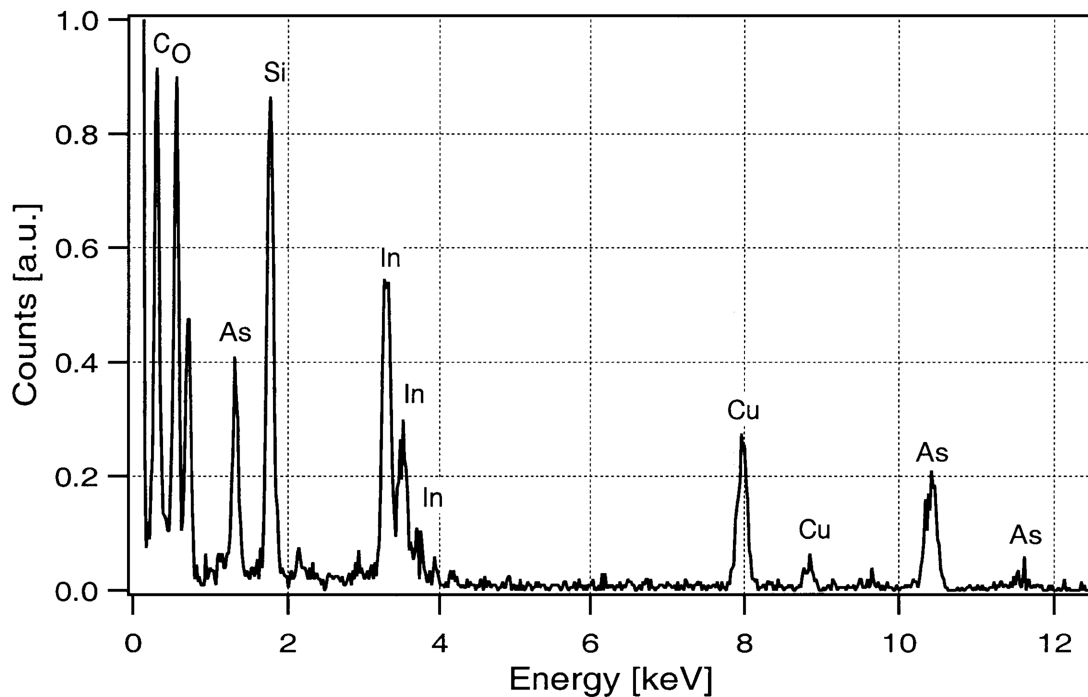

FIGURE 5-17: EDX spectrum of a 150-Å-thick InAs-doped silica film on a 100-Å-thick carbon film on a copper grid.

clearly shows the presence of the characteristic x-ray peaks for carbon, oxygen, arsenic, silicon, indium, and copper. The presence of the copper peaks is due to the copper mesh substrate used

for the samples. The carbon peaks are produced by the carbon substrate film along with the oils and carbohydrates on the film surface contaminated by exposure to air. The indium, arsenic, oxygen, and silicon peaks are due to the elements in the film.

In order to determine the spatial distribution of the elements, compositional maps were acquired. Windows were set around the 6 characteristic x-ray peaks of the elements of interest in the EDX spectrum and a background region. The total count from each of these channels was recorded every time a scanning electron beam moved to a new pixel. L and K_α lines were used in

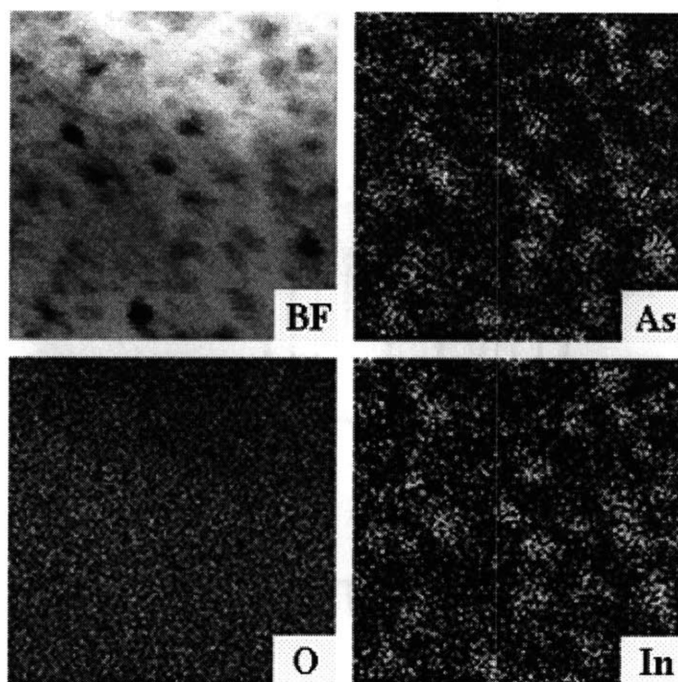

FIGURE 5-18: Compositional maps of an InAs-doped silica film. The image size is 80 by 80 nm. BF, bright field image; As, arsenic; O, oxygen; In, indium.

order to identify arsenic, L_α and L_β lines for indium, K line for oxygen, and K line for silicon. A 80 nm by 80 nm bright-field STEM image and the compositional maps for In, As, O, and Si were acquired simultaneously. The images were 128x128 pixels and the scan rate was 50 ms/pixel. The images took approximately 13.5 minutes to acquire. The compositional maps for As, In, and O, along with a bright field STEM image are shown in Figure 5-18. From the images, it can be seen that In and As are concentrated in the same regions of the film corresponding to the nanopar-

ticle positions on the bright-field image. In contrast, O and Si (not shown) are uniformly distributed, as expected. The poor image quality of the compositional maps is due to the poor statistics of the detected x-rays. Even the most intense pixels on the maps contain only about 10 counts. It was not possible to use a longer exposure time because of the sample damage produced by the electron beam.

In conclusion, the EDX+STEM images demonstrate that the films contain InAs nanoparticles embedded in a glass matrix.

5.6 Nanoparticle crystalline structure (electron diffraction)

Once it has been established that the films contain InAs nanoparticles, the next step is to determine whether the nanoparticles are crystalline, and if so, what the lattice structure is. Electron diffraction can be used to provide the answers to these questions.

When an image is formed in the object plane of an electron microscope, an electron diffraction pattern produced by the specimen under investigation is present in the back focal plane of the objective lens (Figure 5-19). If the specimen is a single crystal, then the diffraction pattern will contain an array of spots. The arrangement of the spots will depend on the crystal orientation. If the specimen is polycrystalline, i.e. it contains a large number of single crystals with random orientations, then the diffraction pattern will consist of a number of concentric rings. Such a diffraction pattern is actually a number of single crystal diffraction patterns, each rotated by a small angle with respect to each other. The same pattern would be formed if a single crystal were continuously rotated about random axes. If the specimen is amorphous, i.e. the atoms and molecules are arranged randomly, then the diffraction pattern will have no distinct maxima and will consist of a diffuse scattering around the bright central nondiffracted spot [169].

The electron diffraction measurements were performed using a JEOL 200 CX TEM. The electron beam energy was 200 keV, the camera length was 100 cm. The specimen was a 150-Å-thick InAs-doped silica film on a 100-Å-thick carbon film on a 200-μm-mesh copper grid. The observed diffraction pattern shown in Figure 5-20 consists of a number of distinct concentric

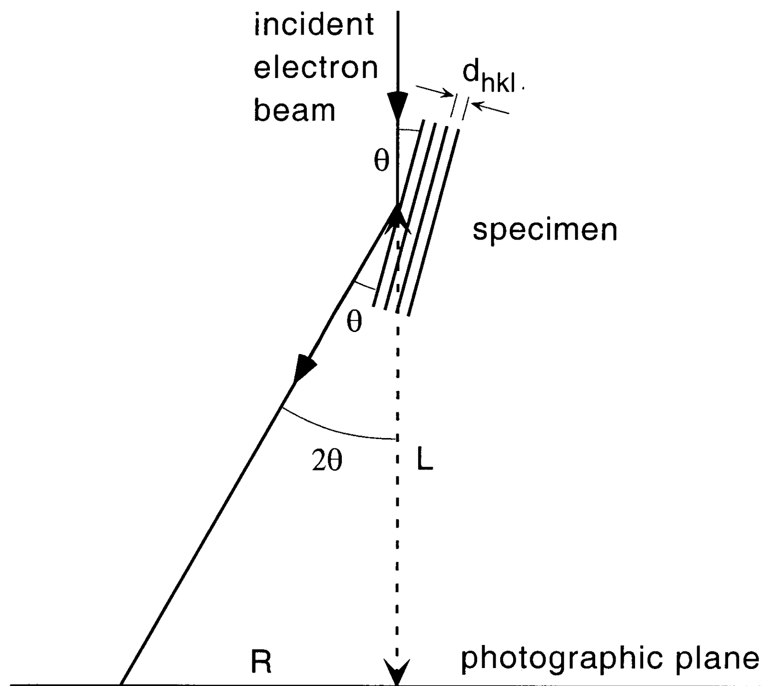

FIGURE 5-19: Electron diffraction from a crystalline specimen. d_{hkl} is the interplane separation, θ is the diffraction angle, L is the camera length, and R is the radius of the diffraction ring.

rings, which is the pattern produced by a polycrystalline material or a number of randomly oriented single crystals. The width of the diffraction rings resulted from the finite size of the crystallites. The observed electron diffraction pattern conclusively determines that the InAs nanoparticles are crystalline.

The diffraction angle θ obeys the Bragg law:

$$\lambda = 2d_{hkl}\sin\theta \tag{5-4}$$

where λ is the electron wavelength and d_{hkl} is the spacing between the crystal planes with Miller indices h, k, and l. For a particular lattice type, the interplane separations can easily be found. For example, if the crystal is cubic, as it will turn out to be the case for the InAs nanoparticles in silica, then [170]

$$\frac{1}{d^2} = \frac{h^2 + k^2 + l^2}{a^2} \tag{5-5}$$

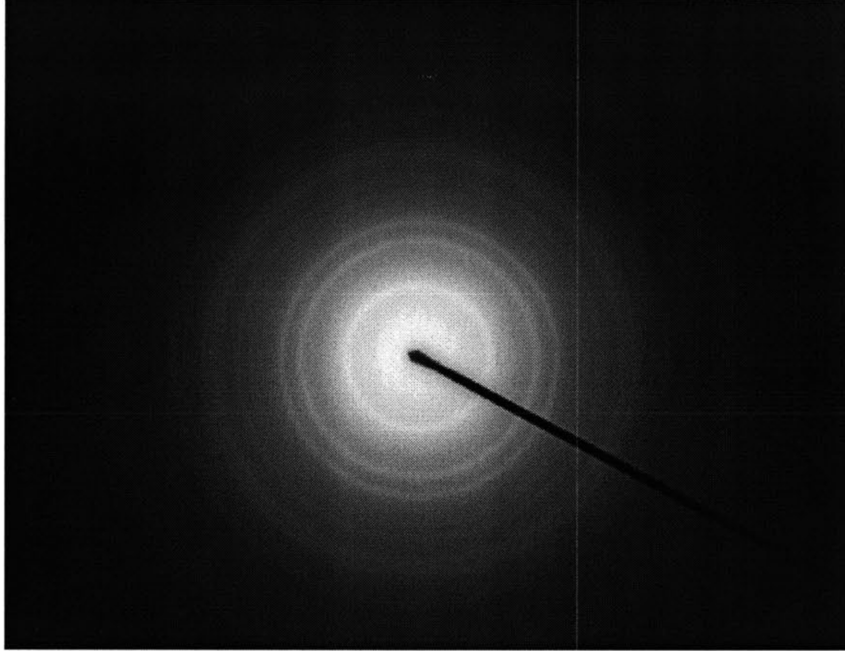

FIGURE 5-20: Electron diffraction pattern observed for InAs-doped silica films. The concentric rings indicate a polycrystalline nature of the specimen, while the ratio of the ring radii corresponds to diamond cubic and zinc blende lattice types.

Combining the equations (5-4) and (5-5), the condition for all possible diffraction angles for a cubic lattice is obtained:

$$\sin^2\theta = \frac{\lambda^2}{4a^2}(h^2 + k^2 + l^2) \tag{5-6}$$

where a is the unit cell size. Therefore, for a cubic lattice,

$$\frac{\sin^2\theta}{(h^2 + k^2 + l^2)} = \frac{\sin^2\theta}{s} = \frac{\lambda^2}{4a^2} \tag{5-7}$$

where $s = (h^2 + k^2 + l^2)$ is always an integer and the ratio $\frac{\lambda^2}{4a^2}$ is a constant for a given crystal. This shows that the diffraction directions are determines solely by the shape and the lattice constant of the unit cell. Conversely, the lattice type and the lattice constant can be determined from the measurements of the diffraction ring radii. By observing the diffraction pattern and measuring the radii of the concentric rings, a series of s-numbers can be obtained. The measured s-numbers

can then be compared to the numbers, theoretically predicted for various lattice types and the lattice structure of the specimen can be determined.

Bulk InAs has a zinc blende lattice, which is a diamond cubic lattice with the lattice positions occupied by two different kinds of atoms, In and As [163]. By measuring the diffraction ring radii, calculating the diffraction angles, and taking their ratios, a series of s-numbers was obtained. Nine diffraction rings could be observed on the photographic negative. The set of measured s-numbers 3.0, 8.0, 11.0, 16.8, 19.3, 24.1, 27.0, 32.0, 35.4, closely corresponded to the set predicted for the zinc blende (or diamond cubic) lattice 3, 8, 11, 16, 19, 24, 27, 32, 35 [170]. The comparison with a number of other lattice types does not reveal any similarities. This measurement relied solely on the relative radii of the diffraction rings and did not require the knowledge of the electron energy or the camera length. In conclusion, the InAs nanocrystallites maintain the zinc blende lattice structure of the bulk InAs material.

Once the lattice type has been determined, the value of the lattice constant can be obtained from the absolute value of the diffraction angles. The electron energy in the TEM was 200 keV. The DeBroglie wavelength is given by

$$\lambda = \frac{h}{p} \tag{5-8}$$

where h is the Plank's constant and p is the momentum of the electron. As the electron kinetic energy E_K of 200 keV is comparable to the rest energy of 0.51 MeV, the electron momentum should be calculated from the total electron energy $E = E_K + m_0c^2$ using the relativistic relation

$$E^2 = m_0^2c^4 + p^2c^2 \tag{5-9}$$

where m_0c^2 is the rest energy of the electron equal to 0.51 MeV. Using equations (5-8) and (5-9), the electron DeBroglie wavelength was calculated to be $2.52 \cdot 10^{-2}$ Å. The TEM camera length was 100 cm and was the main source of measurement uncertainty, of ~ 5%. The lattice constant of the InAs nanoparticle zinc blende lattice was calculated to be 5.82 Å, which is within the 5% measurement error from the bulk InAs lattice constant of 6.05 Å [163].

In order to confirm that the observed diffraction rings were produced by the InAs nanoparticles and not by some other material present in the system, an aperture was used in the back focal plane of the TEM objective lens to select an azimuthal part of the diffraction rings depicted in Figure 5-20. This way only the electrons diffracted by the nanocrystallites with certain orientations

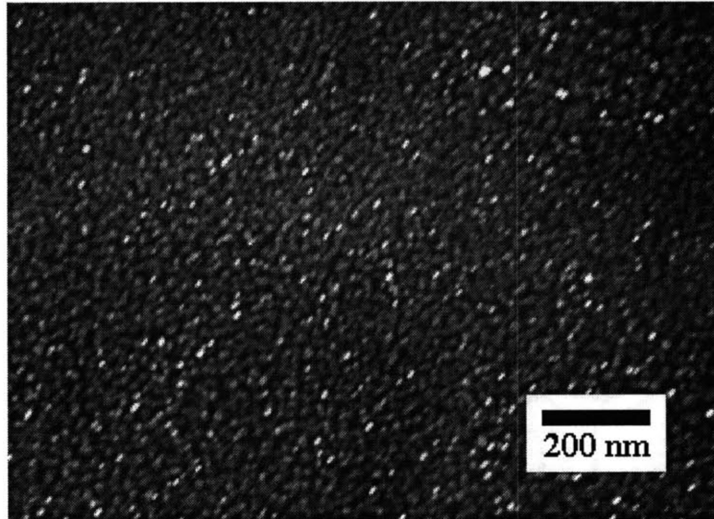

FIGURE 5-21: Selected angle dark-field image. InAs nanocrystallites oriented to match the selected diffraction angles show up as bright spots, significantly brighter then the misoriented crystallites.

were selected. A dark-field image depicted in Figure 5-21 was subsequently acquired using the diffracted electrons selected by the aperture. The nanocrystallites which were oriented to match the selected diffraction direction showed up significantly brighter than the remaining nanocrystallites, thus proving that they produce the observed diffraction rings. A corresponding bright-field TEM image is shown in Figure 5-22.

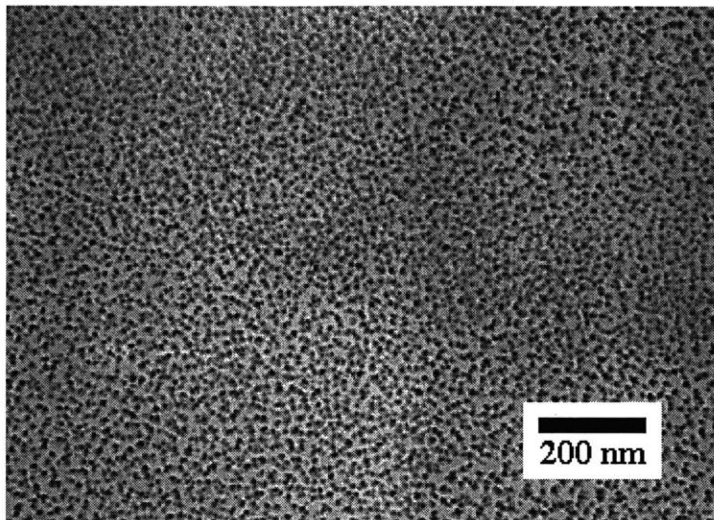

FIGURE 5-22: Bright field TEM image corresponding to the selected angle dark-field image in Figure 5-21.

5.7 Linear optical properties

Figure 5-23 shows a typical absorption spectrum of InAs-doped films. The measurements

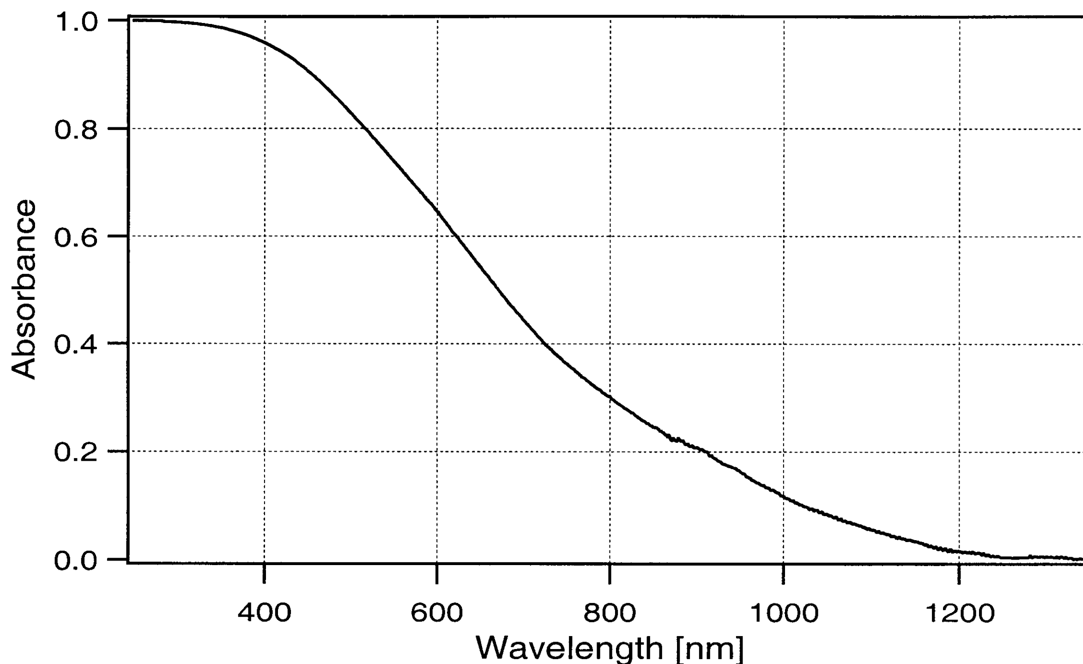

FIGURE 5-23: Optical absorption spectrum of an InAs-doped silica film on sapphire. Film thickness 2500 Å.

were performed using a CARY 5E spectrophotometer. A significant blue shift of the absorption edge from the bulk InAs absorption edge of 3.47 μm resulted from the semiconductor nanoparticle quantum confinement effects. From the position of the absorption edge, the InAs nanocrystallite size could be estimated using a simple model described in the previous Chapter:

$$\Delta E = \frac{\hbar^2}{2\mu}\left[\frac{\pi}{R}\right]^2 \qquad (5\text{-}10)$$

The observed absorption edge is due to the larger crystallites in the distribution. Therefore, for the InAs electron and heavy hole effective masses of $0.027m_0$ and $0.41m_0$ respectively [163], and the measured absorption edge of ~1.2 μm, the diameter of the largest InAs nanocrystallites in the film is estimated to be ~90 Å. This value is in agreement with the crystallite sizes up to ~ 80 Å

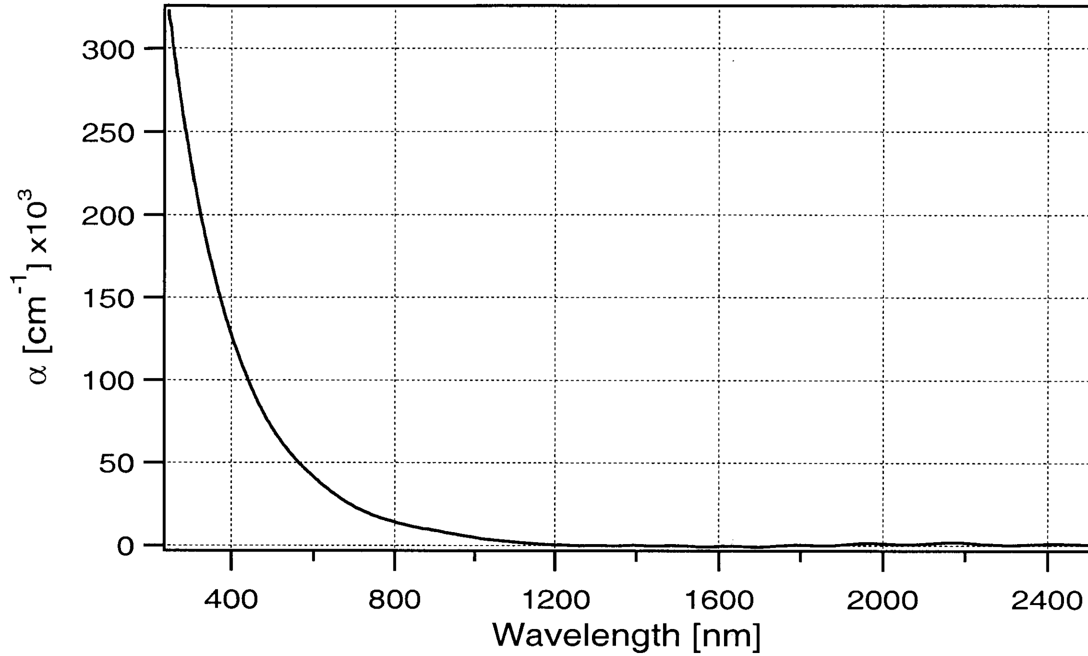

FIGURE 5-24: Absorption coefficient of an InAs-doped silica film on sapphire.

obtained from the TEM measurements. The InAs crystallite size was significantly smaller then the InAs exciton Bohr radius,

$$a_B = \frac{\varepsilon\hbar^2}{\mu e^2} \tag{5-11}$$

calculated to be ~320 Å. The measured correlation between the InAs nanocrystallite size and the blue shift of the absorption edge was also in good agreement with the data published for InAs nanoparticles produced by colloidal chemical synthesis [171].

The films had an appreciable absorption around 800 nm suggesting that they could potentially be used as saturable absorbers for a Ti:Al_2O_3 laser. The optical absorption edge was relatively smooth due to the broad nanoparticle size distribution. Unlike the experiments aimed at studies of the quantum confinement effects where a narrow particle size distribution is required, a broad size distribution is actually desired for saturable absorber applications because it allows a broader wavelength tuning range of the saturable absorber device.

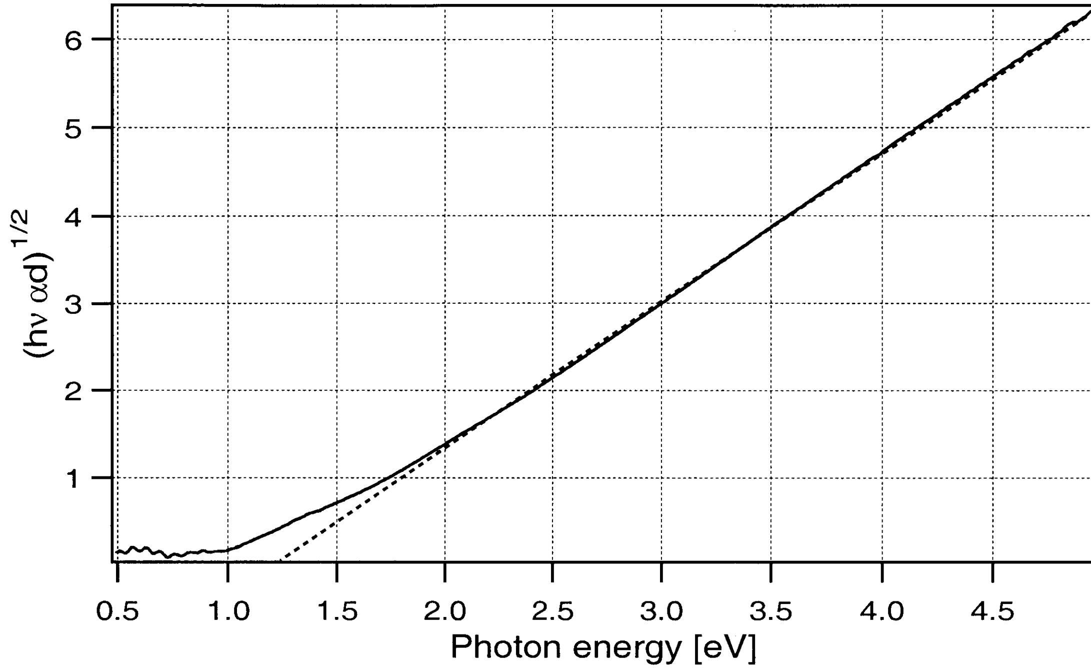

FIGURE 5-25: Tauc plot for the absorption coefficient of an InAs-doped silica film. At higher energies, $\sqrt{h\nu\alpha}$ linearly depends on photon energy. The intercept of the extrapolated linear part of the curve with the energy axis is the Tauc optical gap.

In a semiconductor quantum dot, the wavefunctions are localized rather than extended over the whole volume of the sample, as in bulk crystals. Due to the localization, the k-vector in quantum dots is no longer conserved. Assuming non-conservation of the k-vector, parabolic energy bands, and constant dipole matrix elements for the transition probabilities, the absorption coefficient α at higher energies can be shown to obey the relation [172]

$$\alpha h\nu \propto (h\nu - E_g^{opt})^2 \tag{5-12}$$

where E_g^{opt} is a Tauc optical band gap and $h\nu$ is the photon energy. The absorption coefficient is expected to deviate from the Tauc dependence (5-12) at the energies close to the band edge. The same energy dependence is predicted for the absorption coefficient of amorphous semiconductors where the wavefunctions are localized due to a long-range disorder. This energy dependence of

the absorption coefficient is quite different from the one expected for direct interband transitions in bulk semiconductors [173]:

$$\alpha \propto (h\nu - E_g)^{1/2} \tag{5-13}$$

Figure 5-25 shows that the absorption coefficient of sputtered InAs-doped silica films obeys the relation (5-12) at higher energies. The Tauc optical gap, determined by the intercept of the extrapolated linear part of $(h\nu\alpha d)^{1/2}$ with the energy axis, is approximately 1.2 eV.

Some of the fabricated films were subjected to rapid thermal annealing treatment at 500 - 750 °C in nitrogen at atmospheric pressure. After the anneal, the optical absorption of the films diminished because of a loss of semiconductor from the film due to diffusion and oxidation. For the films annealed at temperatures above 600 °C, a slight red shift of the absorption edge, owing to the increased crystallite size, could be observed (Figure 5-26). The shoulder in the absorption

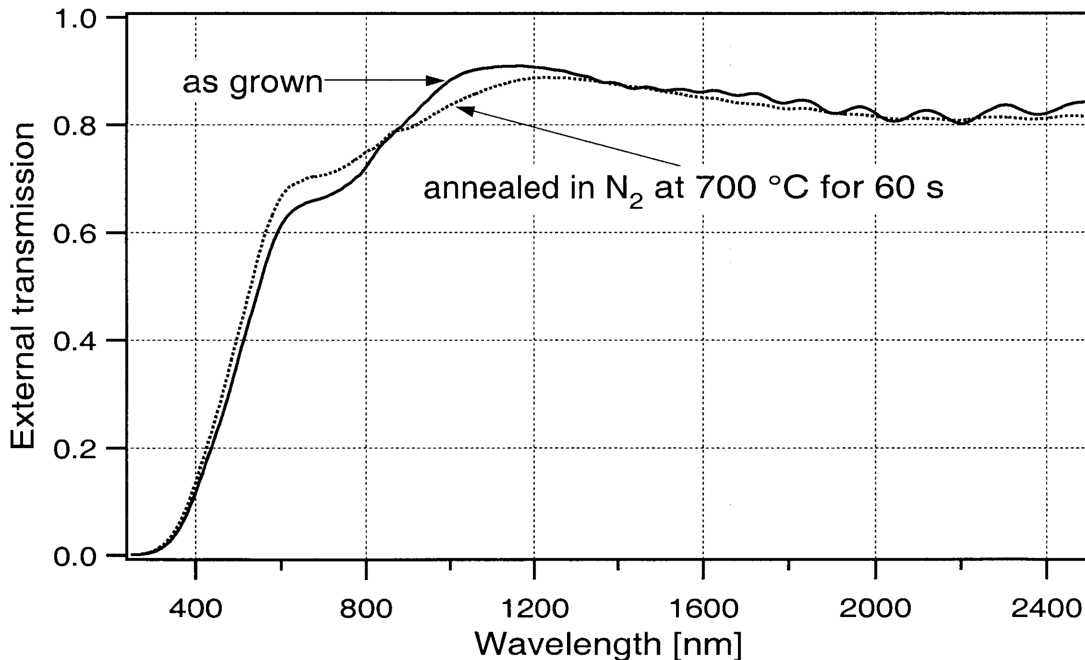

FIGURE 5-26: Optical absorption spectrum of InAs-doped silica films before and after RTA treatment. Film thickness ~ 2500 Å on a sapphire substrate.

spectrum around 800 nm as well as the slowly varying transmission from 1200 to 2500 nm result from interference in the film. Faster oscillations in the 2000 nm region are due to the birefringence in the sapphire substrate, and depend on the substrate orientation.

5.8 Nonlinear optical properties

In order to characterize the nonlinear absorption properties of the sputtered InAs-doped silica films, two sets of experiments were performed. Pump-probe measurements were used to investigate the absorption saturation dynamics on a femtosecond time scale. The absorption saturation fluence and the optical damage threshold were also obtained from single-beam absorption saturation measurements.

5.8.1 Pump-probe measurements

Femtosecond pump-probe measurements were performed in order to measure the absorption saturation dynamics of the films and characterize their saturable absorber performance. Semiconductor-nanoparticle-doped films are expected to have a fast absorption saturation recovery time owing to recombination centers on the surface of the nanocrystallites and a large surface-to-volume ratio for small particles. Fast absorption saturation recovery has been previously measured in $CdSe_xS_{1-x}$ and $CdSe_xTe_{1-x}$-doped glasses [121] and CdTe-doped thin silica films [152] but, to date, no studies have been performed on InAs-doped thin films.

The pump-probe experimental setup was similar to the one used for the measurements performed on the semiconductor-doped glasses described in Chapter 4. The pulses were generated by a home-built Kerr lens modelocked $Ti:Al_2O_3$ laser pumped by an Argon ion laser. The pump and probe were cross-polarized and the wavelength was fixed at 820 nm. Pulse durations of 30 fs at 80 MHz repetition rate were used in the experiment. The pump power was 130 mW and the pump spot size was measured to be 40 μm. The measurements were performed on several InAs-doped silica films on sapphire, both as-deposited and subjected to RTA at various temperatures.

For as-deposited films, the pump-probe signal did not fully recover between the subsequent pulses indicating the presence of a slow component with the decay time greater than the 10 ns (Figure 5-27). The long absorption saturation recovery time for unannealed films could be caused by the large density of long-lived defect states created during fabrication.

No photodarkening was observed for InAs-doped silica films.

Significant changes in the pump-probe traces were observed for the films subjected to RTA treatment in nitrogen, with faster relaxation dynamics for samples annealed at higher temperatures (Figure 5-27). Although the exact mechanism of the effect of RTA on the carrier dynamics

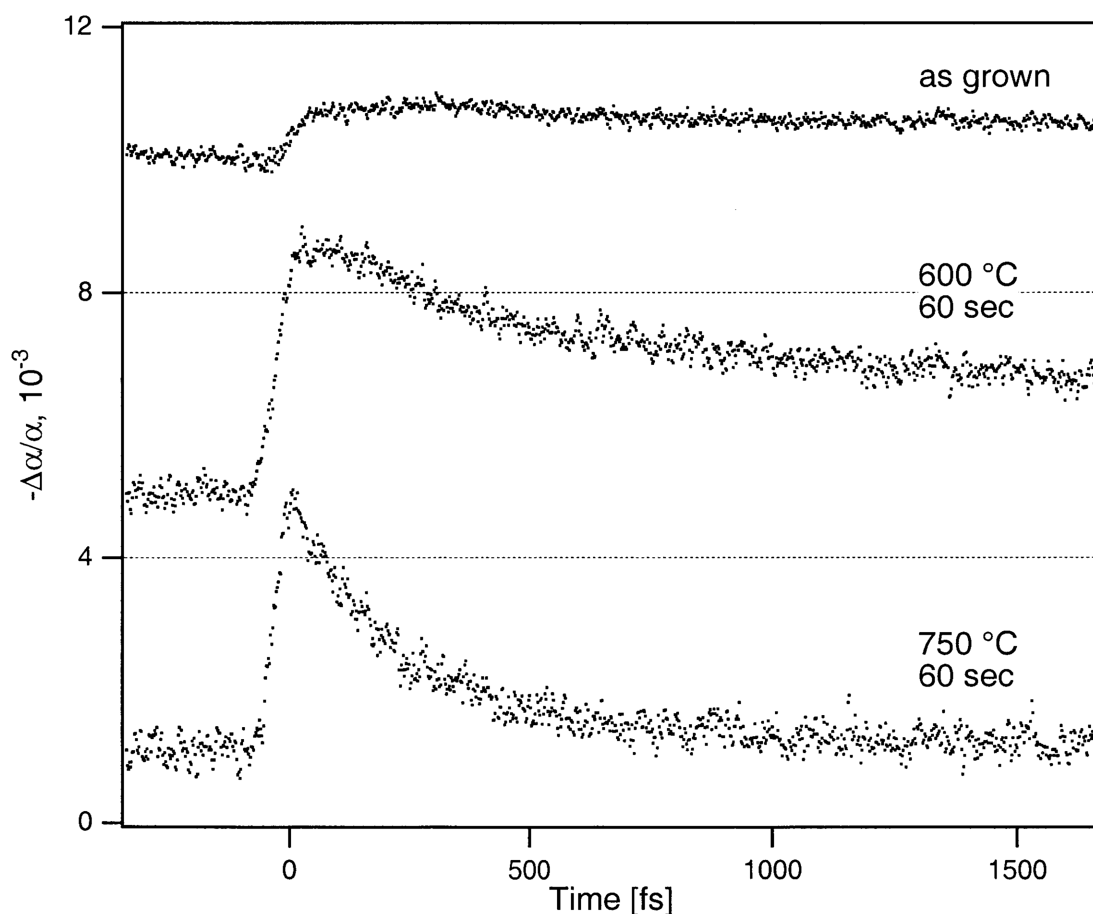

FIGURE 5-27: Absorption saturation dynamics of InAs-doped silica films before and after RTA treatment at different temperatures. Absorption recovery time becomes faster for films annealed at higher temperatures. The top two traces have been vertically displaced for clarity by $4\cdot10^{-3}$ and $8\cdot10^{-3}$.

has not yet been established, the decrease in the absorption recovery times could probably be attributed to the traps and recombination centers created on the surface of the InAs nanocrystallites during the RTA process. Rapid thermal annealing was also performed in argon and in forming gas (95% N_2 and 5% H_2) for a set of annealing temperatures from 500 to 750 °C. The films annealed in argon and forming gas exhibited the same absorption saturation dynamics as the films annealed in nitrogen, suggesting that the ambient gas does not play a significant role in the modification of carrier dynamics by RTA. While initially RTA was used in attempt to increase the InAs crystallite size within the film, it eventually provided an efficient way to control the absorption saturation dynamics of the films and allowed us to tailor the carrier relaxation dynamics for the saturable absorber applications.

The peak change in the absorption coefficient under identical experimental conditions was about a factor of 2 higher for the InAs-doped films annealed at 500 °C and higher than for as-deposited films, which indicates a factor of 2 decrease in the saturation fluence. Above 500 °C, the absorption saturation fluence was independent of the anneal temperature, while the recovery times decreased for higher anneal temperatures. The absorption saturation fluence of the annealed films measured in the pump-probe experiments and calculated according to equation (4-33) was ~ 25 mJ/cm^2. The same value was obtained in a single beam absorption saturation measurement (see below). A similarly high magnitude of the absorption saturation fluence was previously observed for $CdSe_xS_{1-x}$-doped glasses with strong quantum confinement [122].

Pump-probe measurements were also performed with pulses of various durations having different spectral bandwidths. Both the magnitude of absorption saturation and the absorption saturation dynamics were the same for ~50 fs and ~25 fs excitation pulses, with bandwidths of 14 nm and 30 nm respectively. This indicates that inhomogeneous broadening does not play an important role in the measured absorption saturation behavior of the films, consistent with the fast dephasing times (as short as ~ 5 fs) in small quantum dots at room temperature [130] [133] which lead to a broad homogeneous line width.

Several pump-probe traces were acquired for different pump powers in order to test the intensity scaling behavior of the absorption saturation signal (Figure 5-28). The pump-probe signal was directly proportional to the pump intensity, as expected for small changes in the absorption coefficient.

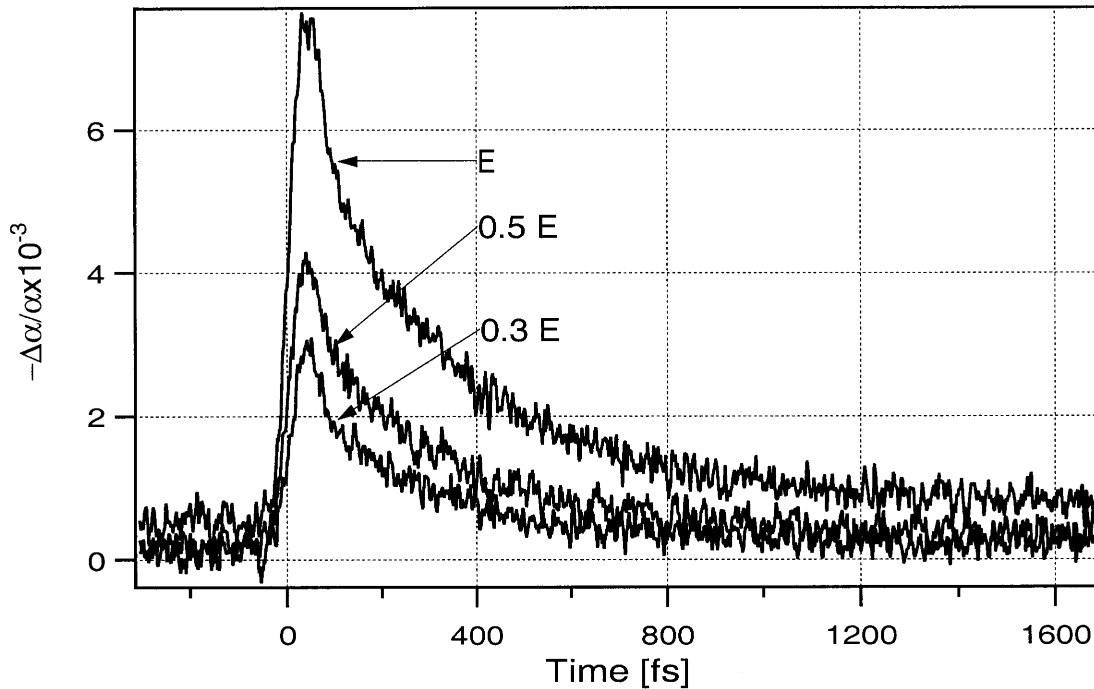

FIGURE 5-28: Absorption saturation dynamics of an InAs-doped silica film annealed in N_2 at 750 °C for 60 s for 3 different pump energy fluences. The absorption bleaching scales with pump fluence. The pump average power corresponding to the highest energy fluence was 140 mW at an 80 MHz repetition rate, the pump spot size was 40 μm.

5.8.2 Single-beam absorption saturation measurements

Another way to determine the absorption saturation fluence of the sample is to directly measure the sample transmission as a function of the incident fluence. The absorption saturation fluence can then be calculated.

Absorption saturation measurements on the InAs-doped silica films were performed using a single-beam setup depicted in Figure 5-29. Pulses were generated by a Spectra Physics Tsunami

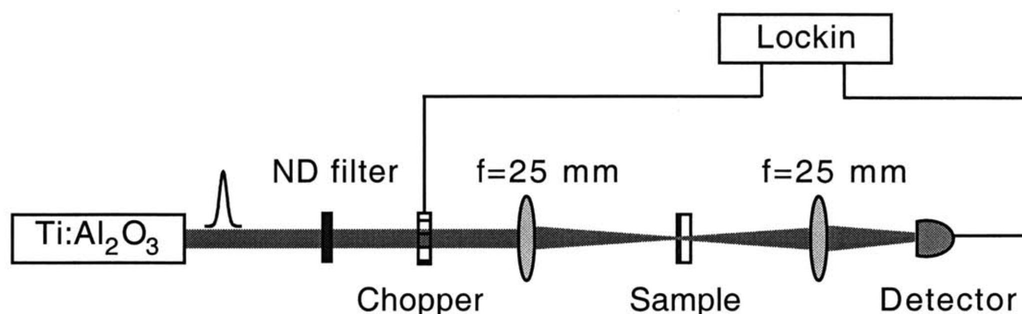

FIGURE 5-29: Schematic of the single-beam absorption saturation measurement setup.

Ti:Al_2O_3 laser pumped by an argon ion laser. The pulses were 100 fs long, with an 80 MHz repetition rate and a center wavelength of 810 nm. The laser power on the sample with no ND filters in the beam path was 1.85 W. The sample was a 2500-Å-thick InAs-doped silica film deposited on a sapphire substrate by rf sputtering. After the deposition, the film was subjected to an RTA treatment in nitrogen at 750 °C for 60 seconds. The film absorption at the laser wavelength was 21%. The laser beam was focused onto a sample using an f=25 mm lens. The beam spot size at the focus was measured to be 12 μm using a knife edge scan, corresponding to a Raleigh range of ~135 μm. The beam transmitted through the sample was then focused onto a detector. To increase the measurement sensitivity, a mechanical chopper was positioned in the beam path and the detector signal was acquired by a lockin amplifier.

Calibrated neutral density (ND) filters were used to vary the laser power incident on the crystal. However, the precision of the ND filter calibration was not sufficient to allow a sensitive measurement of the sample absorption as a function of intensity. Therefore, a different method was chosen to vary the laser intensity on the sample. For each value of the laser power, the sample transmission was measured for two sample positions, one at the focus, and one ~4 mm away from the focus, where the laser mode area was increased by a factor of several hundred. This way, the relative change in sample absorption for a given intensity and a small signal absorption could

be measured for each laser power, without relying on the exact knowledge of the ND filter absorption. Special care was taken to ensure that, after passing through the sample, the whole laser beam was focused onto the detector without clipping. This was done in order to avoid the signal dependence on the sample position due to self-focusing in the sample, an effect commonly used in a z-scan measurements of nonlinear refraction and absorption [174].

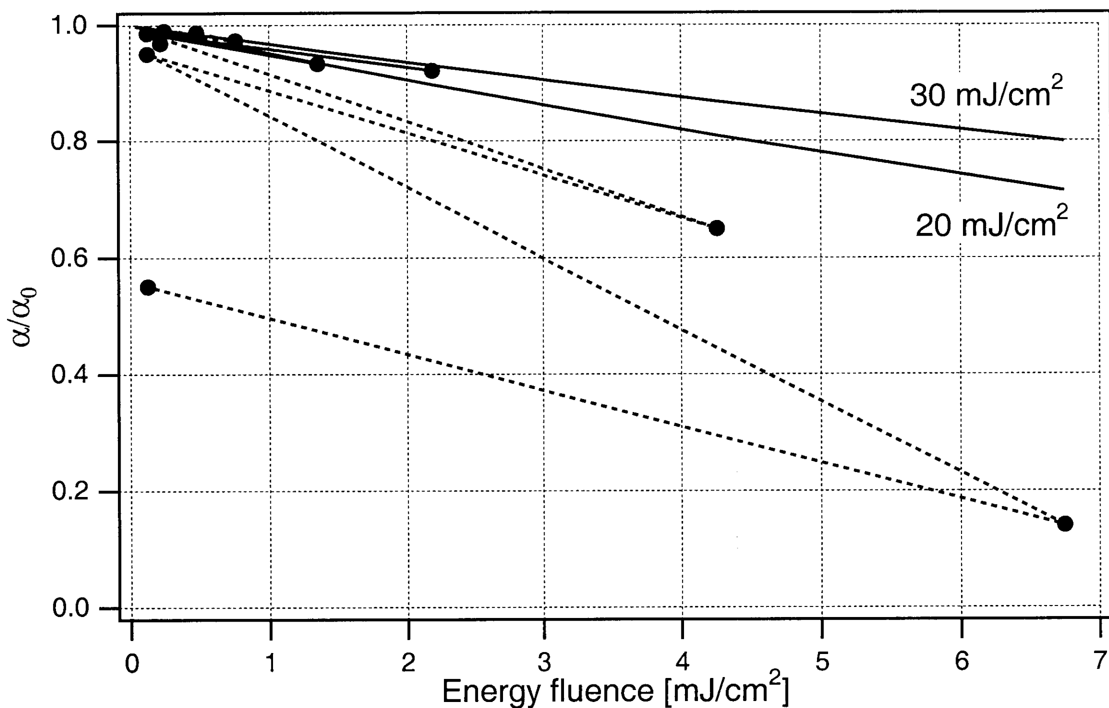

FIGURE 5-30: Single-beam absorption saturation measurement of InAs-doped silica film. The solid lines represent the theoretical fits for the absorption saturation fluences of 20 and 30 mJ/cm^2. The dashed lines show the sequence in which the experimental data points were acquired. The dashed lines do not return all the way to 1 due to the optical damage which occurs beyond ~ 3 mJ/cm^2.

The laser power incident on the crystal was gradually increased by decreasing the ND filter magnitude from 2.3 ND to 0.3 ND, bringing the power up to 0.93 W. For higher powers, the laser power was brought back down to $1.85 \cdot 10^{-2.3}$ W after each measurement, and then another mea-

surement was performed to ensure that the small signal absorption has not changed due to optical damage. The results of the measurements are shown in Figure 5-30. For low energy fluences, the measured absorption coefficient depends on the incident fluence as

$$\alpha = \alpha_0 \exp(-\Gamma/\Gamma_{sat}) \tag{5-14}$$

with the saturation fluence Γ_{sat} approximately 25 mJ/cm^2, in good agreement with the value obtained from the pump-probe measurements.

The data presented in Figure 5-30 indicates that, for incident fluences above ~3 mJ/cm^2, the absorption is decreased more rapidly than predicted by equation (5-14). Small signal absorption is also decreased indicating the onset of film damage by the laser radiation. Therefore, the damage threshold for the InAs-doped films on sapphire substrates was estimated to be ~1 mJ/cm^2 absorbed fluence at an 80 MHz repetition rate or ~100 kW/cm^2 average absorbed intensity.

The high absorption saturation fluence measured in InAs quantum dots (25 mJ/cm^2 compared to 1mJ/cm^2 in CdTe-doped RG-850 glass) can be attributed to the fast exciton dephasing time T_2. Generally, the dephasing time in quantum dots becomes faster with decreasing dot radius, increasing temperature, higher defect density, and with excitation higher above the bandgap [132] [130] [133]. Increasing temperature shortens the dephasing time due to phonon scattering. Smaller particle size leads to short dephasing times owing to scattering on the interface defects. Excitation higher above bandgap creates electron-hole pairs with greater momentum and thus decreases the time between the scattering events on defects. Similarly, a large number of defects in the material also leads to fast exciton dephasing. Dephasing times shorter than 5 fs have been reported for small CdSeS quantum dots at room temperature [130].

The sputtered InAs dots are expected to have a relatively large density of lattice structural defects owing to rf sputtering being a rough deposition method. The high defect density, combined with the room operating temperature and the nanocrystallite size small compared to the exciton Bohr radius, should lead to short dephasing times, on the order of 1 fs, and a broad homogeneous linewidth.

The absorption cross-section σ of a homogeneously broadened transition depends on the linewidth γ as [27] [26]

$$\sigma(\nu) \propto \frac{|d|^2}{\gamma} L(\nu - \nu_0, \gamma) \tag{5-15}$$

where d is the dipole matrix element of the transition and $L(\nu - \nu_0, \gamma)$ is a Lorentzian normalized to unity at the center frequency ν_0. For the laser pulse bandwidth narrower than the homogeneous absorption linewidth (30 fs pulses vs. ~1 fs dephasing time), the absorption cross-section at the laser wavelength decreases with increasing homogeneous linewidth, leading to an increasing absorption saturation fluence. Therefore, the high absorption saturation fluence of InAs-doped films can be explained by the fast exciton dephasing time in the InAs nanocrystallites owing to a small particle size, large defect density, and room operating temperature.

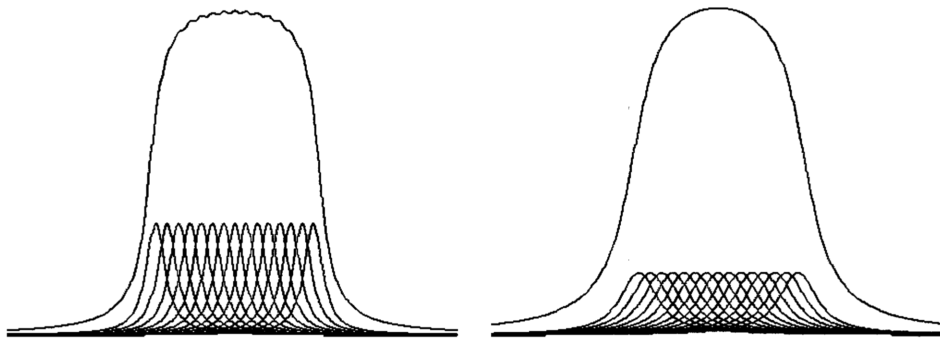

FIGURE 5-31: A schematic example of two inhomogeneously broadened spectra with homogeneous linewidths different by a factor of 2. The total absorption is approximately the same, but the nonlinearity is a factor of 2 higher for the spectrum with a narrower homogeneous linewidth.

The absorption coefficient of the films can still remain relatively high owing to inhomogeneous broadening of the absorption spectrum. The integrated absorption cross-section depends only on the *radiative* lifetime τ_{rad}, or the transition matrix element, and not on the linewidth [175]:

$$\int \sigma(\nu) d\nu = \frac{\lambda^2}{8\pi} \frac{1}{\tau_{rad}} \tag{5-16}$$

Therefore, for an inhomogeneously broadened spectrum, the total absorption at a given wavelength will not depend on the homogeneous broadening with the exception of the edges of the absorption spectrum (Figure 5-31).

The above hypothesis agrees with the observed decrease in the absorption saturation fluence in the films subjected to RTA above 400 °C. During RTA, the structural defects in the InAs dots are annealed out, the dephasing time becomes longer leading to a decrease in the saturation fluence. These results suggest that the saturation fluence can be decreased by fabricating the films with a lower defect density in the nanocrystallites.

5.9 Conclusions

In conclusion, an entirely new class of materials for saturable absorber applications was suggested, several novel materials were fabricated, and their properties were characterized. Semiconductor-doped dielectric films were fabricated by rf sputtering, and included the films of RG-850 CdSeTe-doped glass, GaSb-doped silica, and InAs-doped silica. GaSb-doped and InAs-doped silica films were fabricated for the first time.

GaSb-doped films and RG-850 films presented interesting materials systems for studies of confinement effects on the electronic band structure. However, because of the large blue shift of the optical absorption edge, from near-IR to the visible, these two films could not be used for near-IR laser modelocking. On the other hand, InAs-doped silica films proved to be the right choice of material for $Ti:Al_2O_3$ laser modelocking.

InAs-nanocrystallite-doped silica films were fabricated by rf sputtering and their optical and materials properties were comprehensively characterized. The fabricated films had good adhesion to various substrates, including glass, metals, and semiconductors. The films were stable and no changes in the film properties were observed over time. Using x-ray photoemission spectroscopy, the films were found to contain ~10% of InAs nanocrystallites. InAs nanoparticle size, measured by means of transmission electron microscopy, was found to be as large as ~80Å, with a broad nanoparticle size distribution. Scanning transmission electron microscopy, in conjunction with

energy dispersive x-ray spectroscopy, was used to obtain a compositional map of the films, demonstrating that In and As were concentrated in the same areas of the sample while O and Si were uniformly distributed. Electron diffraction demonstrated that the InAs nanoparticles maintained the zinc blende lattice structure of bulk InAs. The optical absorption edge was significantly blue shifted, to ~ 1 μm, from the bulk InAs absorption edge of 3.5 μm, due to confinement effects. The absorption saturation dynamics of the films were investigated using femtosecond pump-probe measurements. Significant changes in the carrier dynamics were observed for the films subjected to rapid thermal annealing treatment, with faster absorption recovery dynamics for higher annealing temperatures. RTA was demonstrated as a simple and effective approach for tailoring the saturable absorber properties of the films. Overall, the InAs-doped silica films possessed all the necessary characteristics for the saturable absorber applications.

The approach presented in this Chapter can be applied to develop novel semiconductor-doped films using various semiconductor dopants and various host materials (such as for example sapphire). In addition to rf sputtering, other non-epitaxial deposition techniques, such as laser ablation or rf magnetron sputtering, can also be used for film fabrication. Rf magnetron sputtering should provide significantly faster deposition rates and in addition should allow better control over the nanocrystallite size distribution.

In contrast to semiconductor quantum well materials grown by molecular beam or chemical beam epitaxy, nonepitaxial saturable absorbers permit the deposition of a wider range of materials and allow greater freedom in design. In addition, materials deposited by nonepitaxial techniques such as sputtering, laser ablation, or evaporation, have significantly lower cost than epitaxially grown materials. Finally, these materials may be integrated with standard thin film optical coatings to create nonlinear saturable absorber mirrors and other devices. These features make nonepitaxially-grown semiconductor films a promising materials system for laser mode-locking and other nonlinear optical applications.

Chapter 6

Application of InAs-doped films to modelocking initiation in a $Ti:Al_2O_3$ laser

6.1 Introduction

The preceding Chapter described the fabrication of semiconductor-doped thin films and the characterization of their structural and optical properties. The properties of the sputtered films were examined from a standpoint of saturable absorber applications and InAs-doped silica films were found to possess the right combination of characteristics to be used for near-IR laser modelocking. The next logical step is to demonstrate that this newly developed saturable absorber materials system can be utilized to modelock a realistic solid-state laser. $Ti:Al_2O_3$ was chosen as a laser system for the first practical modelocking application of InAs-doped saturable absorbers because of the overlap of its tuning range with the optical absorption region of the films, the relatively high laser gain, and the fact that $Ti:Al_2O_3$ is probably the most widely used solid-state laser for femtosecond pulse generation at this time.

This Chapter is organized as follows. The design of InAs-doped-silica transmitting geometry saturable absorber devices for $Ti:Al_2O_3$ modelocking is presented in Section 6.2. Section 6.3 describes the $Ti:Al_2O_3$ laser cavity design. Section 6.4 describes the results obtained with self-starting modelocked operation of a $Ti:Al_2O_3$ laser using InAs-doped silica films for Kerr lens modelocking initiation. The operating bandwidth of the saturable absorber and the achieved wavelength tuning range of the modelocked laser operation are presented in Section 6.5. Section 6.6 discusses self-starting saturable-absorber-assisted KLM for various values of intracavity dis-

persion. The modelocked pulse train instabilities for high pump and output powers are described and their origins are discussed in Section 6.7. Section 6.8 focuses on the operation of a $Ti:Al_2O_3$ laser with an intracavity InAs-doped absorber without taking advantage of KLM action. The ideas for saturable absorber mirror design using InAs-doped films and the first fabrication results are presented in Section 6.9. Section 6.10 summarizes the results.

6.2 Transmissive saturable absorber devices

Having characterized the linear and nonlinear optical properties of the InAs-doped silica films, we designed saturable-absorber devices for $Ti:Al_2O_3$ laser modelocking. For the laser modelocking experiments, 300-Å-thick InAs-doped films were deposited upon 3-mm-thick sapphire substrates. The film thickness was chosen to provide ~ 2% absorption at 800 nm, which was expected to be center operation wavelength of the laser.

Sapphire was chosen as a substrate material because of its good thermal conductivity, 24 W/m·K for sapphire vs. 1.4 W/m·K for fused silica [176], and high transmission near 800 nm. Sapphire is a birefringent material, with ordinary and extraordinary refractive indices n_o=1.760 and n_e=1.752 at 800 nm. In order to avoid birefringence effects in the sapphire substrate, 0°-oriented sapphire was used, with an optic axis parallel to the surface normal.

In order to modify the absorption saturation dynamics of the sputtered films, the films were subjected to an RTA treatment in dry nitrogen at atmospheric pressure at temperatures ranging from 500 to 750 °C for 60 seconds.

6.3 Laser cavity design

The laser used for the modelocking experiments was a $Ti:Al_2O_3$ laser pumped by an Ar-ion laser. The laser cavity, shown in Figure 6-1, consisted of a standard z-cavity with 10-cm radius-of-curvature (ROC) folding mirrors CM1 and an additional focusing fold consisting of 5- and 7.5-cm ROC mirrors, CM 3 and CM2. The separation between mirrors CM2 and CM3 was approxi-

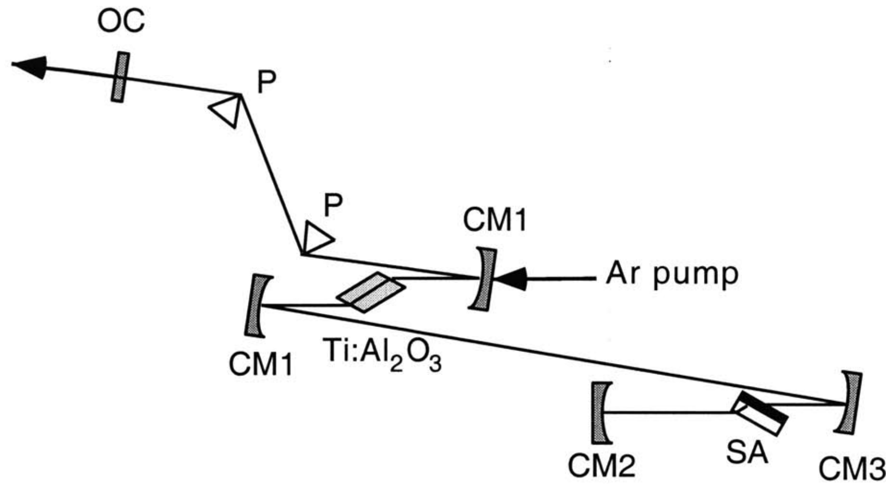

FIGURE 6-1: Schematic diagram of the Ti:Al_2O_3 laser cavity. OC, output coupler; SA, saturable absorber; CM1, 10-cm ROC mirrors; CM2, 7.5-cm ROC mirror; CM3, 5-cm ROC mirror; P, fused silica prisms.

mately 10 cm, to make the ABCD matrix of the additional fold unity. The Ti:Al_2O_3 laser crystal was 4.5 mm long with pump absorption of 80%. The InAs-doped saturable absorber film on sapphire (or a blank sapphire substrate used for test purposes) was positioned at Brewster's angle in the focus of the additional resonator fold. The optical loss introduced by the saturable absorber was ~2% per pass. The laser mode FWHM on the saturable absorber was estimated to be 25 μm. The tight focusing was necessary because of the high absorption saturation fluence of the InAs-doped films. The incidence angle on the curved mirror CM3 was set to ~13° in order compensate for the astigmatism introduced by the 3-mm-thick sapphire substrate, according to the formula [146]:

$$f\left(\frac{1}{\cos\theta} - \cos\theta\right) = d\frac{\sqrt{1+n^2}}{n^2}\left(1 - \frac{1}{n^2}\right) \qquad (6\text{-}1)$$

where f is the mirror focal length equal to 2.5 cm, and d and n are, respectively, the thickness and the refractive index of the sapphire substrate. Dispersion compensation was provided by a pair of fused-silica prisms with a 76-cm separation. A 2% output coupler with a 30-minute wedge was positioned in the prism arm of the cavity. An additional extracavity fused-silica prism pair was used to eliminate the spatial wavelength dispersion in the output beam. It also compensated for

the group velocity dispersion due the output coupler material, and precompensated the GDD for the autocorrelation measurement.

6.4 Self-starting modelocking operation using InAs-doped films for KLM initiation

With a blank sapphire substrate in the additional cavity fold, the laser resonator was optimized for KLM operation. Without a saturable absorber, modelocking was not self-starting. When an InAs-doped saturable absorber was positioned at the focus of the additional resonator fold, stable self-starting modelocking operation was obtained. Modelocking was initiated by an InAs-doped absorber, and KLM acted as a final pulse shortening and pulse stabilization mechanism. The stability region for KLM modelocking (measured in terms of the separation of the folding mirrors around the crystal) was increased, and the cavity alignment was less critical, when the saturable absorber was used to initiate modelocking. The repetition rate of the laser was approximately 80 MHz.

The cw lasing threshold with the saturable absorber in the cavity was 3.0 W of pump power incident upon the laser crystal. The threshold for modelocking operation was 4.0 W of pump power with an output power of 30 mW. However, at this level of pump power, modelocking was not self-starting and was initiated by shaking one of the intracavity prisms. The threshold for self-starting modelocking operation was 5.0 W of incident pump power with an output power of 50 mW. The maximum obtained output power was 100 mW for a pump power of 7.0 W. The dependence of the laser output power on the pump power is shown in Figure 6-2. Self-starting was optimized when the saturable absorber was positioned within ~1 mm from the focus of the resonator fold. The modelocking build up time was relatively slow, on the order of 50 ms.

The laser pulse duration was measured by collinear autocorrelation using a wedged KTP crystal with thickness varying from ~20 to ~ 150 μm. The shortest pulse duration obtained for self-starting saturable-absorber-assisted KLM operation was 25 fs assuming a $sech^2$ pulse shape. The autocorrelation trace is shown in Figure 6-3 and the corresponding pulse spectrum in Figure 6-4. The FWHM bandwidth of the pulse spectrum was 53 nm and the time-bandwidth product

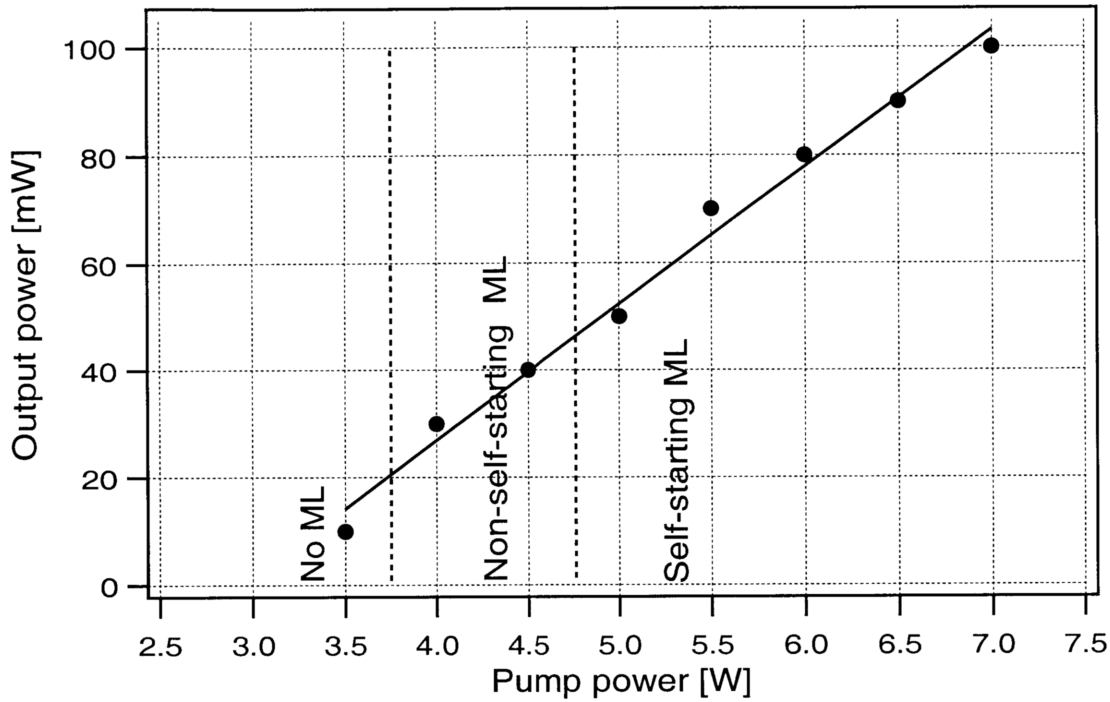

FIGURE 6-2: $Ti:Al_2O_3$ laser output power as a function of the incident pump power. Modelocking threshold was 4.0 W and self-starting modelocking threshold was 5.0 W.

$\Delta\tau\Delta\nu \approx 0.59$, greater than the transform limit for a sech^2 pulse $\Delta\tau\Delta\nu = 0.315$. The pulses are believed to be non-transform-limited because of the excess self-phase modulation introduced by the saturable-absorber substrate.

The average intensity *absorbed* by the InAs-doped films on sapphire during normal modelocked laser operation was ~ 30 kW/cm^2, well below the measured damage threshold of 100 kW/cm^2 absorbed average intensity. In contrast, InAs-doped films deposited upon fused silica substrates had relatively poor thermal properties and could not withstand the high intracavity laser intensities without damage.

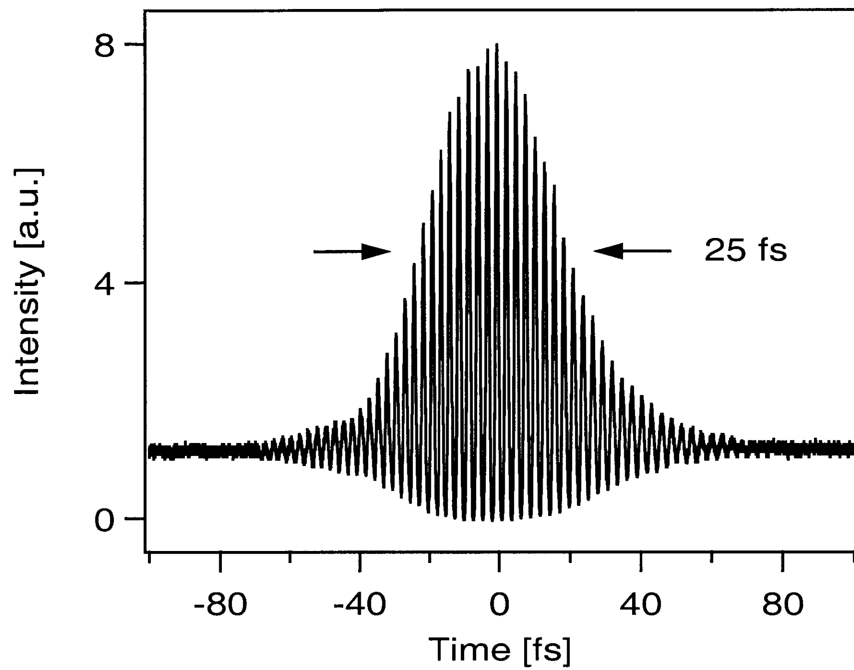

FIGURE 6-3: Interferometric autocorrelation of self-starting saturable-absorber-assisted KLM pulses. The pulse duration is 25 fs assuming a sech^2 pulse shape.

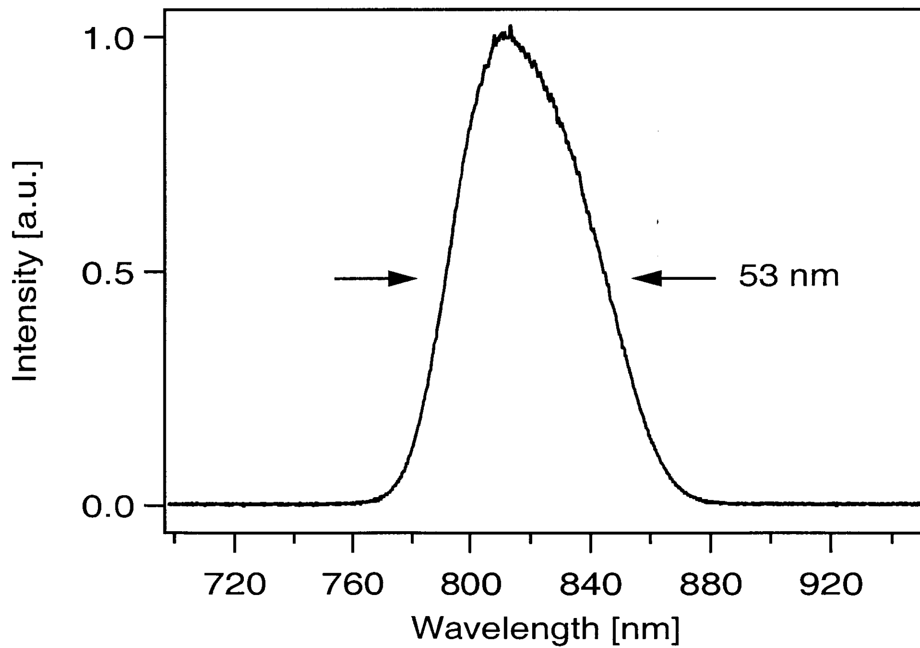

FIGURE 6-4: Spectrum of self-starting 25 fs pulses corresponding to the autocorrelation in Figure 6-3.

6.5 Wavelength tuning

Many applications of femtosecond lasers, such as for example ultrafast time-resolved laser spectroscopy, require a broad wavelength tunability of the modelocked laser output. An ideal saturable absorber should be able to support modelocked laser operation throughout the whole laser tuning range.

As seen from the previous Chapter, the InAs-doped films were found to have a smooth absorption edge owing to a broad size distribution of the semiconductor nanocrystallites. Such films should have a broad wavelength operation range and should allow to obtain modelocking initiation over the whole Ti:Al_2O_3 laser tuning range.

By use of a knife edge in the prism arm of the resonator, the lasing wavelength was tunable from 800 to 880 nm while sustaining self-starting modelocking operation. The normalized pulse spectra of modelocked pulses are shown in Figure 6-5. The tuning range was limited by the bandwidths of the resonator mirrors.

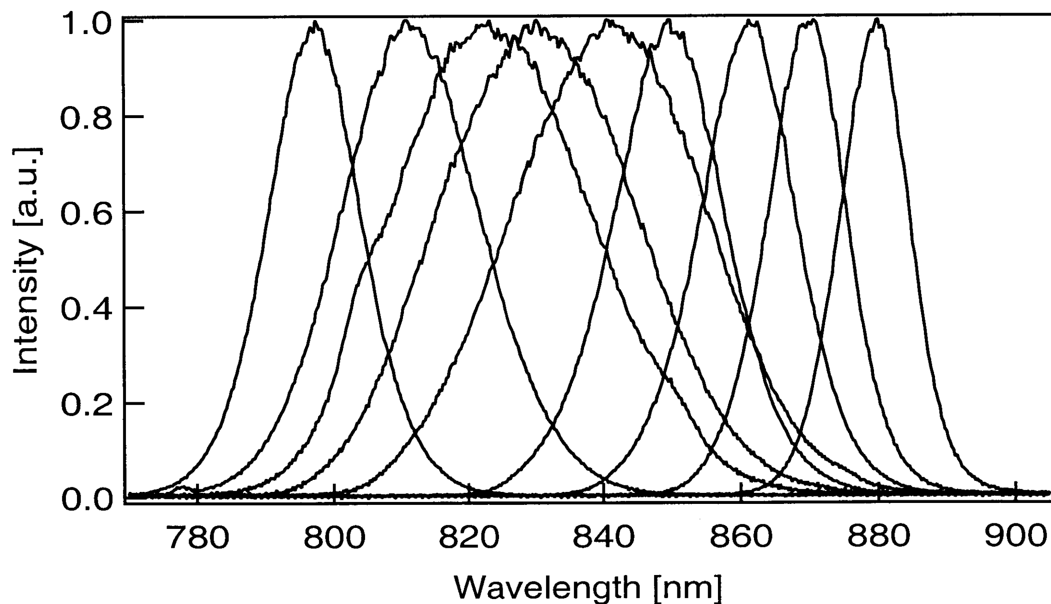

FIGURE 6-5: Normalized pulse spectra of modelocked pulses. The center wavelength could be tuned over 80 nm while sustaining self-starting modelocking operation.

6.6 Self-starting operation for various intracavity dispersions

Self-starting modelocked operation of a $Ti:Al_2O_3$ laser using InAs-doped films for KLM initiation was obtained for various intracavity group delay dispersions, both negative and positive. Figure 6-6 and Figure 6-7 show a non-collinear autocorrelation and spectrum of 2.8-ps-long pulses obtained in the positive dispersion regime. The measured spectrum has steep edges, typi-

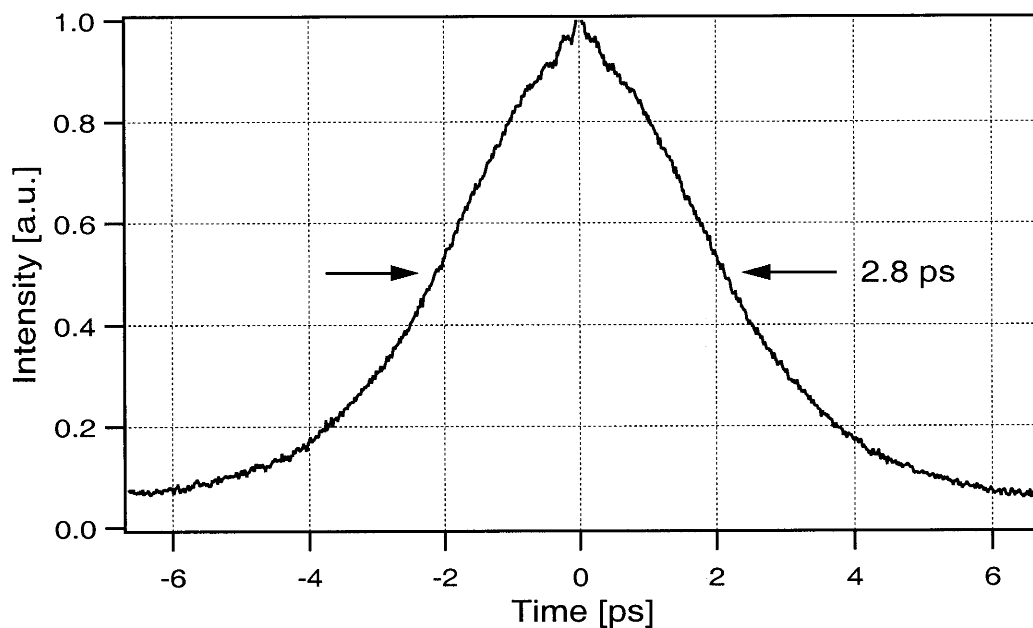

FIGURE 6-6: Non-collinear autocorrelation of self-starting saturable-absorber-assisted KLM $Ti:Al_2O_3$ laser output with positive intracavity GDD.

cal for the positive intracavity dispersion. The pulse duration is long, and the time-bandwidth product is 15.4, much greater than the transform limit of 0.315 for $sech^2$ pulses. As predicted by the modelocking master equation, negative dispersion is required to produce short transform limited pulses [33].

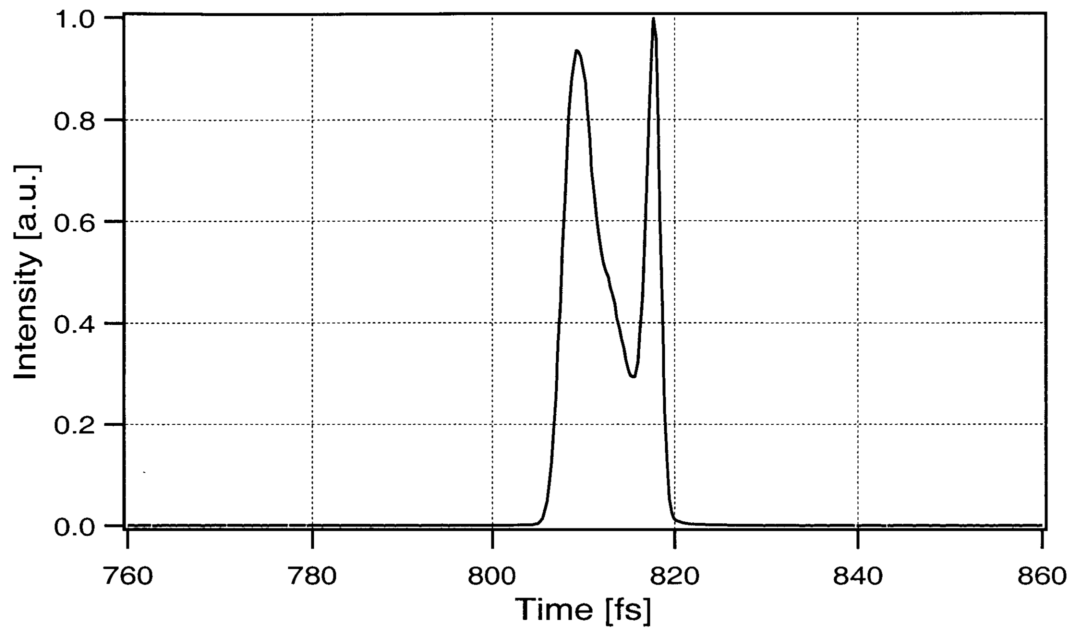

FIGURE 6-7: Spectrum of self-starting saturable-absorber-assisted KLM $Ti{:}Al_2O_3$ laser output with positive intracavity GDD.

The resonator dispersion was continuously varied by changing the intracavity prism insertion (the prism glass path length). Using an InAs-doped film for KLM initiation, self-starting modelocked operation was obtained for a set of negative and positive intracavity dispersions with the exception of the near-zero-GDD point. The modelocked pulse spectra were acquired for intracavity dispersion values separated by ~ 50 fs^2 per spectrum. The normalized spectra are shown in Figure 6-8.

6.7 Pulse instabilities for high pump powers

Stable self-starting modelocking using InAs-doped films for KLM initiation was described in the previous Section. The laser output was a train of pulses with a repetition rate equal to the laser cavity round trip time. However, for high pump powers, of 7.0 W and higher, multiple pulsing instabilities, caused by the high self-phase modulation in the sapphire substrate positioned at the focus of the saturable absorber cavity fold, were often observed in the modelocked pulse train. A typical double-pulse autocorrelation and spectrum are shown in Figure 6-9 and Figure 6-10.

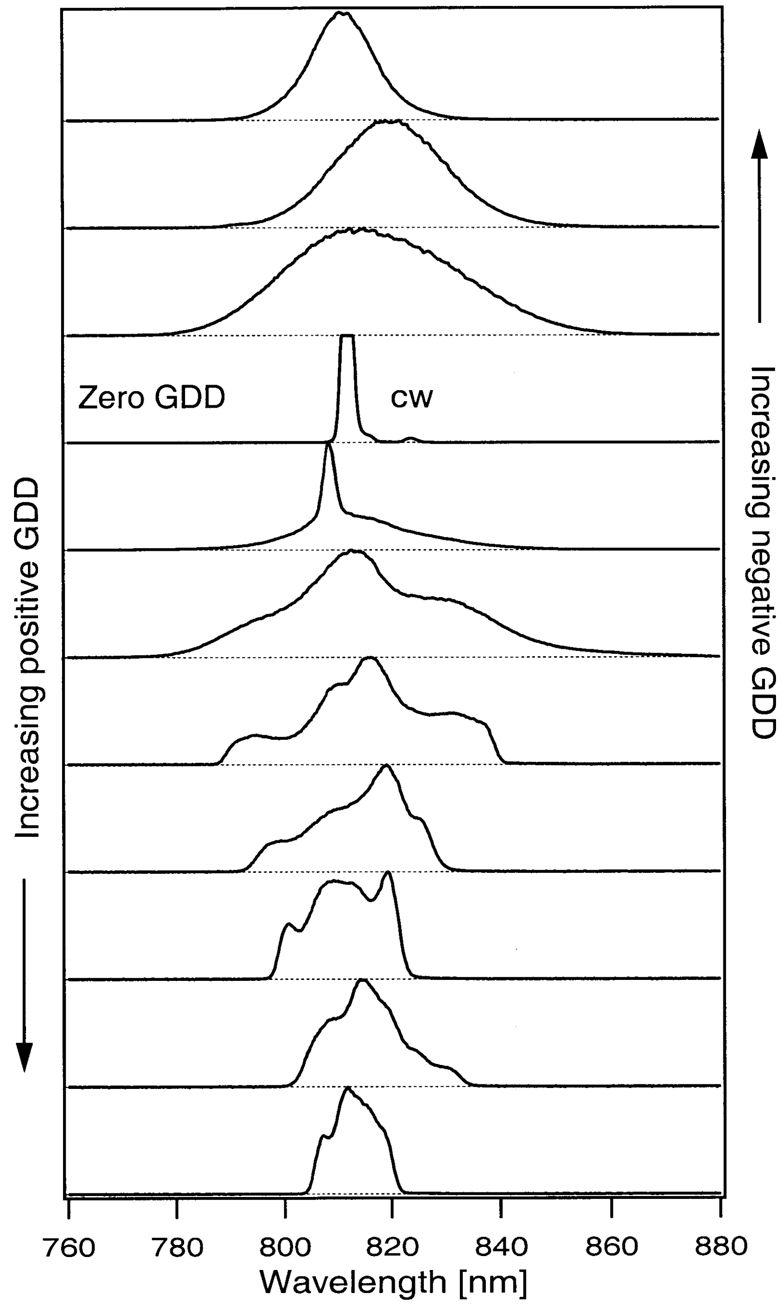

FIGURE 6-8: Normalized pulse spectra of self-starting modelocked pulses for various intracavity dispersions. Modelocking could not be obtained around zero-dispersion point. The relative change in the net intracavity GDD between the adjacent spectra is on the order of 50 fs^2.

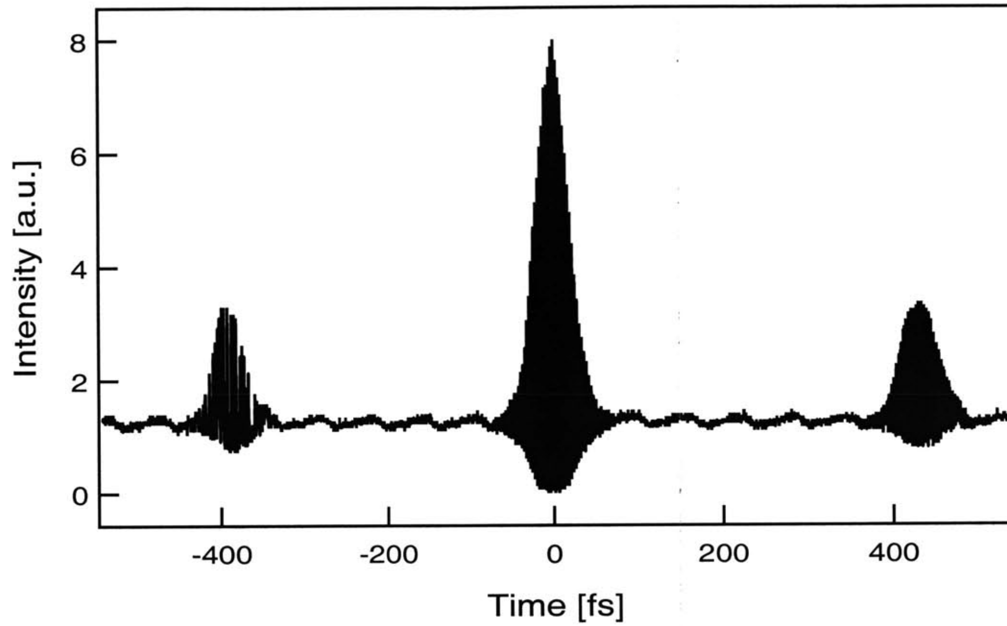

FIGURE 6-9: Collinear interferometric autocorrelation of a laser output in a double-pulse operation mode.

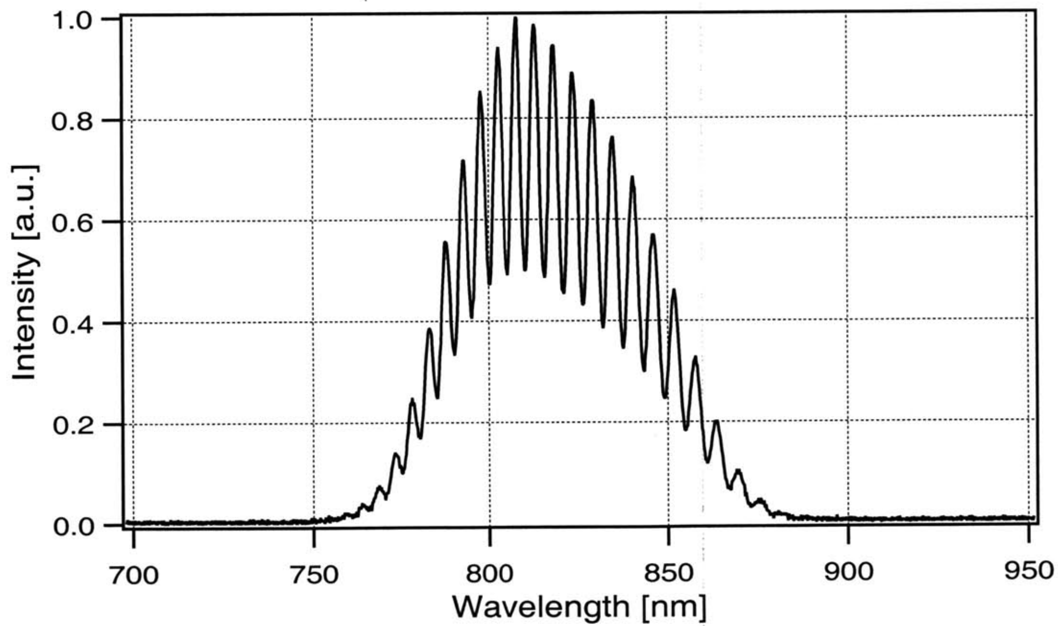

FIGURE 6-10: Spectrum of a laser output in a double-pulse operation mode corresponding to autocorrelation in Figure 6-9.

To explain the laser behavior in the double pulse regime, recall that the width of a $sech^2(t/\tau)$ laser pulse due to soliton pulse shaping stabilized by a saturable absorber is determined by the interplay of self-phase modulation and group delay dispersion and is given by [60] [177]:

$$\tau = \frac{4|D|}{\delta E_p} \tag{6-2}$$

where τ is related to the pulse duration ($\tau = \tau_{FWHM}/1.76$), D is the intracavity group delay dispersion, E_p is the pulse energy, and

$$\delta = \frac{2\pi n_2}{\lambda_0 A_{eff}} l \tag{6-3}$$

is the self-phase modulation (SPM) coefficient, with λ_0 the center wavelength, A_{eff} the laser mode spot size in the nonlinear medium, n_2 and l the nonlinear refractive index and the length of the medium. However, the pulse will only be stable if the saturable absorber modulation depth is strong enough to overcome the pulse losses in the gain medium due to a finite gain bandwidth and the following condition is satisfied [60] [177]:

$$\frac{D_g}{\tau^2} < 2q_0 \tag{6-4}$$

where $D_g = g/\Omega_g^2$ is the laser gain dispersion, g is the saturated gain, Ω_g is the laser gain bandwidth, and q_0 is the saturable absorber modulation depth per round trip. If the condition (6-4) is not satisfied, instabilities will occur, including multiple pulsing and a longer background pulse formation. The observed double-pulsing of the $Ti:Al_2O_3$ laser for high pump powers may be explained using the following argument. First of all, the SPM coefficient is already high owing to a sapphire substrate in a focus of the saturable absorber fold with tight focusing. The high SPM coefficient leads to a short soliton-supported pulse according to equation (6-2), which in turn requires a large saturable absorber modulation depth for stability (equation (6-4)). When the pump power and the laser output power are increased, the pulse duration determined by ideation (6-2) gets shorter, increasing the left-hand-side of inequality (6-4). The KLM saturable absorber action, however, eventually saturates (the self-focusing-induced decrease in the laser mode spot size no longer leads to an increase in gain), so that the condition (6-4) is no longer fulfilled. The

pulse becomes unstable. At this point, the pulse can break up into two pulses, with smaller energy and longer duration (see eq. (6-2)), and the stability condition is then satisfied for a double-pulse laser output [62].

The observed irregular shape of the modelocked spectrum is due to the interference of the phase-locked spectra of the two pulses. The effects that govern the separation of the two pulses are not yet well understood. It should be stressed, that for lower pump powers, stable single-pulse self-starting modelocked operation could be always obtained.

6.8 Saturable absorber operation without KLM

It was demonstrated above that the InAs-doped silica films can be used for KLM initiation in a $Ti:Al_2O_3$ laser. Self-starting saturable-absorber-assisted KLM was obtained. Another important step would be show that such films could modelock the laser without KLM action. Although the pulse duration may not be as short without KLM, the laser cavity design would be greatly simplified by relaxing the strict design constraints associated with KLM. For a number of applications, the simplicity of the laser design is more important than the ultrashort pulse width.

The laser cavity in Figure 6-1 was modified by changing the positions of the curved mirrors CM1 around the laser crystal, so that no KLM action was present and the saturable absorber action was due solely to the InAs-doped film. It was found that stable single-pulse modelocked operation could not be obtained in this regime because of the small saturable absorber modulation depth. For an output power of 100 mW, the fluence that was incident upon the saturable absorber intracavity was estimated to be 8 mJ/cm^2. This was approximately 1/3 of the saturation fluence measured by the pump-probe and absorption saturation experiments. For a small-signal absorption of 2% per pass and no unsaturable loss, the corresponding modulation depth is 0.5%. Although self-starting saturable-absorber-assisted KLM could be obtained, the modulation depth provided by the saturable absorber was not sufficient for pure saturable-absorber modelocking without KLM. The autocorrelation of the laser output is shown in Figure 6-11 and spectrum in Figure 6-12. The spectrometer resolution was ~ 1.5 nm and no features could be resolved in the spectrum.

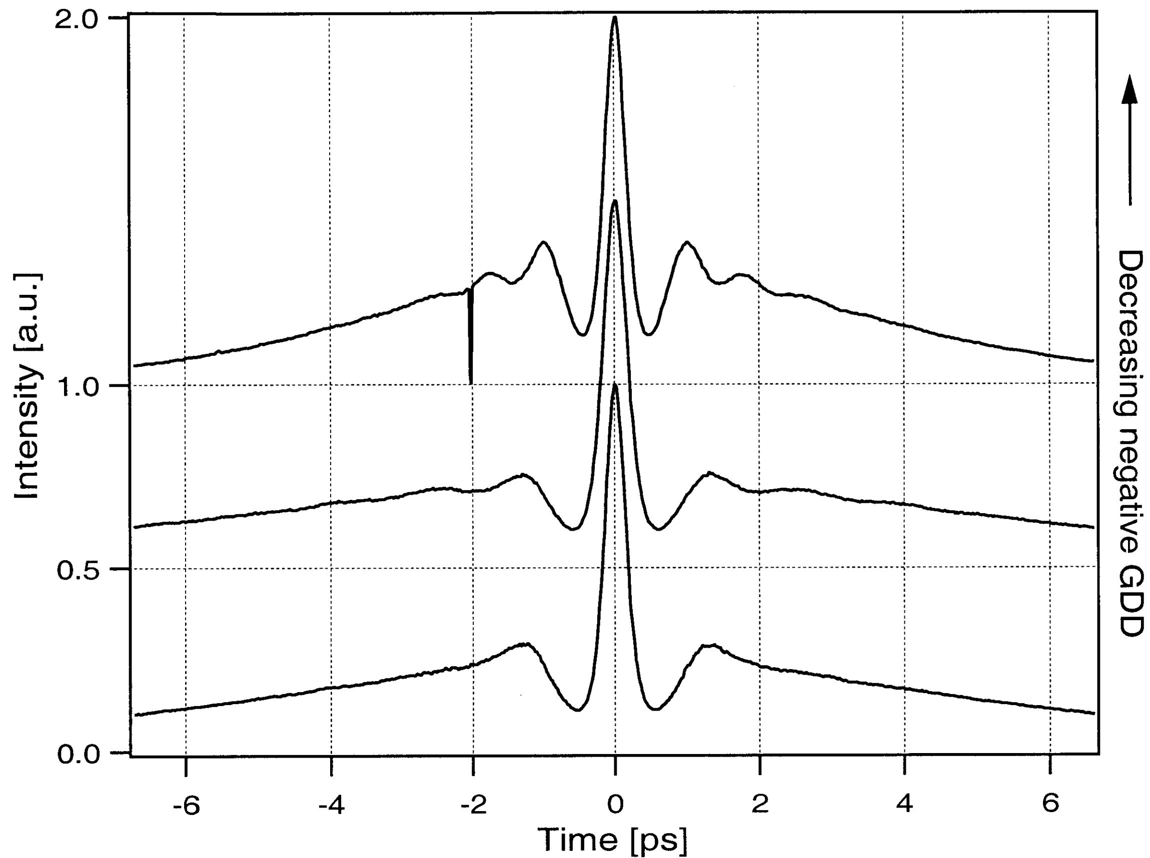

FIGURE 6-11: Non-collinear autocorrelation traces of a Ti:Al_2O_3 laser output using only an InAs-doped film for modelocking, without KLM, for three intracavity group delay dispersions. The laser output consisted of a short pulse and a longer background pulse.

The observed autocorrelation measurement corresponds to a laser output consisting of a short pulse and a longer background pulse [178]. The short laser pulse travelling around the laser cavity sheds energy and a longer background pulse appears. The effect can be explained based on equations (6-2) and (6-4) which define the pulse duration and the stability condition. For a given pulse energy, dispersion, and self-phase modulation, the pulse width is fixed. However, the weak saturable absorber action cannot support such a short pulse and instability develops. The short pulse sheds energy to a cw component and is gradually attenuated. The cw component develops into a longer background pulse with a duration determined by the saturable absorber recovery time, without soliton pulse shaping. The energy of the shorter pulse is decreased and its duration

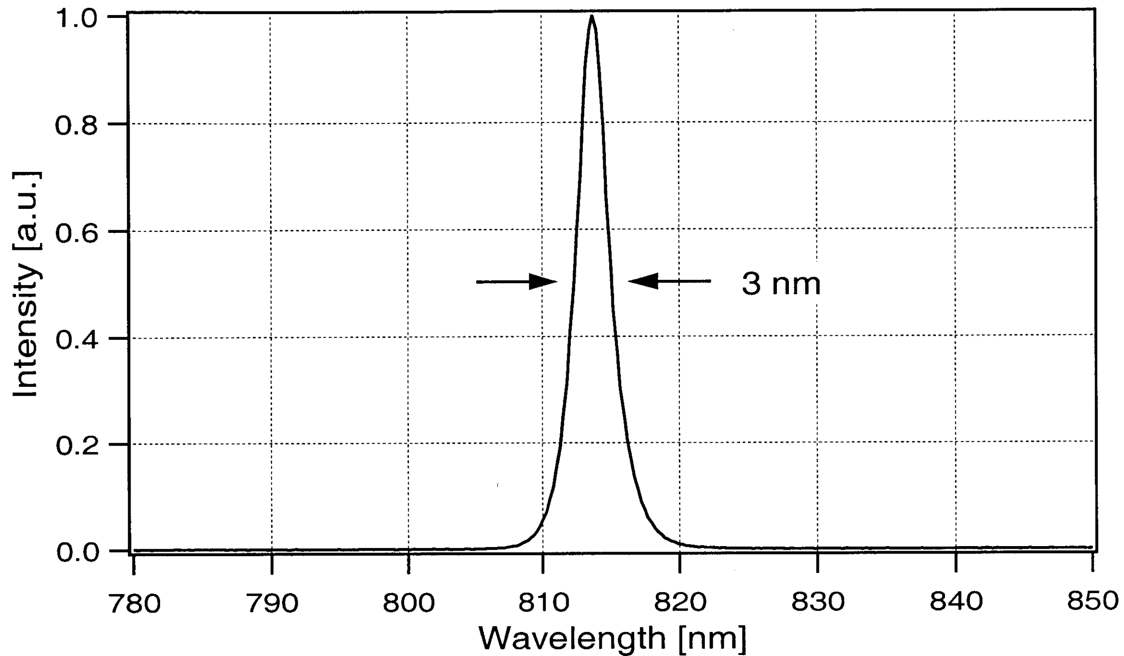

FIGURE 6-12: Spectrum of a Ti:Al_2O_3 laser output using only an InAs-doped film for modelocking, without KLM.

is increased until the stability condition (6-4) is satisfied and the two pulses create a stable system. The positions of the oscillations in the autocorrelation signal and their dependence on the net intracavity GDD remain to be explained.

The difference from the double-pulsing instability in the saturable-absorber-assisted KLM regime, when the two pulses of approximately equal duration are formed, is due to the different saturable absorber recovery dynamics in the two cases. For saturable-absorber-assisted KLM, the dominant saturable absorber mechanism for short pulses is KLM, with an essentially instantaneous temporal response. In contrast, for saturable absorber modelocking without KLM, the saturable absorber has a longer recovery time and a temporal gain window exists behind the pulse.

Equations (6-2) and (6-4) suggest that in order to obtain stable single-pulse modelocked operation with InAs-doped thin film sole responsible for the saturable absorber action, higher intracavity negative group velocity dispersion is required. Although the pulse width would then be longer, the stability condition would be satisfied for a higher GDD. For the experimental laser cavity parameters, the shortest pulse duration is estimated from the stability condition to be ~ 300

fs, and the net intracavity GDD ~ -3000 fs^2. To obtain such a net GDD with a fused silica prism pair used intracavity, the prism separation would have to be increased by ~ 1.5 meters in addition to the current separation of 76 cm, making the cavity unrealistically long. The solution may be to use a prism pair made of a more dispersive glass, e.g. SF-10, which would allow to obtain higher net GDD with smaller prism separation. Fabricating saturable absorber films with a lower absorption saturation fluence should also allow laser modelocking without the use of KLM.

6.9 Design of reflective saturable absorber devices

A major advantage of saturable absorber films deposited by rf sputtering is that they can be deposited upon a variety of substrates, including metals and dielectrics, in contrast to epitaxially-grown semiconductor quantum wells which require lattice-matching for defect-free fabrication. Because of this freedom in substrate choice for sputtered films, it should be possible to incorporate them into metal or dielectric saturable absorber mirrors which have broader bandwidth, superior dispersion properties, and in addition are much easier to fabricate than the quantum-well-based epitaxially-grown structures.

The preceding Sections of this Chapter described KLM initiation in a $Ti:Al_2O_3$ laser using InAs-doped films in the transmission device geometry. Stable self-starting modelocked operation was achieved using the films for KLM initiation. It was shown that the excess self-phase modulation in the sapphire substrate could act as a pulse width limiting factor and led to generation of non-transform-limited pulses. In addition, the dispersion of the sapphire substrate had to be compensated and would in a general case make compensation of higher order intracavity dispersion difficult. Using saturable absorber films in a reflective geometry, as part of a nonlinear mirror, would provide a more elegant saturable absorber devices design, eliminate the above problems, and also somewhat simplify the resonator design (Figure 6-13).

The first design considered for a saturable absorber mirror consisted of an InAs-doped silica film on top of a gold film reflector. Gold was chosen because of its broad reflectivity bandwidth, with a reflectivity greater than 97% from 700 nm to the mid-IR.

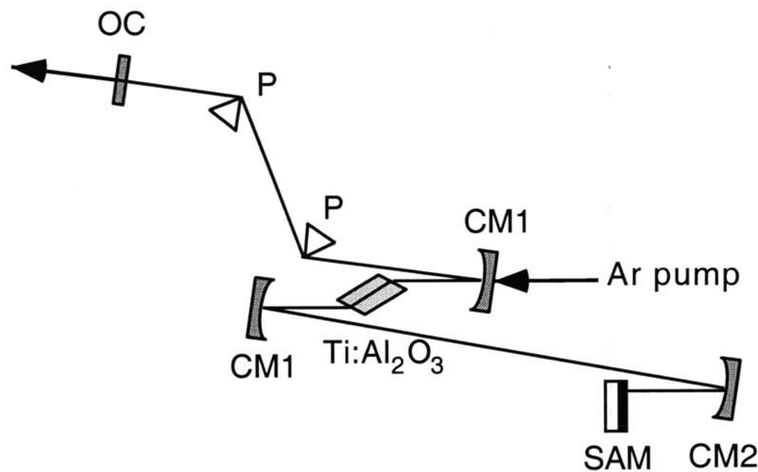

FIGURE 6-13: Schematic diagram of the Ti:Al_2O_3 laser cavity with a saturable absorber mirror. OC, output coupler; SAM, saturable absorber mirror; CM1, 10-cm ROC mirrors; CM2, 5-cm ROC mirror; P, fused silica prisms.

In order to test the adhesion properties of InAs-doped silica to gold, a trial sputtering run was performed. The substrates were fused silica and sapphire. A 400-Å-thick titanium film was deposited on top of the substrates to provide good adhesion between gold and the substrate. The titanium layer was followed by a 1600-Å-thick gold film. The choice of the gold film thickness was based on the skin depth of gold at 800 nm equal to ~ 300 Å. A 300-Å-thick InAs-doped silica film with ~ 2% absorption at 800 nm was deposited on top of the gold mirror. The whole structure was deposited in a single sputtering run using an MRC 8800 rf sputtering system. The deposited films were subsequently subjected to an RTA treatment in nitrogen at temperatures ranging from 500 to 700 °C. The annealed films had good optical and adhesion properties.

However, the trial saturable absorber mirror design, described above, is not appropriate for laser modelocking applications. When an EM wave is reflected from a mirror, a standing wave is formed by the incident and reflected waves. For a metal mirror, the node of the standing wave is positioned near the mirror surface. If a saturable absorber film is deposited immediately on the gold mirror, it would be located at the node of the standing wave and, as discussed in Chapter 3, its effective absorption saturation fluence would be increased considerably. InAs-doped silica

films, already having a high absorption saturation fluence of ~25 mJ/cm^2, should be placed at the peak rather than at the node of the standing wave so that their effective saturation fluence remain suitable for modelocking applications.

In addition, the reflective geometry with a saturable absorber film at the peak of the standing wave should make the film absorption easier to bleach and should reduce the absorption saturation fluence by a factor of 4, compared to the transmitting geometry. The electric field near the mirror is given by the sum of the incident and reflected waves with approximately equal amplitudes:

$$E = E_0 e^{-ikz} - E_0 e^{+ikz} = -2iE_0 \sin kz \tag{6-5}$$

The intensity of the standing wave is then equal to

$$I = 4I_0 \sin^2 kz \tag{6-6}$$

and is a factor of 4 higher at the peak then the travelling wave intensity I_0. Therefore, the effective saturation fluence is increased by a factor of 4. The small signal absorption is increased by only a factor of 2 (a factor of 4 compared to a single pass the a transmitting absorber structure, but the absorber is double-passed in the transmitting geometry).

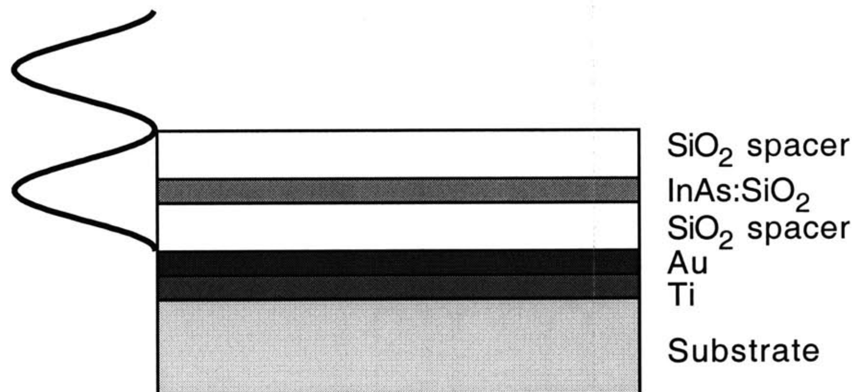

FIGURE 6-14: Saturable absorber mirror with a gold high reflector, InAs-doped silica saturable absorber, and silica spacers.

In order to place an InAs-doped film at the peak of a standing wave, a quarter-wave SiO_2 transparent spacer layer can be used (Figure 6-14). In order to maintain the high total reflectivity of the saturable absorber mirror, the total optical thickness of the structure on top of the gold mirror should be $(\lambda/2)m$ where m is an integer. In this resonant case, the wave reflected from the top surface of the structure acquires a phase of π and the wave reflected from the gold mirror acquires a phase $\pi + 2\pi m$ and the two wave interfere constructively.

A saturable absorber mirror with a silica spacer was deposited by rf sputtering. The titanium and gold layers, described above, were followed by 124 nm of SiO_2, 30 nm of InAs:SiO_2 and 124 nm of SiO_2, making the total optical thickness of the transparent structure equal to 400 nm. Prior to the structure fabrication, the SiO_2 deposition rate was calibrated by both ellipsometry and photolithography measurements and was found to be 17 Å/min. The deposition of the whole saturable absorber mirror structure took ~3.5 hours. The deposition rate could be increased by up to an order of magnitude with the application of a magnetron rf sputtering system.

The deposited saturable absorber mirrors were subjected to an RTA treatment in nitrogen in order to modify the absorption saturation dynamics of the InAs-doped films. Following the annealing, the films deposited both on silica and sapphire substrates were found to be cracked and not suitable for optical applications. An image of a 640 by 480 μm region of the annealed film on a glass substrate was acquired using a microscope and is shown in Figure 6-15. The cracks are believed to be caused by a large difference between the thermal expansion coefficients of gold and fused silica, respectively $14.2 \cdot 10^{-6}$ and $0.51 \cdot 10^{-6}$ K^{-1} [176]. Several interference fringes were observed near the edges of the darker regions in Figure 6-15 indicating that the distance between the reflective surfaces was on the order of several wavelength of light in the visible. However, the deposited film optical thickness was only 400 nm, suggesting that the film was elevated above the gold reflector. The contrast of the interference fringes decreased toward the center of the darker islands, as would be expected for higher order interference fringes produced by a low-coherence source. These observations suggest that the centers of the darker islands were elevated by a few microns above the surface of the substrate. Profilometry measurements showed that the darker islands on the image corresponded to the regions elevated by ~3 μm above the surface of the substrate. The following explanation can be suggested to the observed cracks in the film. When the

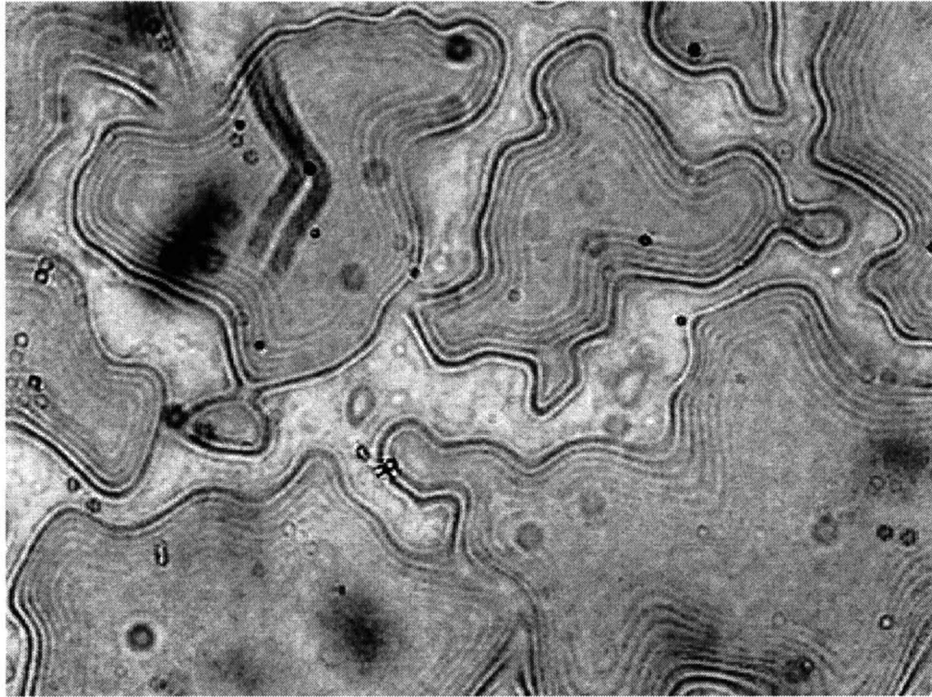

FIGURE 6-15: Surface of a saturable absorber mirror structure with a gold reflector and silica spacer layers following rapid thermal annealing at 500 °C for 60 seconds. The image size is 640 by 480 μm.

sample is heated during the RTA, gold expands more than the silica film. The silica film cannot accommodate the strain and breaks, creating SiO_2 islands on top of gold. When the sample cools down, gold contracts more than silica, and the silica islands form dome-shaped structures.

Two kinds of commercial multilayer dielectric mirrors, one formed by quarter-wave layers of TiO_2 and SiO_2, the other formed by layers of ZrO_2 and SiO_2, on silica and sapphire substrates, were also considered as reflectors for the InAs-doped-film-base saturable absorber mirrors. It was found however, that the dielectric mirrors did not withstand the RTA treatment well and were covered by a number of cracks following the annealing.

A solution to the problem of mirror surface degradation during RTA was found in a form of sapphire spacer layers. Sapphire has a thermal expansion coefficient of $\sim 7 \cdot 10^{-6}$ K^{-1}, closer to the thermal expansion coefficient of gold. A sapphire target was installed into the sputtering system and the deposition rate was calibrated to be ~9 Å/min. Saturable absorber mirror structures described above were fabricated, with the silica spacer layers replaced by sapphire. The mirrors

were subsequently annealed in nitrogen at temperatures ranging from 500 to 700 °C and were found to preserve high optical quality. The experiments aimed at the application of these InAs-doped-silica-based saturable absorber mirrors to Ti:Al_2O_3 laser modelocking are currently under way.

6.10 Conclusions

To summarize, for the first time, semiconductor-doped dielectric thin films were used for laser modelocking. Using 30-nm-thick InAs-doped silica films grown by rf sputtering, self-starting saturable-absorber-assisted KLM operation of a Ti:Al_2O_3 laser was demonstrated. Pulse durations as short as 25 fs were generated with a wavelength tuning range from 800 to 880 nm. Self-starting modelocked operation was obtained for various net intracavity group delay dispersion, both negative and positive.

A number of further improvements to the nonepitaxial saturable absorbers for modelocking can be envisioned. Fabrication of films with lower absorption saturation fluences would further simplify the laser design, would not require very tight focusing, would allow higher absorption modulation depth, would reduce the effects of excessive self-phase modulation, and would bring the absorber operating point further down from the optical damage threshold. The above improvements should all add up to enable researchers to generate even shorter pulses using semiconductor-doped absorber films. Saturable absorber mirrors incorporating semiconductor-doped films would make the laser cavity design even simpler, would entirely eliminate the SPM effects in the absorber substrate, and would allow to tailor the film absorption properties in a manner similar to SESAMs and SBRs. Using various semiconductor dopants should allow to extend the operating range of the saturable absorber films and apply them to modelocking of such solid-state lasers as Cr:forsterite and Cr:YAG, which operate in the wavelength regions around 1.3 and 1.5 μm important for optical communications.

From the demonstrated modelocking and film characterization results it is clear that semiconductor-doped films are a promising materials system for solid-state laser modelocking and a lot of new exciting modelocking applications of such films are still ahead. Because semiconduc-

tor-doped films are simple in design and easy to fabricate, they should allow further progress toward development of compact, simple and inexpensive ultrashort pulse laser sources, make femtosecond lasers more accessible to researchers, and open new applications which require robustness and simplicity of laser sources. On the other hand, semiconductor-doped films should facilitate advances in the development of broadly tunable femtosecond lasers sources owing to the films' smooth wavelength dependence of absorption. In addition, the ability to incorporate the semiconductor-doped films into broadband saturable absorber mirrors should allow further progress in the development of self-starting femtosecond laser oscillators with record pulse durations.

Chapter 7

Summary and future work

This thesis has presented the most recent advances in the development of saturable absorbers for laser modelocking. Several aspects of the saturable absorber research were investigated including the design, modeling, and fabrication of novel saturable absorber materials and devices, characterization of their linear and nonlinear optical, compositional and structural properties, and applications of the newly developed saturable absorbers to solid-state laser modelocking.

The thesis has considered three types of saturable absorber materials and devices, namely epitaxially grown saturable Bragg reflectors, semiconductor-doped glasses, and thin silica films doped with semiconductor quantum dots.

The discussion of the saturable Bragg reflectors focused on the theoretical aspects of modeling and design of such devices. SBR parameters such as reflectivity, group delay dispersion, third order dispersion, and electric field distribution inside the device were calculated for various structures. Such calculations are necessary to build saturable absorber devices and better understand their performance inside a laser resonator. The developed modeling techniques can be extended to design novel saturable absorber structures. Two-photon absorption effects in the SBRs were theoretically investigated and were found to have a significant detrimental impact on the sub-100-fs pulse generation.

The second part of the thesis considered the applications of semiconductor-doped glasses to laser modelocking. Femtosecond pump-probe experiments at 800 nm were performed on the commercial semiconductor-doped glasses from Schott Glass Technologies to investigate their absorption saturation dynamics. The absorption saturation fluence of the RG-830 and RG-850

glasses was measured to be ~ $1 mJ/cm^2$. Photodarkening effects in the glasses were observed resulting in faster absorption recovery times with increasing exposure to laser radiation of high intensity. The measurements demonstrated a decrease in carrier lifetime from several picoseconds in fresh glasses to as short as ~ 400 fs in photodarkened glasses owing to an increased density of surface recombination centers in the semiconductor nanocrystallites and a faster non-radiative recombination time. In order to incorporate semiconductor-doped glasses into a $Ti:Al_2O_3$ laser cavity, a wedge-shaped saturable absorber structure was designed and fabricated. It allowed to continuously vary the absorption introduced into the laser resonator and to obtain absorption suitable to support a broad wavelength tuning range of the laser. Both saturable absorber modelocking and saturable-absorber-assisted KLM operation of a $Ti:Al_2O_3$ laser were demonstrated using semiconductor doped glasses RG-780, RG-830, and RG-850. Self-starting pulses of 2-ps duration with a wavelength tunable from 780 to 860 nm with up to 100 mW of average power were obtained using just the colored glasses to provide saturable absorption. 52-fs transform-limited pulses were obtained using colored glass absorbers in conjunction with KLM; this pulse duration is a factor of 40 shorter than the previously demonstrated result with semiconductor-doped glasses in a laser cavity. Overall, semiconductor-doped glasses were demonstrated to have the absorption saturation fluences and absorption recovery times required for solid-state laser modelocking applications; they present a simple alternative to epitaxially grown saturable absorbers. The main drawbacks of the colored glasses include the steep optical absorption edge, which limits the bandwidth of operation, the photodarkening effects, which limit the intensity incident on the colored glass, and the bulk nature of the material, which does not allow to incorporate these glasses into thin film structures. The carrier trapping and the surface defect state formation in the colored glasses, which are the processes responsible for photodarkening, depend on the chemical composition of the host glass material. With further development of colored glasses, these effects can potentially be utilized to control the carrier dynamics and tailor the absorption saturation properties for various applications.

The third part of the thesis demonstrated a novel materials system, namely semiconductor-doped silica films, for saturable absorber applications. This was the first time such materials were considered as saturable absorbers for modelocking. Rf sputtering was used to fabricate the films of RG-850 glass, silica films doped with GaSb quantum dots and silica films doped with InAs

quantum dots. The optical, compositional, and structural properties of the InAs-doped films were investigated by means of linear absorption spectroscopy, femtosecond pump-probe experiments, absorption saturation experiments, x-ray photoelectron spectroscopy, transmission electron microscopy, energy dispersive x-ray spectroscopy, and electron diffraction. The films were found to contain InAs nanocrystallites with sizes as a large as ~ 80 Å. The nanocrystallites preserved the zinc blende lattice structure of bulk InAs. The optical absorption edge of the InAs quantum dots was shifted to ~ 1 μm from the InAs bulk absorption edge of 3.5 μm owing to quantum confinement effects. Rapid thermal annealing was found to have a significant effect on the carrier dynamics in InAs dots, with faster absorption recovery times for higher annealing temperatures, down to ~ 300 fs for films annealed at 750 °C. RTA was also found to decrease the absorption saturation fluence of the films by a factor of ~2 which can be attributed to the reduced defect density inside the annealed quantum dots and a slower exciton dephasing time. The saturation fluence of the annealed InAs-doped films was measured to be ~ 25 mJ/cm^2. The films were found to have an optical damage threshold ~ 1 mJ/cm^2 absorbed fluence at 100 MHz repetition rate, which suggested that they could be used inside a typical laser resonator.

Finally, for the first time, semiconductor-doped thin dielectric films have been applied to laser modelocking. Self-starting saturable-absorber-assisted KLM operation of a $Ti{:}Al_2O_3$ laser was demonstrated using 30-nm-thick InAs-nanocrystallite-doped silica films grown by rf sputtering. Pulses of durations as short as 25 fs were generated. Self-starting modelocked operation was demonstrated in a broad wavelength tuning range, from 800 to 880 nm. The broad operating range of the InAs-nanocrystallite-doped absorbers was made possible by the broad distribution of the nanocrystallite sizes. Self-starting modelocked operation was obtained with various values of intracavity group delay dispersion, both negative and positive. Multiple pulsing modelocking instabilities were observed and investigated at higher intracavity powers. Overall, the absorption modulation depth provided by the InAs-doped films was sufficient to initiate KLM in a $Ti{:}Al_2O_3$ but was too low to modelock the laser without KLM action. Films with a lower absorption saturation fluence or possibly a laser resonator with a larger negative intracavity group delay dispersion could be used to modelock a laser without KLM.

Semiconductor-doped films possess a number of advantages compared to epitaxially grown semiconductors. Doped silica films can be deposited on a variety of substrates without the stringent lattice-matching requirements typical for epitaxial growth. A variety of semiconductors can be incorporated into the films as dopants. The nanoparticle size, together with the choice of the semiconductor dopant can be used to control the optical absorption edge. A broad nanocrystallite particle size distribution can be used to provide a smooth optical absorption edge and a broad optical bandwidth of operation. The doping density can control the linear optical absorption coefficient and the film thickness can be adjusted to obtain the desired total absorption. Semiconductor-doped films have the potential to be deposited in conjunction with standard dielectric thin films to create nonlinear dielectric mirrors and other structures. Finally, rf-sputtering technique used for the fabrication of semiconductor-doped films is significantly simpler and less expensive than molecular or chemical beam epitaxy.

With further development, semiconductor-doped thin film saturable absorbers can have a significant impact on the whole field of ultrashort pulse laser physics. The broad bandwidth of operation and the ability to incorporate such absorbers into broadband dielectric mirrors should allow researchers to develop self-starting ultrashort pulse laser systems with record pulse durations. The development of simpler, more robust and less expensive femtosecond pulse sources would greatly benefit many scientific applications, would make ultrashort pulse lasers practical research tools, and would stimulate numerous new applications outside a laboratory environment.

Several directions for the future research efforts in the development of semiconductor-doped dielectric saturable absorber films may be suggested:

- Implement the saturable absorber mirror design incorporating InAs-doped silica films which is described in Chapter 6 and apply such nonlinear mirrors to $Ti:Al_2O_3$ laser modelocking. The reflective design should allow to eliminate the excessive self-phase modulation in the laser resonator and should support generation of shorter pulses.

- Use the techniques of the SBR design described in Chapter 3 to incorporate semiconductor-doped films into multilayer dielectric structures to adjust the optical properties of the saturable absorber films.

- Perform multiple-wavelength pump-probe experiments on the InAs-doped films to investigate the spectral hole burning effects and determine the exciton dephasing time.

- Develop semiconductor-doped films with lower absorption saturation fluences (higher absorption cross-sections). A lower saturation fluence would require a lower intensity incident on the films which in turn would allow less tight focusing and a simpler laser design, would reduce the self-phase modulation in the substrate, would reduce potential optical damage problems, and would allow deeper absorption modulation depth. Taken together, these changes should make the semiconductor-doped films more practical for saturable absorber applications, should allow generation of shorter laser pulses, and should allow to apply the films to laser modelocking without the need for KLM. Several approaches can be suggested to obtain films with a lower saturation fluence including:

  - Reducing the effective absorption saturation fluence by placing the films inside a resonant multilayer structure. However, such a resonant design would limit the wavelength tuning range and would produce high group delay and third order dispersions.

  - Using films with larger semiconductor quantum dots. Larger dots are expected to have a longer exciton dephasing time and a lower absorption saturation fluence.

  - Fabricating films with semiconductor quantum dots that have a lower defect density. As in the case of larger dots, this should lead to a longer dephasing time and a lower saturation fluence.

- Find another way to tailor the absorption saturation dynamics of the semiconductor-doped films. In this thesis, rapid thermal annealing was demonstrated to speed up the carrier recombination times and to reduce the saturation fluence. However, the high temperatures used in the RTA process are not acceptable for many dielectric mirror structures.

- Develop films with various semiconductor dopants including InAs, GaSb, InSb, GeTe, etc.

- Develop semiconductor-doped films with optical absorption in the 1.3 and 1.5 μm wavelength ranges, which are important for optical communications, and apply them to modelocking of

Cr:forsterite, Cr:YAG, and other near-IR lasers.

- Develop films with various dielectric host materials, such as for example Al_2O_3 or TiO_2. The host material would affect both the size and the surface chemistry of the semiconductor quantum dots. The changes in the surface chemistry and the number of dangling bonds would translate into variations in the density of surface traps and recombination centers, and thus affect the carrier dynamics in the semiconductor.

Many of the above improvements may be obtained using an rf magnetron sputtering system for fabrication of the semiconductor-doped films. In a magnetron system, rf discharge plasma is contained in the vicinity of the target and the substrates are not exposed to plasma bombardment. As a result, a magnetron system should allow a more precise control of the substrate temperature using a quartz-lamp or resistive heater and therefore better control over the semiconductor nanocrystallite size distribution within the film. The defect density inside the semiconductor quantum dots may also be decreased owing to the more precise control of the deposition parameters. In addition, a magnetron sputtering system should provide a deposition rate up to an order of magnitude higher than a sputtering system without a magnetron, such as the one used in the presented research.

Appendix A

Design of multilayer dielectric stacks

This Appendix describes in detail the calculations of the properties of multilayer dielectric stacks, utilized in Chapter 3. The calculated properties include reflectivity, dispersion, and field distribution within the stack. The described methods can be applied to model a variety of multilayer dielectric mirrors and saturable absorber structures. The design of multilayer coatings is a well established area of optics and a number of comprehensive reviews exist on the subject [102] [103].

The electric and magnetic fields in the mth layer of the stack can be expressed as a sum of the forward and backward propagating waves:

$$E_m = E_m^+ + E_m^- \qquad \text{(A-1)}$$

$$H_m = \mu_m(E_m^+ - E_m^-) \qquad \text{(A-2)}$$

where

$$\mu_m = n_m/(\cos\theta_m) \text{ for the p-component of polarization,} \qquad \text{(A-3)}$$

$$\mu_m = n_m\cos\theta_m \text{ for the s-component of polarization,} \qquad \text{(A-4)}$$

where θ_m is the angle of incidence in the mth layer which is related to the angles in the medium of incidence θ_0 and in the substrate θ_{sub} by Snell's law:

$$n_0 \sin\theta_0 = n_m \sin\theta_m = n_{sub} \sin\theta_{sub} \tag{A-5}$$

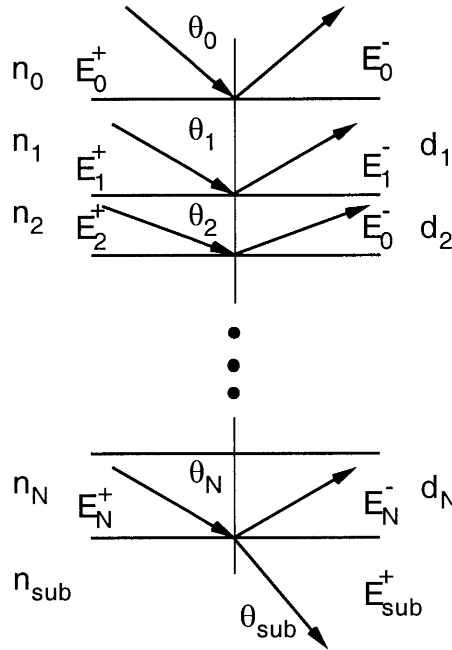

FIGURE A-1: Multilayer notation.

The forward and backward propagating electric waves at the interface are given by:

$$E_m^+ = \frac{\mu_m E_m + H_m}{2\mu_m} \tag{A-6}$$

$$E_m^- = \frac{\mu_m E_m - H_m}{2\mu_m} \tag{A-7}$$

The phase acquired by the wave on passing through the mth layer, also called the phase thickness, is given by:

$$\delta_m = \frac{2\pi n_m d_m \cos\theta_m}{\lambda} \tag{A-8}$$

where λ is the wavelength in vacuum, d_m is the physical thickness of the mth layer. If the media are absorbing, the complex quantity should be used instead of real index of refraction $n_m \rightarrow n_m - ik_m$.

The reflectivity of an interface between the two layers is obtained from the conditions that require the continuity of the tangential components of the electric and magnetic fields across the boundary. For non-absorbing media, the Fresnel reflection and transmission coefficients of the interface between the *(m-1)*th and *m*th layers for *p*-polarization are given by:

$$r_{mp} = \frac{n_{m-1}\cos\theta_m - n_m\cos\theta_{m-1}}{n_{m-1}\cos\theta_m + n_m\cos\theta_{m-1}} \tag{A-9}$$

$$t_{mp} = \frac{2n_{m-1}\cos\theta_{m-1}}{n_{m-1}\cos\theta_m + n_m\cos\theta_{m-1}} \tag{A-10}$$

and for *s*-polarization:

$$r_{ms} = \frac{n_{m-1}\cos\theta_{m-1} - n_m\cos\theta_m}{n_{m-1}\cos\theta_{m-1} + n_m\cos\theta_m} \tag{A-11}$$

$$t_{ms} = \frac{2n_{m-1}\cos\theta_{m-1}}{n_{m-1}\cos\theta_{m-1} + n_m\cos\theta_m} \tag{A-12}$$

Application of the boundary conditions requiring that the tangential components of the electric and magnetic fields be continuous across the boundaries gives a relation for wave propagation across the mth boundary:

$$E^+_{m-1} = \frac{1}{t_m}[E^+_m\exp(i\delta_m) + r_mE^-_m\exp(-i\delta_m)] \tag{A-13}$$

$$E^-_{m-1} = \frac{1}{t_m}[r_mE^+_m\exp(i\delta_m) + E^-_m\exp(-i\delta_m)] \tag{A-14}$$

This is approach is called an *interface* formulation as it used the properties of interfaces between the layers. An alternative recurrence relation can be obtained by using equations (A-1) and (A-2):

$$\begin{bmatrix} E_{m-1} \\ H_{m-1} \end{bmatrix} = \begin{bmatrix} \cos\delta_m & \frac{i}{\mu_m}\sin\delta_m \\ i\mu_m \sin\delta_m & \cos\delta_m \end{bmatrix} \begin{bmatrix} E_m \\ H_m \end{bmatrix} \quad \text{(A-15)}$$

This a so-called *matrix* formulation which uses only the characteristics of separate layers. The matrix in equation (A-15) has unity determinant which is helpful for checking the validity of calculations. The matrix formulation will be used to calculate the reflectivity of a multilayer dielectric stack.

For an N-layer stack

$$\begin{bmatrix} E_0 \\ H_0 \end{bmatrix} = M_1 M_2 \ldots M_N \begin{bmatrix} E_N \\ H_N \end{bmatrix} = \prod_{m=1}^{N} M_m \begin{bmatrix} E_N \\ H_N \end{bmatrix} \quad \text{(A-16)}$$

where

$$M_m = \begin{bmatrix} \cos\delta_m & \frac{i}{\mu_m}\sin\delta_m \\ i\mu_m \sin\delta_m & \cos\delta_m \end{bmatrix} \quad \text{(A-17)}$$

and the field in the last Nth layer is given by

$$\begin{bmatrix} E_N \\ H_N \end{bmatrix} = \begin{bmatrix} 1 \\ \mu_{sub} \end{bmatrix} E_{sub}^{+} \quad \text{(A-18)}$$

It can be seen that for a non-absorbing medium, the matrix product can be written as:

$$\prod_{m=1}^{N} M_m = \begin{bmatrix} A & iB \\ iC & D \end{bmatrix} \quad \text{(A-19)}$$

where A, B, C, and D are real numbers. Then

$$\begin{bmatrix} E_0 \\ H_0 \end{bmatrix} = \begin{bmatrix} A & iB \\ iC & D \end{bmatrix} \begin{bmatrix} 1 \\ \mu_{sub} \end{bmatrix} E^{+}_{sub} \tag{A-20}$$

and the amplitude reflectivity of the stack is given by

$$r = \frac{\mu_0 E_0 - H_0}{\mu_0 E_0 + H_0} = \frac{(\mu_0 A - \mu_{sub} D) + i(\mu_0 \mu_{sub} B - C)}{(\mu_0 A + \mu_{sub} D) + i(\mu_0 \mu_{sub} B + C)} \tag{A-21}$$

The power reflectivity of the stack is

$$R = |r|^2 \tag{A-22}$$

and phase acquired by the wave upon reflection is

$$\varphi = kz - \omega t = \arg r. \tag{A-23}$$

Therefore, given the incidence angle and polarization, the refractive indices and thicknesses of the stack layers, the refractive indices of the medium of incidence and the substrate, the reflectivity and phase of an arbitrary non-absorbing stack can be calculated in the following manner:

1. Calculate μ_0, μ_{sub}, μ_m (m=1...N).
2. Calculate δ_m (m=1...N).
3. Calculate the product of the matrices $M_1 M_2 ... M_N$.
4. From the resulting matrix, calculate A, B, C, and D coefficients and then reflectivity R and phase φ.

The above calculations can be performed for a number of wavelengths of interest to obtain the wavelength dependence of stack reflectivity. In addition, from the wavelength dependence of phase $\varphi(\lambda)$, the dispersion introduced by the stack on reflection can be obtained, giving GDD

$$\frac{d^2\varphi}{d\omega^2} = \frac{d\varphi}{d\lambda}\frac{\lambda^3}{2\pi^2 c^2} + \frac{d^2\varphi}{d\lambda^2}\frac{\lambda^4}{4\pi^2 c^2} \tag{A-24}$$

and third order dispersion

$$\frac{d^3\varphi}{d\omega^3} = -\frac{3}{4\pi^3 c^3}\frac{\lambda^4}{d\lambda}\frac{d\varphi}{d\lambda} - \frac{3}{4\pi^3 c^3}\frac{\lambda^5 d^2\varphi}{d\lambda^2} - \frac{1}{8\pi^3 c^3}\frac{\lambda^6 d^3\varphi}{d\lambda^3} \tag{A-25}$$

Having found the electric and magnetic fields at the layer boundaries according to equations (A-15) and (A-18), the electric field distribution within the layers can be determined. Using equations (A-6) and (A-7), the forward and backward propagating electric field waves can then be found at any position within the layer:

$$E_m^+(z) = E_m^+ \exp\left[-i\frac{2\pi n_m \cos\theta_m}{\lambda}(z - z_m)\right] \qquad \text{for } z \in (z_m - d_m, z_m) \tag{A-26}$$

$$E_m^-(z) = E_m^- \exp\left[+i\frac{2\pi n_m \cos\theta_m}{\lambda}(z - z_m)\right] \qquad \text{for } z \in (z_m - d_m, z_m) \tag{A-27}$$

The field intensity relative to the intensity in free space is then found:

$$I(z) = \frac{1}{4}E(z)E^*(z) = \frac{1}{4}|E^+(z) + E^-(z)|^2 \tag{A-28}$$

for the s-component of polarization and

$$I(z) = \frac{1}{4}[|E^+(z) + E^-(z)|^2\cos^2\theta + |E^+(z) - E^-(z)|^2\sin^2\theta] \tag{A-29}$$

for the p-component of polarization.

Following are the MATLAB codes for calculating the reflectivity, dispersion, and field distribution for an arbitrary multilayer non-absorbing dielectric stack. *Refl_GVD_field* is the main program which defines the structure of the stack, specifies the input wave parameters such as wavelength and polarization, and plots the results. The main program calls subroutines *refl_sub* and *field_sub*. *Refl_sub* calculates reflectivity and phase of the structure. *Field_sub* calculates the field distribution and utilizes a subroutine *layerfieldsub*, which calculates the field within a single layer.

```
function out=refl_GVD_field()
% main program
% calculates reflectivity, dispersion, and field distribution of a multilayer dielectric structure

tic
c=3*10^(8+6-15);%speed of light µm/fs

num=100;          % number of wavelength points to consider

% Dielectric stack:
% refractive indices of the materials
nInP=3.17;
nGaAs=3.37;
nAlAs=2.91;

N=45;             % number of layers in the structure
n0=1;             % refractive index of the medium of incidence
nsub=nGaAs;       % refractive index of the substrate
theta0=0/180*pi;% angle of incidence, radians
pol='p';
%pol='s';         %polarization, either s or p

% *******
% define the refractive indices of the layers
% indices of refraction   air lam/2InP (GaAs AlAs)^22  GaAs sub
n(1)=nInP;        % the top layer is InP
for k=2:N
        if round(k/2)==k/2
                %even
                n(k)=nGaAs;         % even layers are GaAs
        else
                %odd
                n(k)=nAlAs;         % odd layers are AlAs
        end
end

% define the layer thicknesses
phase_thick=pi/2;             %lam/4 layers
ph0(1)=pi;        % lam/2 InP layer on top
for k=2:N
        ph0(k)=phase_thick;           %layer phase thickness at normal incidence at center wavelength
end
% *******

% calculations for different wavelengths
lam0=1.55;        % center wavelength µm
l_min=0.9;        % calculate reflectivity and dispersion for wavelengths between lam0*L_min and lam0*L_max
l_max=1.1;
dl=l_max-l_min;

% vary the wavelength with a total num data points
for k=1:num
        lamfrac=l_min+dl*(k-1)/num;             % in units of center wavelength
        [r(k),phi(k)]=refl_sub(N,n0,nsub,n,ph0,theta0,lamfrac,pol);             % calculate reflectivity and phase for the
lam(k)=lamfrac;                                                 % current wavelength
end

% calculate dispersion
phi=unwrap(phi);
```

```
dphi=[diff(phi),0];
d2phi=[0,diff(phi,2),0];
d3phi=[0,diff(phi,3),0,0];

lam=l_min:dl/num:l_max-dl/num;
lam=lam*lam0;
dlam=dl/num*lam0;
dphi_dlam=dphi/dlam;
d2phi_dlam2=d2phi/dlam^2;
d2phi_domega2=dphi/dlam .*lam.^3/(2*pi^2*c^2)+d2phi/dlam^2 .*lam.^4/(4*pi^2*c^2);
term1= - dphi /dlam  *3/(4*pi^3*c^3).*lam.^4;
term2= - d2phi/dlam^2*3/(4*pi^3*c^3).*lam.^5;
term3= - d3phi/dlam^3  /(8*pi^3*c^3).*lam.^6;
d3phi_domega3= term1 + term2 + term3;

% plot results

figure(1);
plot(lam,r);
xlabel('Wavelength [µm]');
ylabel('Reflectivity');
grid on;

figure(2);
phi=phi+pi;
phi1=phi';
plot(lam,phi);
xlabel('Wavelength [µm]');
ylabel('Phase [radians]');
grid on;

figure(3);
plot(lam,d2phi_domega2);
ylabel('GDD [fs^2]');
xlabel('Wavelength [µm]');
axis([min(lam),max(lam),-400,+400]);
grid on;

figure(4);
plot(lam,d3phi_domega3);
ylabel('TOD [fs^3]');
xlabel('Wavelength [µm]');
axis([min(lam),max(lam),-0,+19900]);
grid on;

% calculate the field distribution

lamfrac=1.55/1.55;          % wavelength for which the field is calculated, as a fraction of center wavelength
layerstoplot=N;             % plot field in how many top layers of the structure
[powerR,phi,Itot,ztot,indextot]=field_sub(N,n0,nsub,n,ph0,theta0,lamfrac,layerstoplot,pol);

% plot the results
figure(5);
plot(ztot,10*Itot,'y',ztot,indextot,'b');
xlabel('Position in units of wavelength vacuum');
ylabel('Field intensity [a.u.]');
grid on;

figure(6);
```

```
subplot(3,1,1);
plot(lam,r);
xlabel('µm');
ylabel('intensity R');
axis([min(lam),max(lam),0.95,1]);
grid on;
subplot(3,1,2);
plot(lam,d2phi_domega2);
ylabel('GVD [fs^2]');
xlabel('µm');
axis([min(lam),max(lam),-400,+400]);
grid on;
subplot(3,1,3);
plot(ztot,Itot,'y',ztot,indextot,'b');
xlabel('Position in units of wavelength vacuum');
ylabel('Field intensity [a.u.]');
grid on;

toc
```

```
function [powerR,phase]=refl_sub(N,n0,nsub,n,ph0,theta0,lamfraction,pol)
% calculates reflectivity and phase of a stack

if size(n) ~= N | size(ph0)~= N
	error('number of layers and index array sizes do not match');
end

% *******
% calculate parameters

% incidence angles at all interfaces
for k=1:N
	%angles
		theta(k)=asin(n0*sin(theta0)/n(k));
	%phases
		ph(k)=ph0(k)*cos(theta(k))/lamfraction;
end
thetasub=asin(n0*sin(theta0)/nsub);

% mu's at all interfaces
if pol=='p'
	mu0=n0/cos(theta0);
	musub=nsub/cos(thetasub);
	for k=1:N
		mu(k)=n(k)/cos(theta(k));
	end
elseif pol=='s'
	mu0=n0*cos(theta0);
	musub=nsub*cos(thetasub);
	for k=1:N
		mu(k)=n(k)*cos(theta(k));
	end
else
	error('polarization not specified');
end
% *******

% *******
% calculate the M-matrices
M=[1,0;0,1];
for k=1:N
	Mnew=[ cos(ph(k)),			i/mu(k)*sin(ph(k));
		i*mu(k)*sin(ph(k)),		cos(ph(k))		];
	M=M*Mnew;
end
% *******

% *******
A=M(1,1);
B=M(1,2)/i;
C=M(2,1)/i;
D=M(2,2);

%calculate the  reflectivity
refl=(mu0*A - musub*D + i*(mu0*musub*B-C)) / (mu0*A+musub*D + i*(mu0*musub*B+C));
% *******

powerR=abs(refl)^2;
phase=angle(refl);
```

```
% IMPORTANT : the above phase is wt-kz
% in this case, GVD = - d2phi/dw2
% change the sign of phase, then GVD = + d2phi/dw2
phase=-phase;
```

```
function [powerR,phase,Itot,ztot,indextot]=field_sub(N,n0,nsub,n,ph0,theta0,lamfraction,layerstoplot,pol)
% calculates the field inside the structure

if size(n) ~= N | size(ph0)~= N
	error('number of layers and index array sizes do not match');
end

% *******
% calculate parameters
for k=1:N
	%angles
		theta(k)=asin(n0*sin(theta0)/n(k));
	%phase thicknesses
		ph(k)=ph0(k)*cos(theta(k))/lamfraction;
end
thetasub=asin(n0*sin(theta0)/nsub);

% mu's
if pol=='p'
	mu0=n0/cos(theta0);
	musub=nsub/cos(thetasub);
	for k=1:N
		mu(k)=n(k)/cos(theta(k));
	end
elseif pol=='s'
	mu0=n0*cos(theta0);
	musub=nsub*cos(thetasub);
	for k=1:N
		mu(k)=n(k)*cos(theta(k));
	end
else
	error('polarization not specified');
end
% *******

% *******
% calculate the fields
EH=zeros(2,N+1);
EH(1,N+1)=1;	%E-field on the interface between N and sub
EH(2,N+1)=musub;%H-field on the interface between N and sub
% *******

% *******
% calculate the M-matrices
M=[1,0;0,1];

for k=N:-1:1
	Mnew=[	cos(ph(k)),				i/mu(k)*sin(ph(k));
			i*mu(k)*sin(ph(k)),cos(ph(k))			];
	M=Mnew*M;
	EH(:,k)=Mnew*EH(:,k+1);%EH is now shifted by +1 from the indexing throughout
								%the rest of the program
end
% *******

% *******
A=M(1,1);
B=M(1,2)/i;
C=M(2,1)/i;
```

```
D=M(2,2);
%calculate the field reflectivity
refl=(mu0*A - musub*D + i*(mu0*musub*B-C)) / (mu0*A+musub*D + i*(mu0*musub*B+C));
% *******

powerR=abs(refl)^2;
phase=angle(refl);

% *******
% Shift EH back to normal notation
EHtrue0=EH(:,1);
for k=1:N
        EHtrue(:,k)=EH(:,k+1);
end

Eplus0 =(mu0*EHtrue0(1)+EHtrue0(2) )/(2*mu0);          % forward propagating wave
Eminus0=(mu0*EHtrue0(1)-EHtrue0(2) )/(2*mu0);          % backward propagating wave

Eplus  =(mu.*EHtrue(1,:)+EHtrue(2,:) )./(2*mu);        % forward propagating wave
Eminus=(mu.*EHtrue(1,:)-EHtrue(2,:) )./(2*mu);         % backward propagating wave

% normalize fields to Eplus0
Eplus=Eplus/Eplus0;
Eminus=Eminus/Eplus0;
Eminus0=Eminus0/Eplus0;
Eplus0=1;

Rcheck=(abs(Eminus0/Eplus0))^2; % for debugging, find power reflection coeff in a different way
% *******

% *******
% field as a function of z
%actual layer thicknesses in units of wavelength in free space
d=ph0./(2*pi*n);

% free space
d0=-1;          % calculate over 1 lambda into free space (negative because it's backward)
N0=40;          % number field points to plot for free space
[Int0z,z0,index0]=layerfieldsub(Eplus0,Eminus0,0,d0,n0,theta0,N0,pol);
Int0z=fliplr(Int0z);         %so that z increases
z0=fliplr(z0);

zprev=0;        % total thickness before the given layer
Nf=20;          % field points to plot for each layer
Itot=Int0z;
ztot=z0;
indextot=index0;

for k=1:layerstoplot
        [Intz,z,index]=layerfieldsub(Eplus(k),Eminus(k),zprev,d(k),n(k),theta(k),Nf,pol);
        zprev=zprev+d(k);  % total thickness of previous layers starting from 1
        Itot=[Itot,Intz];       % Field intensity
        ztot=[ztot,z];          % Position inside the stack in units of free space wavelength
        indextot=[indextot,index];      % index of refraction at this position
end
```

```
function [Intz,z,index]=layerfieldsub(Eplus,Eminus,zprevmax,d,n,theta,N,pol);
%field inside a layer
e=exp(1);
k=N-1:-1:0;
index=n*ones(size(k));

z=-d*k/N;          %we start at the end of the layer
                   %Eplus and minus are fields at the end of the layer
Eplusz=Eplus*e.^(-i*2*pi*n*cos(theta)*z);    % forward propagating wave
Eminusz=Eminus*e.^(i*2*pi*n*cos(theta)*z); % backward propagating wave

if pol=='p'
        Intz=1/2*( abs(Eplusz+Eminusz).^2 * abs(cos(theta)^2) + abs(Eplusz-Eminusz).^2 * abs(sin(theta)^2));
elseif pol=='s'
        Intz=1/2* abs(Eplusz+Eminusz).^2;
else
        error('polarization specified incorrectly');
end

z=z+d+zprevmax;
```

Appendix B

Sputtering deposition procedure

This Appendix describes the rf sputtering deposition procedure using an MRC 8800 sputtering system.

Substrate preparation:

1. Rinse a substrate in acetone.
2. Rinse in methanol.
3. Rinse in soap water.
4. Rinse in methanol.
5. Rinse in DI water.
6. Blow-dry with dry nitrogen.
7. Bake in an oven in a dry nitrogen atmosphere at ~ 80°C for 10 minutes.

Opening the system and loading the substrates:

1. Close cryo pump gate.
2. Open nitrogen bleed valve. Back-fill the sputtering chamber with nitrogen.
3. Shut off nitrogen.
4. Open hoist.
5. Open shutter.
6. Place the substrates on substrate platform.
7. Close shutter.
8. Lower hoist.
9. Turn on mechanical (roughing) pump. The pump will automatically shut down at ~ 100 mTorr.
10. Turn off mechanical pump switch.
11. Open cryo pump gate. Make sure the gate is open.
12. Let the system pump down overnight to low 10^{-7} Torr.

Sputtering deposition:

1. Turn on ion vacuum gauge.
2. De-gas the vacuum gauge for 1 minute. Wait for ~ 10 minutes.
3. Record the vacuum gauge reading. Turn off vacuum gauge.
4. Turn on target cooling water.
5. Turn on substrate plate cooling water.
6. Put proper target in position.
7. Close throttle. The cryo pump will be pumping down slower.
8. Turn on electronics.

Target cleaning by sputter etching, steps 9 through 16. Clean targets in reverse order - the first material to be deposited is cleaned last.

9. Power on - target. Make sure the shutter is closed.
10. Target drive to ~ 20 W.
11. Open argon valve. Adjust Ar pressure to 5 - 5.2 mTorr.
12. Target drive to 100 W (forward).
13. Adjust load, input, and drive to minimize reflected target rf power, while keeping forward power at 100 W.
14. Wait 10 minutes.
15. Target drive to stand by.
16. Turn Ar off.
17. Change target if necessary. Repeat steps 9 through 16 to clean the next target. For the last target to be cleaned, repeat only steps 9 through 14, do not shut off the target drive.

Substrate cleaning by sputter etching, steps 18 through 21. The target drive is still on, at 100 W forward.

18. Set substrate power supply parameters to input 0600, load 1835, target - substrate distance to 5 inches.
19. Substrate power on.
20. Adjust substrate drive, set substrate voltage to 250 V.
21. Wait for 1 minute.

Film deposition, steps 22 through 32.

22. Sample load to 2027.

23. Open shutter.
24. Raise substrate platform to a 3-inch separation.
25. Adjust target load and drive to minimize reflected target power; set the forward power to 100 W.
26. Adjust substrate drive to set substrate voltage to 70 V.
27. Deposit the film for a desired time duration.
28. Target and substrate drives stand by.
29. Target and substrate drives down.
30. Lower the substrate platform to 5 inches.
31. Close shutter.
32. Turn Ar off.

If additional materials are to be deposited,

33. Change target.
34. Sample load to 1835.
35. Target power on, drive up to 25 W.
36. Ar on.
37. Optimize target load and drive, minimize reflected power, set forward power to 100 W.
38. Substrate power on. Set substrate voltage to 250 V.
39. Wait for 1 minute for target and substrates to be cleaned.
40. Sample load to 2027.
41. Open shutter.
42. Platform to 3 inches.
43. Sample voltage to 70 V, target forward power to 100 W, minimize target reflected power.
44. Deposit the film for a desired time.
45. Target and substrate drives stand by.
46. Target and substrate drives down.
47. Lower the substrate platform to 5 inches.
48. Close shutter.
49. Turn Ar off.

If additional materials are to be deposited, go back to step 33. If the deposition is complete, proceed:

50. Turn of electronics.
51. Open throttle.
52. Turn off target cooling water.
53. Turn off substrate cooling water.
54. Wait for 20 minutes.
55. Follow the procedure for opening the system.

Appendix C

Photolithography procedure

This Appendix describes the photolithography procedure for thickness measurements of silica or other films deposited by sputtering or other methods. The film substrates should be such that they are not etched by buffered HF acid. Alternatively, the substrate etch rate should be much slower than that of the film under investigation. The suitable substrate materials include Si and GaAs.

Applying the photoresist.

56. Choose a resist spinner shuck a little smaller than the sample. Put the chuck onto the spinner axis and place the sample on the chuck with the film surface facing up.
57. Turn on the vacuum to hold the sample on the chuck.
58. Set spinner to 5000 rpm.
59. Put a couple of drops of HMDS wetting fluid on the sample.
60. Turn on the spinner for 5 seconds.
61. Put a couple of drops of 1400:30 photoresist on the sample.
62. Turn on the spinner for 30 seconds.
63. Turn off the vacuum. Remove the sample from the chuck.
64. Put the sample on a hot plate set to 80 °C for 20 minutes to dry the photoresist.

Exposing the photoresist using a Zeiss mask aligner.

65. Clean the photolithography mask with acetone and methanol, DI water and blow off the water droplets with dry nitrogen gas.
66. Turn on the UV lamp and the microscope light in the mask aligner.
67. Put the mask onto the holder of the mask aligner, oxide surface up. Turn on the mask vacuum. Slide the mask in upside down (oxide side down), tighten.
68. Place the sample on the sample holder and slide the holder in.
69. Align the mask and the sample using a microscope.

70. Bring the sample in contact with the mask. Under a microscope, monitor the corners of the sample where the resist thickness is the highest and where the interference fringes will appear first when the contact is obtained.
71. Set the exposure time to 7 seconds. Turn on the chamber vacuum. Press the exposure button.
72. Lower the sample. Pull the sample out.
73. Loosen the mask holder and pull it out. Turn off the mask vacuum and remove the mask.

Developing the photoresist. During this step, the exposed photoresist will be removed from the sample.

74. Prepare two dishes, one with DI water, the other with 1 part of 606 photoresist developer to 7 parts water.
75. Develop the sample for ~10 seconds. Rinse in water in the dish. Place the sample onto the sample cleaning chuck and thoroughly rinse with water.
76. Examine the developed photoresist under a microscope. If not all of the exposed resist was removed develop again for several seconds.

Film etching. During this step, the film will be etched in the parts of the sample not covered by photoresist. The photoresist is not etched by buffered HF.

77. Prepare two dishes, one with buffered HF, one with DI water.
78. Immerse the sample into buffered HF. The typical etch rate for SiO_2 is ~ 100 Å/s.
79. Rinse the sample in DI water in the dish. Rinse with DI water on the sample cleaning chuck.
80. Dry the sample with dry nitrogen gas.
81. Examine the sample under a microscope. Repeat etching if necessary.
82. When etching is complete, remove the remaining photoresist by rinsing with acetone, methanol, DI water, and drying with compressed nitrogen.

The sample is ready to be examined with a profilometer to determine the film thickness.

References

[1] T. H. Maiman, "Optical laser action in ruby," *British Communication of Electronics*, vol. 7, pp. 674, 1960.

[2] L. E. Hargrove, R. L. Fork, and M. A. Pollack, "Locking of He-Ne laser modes induced by synchronous intracavity modulation," *Appl. Phys. Lett.*, vol. 5, pp. 4-6, 1964.

[3] M. Mocker and R. Collins, "Mode competition and self-locking effects in a Q-switched ruby laser," *Appl. Phys. Lett.*, vol. 7, pp. 270, 1965.

[4] A. Othonos, "Probing ultrafast carrier and phonon dynamics in semiconductors," *J. Appl. Phys.*, vol. 83, pp. 1789-1830, 1998.

[5] I. P. Christov, J. Zhou, J. Peatross, A. Rundquist, M. M. Murnane, and H. C. Kapteyn, "Non-adiabatic effects in high-harmonic generation with ultrashort pulses," *Phys. Rev. Lett.*, vol. 77, pp. 1753-1745, 1996.

[6] D. Umstadter, S.-Y. Chen, A. Maksimchuk, G. Mourou, and R. Wagner, "Nonlinear optics in relativistic plasmas and laser wake field acceleration of electrons," *Science*, vol. 273, pp. 472-475, 1996.

[7] C. P. J. Barty, T. Guo, C. LeBlanc, F. Raksi, C. Rose-Petruck, J. A. Squier, B. Walker, K. R. Wilson, V. V. Yakovlev, and K. Yamakawa, "Sub-20-fs multiterawatt lasers," presented at Ultrafast Phenomena. 1996 Technical Digest Series, 1996.

[8] A. M. Weiner, "Femtosecond optical pulse shaping and processing," *Progr. Quantum Electron.*, vol. 19, pp. 161-237, 1995.

[9] M. C. Nuss, W. H. Knox, and U. Koren, "Scalable 32 channel chirped-pulse WDM source," *Electronics Lett.*, vol. 32, pp. 1311-1312, 1996.

[10] D. A. Akimov, A. B. Fedotov, N. I. Koroteev, E. V. Levich, S. A. Magnitskii, A. N. Naumov, D. A. Sidorov-Biryukov, N. T. Sokolyuk, and A. M. Zheltikov, "Three-dimensional optical memory systems based on photochromic materials polarization control of two-color data writing and the possibility of nondestructive data reading," *Opt. Memory & Neural Networks*, vol. 6, pp. 31-48, 1997.

[11] D. M. Mittleman, R. H. Jacobsen, and M. C. Nuss, "T-ray imaging," *IEEE J. Selected Top. Quantum Electron.*, vol. 2, pp. 679-692, 1996.

[12] D. Huang, E. A. Swanson, C. P. Lin, J. S. Schuman, W. G. Stinson, W. Chang, M. R. Hee, T. Flotte, K. Gregory, C. A. Puliafito, and J. G. Fujimoto, "Optical coherence tomography," *Science*, vol. 254, pp. 1178-1181, 1991.

[13] P. F. Moulton, "Spectroscopic and laser characteristics of Ti:Al_2O_3," *J. Opt. Soc. Am. B*, vol. 3, pp. 125-133, 1986.

[14] D. E. Spence, P. N. Kean, and W. Sibbett, "60-fs pulse generation from a self-mode-locked Ti:Sapphire laser," *Opt. Lett.*, vol. 16, pp. 42-44, 1991.

[15] R. Szipöcs, K. Ferencz, C. Spielmann, and F. Krausz, "Chirped multilayer coatings for broadband dispersion control in femtosecond lasers," *Opt. Lett.*, vol. 19, pp. 201-203, 1994.

[16] I. D. Jung, F. X. Kärtner, N. Matuschek, D. H. Sutter, F. Morier-Genoud, G. Zhang, U. Keller, V. Scheuer, M. Tilsch, and T. Tschudi, "Self-starting 6.5-fs pulses from a Ti:sapphire laser," *Opt. Lett.*, vol. 22, pp. 1009-1011, 1997.

[17] M. Nisoli, S. D. Silvestri, and O. Svelto, "Generation of high-energy 10-fs pulses by a new pulse compression technique," *Appl. Phys. Lett.*, vol. 68, pp. 2793-2795, 1996.

[18] S. Sartania, Z. Cheng, M. Lenzner, G. Tempea, C. Spielmann, F. Krausz, and K. Ferencz, "Generation of 0.1-TW 5-fs optical pulses at a 1-kHz repetition rate," *Opt. Lett.*, vol. 22, pp. 1562-1564, 1997.

[19] A. Baltuska, Z. Wei, M. S. Pshenichnikov, and D. A. Wiersma, "Optical pulse compression to 5 fs at a 1-MHz repetition rate," *Opt. Lett.*, vol. 22, pp. 102-104, 1997.

[20] U. Keller, D. A. B. Miller, G. D. Boyd, T. H. Chiu, J. F. Ferguson, and M. T. Asom, "Solid-state low-loss intracavity saturable absorber for Nd:YLF lasers: an antiresonant semiconductor Fabry-Perot saturable absorber," *Opt. Lett.*, vol. 17, pp. 505-507, 1992.

[21] R. Mellish, P. M. W. French, J. R. Taylor, P. J. Delfyett, and L. T. Florez, "Self-starting femtosecond Ti:sapphire laser with intracavity multiquantum well absorber," *Electron. Lett.*, vol. 29, pp. 894-896, 1993.

[22] U. Keller, K. J. Weingarten, F. X. Kärtner, D. Kopf, B. Braun, I. D. Jung, R. Fluck, C. Hönninger, N. Matuschek, and J. A. d. Au, "Semiconductor saturable absorber mirrors (SESAM's) for femtosecond to nanosecond pulse generation in solid-state lasers," *IEEE J. Selected Top. Quantum Electron.*, vol. 2, pp. 435-453, 1996.

[23] S. Tsuda, W. H. Knox, S. T. Cundiff, W. Y. Jan, and J. E. Cunningham, "Mode-locked ultrafast solid-state lasers with saturable Bragg reflectors," *IEEE J. Selected Top. Quantum Electron.*, vol. 2, pp. 454-464, 1996.

[24] E. P. Ippen, "Principles of passive mode locking," *Appl. Phys. B*, vol. 58, pp. 159-170, 1994.

[25] W. Koechner, *Solid-state laser engineering*, 2nd ed. Berlin, Heidelberg: Springer Verlag, 1988.

[26] A. Siegman, *Lasers*. Mill Valley, California: University Science Books, 1986.

[27] O. Svelto, *Principles of Lasers*, 3rd ed. New York: Plenum Press, 1989.

[28] A. J. DeMaria, D. A. Stetsen, and H. Heyman, "Self mode-locking of lasers with saturable absorbers," *Appl. Phys. Lett.*, vol. 8, pp. 22-24, 1966.

[29] C. V. Shank and E. P. Ippen, "Sub-picosecond kilowatt pulses from a mode-locked c.w. dye laser," *Appl. Phys. Lett.*, vol. 24, pp. 373-375, 1974.

[30] H. A. Haus, "Theory of mode locking with a slow saturable absorber," *IEEE J. Quantum Electron.*, vol. 11, pp. 736-746, 1975.

[31] J. A. Valdmanis, R. L. Fork, and J. P. Gordon, "Generation of optical pulses as short as 27 fs from a laser balancing self-phase-modulation, group-velocity-dispersion, saturable-absorption and saturable-gain," *Opt. Lett.*, vol. 10, pp. 131-133, 1985.

[32] H. A. Haus, "Theory of modelocking with a fast saturable absorber," *J. Appl. Phys.*, vol. 46, pp. 3049-3058, 1975.

[33] H. A. Haus, E. P. Ippen, and J. G. Fujimoto, "Structures for additive pulse modelocking," *J. Opt. Soc. Amer. B*, vol. 8, pp. 2068-2076, 1991.

[34] R. Adair, L. L. Chase, and S. A. Payne, "Nonlinear refractive index of optical crystals," *Phys. Rev. B*, vol. 39, pp. 3337-3350, 1989.

[35] H. A. Haus, *Waves and fields in optoelectronics*. Englewood Cliffs: Prentice-Hall, 1984.

[36] S. A. Akhmanov, V. A. Vysloukh, and A. S. Chirkin, *Optics of femtosecond laser pulses*. New York: American Institute of Physics, 1992.

[37] E. B. Treacy, "Optical pulse compression with diffraction gratings," *IEEE J. Quantum Electron.*, vol. 5, pp. 454-458, 1969.

[38] R. L. Fork, O. E. Martinez, and J. P. Gordon, "Negative dispersion using pairs of prisms," *Opt. Lett.*, vol. 9, pp. 150-152, 1984.

[39] R. L. Fork, C. H. B. Cruz, P. C. Becker, and C. V. Shank, "Compression of optical pulses to six femtoseconds by using cubic phase compression," *Opt. Lett.*, vol. 12, pp. 483-485, 1987.

[40] R. Szipocs and A. Kohazi-Kis, "Theory and design of chirped dielectric laser mirrors," *Appl. Phys. B*, vol. 65, pp. 115-135, 1997.

[41] F. X. Kärtner, N. Matuschek, T. Schibli, U. Keller, H. A. Haus, C. Heine, R. Morf, V. Scheuer, M. Tilsch, and T. Tshudi, "Design and fabrication of double-chirped mirrors," *Opt. Lett.*, vol. 22, pp. 831-833, 1997.

[42] D. J. Kuizenga and A. E. Siegman, "FM and AM mode locking of the homogeneous laser-Pt.I: theory," *IEEE J. Quantum Electron.*, vol. 6, pp. 694-708, 1970.

[43] E. P. Ippen, L. Y. Liu, and H. A. Haus, "Self-starting condition for additive-pulse mode-locked lasers," *Opt. Lett.*, vol. 15, pp. 183-185, 1990.

[44] F. Krausz, T. Brabel, and C. Spielmann, "Self-starting passive mode locking," *Opt. Lett.*, vol. 16, pp. 235-237, 1991.

[45] H. A. Haus and E. P. Ippen, "Self-starting of passively mode-locked lasers," *Opt. Lett.*, vol. 16, pp. 1331-1333, 1991.

[46] A. Owyoung, R. W. Hellwarth, and N. George, "Intensity-induced changes in optical polarization in glasses," *Phys. Rev. B*, vol. 5, pp. 628-633, 1972.

[47] V. Magni, G. Cerullo, S. D. Silvestri, and A. Monguzzi, "Astigmatism in Gaussian-beam self-focusing and in resonators for Kerr-lens mode locking," *J. Opt. Soc. Am. B*, vol. 12, pp. 476-485, 1995.

[48] P. A. Belanger and C. Pare, "Self-focusing of Gaussian beams: an alternate derivation," *Appl. Opt.*, vol. 22, pp. 1293-95, 1982.

[49] D. Huang, M. Ulman, L. H. Acioli, H. A. Haus, and J. G. Fujimoto, "Self-focusing-induced saturable loss for laser modelocking," *Opt. Lett.*, vol. 17, pp. 511-513, 1992.

[50] M. Sheik-Bahae, A. A. Said, D. J. Hagan, M. J. Soileau, and W. V. V. Stryland, "Self-focusing distributed lens model," *Opt. Eng.*, vol. 30, pp. 1228, 1991.

[51] V. Magni, G. Cerullo, and S. D. Silvestri, "Closed form Gaussian beam analysis of resonators containing a Kerr medium for femtosecond lasers," *Opt. Comm.*, vol. 101, pp. 365-370, 1993.

[52] G. Cerullo, S. D. Silvestri, and V. Magni, "Self-starting Kerr-lens mode locking of a Ti:sapphire laser," *Opt. Lett.*, vol. 19, pp. 1040-1042, 1994.

[53] G. Cerullo, S. D. Silvestri, V. Magni, and L. Pallaro, "Resonators for Kerr-lens mode-locked femtosecond Ti:sapphire lasers," *Opt. Lett.*, vol. 19, pp. 807-809, 1994.

[54] V. Magni, "Perturbation theory of nonlinear resonators with an application to Kerr-lens mode locking," *J. Opt. Soc. Am. B*, vol. 13, pp. 2498-2507, 1996.

[55] J. Zhou, G. Taft, C. P. Huang, M. M. Murnane, H. C. Kapteyn, and I. P. Christov, "Pulse evolution in a broad-bandwidth Ti:sapphire laser," *Opt. Lett.*, vol. 19, pp. 1149-1151, 1994.

[56] A. Stingl, M. Lenzner, C. Spielmann, F. Krausz, and R. Szipöcs, "Sub-10-fs mirror-controlled Ti:sapphire laser," *Opt. Lett.*, vol. 20, pp. 602-604, 1995.

[57] G. Gerullo, S. D. Silvestri, and V. Magni, "Self-starting Kerr lens modelocking of a Ti:Sapphire laser," *Opt. Lett.*, vol. 19, pp. 1040-1042, 1994.

[58] F. X. Kärtner, L. R. Brovelli, D. Kopf, M. Kamp, I. Calasso, and U. Keller, "Control of solid-state laser dynamics by semiconductor devices," *Opt. Eng.*, vol. 34, pp. 2024-2036, 1995.

[59] H. Haug and S. Schmitt-Rink, "Basic mechanisms of the optical nonlinearities of semiconductors near the band edge," *J. Opt. Soc. Am. B*, vol. 2, pp. 1135-1142, 1985.

[60] F. X. Kärtner, I. D. Jung, and U. Keller, "Soliton modelocking with saturable absorbers," *IEEE J. Selected Top. Quantum Electron.*, vol. 2, pp. 540-556, 1996.

[61] H. A. Haus, "Parameter ranges for cw passive mode locking," *IEEE J. Quantum Electron.*, vol. 12, pp. 169-176, 1976.

[62] C. Spielmann, P. F. Curley, T. Brabec, and F. Krausz, "Ultrabroadband femtosecond lasers," *IEEE J. Quantum Electron.*, vol. 30, pp. 1100-1114, 1994.

[63] J. A. d. Au, D. Kopf, F. Morier-Genoud, M. Moser, and U. Keller, "60 fs pulses from a diode-pumped Nd:glass laser," *Opt. Lett.*, vol. 22, pp. 307-309, 1997.

[64] S. T. Cundiff, W. H. Knox, E. P. Ippen, and H. A. Haus, "Frequency-dependent mode size in broadband Kerr-lens mode locking," *Opt. Lett.*, vol. 21, pp. 662-664, 1996.

[65] M. N. Islam, E. R. Sunderman, C. E. Soccolich, I. Bar-Joseph, N. Sauer, T. Y. Chang, and B. I. Miller, "Color center lasers passively mode locked by quantum wells," *IEEE J. Quantum Electron.*, vol. 25, pp. 2454-2463, 1989.

[66] P. W. Smith, Y. Silverberg, and D. A. B. Miller, "Mode locking of semiconductor diode lasers using saturable excitonic nonlinearities," *J. Opt. Soc. Amer. B*, vol. 2, pp. 1228-1236, 1985.

[67] L. R. Brovelli, U. Keller, and T. H. Chiu, "Design and operation of antiresonant Fabry-Perot saturable semiconductor absorbers for mode-locked solid-state lasers," *J. Opt. Soc. Am. B*, vol. 12, pp. 311-322, 1995.

[68] U. Keller, "Ultrafast all-solid-state laser technology," *Appl. Phys. B*, vol. 58, pp. 347-363, 1994.

[69] I. D. Jung, L. R. Brovelli, M. Kamp, U. Keller, and M. Moser, "Scaling of the antiresonant Fabry-Perot saturable absorber design toward a thin saturable absorber," *Opt. Lett.*, vol. 20, pp. 1559-1561, 1995.

[70] L. R. Brovelli, I. D. Jung, D. Kopf, M. Kamp, M. Moser, F. X. Kärtner, and U. Keller, "Self-starting soliton modelocked Ti:sapphire laser using a thin saturable absorber," *Electron. Lett.*, vol. 31, pp. 287-289, 1995.

[71] S. Tsuda, W. H. Knox, E. A. d. Souza, W. Y. Jan, and J. E. Cunningham, "Low-loss intracavity AlAs/AlGaAs saturable Bragg reflector for femtosecond mode locking in solid-state lasers," *Opt. Lett.*, vol. 20, pp. 1406-1408, 1995.

[72] R. Fluck, I. D. Jung, G. Zhang, F. X. Kärtner, and U. Keller, "Broadband saturable absorber for 10-fs pulse generation," *Opt. Lett.*, vol. 21, pp. 743-745, 1996.

[73] K. F. Lamprecht, S. Juen, L. Palmtshofer, and R. A. Hopfel, "Ultrashort carrier lifetimes in H^+ bombarded InP," *Appl. Phys. Lett.*, vol. 59, pp. 926-928, 1991.

[74] B. Lambsdorff, J. Kuhl, J. Rosenzweig, A. Axmann, and J. Schneider, "Subpicosecond carrier lifetimes in radiation-damaged GaAs," *Appl. Phys. Lett.*, vol. 58, pp. 1881-1883, 1991.

[75] F. E. Doany, D. Grischkowsky, and C.-C. Chi, "Carrier lifetime versus ion-implantation dose in silicon on sapphire," *Appl. Phys. Lett.*, vol. 50, pp. 460-462, 1987.

[76] S. Gupta, M. Y. Frankel, J. A. Valdmanis, J. F. Whitaker, G. A. Mourou, F. W. Smith, and A. R. Calawa, "Subpicosecond carrier lifetime in GaAs grown by molecular beam epitaxy at low temperatures," *Appl. Phys. Lett.*,vol. 59, pp. 3276-3278, 1991.

[77] X. Q. Zhou, H. M. v. Driel, W. W. Rühle, Z. Gogolak, and K. Ploog, "Femtosecond carrier kinetics in low-temperature-grown GaAs," *Appl. Phys. Lett.*, vol. 61, pp. 3020-3022, 1992.

[78] *J. Elecron. Mater.*, vol. 22, no. 12, Special issue on low-temperature-grown GaAs and related materials, 1993.

[79] L. Qian, S. D. Benjamin, P. W. E. Smith, B. J. Robinson, and D. A. Thompson, "Picosecond carrier lifetime and large optical nonlinearities in InGaAsP grown by He-plasma-assisted molecular beam epitaxy," *Opt. Lett.*, vol. 22, pp. 108-110, 1997.

[80] M. Kaminska, E. R. Weber, Z. Liliental-Weber, R. Leon, and Z. U. Rek, "Stoichiometry-related defects in GaAs grown by molecular-beam epitaxy at low temperatures," *J. Vac. Sci. Technol B*, vol. 7, pp. 710-713, 1989.

[81] S. Gupta, J. W. Whitaker, and G. A. Mouror, "Ultrafast carrier dynamics in III-V semiconductors grown by molecular-beam epitaxy at very low substrate temperatures," *IEEE J. Quantum Electron.*, vol. 28, pp. 2464-2472, 1992.

[82] A. J. Lochtenfeld, M. R. Melloch, and J. C. P. Chang, "The role of point defects and arsenic precipitates in carrier trapping and recombination in low-temperature grown GaAs," *Appl. Phys. Lett.*, vol. 69, pp. 1465-1467, 1996.

[83] S. D. Benjamin, H. S. Loka, A. Othonos, and P. W. E. Smith, "Ultrafast dynamics of nonlinear absorption in low-temperature-grown GaAs," *Appl. Phys. Lett.*, vol. 68, pp. 2544-2546, 1996.

[84] P. W. E. Smith, S. D. Benjamin, and H. S. Loka, "Tailoring of trap-related carrier dynamics in low-temperature-grown GaAs," *Appl. Phys. Lett.*, vol. 71, pp. 1156-1158, 1997.

[85] U. Keller, T. H. Chiu, and J. F. Ferguson, "Self-starting femtosecond mode-locked Nd:glass laser using intracavity saturable absorbers," *Opt. Lett.*, vol. 18, pp. 1077-1079, 1993.

[86] D. Kopf, F. X. Kärtner, U. Keller, and K. J. Weingarten, "Diode-pumped mode-locked Nd:glass lasers with an antiresonant Fabry-Perot saturable absorber," *Opt. Lett.*, vol. 20, pp. 1169-1171, 1995.

[87] D. Kopf, A. Prasad, G. Zhang, M. Moser, and U. Keller, "Broadly tunable femtosecond Cr:LiSAF laser," *Opt. Lett.*, vol. 22, pp. 621-623, 1997.

[88] C. Hönninger, G. Zhang, and U. Keller, "Femtosecond Yb:YAG laser using semiconductor saturable absorbers," *Opt. Lett.*, vol. 20, pp. 2402-2404, 1995.

[89] Z. Zhang, K. Torizuka, T. Itatani, K. Kobayashi, T. Sugaya, and T. Nakagawa, "Self-starting mode-locked femtosecond forsterite laser with a semiconductor saturable-absorber mirror," *Opt. Lett.*, vol. 22, pp. 1006-1008, 1997.

[90] B. C. Collins, J. B. Stark, S. Tsuda, W. H. Knox, J. E. Cunningham, W. Y. Jan, R. Pathak, and K. Bergman, "Saturable Bragg reflector self-starting passive mode locking of a Cr^{4+}:YAG laser pumped with a diode-pumped Nd:YVO_4 laser," *Opt. Lett.*, vol. 21, pp. 1171-1173, 1996.

[91] S. Spälter, M. Böhm, M. Burk, B. Mikulla, R. Fluck, I. D. Jung, G. Zhang, U. Keller, A. Sizmann, and G. Leuchs, "Self-starting soliton-modelocked femtosecond Cr(4+):YAG laser using an antiresonant Fabry-Perot saturable absorber," *Appl. Phys. B*, vol. 65, pp. 335-338, 1997.

[92] M. Hayduk, S. T. Johns, M. F. Krol, C. R. Pollock, and R. P. Leavitt, "Self-starting passively mode-locked tunable femtosecond Cr^{4+}:YAG laser using a saturable absorber mirror," *Opt. Comm.*, vol. 137, pp. 55-58, 1997.

[93] B. Braun, C. Hönninder, G. Zhang, U. Keller, F. Heine, T. Kellner, and G. Huber, "Efficient intracavity frequency doubling of a passively modelocked diode-pumped Nd:LSB laser," *Opt. Lett.*, vol. 21, pp. 1567-1569, 1996.

[94] R. Fluck, B. Braun, E. Gini, H. Melchior, and U. Keller, "Passively Q-switched 1.34-μm Nd:YVO_4 microchip laser with semiconductor saturable-absorber mirrors," *Opt. Lett.*, vol. 22, pp. 991-993, 1997.

[95] D. Kopf, A. Prasad, G. Zhang, M. Moser, and U. Keller, "Broadly tunable femtosecond Cr:LiSAF laser," *Opt. Lett.*, vol. 22, pp. 621-623, 1997.

[96] D. H. Sutter, I. D. Jung, F. X. Kärtner, N. Matuschek, F. Morier-Genoud, V. Scheuer, M. Tilsch, T. Tschudi, and U. Keller, "Self-starting 6.5-fs pulses from a Ti:sapphire laser using a semiconductor saturable absorber and double chirped mirrors," *IEEE J. Selected Top. Quantum Electron.*, vol. 4, pp. 169-178, 1998.

[97] D. H. Sutter, I. D. Jung, N. Matuschek, F. Morier-Genoud, F. X. Kärtner, U. Keller, V. Scheuer, M. Tilsch, and T. Tschudi, "300 nm tunability of a 30-fs Ti:sapphire laser pulses with a single set of double-chirped mirrors," presented at Conference on Lasers and Electro-Optics, San Francisco, 1998.

[98] S. Tsuda, W. H. Knox, and S. T. Cundiff, "High efficiency diode pumping of a saturable Bragg reflector-mode-locked Cr:LiSAF femtosecond laser," *Appl. Phys. Lett.*, vol. 69, pp. 1538-1540, 1996.

[99] K. J. Weingarten, U. Keller, T. H. Chiu, and J. F. Ferguson, "Passively mode-locked diode-pumped solid-state lasers using an antiresonant Fabry-Perot saturable absorber," *Opt. Lett.*, vol. 18, pp. 640-642, 1993.

[100] R. Fluck, G. Zhang, U. Keller, K. J. Weingarten, and M. Moser, "Diode-pumped passively mode-locked 1.3-μm Nd.:YVO_4 and Nd:YLF lasers by use of semiconductor saturable absorbers," *Opt. Lett.*, vol. 21, pp. 1378-1380, 1996.

[101] Z. Zhang, K. Torizuka, T. Itatani, K. Kobayashi, T. Sugaya, and T. Nakagawa, "Femtosecond Cr:forsterite laser with mode locking initiated by a quantum-well saturable absorber," *IEEE J. Quantum Electron.*, vol. 33, pp. 1975-1981, 1997.

[102] H. A. Macleod, *Thin film optical filters*. New York: American Elsevier Publishing Company, 1969.

[103] H. M. Liddell, *Computer-aided techniques for the design of multilayer filters*. Bristol: Adam Hilger Ltd., 1981.

[104] S. Adachi, "GaAs, AlAs, and AlGaAs: Material parameters for use in research and device applications," *J. Appl. Phys.*, vol. 58, pp. R1-R28, 1985.

[105] *GaInAsP Alloy Semiconductors*: John Wiley & Sons Ltd., 1982.

[106] J. A. Dobrowolski and R. A. Kemp, "Refinement of optical multilayer systems with different optimization procedures," *Appl. Opt.*, vol. 29, pp. 2876-2893, 1990.

[107] P. Chaton, P. Pinston, and J. P. Gailliard, "Synthesis of optical coatings using a simulated thermal annealing algorithm," presented at Optical Interference Coatings, 1994.

[108] M. D. Dvorak and B. L. Justus, "Z-scan studies of nonlinear absorption and refraction in bulk, undoped InP," *Opt. Comm.*, vol. 114, pp. 147-150, 1995.

[109] B. S. Wherrett, "Scaling rules for multiphoton interband absorption in semiconductors," *J. Opt. Soc. Am. B*, vol. 1, pp. 67-72, 1984.

[110] A. T. Obeidat, W. H. Knox, and J. B. Khurgin, "Effects of two-photon absorption in saturable Bragg reflectors used in femtosecond solid state lasers," *Opt. Express*, vol. 1, 1997.

[111] E. Thoen, unpublished data, 1997.

[112] K. Sedeeek, "Influence of As excess on the optical properties of amorphous GaAs," *J. Phys. D*, vol. 26, pp. 130-132, 1993.

[113] M. I. Mansoor and E. A. Davis, "Optical and electrical characteristics of a-GaAs and a-AlGaAs prepared by radio-frequency sputtering," *J. Phys.: Condens. Matter*, vol. 2, pp. 8063-8074, 1990.

[114] M. R. Harwood and D. E. Brodie, "Some properties of flash-evaporated $Ga_{1-x}As_x$ films," *Can. J. Phys.*, vol. 69, pp. 738-742, 1991.

[115] S. Tsuji and E. Iri, "Poly-GaAs thin film deposited on silica substrate by RF sputtering and its light transmissional characteristics," *Jpn. J. Appl. Phys.*, vol. 25, pp. L896-898, 1986.

[116] U. Coscia, R. Murri, N. Pinto, and L. Trojani, "Photoconductivity of amorphous GaAs," *J. Non-Cryst. Solids*, vol. 194, pp. 103-108, 1996.

[117] A. Maslyukov, S. Sokolov, M. Kaivola, K. Nyholm, and S. Popov, "Solid-state dye laser with modified poly(methyl methacrylate)-doped active elements," *Appl. Opt.*, vol. 34, pp. 1516-1518, 1995.

[118] A. Costela, I. Garcia-Moreno, J. M. Figuera, F. Amat-Guerri, R. Mallavia, M. D. Santa-Maria, and R. Sastre, "Solid-state dye lasers based on modified rhodamine 6G dyes copolymerized with the methacrylic monomers," *J. Appl. Phys.*, vol. 80, pp. 3167-3173, 1996.

[119] R. Hermes, T. H. Alik, and S. Chandra, "High-efficiency pyrromethene doped solid-state dye lasers," *Appl. Phys. Lett.*, vol. 63, pp. 877-879, 1993.

[120] M. Canva, P. Georges, J.-F. Perelgritz, A. Brum, F. Chaput, and J.-P. Boilot, "Perylene- and pyrromethene-doped xerogel for a pulsed laser," *Appl. Opt.*, vol. 34, pp. 428-431, 1995.

[121] M. C. Nuss, W. Zinth, and W. Kaiser, "Femtosecond carrier relaxation in semiconductor-doped glasses," *Appl. Phys. Lett.*, vol. 49, pp. 1717-1719, 1986.

[122] D. W. Hall and N. F. Borelli, "Absorption saturation in commercial and quantum-confined $CdSe_xS_{1-x}$-doped glasses," *J. Opt. Soc. Am. B*, vol. 5, pp. 1650-1654, 1988.

[123] N. Sarukura, Y. Ishida, and T. Yanagawa, "All solid-state cw passively mode-locked Ti:sapphire laser using a colored glass filter," *Appl. Phys. Lett.*, vol. 57, pp. 229-230, 1990.

[124] L. Banyai and S. W. Koch, *Semiconductor quantum dots*. Singapore: World Scientific, 1993.

[125] U. Woggon, *Optical properties of semiconductor quantum dots*. Berlin Heidelberg: Springer-Verlag, 1997.

[126] H. P. Rockby, *J. Soc. Glass Techn.*, vol. 16, pp. 171, 1932.

[127] L. D. Landau and E. M. Lifshitz, *Quantum mechanics: non-relativistic theory.* Oxford New York: Pergamon Press, 1977.

[128] J. J. Sakurai, *Modern quantum mechanics*. Reading: Addison-Wesley, 1994.

[129] L. Brus, "Quantum crystallites and nonlinear optics," *Appl. Phys. A*, vol. 53, pp. 465-474, 1991.

[130] G. L. Huang and H. S. Kwok, "Femtosecond dephasing times in semiconductor microcrystals measured with incoherent light," *J. Opt. Soc. Am. B*, vol. 1992, pp. 2019-2024, 1992.

[131] S. V. Gaponenko, "Optical processes in semiconductor nanocrystallites (quantum dots)," *Semiconductors*, vol. 30, pp. 315-336, 1996.

[132] L. H. Acioli, A. S. L. Gomes, J. M. Hickmann, and C. B. d. Araujo, "Femtosecond dynamics of semiconductor-doped glasses using a new source of incoherent light," *Appl. Phys. Lett.*, vol. 56, pp. 2279-2281, 1990.

[133] D. M. Mittleman, R. W. Shoenlein, J. J. Shiang, V. L. Colvin, A. P. Alivisatos, and C. V. Shank, "Quantum size dependence of femtosecond electronic dephasing and vibrational dynamics in CdSe nanocrystals," *Phys. Rev. B*, vol. 49, pp. 14435-14447, 1994.

[134] J. C. Maxwell-Garnett, *Philos. Trans. R. Soc. London*, vol. 203, pp. 385, 1904.

[135] K. C. Rustagi and C. Flytzanis, "Optical nonlinearities in semiconductor-doped glasses," *Opt. Lett.*, vol. 9, pp. 344-347, 1984.

[136] H. Bach and N. Neuroth, *The properties of optical glass*. Berlin Heidelberg New York: Springer-Verlag, 1995.

[137] R. K. Jain and R. C. Lind, "Degenerate four-wave mixing in semiconductor-doped glasses," *J. Opt. Soc. Am.*, vol. 73, pp. 647-653, 1983.

[138] A. I. Ekimov, F. Hache, M. C. Schanne-Klein, D. Ricard, C. Flytzanis, I. A. Kudryavtsev, T. V. Yazeva, A. V. Rodina, and A. L. Efros, "Absorption and intensity-dependent photoluminescence measurements on CdSe quantum dots: assignment of the first electronic transitions," *J. Opt. Soc. Am. B*, vol. 10, pp. 100-107, 1993.

[139] W. Wittmann and A. Penzkofer, "Spectroscopic characterization of semiconductor doped colour filter glasses," *Opt. and Quantum Electron.*, vol. 27, pp. 705-724, 1995.

[140] R. Roussignol, D. Ricard, J. Lukasik, and C. Flytzanis, "New results on optical phase conjugation in semiconductor-doped glasses," *J. Opt. Soc. Am. B*, vol. 4, pp. 5-13, 1987.

[141] C. Flytzanis, D. Ricard, and M. C. Schanne-Klein, "The role of photodarkening and Auger recombination in the dynamics of the optical response for Cd(S,Se) nanoparticles," *J. Luminesc.*, vol. 70, pp. 212-221, 1996.

[142] M. Tomita and M. Matsuoka, "Laser-induced irreversible change of the carrier-recombination process in CdS_xSe_{1-x}-doped glasses," *J. Opt. Soc. Am B*, vol. 7, 1990.

[143] J. Malhorta, D. J. Hagan, and B. G. Potter, "Laser-induced darkening in semiconductor-doped glasses," *J. Opt. Soc. Am. B*, vol. 8, pp. 1531-1536, 1991.

[144] P. Nemec, F. Trojanek, and P. Maly, "Effect of photodarkening on dynamics of visible and infrared photoluminescence in CdS_xSe_{1-x}-doped glass," *Phys. Rev. B*, vol. 52, pp. R8605-8608, 1995.

[145] M. Mitsunaga, H. Shinojima, and K. Kubodera, "Laser annealing effect on carrier recombination time in CdS_xSe_{1-x}-doped glasses," *J. Opt. Soc. Am. B*, vol. 5, pp. 1448-1452, 1988.

[146] H. W. Kogelnik, E. P. Ippen, A. Dienes, and C. V. Shank, "Astigmatically compensated cavities for cw dye lasers," *IEEE J. Quantum Electron.*, vol. 8, pp. 373-379, 1972.

[147] K. Tsunetomo, H. Nasu, H. Kitayama, A. Kawabuchi, Y. Osaka, and K. Takiyama, "Quantum size effect of semiconductor microcrystallites doped in $Si0_2$-glass thin films prepared by RF sputtering," *Jpn. J. Appl. Phys.*, vol. 28, pp. 1928-1933, 1989.

[148] I. Tanahashi, A. Tsujimura, T. Mitsuyu, and A. Nishino, "Optical properties of CdS microcrystallite-doped SiO_2 glass thin films," *Jpn. J. Appl. Phys.*, vol. 29, pp. 2111-2115, 1990.

[149] B. G. Potter and J. H. Simmons, "Quantum confinement effects in CdTe-glass composite thin films produced using rf magnetron sputtering," *J. Appl. Phys.*, vol. 68, pp. 1218-1224, 1990.

[150] M. Hirasawa, N. Ichikawa, Y. Egashira, I. Honma, and H. Komiyama, "Synthesis of GaAs nanoparticles by digital radio frequency sputtering," *Appl. Phys. Lett.*, vol. 67, pp. 3483-3485, 1995.

[151] S. Ohtsuka, K. Tsunetomo, T. Koyama, and S. Tanaka, "Embedment of gold and CdTe particles in glass matrix and their nonlinear optical properties," *Nonlin. Opt.*, vol. 13, pp. 101-108, 1995.

[152] K. Tsunetomo, S. Ohtsuka, T. Koyama, S. Tanaka, F. Sasaki, and S. Kobayashi, "Ultrafast nonlinear optical response of CdTe microcrystallite-doped glasses fabricated by laser evaporation," *Nonlin. Opt.*, vol. 13, pp. 109-126, 1995.

[153] K. Tsunetomo, R. Shimizu, A. Kawabuchi, H. Kitayama, and Y. Osaka, "CuCl microcrystallite-doped SiO_2 glass thin films prepared by RF sputtering," *Jpn. J. Appl. Phys.*, vol. 30, pp. L764-L767, 1991.

[154] Y. Maeda, N. Tsukamoto, Y. Yazawa, Y. Kanemitsu, and Y. Masumoto, "Visible photoluminescence of Ge microcrystals imbedded in SiO_2 glassy matrices," *Appl. Phys. Lett.*, vol. 59, pp. 318-3170, 1991.

[155] M. Yamamoto, R. Hayashi, K. Tsunetomo, K. Kohno, and Y. Osaka, "Preparation and properties of Si microcrystals embedded in SiO_2 glass films," *Jpn. J. Appl. Phys.*, vol. 30, pp. 136-142, 1991.

[156] K. Tsunetomo, M. Yamamoto, and Y. Osaka, "Preparation and properties of $In_xGa_{1-x}As$ microcrystallites embedded in $Si0_2$ glass films," *Jpn. J. Appl. Phys.*, vol. 30, pp. L521-L524, 1991.

[157] R. F. Bunshah, *Handbook of deposition technologies for films and coatings*. Park Ridge: Noyes Publications, 1994.

[158] L. S. Wang, M. S. Lin, C. S. Yoo, and F. S. Huang, "Improvement of oxide quality by rapid thermal annealing in N_2," *J. Appl. Phys.*, vol. 74, pp. 3966-3969, 1993.

[159] B. H. Augustine, Y. Z. Hu, and E. A. Irene, "An annealing study of luminescent amorphous silicon-rich oxynitride thin films," *Appl. Phys. Lett.*, vol. 67, pp. 3694-3696, 1995.

[160] M. L. Reed and J. D. Plummer, "Chemistry of Si-SiO_2 interface trap annealing," *J. Appl. Phys.*, vol. 63, pp. 5776-5793, 1988.

[161] A. Barhdadi, H. Amzil, J. C. Muller, and P. Siffert, "Thermal annealing effects on grain boundary recombination activity in silicon," *Appl. Phys. A*, vol. 49, pp. 233-237, 1989.

[162] C. Rogers, personal communication, 1998.

[163] O. Madelung, *Semiconductors: group IV elements and III-V compounds*. Berlin New York: Springer-Verlag, 1991.

[164] S. Hüfner, *Photoemission spectroscopy.* Berlin Heidelberg New York: Springer-Verlag, 1995.

[165] M. D. Crescenzi and M. N. Pincastelli, *Electron scattering and related spectroscopies.* Singapore: World Scientific, 1996.

[166] Briggs, *Handbook of x-ray and ultraviolet photoelectron spectroscopy.* London Philadelphia Rheine: Heyden, 1977.

[167] C. D. Wagner, W. M. Riggs, L. E. Davis, J. F. Moulder, and G. E. Muilenberg, *Handbook of x-ray photoemission spectroscopy.* Edem Prairie MN: Perkin-Elmer Corporation, 1979.

[168] J. Russ, *Fundamentals of energy dispersive x-ray analysis.* London Boston: Butterworths, 1984.

[169] B. E. P. Beeston, R. W. Horne, and R. Markham, "Electron diffraction and optical diffraction techniques," in *Practical methods in electron microscopy part 2*, A. Glauert, Ed. Amsterdam New York Oxford: North-Holland, 1979.

[170] B. D. Cullity, *Elements of x-ray diffraction.* Reading Menlo Park: Addison-Wesley, 1980.

[171] A. A. Guzelian, U. Banin, A. V. Kadavanich, X. Peng, and A. P. Alivisatos, "Colloidal chemical synthesis and characterization of InAs nanocrystal quantum dots," *Appl. Phys. Lett.*, vol. 69, pp. 1432-1434, 1996.

[172] J. Tauc, "Optical properties of amorphous semiconductors," in *Amorphous and liquid semiconductors*, J. Tauc, Ed. London and New York: Plenum Press, 1974.

[173] K. Seeger, *Semiconductor physics.* Berlin Heidelberg New York: Springer-Verlag, 1982.

[174] M. Sheik-Bahae, A. A. Said, T. H. Wei, D. J. Hagan, and E. W. V. Stryland, "Sensitive measurement of optical nonlinearities using a single beam," *IEEE J. Quantum Electron.*, vol. 26, pp. 760-769, 1990.

[175] B. D. Bartolo, *Optical interaction in solids.* New York: John Wiley & Sons, 1968.

[176] *Handbook of optics*: McGraw-Hill Inc., 1995.

[177] F. X. Kärtner, J. A. d. Au, and U. Keller, "Modelocking with slow and fast saturable absorbers - what's the difference?," *IEEE J. Selected Top. Quantum Electron.*, vol. 4, pp. 159-168, 1998.

[178] F. X. Kärtner, personal communication, 1998.

[179] U. Morgner, F.X. Kärtner, S. Cho, Y. Chen, H.A. Haus, J.G. Fujimoto, E.P. Ippen, V. Scheuer, G. Angelow, T. Tschudi, "5.5 fs pulses from a Kerr-lens modelocked Ti:sapphire laser," *submitted to Optics Letters*, 1998.